



Politecnico di Bari

Repository Istituzionale dei Prodotti della Ricerca del Politecnico di Bari

Seismic fragility and risk assessment of large bridge portfolios: efficient mechanical approaches based on multi-source data collection and integration

This is a PhD Thesis

Original Citation:

Seismic fragility and risk assessment of large bridge portfolios: efficient mechanical approaches based on multi-source data collection and integration / Nettis, Andrea. - ELETTRONICO. - (2021). [10.60576/poliba/iris/nettis-andrea_phd2021]

Availability:

This version is available at <http://hdl.handle.net/11589/229598> since: 2021-11-05

Published version

DOI:10.60576/poliba/iris/nettis-andrea_phd2021

Publisher: Politecnico di Bari

Terms of use:

(Article begins on next page)



D.R.R.S

POLITECNICO DI BARI

10

PhD Program in Environmental and Building Risk and Development

2021

Coordinator: Prof. Michele Mossa

XXXIII CYCLE
ICAR/09 – Structural Engineering

DICATECh
Department of Civil, Environmental, Building Engineering and Chemistry

Seismic fragility and risk assessment of large bridge portfolios: efficient mechanical approaches based on multi-source data collection and integration

Prof. Giuseppina Uva
Prof. Eufemia Tarantino
Prof. Domenico Raffaele
Department of Civil, Environmental, Land, Building Engineering and Chemistry
Politecnico di Bari

Prof. Jose M. Adam
ICITECH
Universitat Politècnica de Valencia

Eng. Sergio Samarelli
Planetek Italia s.r.l.

Andrea Nettis



POLITECNICO DI BARI

D.R.R.S

10

Dottorato di Ricerca in Rischio e Sviluppo ambientale, territoriale ed edilizio

2021

Coordinator: Prof. Michele Mossa

XXXIII CICLO

ICAR/09 – Tecnica delle costruzioni

DICATECh

Dipartimento di Ingegneria Civile, Ambientale, del Territorio, Edile e di Chimica

Valutazione di fragilità e rischio sismico di inventari estesi di viadotti: efficienti approcci meccanici basati su raccolta e integrazione di dati multi-sorgente

Prof. Giuseppina Uva
Prof. Eufemia Tarantino
Prof. Domenico Raffaele
Dipartimento di Ingegneria Civile, Ambientale, del Territorio, Edile e di Chimica
Politecnico di Bari

Prof. Jose M. Adam
ICITECH
Universitat Politècnica de Valencia

Eng. Sergio Samarelli
Planetek Italia s.r.l.

Andrea Nettis

Extended Abstract

The safety of transportation infrastructure systems is essential for the economic and social development of modern countries and the resilience of populated contexts concerning natural hazards. The research activity oriented to the understanding and reduction of disaster risk for people and assets, such as transportation infrastructure systems, is indeed explicitly promoted in the Nations (2015) within the *Transforming our World: The 2030 Agenda for Sustainable Development (A/RES/70/1)* (2015) by the United Nations. Particularly, the structural vulnerability of bridges and viaducts, which are key components of the roadway or railway infrastructure, is of strong concern for transportation authorities and other stakeholders. In earthquake-prone countries, most of the existing bridges were designed in the past decades without appropriate anti-seismic regulations and can induce important direct or indirect losses if subjected to severe seismic ground shaking. The main challenges in the extensive seismic risk assessment of existing bridge portfolios are related to the large number of existing structures to be inspected and the limited available resources (e.g. time and cost) to deal with it. In this context, this dissertation investigates efficient (i.e. low time and cost demand) methodologies for data collection and probabilistic seismic assessment algorithms for bridges to be used for calculating seismic risk metrics within portfolio analysis.

The first Chapter aims to propose low-demanding data collection approaches to deal with the lack of knowledge data on existing bridges and lack of resources to perform accurate on-site surveys. Methodologies for multi-source data collection and integration suitable for structural (and particularly seismic) vulnerability assessment of bridge portfolios are presented. The applicability of remote-sensing data is discussed, analysing

the potentials of different data sources in populating bridge inventories. Recommendations for performing observation-based data gathering utilizing street-view images and appropriate data forms are listed. A methodology to adopt Remotely Piloted Aircraft Systems (RPAS) coupled with photogrammetry techniques to retrieve exhaustive geometric/constructive information of bridges is described. These data collection approaches are applied to eight case-study bridges part of the Basilicata road network. For one of these, an RPAS-based data collection methodology is illustrated.

The second and third Chapters investigate bridge-specific seismic performance assessment procedures which represent a trade-off between accuracy and simplicity to be used for large portfolio analysis. Analytical displacement-based assessment (DBA) approaches, coupled with the capacity spectrum method (CSM) for multi-span bridges are investigated. The second Chapter deals with reinforced-concrete (RC) continuous-deck bridges. After describing the modal analysis-based DBA procedure proposed in the literature, a static analysis-based alternative is proposed. Moreover, an extension of the procedure is proposed to derive the force-displacement curve of the investigated bridge. Both the DBA versions are applied through simplified mechanical models. The effectiveness of these algorithms is discussed through a main parametric analysis (36 case-study bridges up to six spans, varying the height of the piers and the deck transverse stiffness). Additional sensitivity analyses (24 case studies) are performed to investigate the accuracy of the DBA approaches considering "long" bridges (up to 12 spans), the amount of longitudinal reinforcement in the piers and different pier typologies. The results are compared to other nonlinear static procedures and nonlinear time-history analyses. Based on the outcomes, practical recommendations for the applicability of DBA approaches depending on the structural characteristics of the investigated bridge are provided. In the third Chapter, the effectiveness of the DBA and CSM is tested for historical steel truss railway bridges with supporting steel tower. These bridges, although built in the first part of the 20th century, are currently in service on the European railway networks and their seismic performance is poorly discussed in the literature. An effective equivalent viscous damping formulation is proposed for the performance assessment of steel towers via the CSM. Subsequently, algorithms based on the DBA and CSM for the direct seismic performance assessment of hyperstatic steel truss bridges

under a given seismic action are presented. These are applied on case-study bridges generated via a parametric analysis using a real archetype bridge. Nonlinear time-history analyses are used for benchmarking the accuracy of the simplified approaches.

The fourth Chapter investigates the use of the CSM for fragility analysis of structures. Specifically, the application of the CSM with real (i.e. recorded) ground-motion spectra (as opposed to code-based conventional spectra) to explicitly consider record-to-record variability in fragility analysis is evaluated. The CSM with real spectra is combined with a cloud-based approach (Cloud-CSM) to derive fragility relationships. The study focuses on single-degree-of-freedom systems, intending to provide an essential basis for future multi-degree-of-freedom system applications. A case-study database of 2160 inelastic oscillators is defined through parametric backbones with different elastic periods, (yield) base shear coefficients, values of the ductility capacity, hardening ratios, residual strength values and hysteresis rules. The considered parametric case studies are representative of bridge components (e.g. RC-piers and bearing devices), but also of other structural typologies. These case studies are analysed through 100 real ground motions. The effectiveness of the proposed Cloud-CSM is discussed through extensive comparisons with nonlinear time-history analyses, the code-based N2 method, and a simple method involving an intensity measure as a direct proxy for the performance displacement.

The final Chapter of this dissertation proposes a framework for seismic risk assessment of bridges combining a multi-source data integration, and efficient seismic assessment approaches including the above-mentioned simplified methodologies (i.e. DBA and Cloud-CSM). Fragility functions and seismic risk metrics are calculated accounting for the influence of knowledge-based uncertainties associated with incomplete data collection. The proposed approach can be used for risk-based prioritisation within portfolio analyses, and to target refined inspections on structures where a relevant impact on seismic risk is expected, optimising the involved resources. The approach is based on the statistical generation of a population of index-bridges, which are analysed via analytical seismic performance assessment approaches and the Cloud-CSM. A population of fragility curves for the index-bridge dataset is calculated and used to quantify the fragility/risk of the main bridge and the influence of epistemic uncertainty by ex-

tracting appropriate fragility percentiles. The proposed approach is applied on eight simply-supported RC bridges of the Basilicata national road network. The influence of the knowledge-based uncertainty on both the fragility and the seismic risk (i.e. mean annual frequency of exceeding a limit state) is discussed depending on specific bridge structural features. The bias involved by this simplified approach is evaluated through a comparison with nonlinear time history analyses on refined numerical models.

Keywords

RC bridges, steel truss bridges, seismic risk, fragility analysis, capacity spectrum method, nonlinear time history analysis, pushover analysis, displacement-based assessment, cloud analysis

Sommario Esteso

La sicurezza delle infrastrutture di trasporto è essenziale per lo sviluppo economico e sociale dei Paesi moderni e la resilienza dei contesti popolati rispetto ad eventi catastrofici naturali. La ricerca orientata alla comprensione e riduzione dei rischi legati a disastri da causa artificiale o naturale sull'ambiente costruito, e quindi le infrastrutture di trasporto, viene esplicitamente promossa dal Nations (2015) nell'ambito del documento *Transforming our World: The 2030 Agenda for Sustainable Development (A/RES/70/1)* (2015) emessa dall'Assemblea Generale delle Nazioni Unite. La vulnerabilità strutturale di ponti e viadotti, componenti chiave dell'infrastruttura stradale o ferroviaria, è di crescente interesse per le autorità di trasporto e vari portatori di interesse. Nei paesi soggetti a forte sismicità, i viadotti esistenti possono indurre importanti perdite dirette o indirette se sottoposti a forti scosse sismiche, poiché queste strutture sono state per lo più progettate in passato senza adeguate normative antisismiche. Le sfide principali nell'estesa valutazione del rischio sismico di *portfolios* di viadotti esistenti sono legate all'elevato numero di strutture da ispezionare e alle limitate risorse disponibili (e.g. tempi e costi). In questo contesto, questa tesi indaga metodologie efficienti (bassa domanda di risorse impiegate) per la raccolta dei dati e la valutazione sismica probabilistica dell'analisi di *portfolios* di viadotti da utilizzare per il calcolo di misure di rischio sismico.

Il primo capitolo propone approcci di raccolta dati efficienti per affrontare il problema della mancanza di dati di conoscenza sui viadotti esistenti e di risorse per eseguire indagini accurate in loco. Vengono presentate metodologie multi-sorgente per la raccolta dei dati adatte alla valutazione della vulnerabilità strutturale (e in particolare sismica) di *portfolios* di viadotti. Viene discussa l'applicabilità dei set di dati acquisiti con tecni-

che di telerilevamento, analizzando le potenzialità di diverse fonti nel popolamento degli inventari dei viadotti. Sono proposte raccomandazioni per eseguire la raccolta di dati basata sull'osservazione utilizzando immagini di street view e moduli appropriati. Inoltre, viene descritta una metodologia per applicare sistemi di aeromobili a pilotaggio remoto (RPAS) accoppiati a tecniche di fotogrammetria per recuperare informazioni geometriche/costruttive esaurienti. Questi approcci vengono applicati a otto viadotti casi-studio che fanno parte della rete stradale della Basilicata. Per uno di questi, viene illustrata una metodologia di raccolta dati basata su RPAS.

Il secondo e il terzo capitolo esaminano procedure analitiche semplificate di valutazione delle prestazioni sismiche (o di domanda sismica) di viadotti da utilizzare in analisi di *portfolio*. Vengono studiati approcci analitici di valutazione basata sullo spostamento (DBA), accoppiati con il *capacity spectrum method* (CSM) per viadotti multi-campata. Il secondo capitolo tratta di viadotti a travata continua in calcestruzzo armato. Dopo aver descritto la procedura DBA basata sull'analisi modale proposta in letteratura, viene proposta un'alternativa basata sull'analisi statica. Inoltre, viene proposta un'estensione della procedura per derivare la curva forza-spostamento dell'opera indagata. Entrambe le versioni DBA vengono applicate tramite modelli meccanici semplificati. L'efficacia di questi algoritmi viene discussa attraverso un'analisi parametrica principale (36 casi studio viadotti fino a sei campate, variando l'altezza del pilastro e la rigidità trasversale dell'impalcato). Ulteriori analisi di sensibilità (24 casi di studio) vengono eseguite per indagare l'accuratezza degli approcci DBA considerando viadotti "lunghi" (fino a 12 campate), la quantità di rinforzo longitudinale nelle pile monofusto e diverse tipologie di pila. I risultati vengono confrontati con altre procedure statiche non lineari e analisi *time-history* non lineari. Sulla base dei risultati, vengono fornite raccomandazioni pratiche per l'applicabilità degli approcci DBA a seconda delle caratteristiche strutturali del viadotto studiato. Nel terzo capitolo viene testata l'efficacia del DBA e del CSM per i viadotti ferroviari storici a traliccio in acciaio con sottostruttura composta da torri tralicciate in acciaio. Questi viadotti, sebbene costruiti nella prima parte del XX secolo, sono attualmente in servizio sulle reti ferroviarie europee e le loro prestazioni sismiche sono scarsamente discusse in letteratura. Viene proposta una formulazione di smorzamento viscoso equivalente efficace per la valutazione delle prestazioni delle torri in acciaio

tramite il CSM. Successivamente, vengono presentati algoritmi basati su DBA e CSM per la valutazione diretta delle prestazioni sismiche di viadotti reticolari iperstatici in acciaio sotto una data azione sismica. Questi vengono applicati su un set di casi studio generati tramite un'analisi parametrica basata su un caso archetipo. Analisi *time-history* non lineari vengono utilizzate per valutare l'accuratezza degli approcci semplificati.

Il quarto capitolo studia l'uso di approcci semplificati basati sul CSM per analisi di fragilità. In particolare, viene valutata l'applicazione del CSM con spettri di risposta reali (i.e. registrati) (al contrario degli spettri convenzionali basati su forme "liscie" da codice) per considerare esplicitamente la variabilità da record a record nell'analisi di fragilità. Il CSM con spettri reali è combinato con un approccio basato su *cloud* (Cloud-CSM) per derivare funzioni di fragilità. Lo studio si rivolge a sistemi a un grado di libertà, con l'intenzione di fornire una base essenziale per le future applicazioni di sistemi a più gradi di libertà. Un database di casi studio di 2160 oscillatori inelastici è definito attraverso *backbones* parametriche aventi diversi periodi elastici, coefficienti di taglio alla base (di snervamento), valori di duttilità, rapporti di incrudimento, valori di resistenza residua e legge ciclica di isteresi. I casi studio parametrici considerati sono rappresentativi di componenti strutturali di viadotti (es. pile in c.a. e dispositivi di appoggio), ma anche di altre tipologie strutturali. Questi casi studio vengono analizzati utilizzando 100 registrazioni di scuotimenti al suolo reali. L'efficacia del Cloud-CSM proposto viene discussa attraverso confronti con analisi *time-history* non lineari, il metodo N2 basato su codice e un metodo semplice che usa una misura di intensità come proxy diretto per lo spostamento di domanda.

Il capitolo finale di questa tesi propone un quadro per la valutazione del rischio sismico dei viadotti che combina una raccolta dati efficiente e approcci analitici di valutazione di domanda e rischio sismico, comprese le metodologie semplificate di cui sopra. Le funzioni di fragilità e le misure di rischio sismico sono calcolate tenendo conto dell'influenza delle incertezze basate sulla conoscenza associate ad un eventuale raccolta dei dati incompleta. L'approccio proposto può essere utilizzato per la prioritizzazione basata sul rischio all'interno delle analisi di *portfolio* e per mirare a ispezioni raffinate su strutture in cui è previsto un impatto rilevante del processo conoscitivo sul rischio sismico, ottimizzando le risorse coinvolte. L'approccio si basa sulla generazione statistica di una

popolazione di viadotti indice, che vengono analizzati tramite approcci analitici di valutazione di domanda sismica e Cloud-CSM. Una popolazione di curve di fragilità per il dataset di viadotti indice viene calcolata e utilizzata per quantificare la fragilità/rischio del viadotto principale. L'influenza dell'incertezza epistemica è rappresentata da percentili estratti dalla popolazione di funzioni fragilità. L'approccio proposto è applicato su otto viadotti in c.a. a travata semplicemente appoggiata, esistenti sulla rete stradale nazionale della Basilicata. L'influenza dell'incertezza basata sulla conoscenza, sia sulla fragilità che sul rischio sismico, viene discussa in base alle caratteristiche strutturali specifiche dell'opera. Il bias indotto dall'approccio semplificato viene valutato attraverso un confronto con un approccio di modellazione raffinato e analisi *time-history* non lineare.

Parole chiave

viadotti in C.A., viadotti tralicciati in acciaio, rischio sismico, analisi di fragilità, capacity spectrum method, analisi dinamica non lineare, analisi statica non lineare, displacement-based assessment, analisi cloud

Contents

1	Introduction	19
1.1	Seismic assessment of bridges: background	19
1.2	Framework for seismic risk analysis	24
1.3	Research motivations	26
1.4	Objectives	29
1.5	Outline of the dissertation	31
2	Multi-source data collection for seismic vulnerability of bridge portfolios	35
2.1	Multi-source data collection for large bridge portfolios	36
2.1.1	Remote-sensing methodologies	37
2.1.2	Street view-based surveys	40
2.1.3	RPAS-based surveys and photogrammetry	42
2.1.4	Multilevel approaches	44
2.2	Methodology for RPAS-based photogrammetry for structural data gathering of bridges	46
2.2.1	Recommendations for RPAS-based survey	46
2.2.2	Structure-from-Motion techniques for 3D modelling	49
2.2.3	Further applications of 3D models by RPAS-based photogrammetry	51
2.3	Case study: application of multi-source data collection and integration	52
2.3.1	Screening and case-study identification	52
2.3.2	Data acquired on case-study bridges	57
2.3.3	Application of RPAS-based survey	60
2.4	Summary	66
3	Effectiveness of the displacement-based seismic performance assessment for continuous RC bridges and proposed extensions	69

3.1	Introduction and motivation	70
3.2	Description of the DBA for bridges and proposed extensions	73
3.2.1	Overview of the DBA procedure based on modal analysis	73
3.2.2	Proposed alternative DBA procedure based on static analysis	77
3.2.3	Analytical displacement-based pseudo pushover	79
3.2.4	Overview of the capacity spectrum method	81
3.3	Assumptions for the parametric analysis	82
3.3.1	Description of the case study bridges	82
3.3.2	Assumptions for analytical and numerical analyses	84
3.3.3	Seismic demand	86
3.4	Results of the parametric analyses	87
3.4.1	Calculation of the capacity demand ratio and the bridge index	87
3.4.2	Detailed results for selected bridge case studies	88
3.4.3	Discussion of the results considering the entire dataset	93
3.4.4	Sensitivity analysis for long bridges	96
3.4.5	Further sensitivity analyses	100
3.5	Application to real continuous-deck bridges	102
3.5.1	Description of the case-study bridges	103
3.5.2	Modelling strategy and analysis assumptions	103
3.5.3	Eigenvalue analysis	105
3.5.4	Discussion of the results in transverse direction	105
3.5.5	Analysis in longitudinal direction	107
3.6	Conclusions	109

4 Displacement-based seismic performance assessment for multi-span steel truss bridges 113

4.1	Introduction and motivations	114
4.2	Description of the archetype bridge	117
4.3	Seismic performance assessment of steel braced towers	118
4.3.1	Description of the modelling strategy	119
4.3.2	Seismic analysis procedures	122

4.3.3	Damage states and seismic response of steel towers under monotonic loading	125
4.3.4	Seismic action	128
4.3.5	Equivalent viscous damping strategies for seismic performance assessment of steel towers	129
4.4	Displacement-based assessment of continuous truss deck bridges . .	136
4.4.1	Description of the analysis approaches	137
4.4.2	Case study bridges and modelling assumptions	141
4.4.3	Results of the parametric analysis	143
4.5	Conclusions	149
5	Cloud-CSM: including record-to-record variability in fragility analysis using the capacity spectrum method	151
5.1	Introduction and motivation	152
5.2	Methodology	155
5.2.1	Considered SDoF case-study database and seismic action . .	156
5.2.2	Proposed CSM algorithm for real spectrum application	157
5.2.3	Optimal IM analysis for PP selection	162
5.2.4	Candidate strategies for PP selection	165
5.2.5	N2 method for application with real spectra and proposed IM-based approach	166
5.2.6	Cloud-based approach for fragility analysis	168
5.3	Discussion on selection strategies for multiple CSM solutions	170
5.3.1	Effectiveness of the proposed strategies for PP selection . . .	170
5.3.2	Effect of multiple-solution cases in fragility analysis	173
5.4	Cloud-CSM for fragility analysis: Discussion of results	178
5.4.1	Influence of the base shear coefficient and comparison with other nonlinear static approaches	178
5.4.2	Influence of the hysteresis rule	184
5.4.3	Influence of other backbone parameters	188
5.4.4	Influence of cyclic strength degradation	191

5.5	Conclusions	191
6	Seismic risk assessment of roadway bridges accounting for knowledge-based uncertainty	195
6.1	Introduction and motivations	195
6.2	Description of the methodology	199
6.2.1	Modelling uncertainties in fragility analysis	199
6.2.2	Damage states	201
6.2.3	Simplified methodology for seismic demand evaluation	203
6.2.4	Adopted methodology for fragility analysis	209
6.2.5	Risk quantification	213
6.3	Application of the framework on case-study bridges	214
6.3.1	Data collection and modelling uncertainty for data completion	215
6.3.2	Warning Class definition according to the Italian guidelines on existing bridges	219
6.3.3	Modelling and analysis assumptions	220
6.3.4	Sample size calibration	223
6.3.5	Discussion on fragility analysis	223
6.3.6	Simplified risk assessment	229
6.3.7	Fragility analysis with a refined knowledge level and validation	238
6.4	Final remarks	242
7	Conclusion	245
7.1	Overall conclusion and key findings	245
7.2	Future research	251
	References	278
A	Filled forms for data collection on real case-study bridges	279
B	Extended result collection of DBA and NSPs on parametric multi-span continuous-deck RC bridges	289

C Example dataset of fragility curves calculated with Cloud-CSM and benchmark approaches	299
Acknowledgements	321
Curriculum Vitae	323

Chapter 1

Introduction

1.1. Seismic assessment of bridges: background

The safety of transportation infrastructure systems is essential for the economic and social development. The existing transportation networks are affected by obsolescence, inadequacy to current traffic conditions and natural hazard-induced actions. In this context, the structural vulnerability of bridges and viaducts, which are key components of highway or railway infrastructure, is of increasing concern for users and, particularly, for the transportation authorities. In Italy, a large number of these structures was built in the 1950-1990 period and exhibits structural deficiencies caused by different factors. As an example, these structures show severe degradation conditions due to the absence of adequate theoretical design knowledge on the durability of construction materials. Moreover, bridges and viaducts were designed according to regulatory codes less demanding in terms of design traffic load with respect to the the current service demand. These structures were designed and built without an appropriate awareness of the effects of natural hazards such as earthquakes, floods or landslides. Additionally, a general lack of consistent maintenance plans, necessary to ensure a reliable structural performance during the design life of these structures, is registered. Tragic experiences such as the recent failures of several bridges in Italy, e.g. (Bazzucchi et al. 2018) (Figures 1.1 and 1.2), and other countries (Figure 1.3), prove that extensive assessment and intervention plans are urgently required.

In earthquake-prone areas, recent seismic events (e.g. 2010 Chile earthquakes, Figure 1.4) showed the inadequacy of the seismic performance of the construction heritage which was designed without or with low-demanding anti-seismic requirements. The seismic response of bridges and viaducts is decisive for the resilience of entire populated contexts since these strategic structures determine the post-event serviceability of



Figure 1.1: Collapse of the Polcevera bridge in Genova (Italy), 14th August 2018



Figure 1.2: Collapse of a bridge in Albiano Magra (Massa-Carrara, Italy), 8th April 2020

critical transportation networks affecting an appropriate management of the emergency. The first specific guidelines for seismic assessment and retrofit of bridges followed post-earthquake damages related to disastrous seismic events. The first experiences are the San Fernando (Housner & Jennings 1972) and Loma Prieta (Housner & Thiel 1990) earthquakes in 1971 and 1989, respectively, in the United States. After these events, the Federal Highway Administration (FHWA) published the first guidelines about seismic assessment and retrofit of bridges: the *Retrofitting guidelines for Highway Bridges* (ATC 1983) and the *Seismic Retrofitting Manual for Highway Structures* (FHWA 1995),

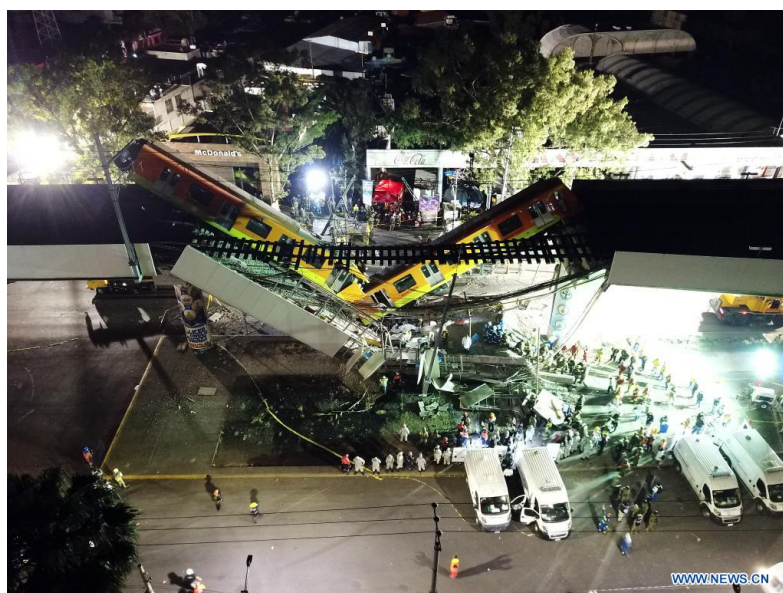


Figure 1.3: Collapse of a metro bridge in Mexico City (Mexico), 4th May 2021

currently updated in (FHWA 2006).

In Italy, the issue of the seismic vulnerability of strategic structures and bridges was firstly addressed by the *Ordinanza del Presidente del Consiglio dei Ministri* n. 3274/2003 (OPCM 2003) which required a mandatory structural assessment on the strategic structures in five years from its adoption. The first advanced Italian structural design codes, i.e. the NTC2008 (Ministero delle Infrastrutture e dei Trasporti 2008), (but also the current NTC2018 (Ministero delle Infrastrutture e dei Trasporti 2018)), mainly focused on the seismic design and assessment of the building heritage and exhibit general shortages of specific prescriptions for bridges and viaducts. This could be a consequence of the lack of damages registered on these structures after the Italian earthquakes in the last 40 years, which mainly occurred in geographical regions in which the construction of transportation network was still in progress (ReLUIS 2009). In Italy, the first appropriate guidelines for seismic assessment and retrofit of bridges, *Linee guida e manuale applicativo per la valutazione della sicurezza sismica e il consolidamento dei ponti esistenti in c.a.* (ReLUIS 2009) were developed within the ReLUIS *Rete dei Laboratori Universitari di Ingegneria Sismica* research project in the 2005-2008 period. Currently, transportation authorities need to include structural vulnerability data in their



Figure 1.4: Failures of roadway bridges during the Chilean earthquakes 2010 <https://www.flickr.com/photos/38631801@N07/4404042277> and http://learningfromearthquakes.org/2010-02-27-chile/images/2010_02_27_chile/



Figure 1.5: Damages on highway bridges, San Fernando earthquake, 1971 <https://www.nbclosangeles.com/news/earthquakes/1971-sylmar-san-fernando-earthquake-california/3104/>

bridge management systems to address regular *in-situ* inspections, timely maintenance process and retrofit where needed. The feasibility of this process is critically affected by the inadequate knowledge on the existing bridges. As an example, in Italy an important re-organization of the national road network induced a general confusion in the management of highway bridges (Borzi et al. 2014). This process resulted in lost or unavailable design documents and blueprints and a general lack of knowledge data about bridges that changed the proper owner. The process of populating electronic databases only recently started and implies the need for extended surveys on the networks and diagnostic tests to be carried out during the *in-situ* inspections.

Recently, the Italian Ministry of the Infrastructure and Transportation approved the new guidelines *Linee Guida per la Classificazione e Gestione del Rischio, la Valutazione*

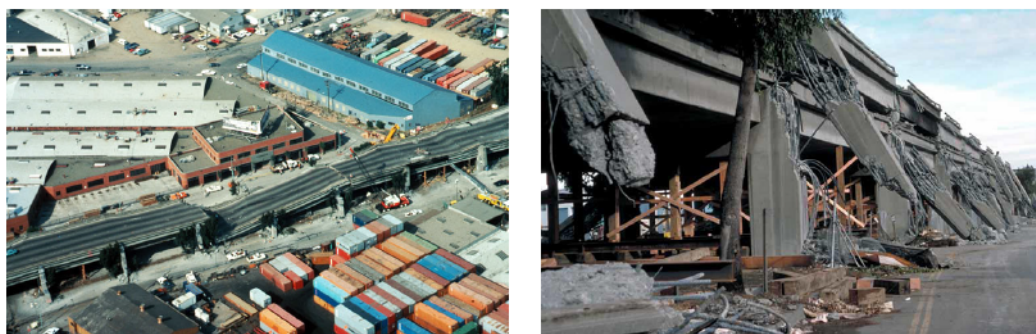


Figure 1.6: Cypress Viaduct collapse, Loma Prieta earthquake, 1989 by USGS <https://www.usgs.gov/media/images/cypress-viaduct-0>

della Sicurezza ed il Monitoraggio dei Ponti Esistenti (Ministero delle Infrastrutture e dei Trasporti 2020), which is aimed at addressing the management of the Italian bridge heritage.

These guidelines propose an innovative approach for the safety assessment of bridges based on multilevel evaluations to identify the most critical structures within a given portfolio and optimise the management of available resources. The proposed procedure considers structural vulnerability under traffic condition together with vulnerability to natural hazards. This multilevel approach is supposed to support transportation authorities which currently deal with a huge number of structures with limited time and financial resources. This is based on different levels of assessment characterised by incremental accuracy and resource demand. Level-by-level it is possible to identify the structures characterised by the most severe deficiencies and, thus, to address accurate inspection or retrofitting where needed. In this way, the road or railroad managers can focus their efforts on critical structures avoiding loss of resources and improving effectively the safety of the transportation networks with timely maintenance or retrofit. These guidelines involve a first screening (named level-0) of all the structures of interest aimed at collecting the main structural data and its collocation in the road network. This data collection is essential for creating digital bridge management systems including all available data about the design, results of inspections, material testing, structural assessment processes etc. of all the strategic structures. This is consistent with the D.M. n.430 - 8/10/2019 (Ministero delle Infrastrutture e dei Trasporti 2019), which es-

tablished the definition and population of a National open-access database of public strategic constructions named *Archivio Nazionale delle Opere Pubbliche*. The execution of the second level of screening on a bridge portfolio (named level-1) should be reasonably planned based on the data collected in the level-0. The level-1 consists of visual-based surveys performed using appropriate data forms suitable for the verification or the completion of the previously collected (geometrical and constructive) data and detection of evident structural deficiencies. Subsequently, the level-2 analysis is aimed at the definition of an *Warning Class* to each investigated bridge based on three well-known factors: hazard, vulnerability and exposition. A seismic *Warning Class* should be defined at this stage. Five classes of seismic hazard are considered based on the peak ground acceleration (PGA) having 10% probability to be exceeded in 50 years and soil category. The seismic vulnerability is assigned based on five classes based on the structural scheme (i.e. isostatic or hyperstatic structure), length of the spans, materials, degradation condition and design period. The seismic exposition is also defined through five exposition classes, depending on the importance of the bridge in the network, its role in the post-event phase and other parameters such as the mean daily traffic and the traffic typology. The seismic *Warning Class* contribute to the global *Warning Class* together with the hydrogeological *Warning Classes*. Based on the results of level-1 and level-2 further levels of structural evaluations are described by the guidelines. In short, level-3 deals with a preliminary evaluation of the structural capacity of the bridge in terms of traffic loads depending on the design code; level-4 requires an accurate structural assessment according to the current reference code requirements for existing structures.

1.2. Framework for seismic risk analysis

This dissertation specifically focuses on the seismic risk of bridges, which, together with the risk related to other natural hazards and to the current traffic condition, strongly contributes to the definition of comprehensive structural risk indicators for existing bridges. In earthquake-prone contexts, transportation authorities are strongly interested in including seismic vulnerability and risk information in bridge management systems. These allow for producing seismic risk maps and calculating expected (direct and indirect)

losses in a given period (time-based risk analysis, Federal Emergency Management Agency (2012)) or for a given earthquake scenario (scenario-based risk analysis). These information datasets are essential for managing the emergency of the post-earthquake phase and addressing policies of financing for retrofitting interventions.

The conventional flowchart for seismic risk calculation of structures is shown in Figure 1.7. The initial step in Figure 1.7 consists of a data collection about the structure/s to be analysed. If a single structure is analysed, on-site surveys with an appropriate diagnostic tests can be performed to obtain a satisfying knowledge level. However, if multiple structures are analysed, a refined data collection can be unaffordable in terms of time and cost and the knowledge-based (i.e. epistemic) uncertainties affecting the seismic risk calculation increase.

After the data collection, the fragility analysis phase is carried out. Fragility functions express the probability of damage given a proxy of the intensity of the seismic excitation. Fragility relationships can be calculated based on post-earthquake damage reports. However, the feasibility of this approach is strictly linked to the availability of damage data representative of the investigated structure and site. The lack of such data makes this approach unfeasible. For this reason, analytical fragility analysis approaches are commonly adopted. These approaches resort to the simulation of the structural response employing a numerical/analytical model of the structure subjected to earthquake-induced excitation. The results of the simulation (i.e. seismic demand data) are elaborated and compared to the structural capacity to carry out a probabilistic seismic assessment and derive fragility relationships. Several simulation techniques are proposed in the literature involving a different level of accuracy. High accuracy generally corresponds to higher modelling and computational demand for the analyst. Therefore, this latter should accept a compromise in terms of accuracy and effort demand, depending on the available resources, the target of the analysis (e.g. single structure or portfolio of structures) and the amount of considered uncertainties.

For the quantification of seismic risk, also a model of the expected hazard intensity at the investigated site is needed. Hazard curves are adopted to this aim expressing the annual frequency of exceedance of a given intensity of the ground shaking. A probabilistic seismic hazard analysis is commonly adopted to calculate hazard curves.

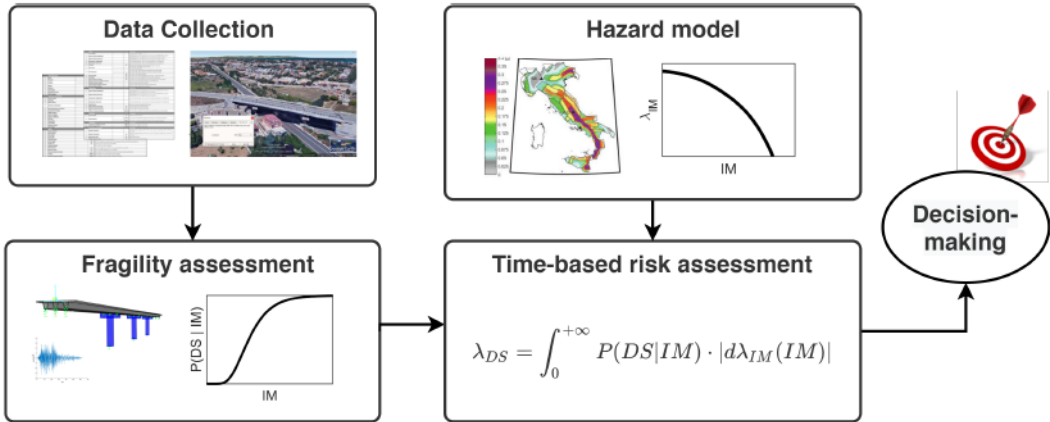


Figure 1.7: Synthetic flowchart for seismic risk assessment of structures.

The seismic risk can be calculated by integrating fragility and hazard functions. Note that the proposed flowchart considers time-based risk assessment (Federal Emergency Management Agency 2012), where the risk is measured in terms of mean annual frequency of reaching a structural failure condition (Cornell et al. 2002). Other risk metrics can be used, such as the expected annual losses which entail other input information such as consequence models useful to calculate vulnerability curves relating the expected (e.g. economic) losses given the seismic intensity measure.

1.3. Research motivations

The research on structural vulnerability assessment and risk reduction of assets such as transportation infrastructure systems is a timely topic according to the Nations (2015) promoted within the *Transforming our World: The 2030 Agenda for Sustainable Development (A/RES/70/1)* (2015) by the United Nations. The future of transportation infrastructure management, particularly concerning bridges, will be characterised by the population of digital databases, incorporating an extended amount of knowledge data about the whole life of the structures, and intelligent algorithms aimed at efficient structural safety and risk analysis for an effective management of surveys and retrofits. These developments will lead to a safer transportation infrastructure and to an optimisation of the employed resources. In this context, technological innovation and scientific research are needed to overcome the strong limitations of traditional approaches.

As an example, the conventional process of data collection on bridges can be very time- and cost-consuming. Conventional inspections are carried out by trained operators that visually assess the condition of the bridge, manually draw up inspection documents or perform diagnostic destructive or non-destructive testing. These may also require the employment of provisional structures that increase the inspection time and demand traffic limitations with service disruptions. These approaches are unaffordable if dealing with urgent structural safety evaluations at network-scale. In this context, the recent research pushes towards the application of intelligent paradigms for data collection and structural assessment of bridges. A huge potential is represented by the big databases of geospatial data which can be used to retrieve census information and approximate geometrical/constructive features of structures. Moreover, remote sensing non-contact techniques, such as Remotely Piloted Aircraft Systems (Chan et al. 2015, Duque et al. 2018) can be used to perform accurate low-cost surveys increasing the safety conditions for the operators. These technologies allow quick data collection and automatic allocation in digital databases in terms of Geographical Information Systems or Building Information Modelling. Moreover, given that the data are allocated in a codified format, automatic algorithms for data interpretation can be used for structural analysis, vulnerability and risk assessment purposes. Unfortunately, at the current state-of-the-art, the incompleteness of available knowledge data could prevent performing accurate numerical analyses. Moreover, even if necessary data was available, numerical analyses could require too high computational effort if wide bridge portfolios (or other structural typologies) are to be analysed. These factors push towards the employment of simplified analysis and assessment approaches, possibly included within a multilevel framework as proposed by the new Italian guidelines.

The prediction of the seismic risk/vulnerability of large portfolios of existing bridges was frequently faced in the last decades via the adoption of typological approaches. These require the identification of homogeneous classes of bridges having similar typological features (e.g. structural scheme, geometrical or constructive characteristics) within a given portfolio of structures and assume that the performance of bridges belonging to the same class is similar. One or more index-structures, representative of each typological class, are identified and analysed probabilistically to achieve class fragility curves.

These express the probability to reach or exceed a determined damage state for a given earthquake-induced shaking intensity. Class fragility curves could be calculated analytically accounting for geometric and material variability within the class. The HAZUS model (FEMA 2003) is a well-known reference within the field of analysis of bridge portfolios (and other types of structures). The HAZUS approach was developed in the U.S. context and propose seismic fragility curves for typological classes of bridges defined considering the seismic design approach, number of spans, span length, structural scheme continuity and bent type. The fragility curves are calculated via simplified nonlinear static analysis-based approaches neglecting material and constructive feature variability within the class.

Typological approaches such as HAZUS are strictly linked to the typical characteristics of the bridge portfolios of the analysed context. In the European context, the RISK-UE methodology (Mouroux & Le Brun 2006) were developed retracing the fundamentals of the HAZUS approach. In this latter, different typological classes more representative of the European context are indeed adopted.

Moreover, various literature studies focused on typological fragility analysis through more refined analysis methodology or class definition, accounting for geometrical and constructive variability (Choi et al. 2004, Avşar et al. 2011, Moschonas et al. 2009, Nielson 2005). However, the accuracy of the typological approaches is strictly linked to the classification scheme (i.e. taxonomy) adopted, usually defined on a judgemental-empirical basis, that could not be directly related to the expected seismic performance (Mangalathu et al. 2017). Furthermore, as evidenced by Stefanidou & Kappos (2019), these approaches, even if based on a refined classification, neglect structure-specific characteristics which could be crucial for the performance of bridges belonging to the same class (e.g. deck and pier geometry, deck-pier connection). To overcome the shortcomings of the typological approaches, the ongoing research investigates simplified analytical procedures aimed at structure-specific fragility and vulnerability analysis (Stefanidou & Kappos 2017) which could be used with poor data and resort to simplified modelling and analysis methodologies.

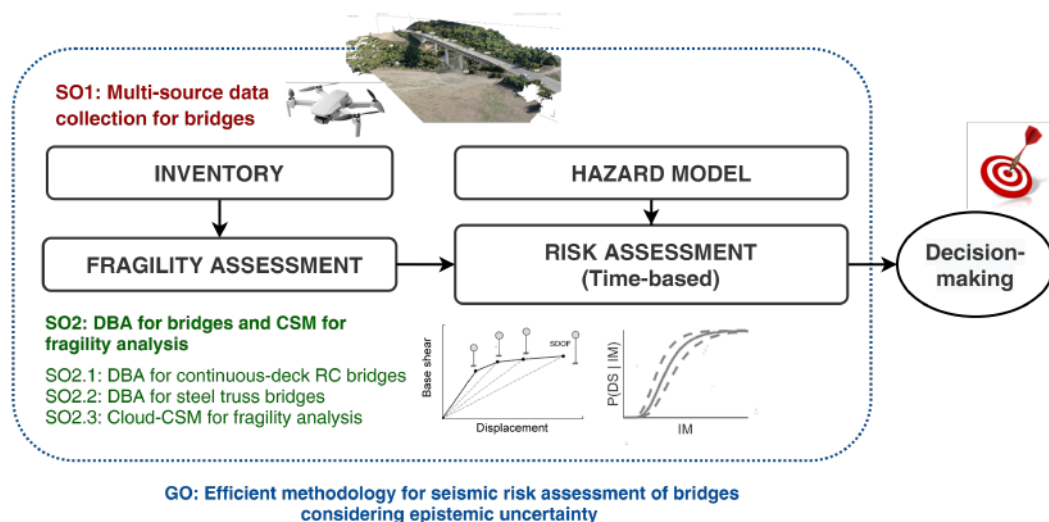


Figure 1.8: Synthetic flowchart for seismic risk assessment of structures and framing of the objectives of the present dissertation - DBA: displacement-based assessment, CSM: capacity spectrum method-.

1.4. Objectives

The present research is aimed to provide contributions in the field of the seismic risk assessment of bridges within the scope of large portfolio analysis. This dissertation is organised in several studies investigating specific phases within the main seismic risk assessment framework. The proposed studies (corresponding to different Chapters) are focused on specific objectives (SO) as shown in Figure 1.8.

- **SO1: Multi-source data collection for bridges**

The potential of innovative remote-sensing approaches for data collection on existing bridge portfolios within the framework of seismic risk analysis is discussed. The applicability of open-source or low-cost data providers is evaluated. Moreover, a process for the use of Remotely Piloted Aircraft Systems together with tridimensional photogrammetry is discussed with advantages and shortcomings. Chapter 2 focuses on this topic.

- **SO2: DBA for bridges and CSM for fragility analysis**

The study aims to investigate and propose simplified algorithms for seismic performance assessment and fragility analysis of bridges. These algorithms are

efficient since can be applied with programming routines rather than resorting to numerical models and dynamic analyses. To this purpose, recently proposed displacement-based assessment (DBA) algorithms and the capacity spectrum method (CSM) are presented, extended and combined to calculate fragility curves. Particularly, the effectiveness of these approaches is discussed referring to multi-span RC continuous-deck and steel truss bridges. Appropriate references are also provided, for the application of DBA and CSM for other widespread bridge typologies (e.g. simply supported RC bridges).

This SO is composed of three sub-objectives:

– **SO2.1: DBA for continuous-deck bridges**

DBA approaches applied together with the CSM for multi-span continuous-deck RC bridges are investigated. A static analysis-based DBA approach is proposed. A strategy to extend the DBA algorithms to calculate capacity curves enabling the seismic demand calculation via the CSM is described. The effectiveness of the approach is discussed varying deck cross-section, layout of the sub-structure, bridge length and pier typology. This study is reported in Chapter 3.

– **SO2.2: DBA for steel-truss bridges**

The applicability and accuracy of DBA and CSM approaches is evaluated for the seismic performance assessment of steel truss bridges. Different strategies for calculating the equivalent viscous damping are investigated. The accuracy of the performance displacement prediction via a direct DBA+CSM approach is discussed. This study is reported in Chapter 4.

– **SO2.3: Cloud-CSM for fragility analysis**

The use of the CSM for fragility analysis is evaluated. The Cloud-CSM is proposed to perform fragility analysis considering record-to-record variability via the CSM. The approach is tested for single-degree-of-freedom systems. This study is reported in Chapter 5.

The main findings of the above-mentioned studies lead to a proposal for an efficient methodology for seismic risk assessment of bridges to be used for regional-scale portfolio analyses and perform risk-based prioritisation, which is the general objective (GO) of this dissertation.

GO: Efficient methodology for seismic risk assessment of bridges considering epistemic uncertainty

Based on the previously described findings on the DBA and CSM algorithms for seismic performance and fragility analysis and multi-source data collection and integration, a complete framework for seismic risk assessment on existing bridges is proposed in Chapter 6. The presented procedure allows for quantifying the uncertainty linked to incomplete data collection with low modelling/computational effort. It can be applied within a multi-level data collection framework since the accuracy of the results depends on the completeness of the acquired knowledge level.

1.5. Outline of the dissertation

Considering the objectives listed in the previous section, the present study is composed as follows.

- Recommendations to perform a multi-source data collection for bridge portfolios are reported in Chapter 2. Part of this Chapter refers to Nettis et al. (2020).
 - The applicability of remote-sensing datasets is discussed, analysing the potentials of different data sources in populating bridge inventories. Recommendations for performing observation-based data gathering utilizing street-view images and appropriate data forms are listed.
 - A methodology to adopt Remotely Piloted Aircraft Systems (RPAS) coupled with photogrammetry techniques to retrieve exhaustive geometric/constructive information of bridges is described.
 - A multi-source data collection and integration procedure is applied to eight case-study bridges part of the Basilicata road network. For one of these, an RPAS-based data extraction methodology is illustrated.

- Chapter 3 is focused on DBA algorithms coupled with CSM for the seismic performance assessment of continuous-deck RC bridges. The contents of Chapter 3 refer to recent literature studies by the author (Gentile, Nettis & Raffaele 2020, Nettis et al. 2019*b,a*).
 - It investigates the effectiveness of state-of-the-art displacement-based performance assessment approaches for continuous-deck RC bridges and proposes suitable extensions which can be used for fragility analysis.
 - A first parametric analysis is carried out to test the DBA coupled with the CSM for 36 case-study bridges, varying the pier layout and the deck cross-section. Additional parametric analyses are performed to evaluate the effectiveness of these algorithms for long bridges, variation in longitudinal reinforcements and varying pier typology.
 - Two real case studies are finally analysed with the investigated methodologies.
- Chapter 4 evaluates the applicability of the DBA approaches for historical steel truss railway bridges with supporting steel towers, typically built between the end of the 19th and the beginning of the 20th century in Europe.
 - An effective equivalent viscous damping formulation is proposed for the performance assessment of steel towers via the CSM.
 - Algorithms based on the DBA and CSM for the direct seismic performance assessment of hyperstatic steel truss bridges under a given seismic action, are presented. These are applied on case-study steel truss bridges generated via a parametric analysis using a real archetype bridge.
- Chapter 5 proposes the CloudCSM, a methodology for performing fragility analysis considering record-to-record variability via the CSM. A case-study database of 2160 inelastic oscillators is used, represented by parametric backbones with different elastic periods, (yield) base shear coefficients, values of the ductility capacity, hardening ratios, residual strength values and hysteresis rules. The

contents of Chapter 5 refer to recent literature studies by the author (Nettis, Gentile, Raffaele, Uva & Galasso 2021).

- The application of the CSM with real (i.e. recorded) ground-motion spectra (as opposed to code-based conventional spectra) is evaluated. Simple criteria to solve the issue of multiple CSM solutions (i.e., two or more points on the backbone satisfying the CSM procedure) are proposed and tested.
- The effectiveness of the proposed Cloud-CSM in fragility analysis is discussed through extensive comparisons with nonlinear time-history analyses, the code-based N2 method, and a simple method involving an intensity measure as a direct proxy for the performance displacement.
- Chapter 6 discusses a framework for seismic risk assessment of existing bridge portfolios. The contents of Chapter 6 are partially included in the study by (Nettis, Raffaele & Uva 2021)
 - The algorithm for seismic risk quantification is presented. It is characterised by simplified mechanics-based approaches for performance assessment and a cloud-based approach for performing fragility analysis. It is designed to consider the uncertainty associated with incomplete initial knowledge.
 - The proposed approach is applied on a dataset of eight simply-supported bridges of the Basilicata national road network. The influence of knowledge-based uncertainty on both the fragility and the seismic risk is discussed depending on the bridge constructive features.
 - A validation of the adopted algorithms is carried out by means of a comparison with nonlinear dynamic analyses based on a refined modelling strategy.

Chapter 2

Multi-source data collection for seismic vulnerability of bridge portfolios

Abstract

In this Chapter, an overview on innovative methodologies for multi-source data collection suitable to structural (and seismic) vulnerability assessment of bridge portfolios is reported. The approaches and tools used in recent literature studies related to vulnerability analysis at regional-scale for portfolios of generic structures are preliminary described. The applicability of remote sensing approaches is discussed, analysing the effectiveness of different data sources in populating bridge inventories. Recommendations for performing observation-based data gathering of existing bridges utilizing suitable spreadsheets for data integration are listed. The second part of this Chapter is aimed at discussing the potentials of innovative Remotely Piloted Aircraft Systems which could represent a breakthrough within *in-situ* surveys, particularly if coupled with photogrammetry techniques to retrieve geometric/constructive information. A final case-study section is reported to illustrate the applicability of the above-mentioned approaches.

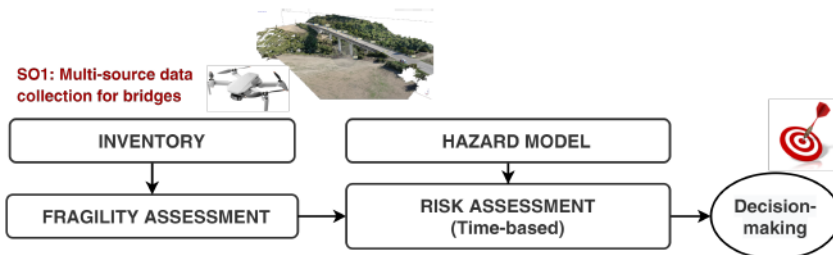


Figure 2.1: Objective of this Chapter (SO1) and framing in the flowchart for seismic risk calculation.

2.1. Multi-source data collection for large bridge portfolios

The population of exposure inventories is the main input step for vulnerability modelling and risk assessment of large contexts. Most of the state-of-the-art studies describe applications in which only the vulnerability data on the building heritage are considered. However, the resilience of populated contexts and their response under an earthquake scenario considering direct and indirect losses is also considerably affected by the vulnerability of infrastructure networks. In this context, the vulnerability data collection about bridges and viaducts which represent critical components of transportation networks is a decisive step. Currently, inadequate knowledge on existing bridges is registered as anticipated in the Introduction^{1.1}. This is caused by general inefficient management and storage of paper design documents and blueprints of the past. Another issue is represented by the differences in the infrastructure management approaches adopted by different authorities operating in the same geographical context. This increases the difficulties in data collection for contexts where road networks managed by different authorities are present.

The process of populating digital data inventories recently started and demands expensive refined surveys or extended digitalisation of data available in paper form. In Italy, the Ministry of Infrastructure systems just started the activity for the population of a National digital database containing public infrastructure data, namely Archivio Nazionale delle Opere Pubbliche (Ministero delle Infrastrutture e dei Trasporti 2019), accessible at <https://ainop.mit.gov.it/>. It aims to include data about the design, geometry, constructive features, degradation condition of infrastructure components. Another ground-breaking example is represented by the IBRID (Italian BRidge Interactive Database project) <http://ibrid.dic.unipd.it/> archive by the University of Padova specific for collecting bridge data of the Veneto region.

Different methodologies of data gathering can be adopted for characterising such digital databases and exposure data inventories. It is easily intuitable that traditional refined surveys are very burdensome, thus the recent research efforts push towards quick and efficient methodologies. In the following subsections, potentials of remote sensing techniques are discussed together with recommendations to effectively perform street-

based surveys.

2.1.1. Remote-sensing methodologies

Remote sensing technologies are aimed at collecting and measuring data of an investigated area/object without direct contact. In the case of bridges, remote sensing techniques could help, with a sustainable amount of resources, in gathering data about geometry, period of construction or their current degradation condition. Each remote sensing technique implies specific advantages and shortcomings concerning the field of application. However, since these tools allow for collecting data without any contact, their use increases the safety of the operators and the users, involving no need for service interruption (or only short-term) or special temporary structures.

Different sensors are used in remote sensing technologies. These are sensitive to different wavelengths of the electromagnetic spectrum and thus can be adopted to catch specific physical features. As an example, optical sensors are sensitive to the visible wavelengths, while radar sensors are sensitive to microwaves and can be used to measure the source-object distance.

Dealing with regional-scale data collection of construction heritage, satellite and airborne remote sensing approaches allow for collecting data in large areas with a single or few images. It is worth mentioning that the correct use of these techniques requires an appropriate understanding of the elaboration/interpretation of imagery considering the corresponding (spatial and temporal) resolution of the adopted sensors. For instance, capabilities in post-processing raw satellite images are needed to retrieve suitable data for populating exposure databases.

Most of the applications of satellite or airborne high-resolution optical imagery are aimed at the characterisation of the urban environment with a specific focus on buildings. Applications in the field of regional-scale vulnerability assessment of building are reported in Mueller et al. (2006), Ehrlich & Tenerelli (2013). Optical imagery suits for detecting exposure data such as footprints and area of the buildings, urban density, roof typologies or building use (Dell'Acqua et al. 2011). With reference to the infrastructure systems, optical imagery is used to detect the geospatial layout of roads (Abraham & Sasikumar 2014) and the location and footprint of bridges (Soergel et al. 2007, Nolte et al. 2011).

These data are very useful for mapping and populating exposure databases within Geographical Information Systems applications (Borzi et al. 2011), particularly if computer-aided visual-based algorithms are adopted (Gamba et al. 2009). These algorithms allow for the (automatic or semi-automatic) interpretation and classification of the available imagery analysis of large areas in a short time. For these purposes, imageries having a spatial resolution from 1x1m to 10x10m are required (Tenerelli & Crowley 2013a).

The choice between airborne and satellite images depends on the available funding and the specific applications. Airborne images exhibit usually higher spatial resolution with respect to satellite ones but are more expensive. The former can, indeed, be adopted also for condition assessment of road surfaces (e.g. detection of cracking and defects of the surfaces) (Liu et al. 2009). Conversely, satellite data are cheaper and available with complete global coverage by different data providers (e.g. <https://discover.digitalglobe.com/>, <https://earth.esa.int/eogateway/>). However, the technology of satellite-based sensors is quickly developing and, currently, the most advanced satellites allows for images having a resolution lower than 0.5m, such as GeoEye-1 or WorldView 2 and 3 (panchromatic band) (Vaghefi et al. 2012).

High-resolution data allows also performing multi-temporal change detection of the urban environment. With this approach, the design year/period of the investigated structures can be estimated. However, the applicability of this approach depends on the data sources adopted. As an example, using satellite imagery a limited time period can be analysed, since the first available satellite-based high-resolution images (IKONOS satellite) are from 1999 (Tenerelli & Crowley 2013a). However, multi-temporal analyses are very useful for performing quick post-earthquake damage detection at a regional scale (Menderes et al. 2015, Syifa et al. 2019).

Height attributes of buildings of bridges are very useful dealing with exposure inventory for vulnerability assessment purposes. To retrieve height attributes, stereo-type images (i.e. two images of the same area taken at two different angles) can be used. Particularly, this type of images can be elaborated by photogrammetry techniques to obtain 3D digital surface models (well-known as DSM). The height attributes can be retrieved by comparing the DSM with the digital terrain model (DTM) which includes the elevation data of the terrain. Satellite-based stereo-type imageries are commonly available

but have a low resolution with respect to normal acquisitions. In this case, airborne imageries which also exhibit various imaging angles, are more suitable for photogrammetry elaboration and represent a better choice. Oblique aerial imagery could be also directly used to extract height information, together with other useful attributes which can be retrieved by ground surveys.

To achieve geometric attributes of the terrain and the building heritage also LiDAR (Light Detection And Ranging) and RADAR (Radio Detection and Ranging) data sources could be used. Both of them work on the same basic principles but use different wavelengths. LiDAR is an optical remote-sensing technique based on LASER light. It is used for retrieving the distance and angle of targets on the terrain measuring the time period between the emission and the return of the laser pulse of the sensors. Through this technique, high-precision position data represented by dense point clouds of the terrain or of the investigated structures can be obtained. LiDAR sensors (LASER scanners) are generally used on airborne platforms. LiDAR applications are very suitable for bridge condition assessment as described by Harris et al. (2016). To populate exposure databases, this technique could be used to achieve surface elevation profiles and thus detecting the height attributes of buildings and bridges or other civil constructions 2.2.



Figure 2.2: Digital Surface Model for the city of Bisceglie (Italy) obtained by using LiDAR data.

Synthetic Aperture Radar sensors use radio waves and, like LiDAR, is suitable to collect position data represented by dense point clouds of the investigated target. These sen-

sors are placed on satellite and aerial platforms. Given the high accuracy, this technique is adopted for monitoring ground displacements and for studying phenomena such as landslides and subsidence. In this latter case, multi-temporal interferometric methodologies of stable Permanent Scatters are used (Bovenga et al. 2005, Crosetto et al. 2016). Within the field of regional-scale vulnerability analysis, these data source could be used for extraction of geometric characteristics of buildings and roads (Gamba et al. 2009). However, the employment of raw data requires high specialisation in radar data processing and thus are rarely used. Examples of building and road extraction using radar or optical data, with reference to the SYNER-G European project (Tenerelli & Crowley 2013b) are shown in Figures 2.3 and 2.4.



Figure 2.3: Optical and radar data on Messina city adopted during the SYNER-G project (Tenerelli & Crowley 2013b).

2.1.2. Street view-based surveys

Traditionally, *in-situ* surveys are performed by the specialised operators of the road/railroad authorities to collect information (e.g. images, measurements, notes) useful to populate bridge management databases. As an example, dealing with condition assessment, *in-situ* surveys are carried out periodically to evaluate the time trend of degradation phenomena. In these cases, paper forms, digital cameras or applications for digital devices are used to collect images and operators' notes which are directly allocated, via

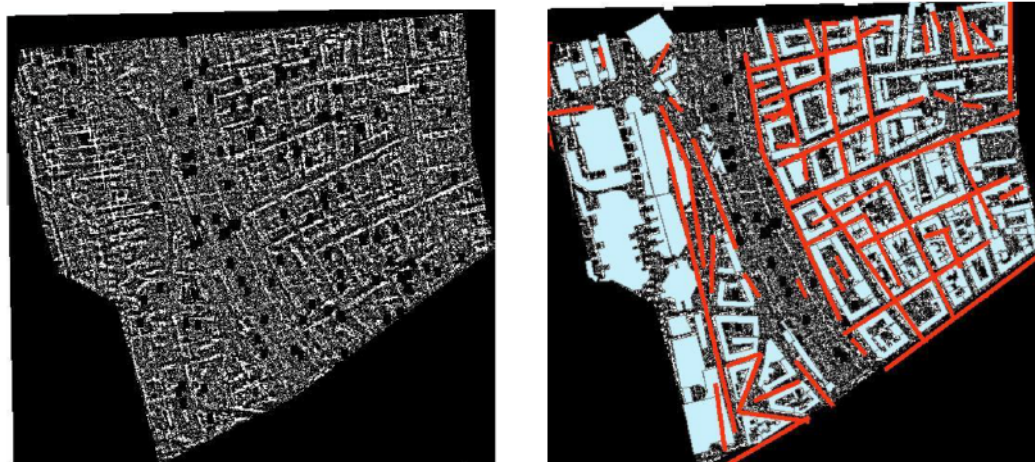


Figure 2.4: Radar data, road and building extraction on Vienna adopted during the SYNER-G project (Tenerelli & Crowley 2013b)

appropriate storage protocols, in digital databases.

Street-view data can be collected exploiting the publicly available street-view services offered by the main data providers such as Google (www.maps.google.com) or Bing (www.bing.com/maps) which gather images through digital cameras mounted on moving vehicles. An example is shown in Figure 2.5. This data source allows collecting data on large areas in a short time. Its application for condition rating purposes was described by Vaghefi et al. (2012). Street-view surveys data can be used to support and further classify preliminary data collected by remote sensing or available in bridge management databases within seismic risk assessment purposes. This data type allows for retrieving various structural characteristics which are not visible from remote sensing images. Applications within the seismic risk assessment framework were proposed by Misra & Padgett (2019) and Costa et al. (2020), in which street-view data by Google were used to integrate available census datasets for bridges in U.S. and buildings in Italy respectively. It is worth mentioning that the availability of street-view style images for bridges is strictly linked to the possibility of the camera-equipped vehicles reaching the investigated bridge. These type of data are commonly available for bridges overpassing (or near) other roads but can not be available in mountainous contexts on bridges overpassing natural obstacles such as valley or rivers (Vaghefi et al. 2012). Rarely street-view data are available for railway bridges.



Figure 2.5: Street-view imagery for a case-study bridge

An inventory dataset can be built associating the data collected by different data sources. If the inventory dataset is defined using Geographical Information Systems (GIS) tools, the images should be elaborated or interpreted by the analysts defining (text, numeric or logic) specific-field attribute to be added to the geospatial location information to the single bridge.

2.1.3. RPAS-based surveys and photogrammetry

Remotely Piloted Aircraft Systems (RPASs), generally labelled as drones, represent a breakthrough in *in-situ* inspections of infrastructure systems. These are small autonomous flight vehicles equipped with low-cost RGB cameras or other more sophisticated sensors (e.g., multispectral and thermal cameras, LiDAR technologies). Several research studies investigated robust methodologies to perform effective RPAS-based inspections on bridges or civil structures (Ayele & Droguett 2020, Barrile, Candela, Fotia & Bernardo 2019). These are aimed at collecting precise and targeted details to be integrated with other information measured on-site. In the U.S. context, the issue of the structural safety of existing bridges has been widely faced in the last decade and various departments of transportation are promoting several research projects to exploit the entire potential of RPASs for inspecting civil structures (Duque et al. 2018). In the field of visual-based inspections, Chan et al. (2015) proposed a review on the advantages and shortcomings of RPAS-based inspections on bridges, analysing different aspects, such as the minimum technical requirements of the drones, restrictions of the regulatory codes and cost-benefits analyses. They claim that an RPAS-based inspection can significantly reduce the time and cost of the survey. Moreover, RPAS can strongly

increase the safety of the operators which usually deal with problematic boundary conditions linked to the traffic or the environment of the bridge. Seo et al. (2018) evaluated the effectiveness of a drone-based inspection on a three-span timber bridge, analysing the image quality and the potentialities in damage identification, comparing the results with a conventional visual inspection. (Otero 2015) discussed the influence of different RPAS features, e.g. manoeuvrability, payload, size, adaptability, that are decisive for an accurate field inspection.

High advantages in the geometrical survey of bridges derive from the employment of drones together with computer-vision algorithms for photogrammetry, namely the Structure-from-Motion (SfM) techniques, capable of providing accurate 3D point clouds and, thus, 3D geometrical models suitable for virtual *ex-situ* inspection and BIM modelling. Various literature applications indeed investigated the extraction of geometrical data and the automatic classification of bridge components via photogrammetry. The study by Khaloo et al. (2018) was aimed at testing 3D photogrammetry techniques to build a 3D dense point cloud of a pedestrian timber truss bridge located in Alaska, starting from drone imagery. The authors stated that the obtained model outperforms (in terms of accuracy and completeness of the details) the one achieved by means of terrestrial laser scanning inspections. Recently, Morgenthal et al. (2019) proposed a comprehensive and automated framework for the condition assessment of bridges based on high-resolution 3D models built using RPAS-based imagery.

Ongoing research efforts focus on algorithms for automatic creation of numerical mechanical models (i.e. finite elements models) from 3D point cloud or geometrical models, in order to directly perform numerical analysis, quantify the structural performance to further evaluate remaining service life (Castellazzi et al. 2015, Lubowiecka et al. 2009) which is of particular interest for transportation authorities. These algorithms aim at performing a simplification of the point cloud model, extracting the features useful to finite element modelling. However, this task is challenging for bridge modelling, since these structures, although characterized by a simple structural scheme, are composed of members having particularly different mechanical behaviour (e.g. bearing devices, shear keys).

2.1.4. Multilevel approaches

A multilevel approach for data collection and integration oriented to structural assessment is a convenient solution to build level-by-level data inventories, as adopted within the recently completed INFRA-NAT *Increased Resilience of Critical Infrastructure to Natural and Human-Induced Hazards* project (O'Reilly et al. 2019) (<http://www.infra-nat.eu/>) and suggested by the new Italian guidelines (Ministero delle Infrastrutture e dei Trasporti 2020). The general framework of a multilevel approach is described in the following and Table 2.1 with specific reference to the data collection process.

Commonly, the multilevel approaches start with a low knowledge level analysis (Census Level in Table 2.1 and usually called Level 0), which is also defined as census level, in which a preliminary screening about number and location of structures in the investigated context is carried out. Open data sources or remote-sensing approaches suit this task. As an example, OpenStreetMap (www.openstreetmap.org/) provides open-access geospatial data, containing basic information about the built-up environment, readily downloadable in GIS-friendly format (i.e. shapefiles). Also, Google Earth (earth.google.com/) and Bing (www.bing.com/maps) provide suitable data for free download (low-cost if large amount of downloads are needed). Local repositories of digital technical cartographies (e.g. regional databases) could also be available depending on the analysed context. In Italy, the Ministry of Environment offers open-access (or low-cost) geospatial data available via the *Geoportale Nazionale* (<http://www.pcn.minambiente.it/>) which can be downloaded and directly used in GIS environment. This first level of knowledge has the scope of a preliminary evaluation of the number of structures to be assessed. No information (or very rough) about the vulnerability of the structures can be normally retrieved at this stage.

The second knowledge level (Low Level in Table 2.1) is aimed at gathering the main characteristics of the structures, such as design period, general geometrical data, the material of construction or structural typology. This level requires a quick structure-specific data collection which can be carried out via traditional fast *in-situ* inspections or innovative approaches. As indicated within the INFRA-NAT project, this task could be performed using street view data provided by Google (www.maps.google.com) or

Bing (www.bing.com/maps), if available. It is worth mentioning that the availability of street view data source is strongly dependent on the analysed context and location of the bridge as indicated in Section 2.1.2. The 3D data provided by Google may be applied for these purposes. Moreover, the design year is commonly a basic information that is usually available by transportation authorities. However, if not available, it can be retrieved by comparing historical cartographies or satellite/aerial imagery collected in different periods as reported in Section 2.1.1. It is worth mentioning that the construction period of main highways or railways (and the related bridges) can be easily retrieved via simple historical researches. At this knowledge level, the vulnerability assessment can be performed only with indirect methods resorting to a typological approach. As an example, the HAZUS or RISK-UE models (FEMA 2003, Mouroux & Le Brun 2006) or more advanced fragility relationships retrieved by the literature could be used.

The further knowledge levels (Medium Level in Table 2.1) involve a more refined structure-specific data gathering approach. These knowledge levels require visual-based inspections and geometrical measurements performed using appropriate data forms suitable for the verification or completion of the previously collected (geometrical and constructive) data. Moreover, these are aimed at evaluating the structural condition, detecting degradation, significant cracking phenomena on critical structural components and other factors that may potentially affect the structural safety. These data can be retrieved by traditional refined *in-situ* surveys or with the use of innovative technologies which enable the collection of images such as Remotely Piloted Aircraft Systems (RPAS) equipped with optical sensors (i.e. RGB cameras). The data can be also obtained by exploiting particularly suitable street view data (2.1.2). The data form (i.e. spreadsheet) adopted in this study to collect geometric and constructive information is reported in Figure 2.10 and 2.10. It is a spreadsheet composed of different sections: identification, general structural, deck, piers, abutments, bearings and materials. Each section includes different fields to be filled out with textual or numerical attributes which can be directly included in shape-files to be used within a GIS environment or simple programming routines which allow analytical risk calculations (6). Simplified mechanical-based assessment procedures suit this knowledge level. As an example, analytical displacement-based assessment approaches, possibly based on simplified mechanical

models, are particularly suitable according to Cademartori et al. (2020) for investigating the fragility and risk of analysed bridges at this knowledge level. It is worth mentioning that at this stage, further data could be necessary for performing mechanical modelling or analytical assessment. These can be assumed by engineering judgement (assumptions for constructive features or detailing, or simulated design approaches) or modelled by statistical distributions, if available, related to the investigated portfolio of structures. As an example, Zelaschi et al. (2016) proposed statistical data on Italian bridges suitable for modelling the uncertainty of incomplete knowledge.

Within a multilevel framework, the high-level knowledge (Table 2.1) should be applied to the most critical structures identified within the previous level. It requires a refined data gathering phase to achieve complete knowledge, as far as possible. As an example, to detect the detailing of the structural components or to investigate the material mechanical properties, non-destructive and destructive diagnostic tests should be performed, following the recommendations of the reference regulatory framework. Once satisfying knowledge is achieved, numerical modelling and refined analysis approaches should be used to calculate fragility and risk.

2.2. Methodology for RPAS-based photogrammetry for structural data gathering of bridges

In this section, an RPAS-based approach for the data collection on existing bridges is proposed. This strategy allows collecting RGB images that are used to perform photogrammetry and create 3D models of the investigated bridge. First, recommendations to perform an *in-situ* survey via RPAS equipped with optical sensors are proposed considering the environmental condition and the regulatory codes. The process of retrieving geometric data via photogrammetry is also described. The final subsection is focused on further developments on the application of these techniques for automatic structural assessment purposes.

2.2.1. Recommendations for RPAS-based survey

RPASs equipped with optical sensors are used to collect a large number of images of a surveyed structure overcoming various challenges affecting the bridge data collection

Table 2.1: General framework of multilevel approaches for bridge portfolios

	Data	Sources	Assessment type
CENSUS	<ul style="list-style-type: none"> • Census Data (Location, Manager, Type of Bridge, etc.) • Length of the bridge 	<ul style="list-style-type: none"> • OpenStreetMap • Google Earth/Bing or other similar • Satellite or Aerial imagery 	None
	<ul style="list-style-type: none"> • Year of Design 	<ul style="list-style-type: none"> • General authority database 	
	<ul style="list-style-type: none"> • Structural scheme • Material • Typological identification 	<ul style="list-style-type: none"> • Historical cartography • Raw street view data • In-situ quick inspection 	Typologic or generic indirect approaches
LOW LEVEL	<ul style="list-style-type: none"> • Geometry of main structural components 	<ul style="list-style-type: none"> • Refined street view data and photogrammetry 	
	<ul style="list-style-type: none"> • Visible constructive details (e.g. bearing types, gap dimensions) • Degradation 	<ul style="list-style-type: none"> • In-situ survey (traditional) • RPAS-based photogrammetry • Ground-based remote sensing tools (e.g. Laser Scanner) 	Direct (possibly simplified) mechanic-based approaches
	<ul style="list-style-type: none"> • Complete knowledge on geometry 		
HIGH LEVEL	<ul style="list-style-type: none"> • Detailing • Foundation and abutments • Mechanical properties 	<ul style="list-style-type: none"> • Refined in-situ survey with diagnostic tests • Design document and blueprints 	Refined approaches (according to the regulations)

process e.g. scarcity of time and cost resources, inaccessibility of sites and safety of operators. The acquired images can be used to perform visual-based inspections and retrieve constructive features, but also allow measuring geometry, particularly using photogrammetry techniques.

Currently, in developed countries, the use of drones is subjected to regulatory codes which define appropriate limitations in terms of safety within the definition of flight paths. As an example, the use of drones in the Italian airspace is governed by the ENAC Regulations Issues No. 3 dated 11 November 2019 (ENAC 2020) which implements the European Commission Regulation (EU) 2019/947 of 24 May 2019 (OJ).

RPAS-based surveys of structures, generally, require an accurate planning phase aimed at identifying environmental constraints and airspace limitations, assessing the potential disturbance of the weather condition. This phase is strictly linked to the geographical location of the investigated structures.

In general, multi-copter drones are adopted for bridge inspection, possibly equipped with a Global Navigation Satellite System (GNSS) receiver and a suitable infrared sensor system capable of keeping obstacles at a safe distance (Darby et al. 2019). This is very important for bridge inspections since infrared no-impact sensors allow the drone for flying in limited spaces and inspecting small-size structural components (e.g. bearing devices, joints). Another solution to detect small components, avoiding undesired impacts connected to turbulent effects of the wind near and under the bridge, is acquiring images in hovering mode (i.e. keeping the drone flying in a stable position), using the zoom function to keep the vehicle at a safe distance. For the survey below the deck, the drone should be equipped with a zenithal camera for the intrados inspection. In these cases, the drone may experience loss of GNSS signal and should be able to fly in Real-Time Kinematic (RTK) mode connected via a radio link to a master station nearby. The survey can be performed in manual or automatic flight mode, depending on the features of the structure itself and its environment (e.g. presence of natural obstacles). In automatic flight mode, regular and repeatable flight paths with low battery consumption optimizing inspection time can be planned. It is worth mentioning that, dealing with the collection of images for photogrammetry, an automatic flight mode has a beneficial effect on the final accuracy results. Indeed, the flight path, which strongly depends on the

morphology of the territory, may be based on single or double grids in which the drone acquires images having a given percentage of longitudinal and lateral overlap (between 70% and 80%) to optimise the photogrammetric process while avoiding redundant acquisitions (Pan et al. 2019). Multiple images of the same target point, varying the grip angle, allow emphasising the altitude differences and recreating complicated geometries in the photogrammetric process. The route speed of the drone should be consistent with the onboard GNSS frequency and the lens shutter speed to avoid distortions and lack of sharpness. The flight altitude should be calibrated depending on the desired spatial resolution, defined in terms of Ground Sample Distance (GSD).

During the survey, a topographic network materialization can be of support to the photogrammetric elaborations, facilitating the roto-translation, scaling and georeferencing of the model during the orientation phase. The use of non-removable targets is effective for multi-temporal acquisition for change detection analysis. The topographic network can be materialized by georeferencing the position of artificial/natural targets in the investigated area which can be easily identifiable through automatic search techniques in the adopted photogrammetric software package. This task can be performed via total stations and GNSS receiver technologies, depending on the expected accuracy.

2.2.2. Structure-from-Motion techniques for 3D modelling

Structure-from-Motion techniques are aimed at retrieving 3D point cloud models using 2D images of a given scene. Currently, various open-access or commercial software packages are available, but the technical skills of the operator in interpreting the input and output products are essential for achieving accurate results. The employment of these techniques together with drones is very effective to dramatically reduce the time and cost of the surveys even in large and inaccessible areas. The different phases composing SfM algorithms are independent of the adopted software package and are described in Saponaro et al. (2020) and shown in Figure 2.6.

A preliminary step is the calibration of the camera model parameters, which can be performed via a manual approach or self-calibration based on the acquired dataset. The lack of this step can induce multiple distortions and affects the accuracy of the final results. Tie points are searched and counted among the collected images via the use

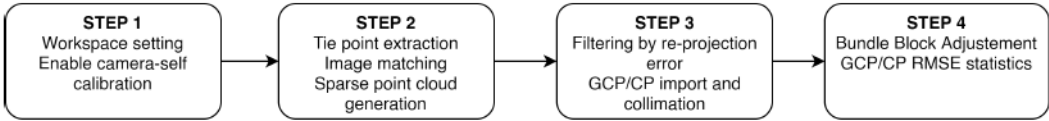


Figure 2.6: General steps of a photogrammetric process algorithm.

of Scale Invariant Feature Transform (Lowe 2004) algorithms. These points are characterised by low sensitivity to changes in scale, orientation, and brightness within the image dataset and thus can be consistently recognised in most of the images. The adopted software package can establish geometric relationships among the tie points detected in all the images. Through these operations, supported by any geo-tags registered in the images, the software can extract a sparse-point cloud, which is a primitive 3D-point cloud model composed of the points whose recognition among the images is more robust.

At this stage, the sparse-point cloud should be corrected and filtered. As an example, some points, affected by high re-projection errors can be identified and neglected (Barba et al. 2019) allowing the software itself to re-calculate the orientation of the different images. Moreover, to reach high (e.g. centimetric) accuracy, which is desirable in structural mechanical modelling (Barrile, Candela, Fotia & Bernardo 2019, Lee & Park 2019), further corrections are required (Bundle Block Adjustment), utilising the orientation and calibration parameters of the camera, the geo-referenced points acquired on-site and the image positions directly acquired by the drone during the flight. As anticipated, a given number of ground-control points surveyed on-site is essential for indirect georeferencing operations to better estimate the position and orientation of the image dataset. The orientation of each image is thus corrected and the re-projection errors are reduced. The general accuracy of the point cloud model determines the accuracy of the following geometry extractions and can be calculated via some error measures such as the Root Mean Squared Errors (RMSE).

Dense image matching algorithms are thus applied to the corrected dataset of images to achieve a dense point cloud model which suits geometrical model extraction. In this case, the average distance among the point is reduced to 1/40 with respect to the sparse point cloud.

2.2.3. Further applications of 3D models by RPAS-based photogrammetry

The 3D point cloud model leads to various applications in the context of the management of infrastructure systems. An obvious application consists in performing conventional visual inspection carried out *in-* and *ex-situ* by analysing the RPAS-based dense point cloud (eventually processed in a textured mesh). If multi-temporal surveys are carried out, visual inspections of models collected in a different time period of the life of the structure allow detecting the occurrence and evolution of degradation phenomena.

Moreover, it is possible, through segmentation and classification of parts of the point cloud, to identify the different structural components and achieving metric and material information which is essential for populating bridge databases and for subsequent vulnerability/risk assessment. This approach is very desirable by transportation authorities since it facilitates the creation of digital models, named digital twins, representative of the structure, that are also comprehensive of heterogeneous information types collected in a single or multi-temporal inspection (i.e. Building Information Models).

The extraction of geometrical data about the different structural components from a 3D point cloud model can be performed automatically, using Scan-to-BIM algorithms, or via manual tracking and visual interpretation (Conde-Carnero et al. 2016, Riveiro et al. 2016). The former approach allows a strong reduction of time and modelling effort and, currently, are subjected to very active research efforts (Wang et al. 2015, Yang et al. 2020). This process is composed of two phases: the segmentation which involves grouping portions of the point cloud into multiple homogeneous regions with similar properties (such as geometric, radiometric) and the classification, requiring the assignment of points to specific classes, called labels.

Another automatic approach is based on machine-learning 2D-image analysis (Barrile, Candela & Fotia 2019) for segmenting the different components. Accordingly, the point cloud is classified, yielding to the recognition of the different structural components within the point cloud model. Consequently, the segmented point cloud parts are transformed into 3D polygons.

Contrarily, conventional manual approaches require the operator directly to recognise the different structural components within the point cloud and re-create 3D geometri-

cal models, involving a larger amount of time with respect to the automatic approach. It is worth mentioning that the automatic approaches are currently under development and not easily applied in the common practice, particularly concerning existing bridges. In these cases, indeed, the manual approach is a preferable solution since the trained operator can recognize different structural components such as bearings, joints, shear keys which exhibit wide variability in typology with special reference to existing bridges designed in the last century. Currently, although literature works are aimed at the classification of components such as deck and piers (Barrile, Candela & Fotia 2019), to the author's best knowledge, no literature applications investigate the automatic characterization of other small but likewise critical structural components such as bearing devices.

2.3. Case study: application of multi-source data collection and integration

This Section shows the application of the data collection methodologies with reference to case-study bridges detected in the Basilicata road network (which are also analysed in the following Chapters). The considered geographical context is selected as one of the most seismic hazard-prone geographical contexts of Southern Italy. The data, extracted with innovative fast approaches, is allocated by hand into appropriate spreadsheets. In this way, the integration of multi-source data is performed. The spreadsheets represent a suitable input for geospatial analysis within a GIS environment or can be directly adopted as input for programming routines aimed at seismic risk calculation.

2.3.1. Screening and case-study identification

The first step of data collection is a screening of the existing bridges of the context. As previously discussed, this task can be accomplished by consulting the geospatial datasets developed by global and local data providers. In this case, the open-access OpenStreetMap data repository (<https://www.openstreetmap.org/>) including geospatial data about the transportation assets, can be used. These can be easily downloaded as shape-files and used within a GIS environment. In this study, QGIS (<https://www.qgis.org/>), an open-source GIS software package, is utilised to download and manage this dataset. It is worth mentioning that open-access geospatial data on the regional

infrastructure systems are also provided by the Basilicata Region (at <http://dati.regione.basilicata.it/>).

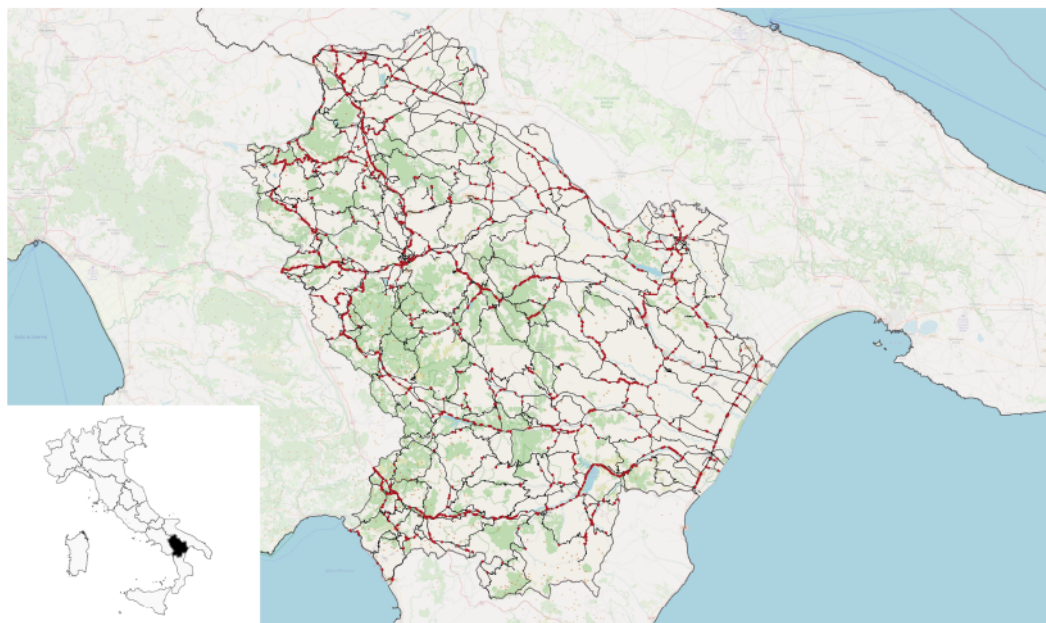


Figure 2.7: Spatial layout of the Basilicata road network and screening of the bridges (red markers).

The geospatial layout of the primary road network of the considered geographical region is extracted, considering only extra-urban roads, and shown in Figure 2.7. A total of 1389 bridges is detected. The preliminary statistics reported in Figure 2.8 shows that single-span bridges represent a percentage between 15% and 30% (assuming judgmentally that single-span bridges exhibit a maximum length of 40 meters). Assuming that the percentage of arch or cable-stayed bridges is negligible, long multi-span girder bridges having length higher than 200 meters represent about 20% of the total. The whole dataset is filtered to identify multi-span bridges having a medium-short length (less than 200 meters). Fast street view surveys are performed within the considered road network and eight case-study bridges are selected. These are multi-span isostatic RC-bridges with single-shaft piers. Only this bridge typology is considered in this study. Clearly, the described data collection approach can be carried out regardless of the considered typology. The geographical position of the case-study bridges is indicated in

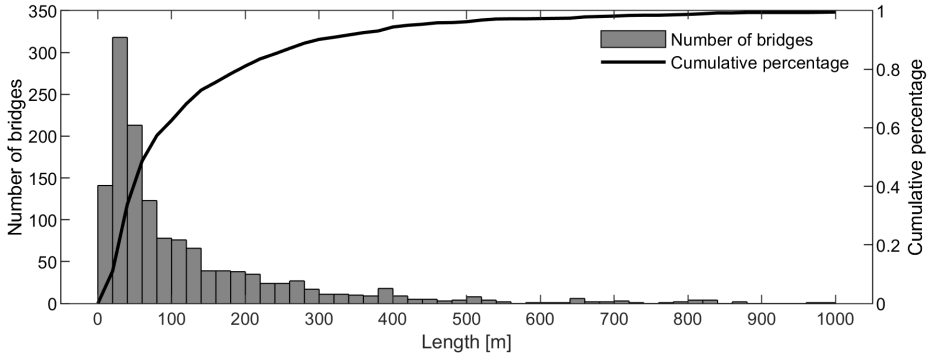


Figure 2.8: Distribution of bridges in Basilicata related to their length.

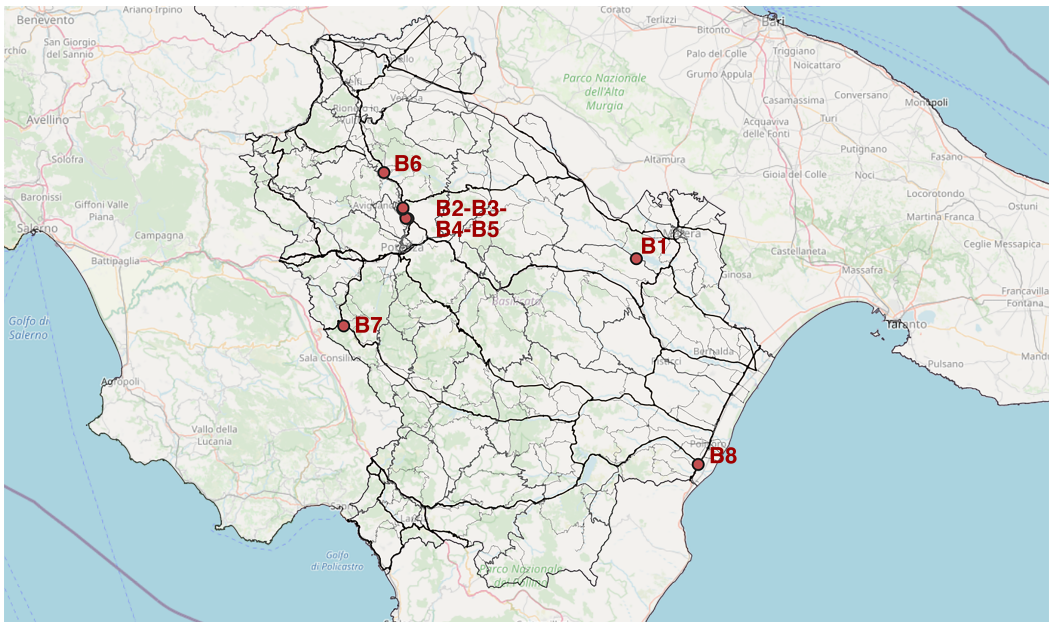


Figure 2.9: Location of the selected case-study bridges.

Figure 2.9.

For each bridge, the data gathering is performed via the adoption of the developed spreadsheet shown in Figure 2.10 and 2.11. The spreadsheet includes the necessary data for directly performing the seismic risk assessment algorithm described in Chapter 6. For this purpose, each field should be filled in accordingly with the indications reported in the commentary. Each field is completed with textual or numerical (single

or in vector-format) variables, identified with a simple code (first column in the spreadsheet), which can be also allocated in a GIS environment, by simply converting the spreadsheet in comma-separated-values file and, in turn, in shape-file format.

Identification		Commentary	
I01	Name		
I02	Manager		
I03			Latitude
I04	Position		Longitude
I05	Region		
I06	Province		
I07	Municipality		
I08	Infrastructure type		
I09	Road category		
General structural		Commentary	
G01	Structure type		GIR: Girder bridge - ARC: Arch bridge - CS: Cable stayed - ...
G02	Deck type		BwS: Beams with slab - BG: Box girder - MS: Monolithic slab - TR: Truss
G03	Static scheme		ISO: Isostatic - HYP: Hyperstatic
G04	Deck-pier connections		Fill in only if HYP - SUPP: Pinned connection - MON: Monolythic connections
G05	Deck-abutments connections		Fill in only if ISO - SUPP: Pinned connection
G06	Year/period of design		SUPP: Pinned connection - MON: Monolythic connections
G07	Bridge category		Fill in design year/period
G08	Seismic category		1: first category, 2: second category
G09	Seismic coefficient		Fill in the following values [0 1 2] if period of design is 1939-1964.
G10	Soil type		Fill in the following values [0 6 9 12] if period of design is 1964-2008.
G11	Topography		Fill in one of the following values [A - B - C - D - E] for soil category
G12	Total length	[m]	Fill in one of the following values [T1 - T2 -T3 -T4] for topographic category
G13	Number of spans		Insert the total length of the bridge
G14	Span length	[m]	Insert the number of spans
			Insert a vector of span lengths
Deck		Commentary	
D01	Girder material		RC: Reinforced Concrete - PC: Precast - ST: Steel
D02	Slab material		RC: Reinforced Concrete - PC: Precast
D03	Deck width	[m]	Insert the total width of the deck
D04	Road width	[m]	Insert the width of the road only
D05	Sidewalk width	[m]	Insert the width of the sidewalk only
D06	Girder height	[m]	Insert the height of the girder (from lower edge of slab to top of the bearing device)
D07	Girder area	[m]	Insert the cross section area of the girder
D08	Number of girder		Fill in with the number of girders
D09	Slab thickness	[m]	Insert the height of the slab (from top edge of girder to top slab)
D10	Deck cross area	[m ²]	Fill in only if D07-D08-D09 are not available
D11	Flexure moment of inertia	[m ⁴]	Fill in only if G03 is HYP with the moment of inertia in transverse direction
D12	G2 deck	[kN/m]	Fill in with the non-structural permanent weight
D13	Concrete Young's modulus	[MPa]	Fill in with the concrete Young's modulus of the deck

Figure 2.10: Spreadsheet for data gathering (Part 1).

A brief description of the spreadsheet is herein reported. The first section (*Location*, Figure 2.10) includes some general features which correspond to a census level knowledge. The second (*General structural*, Figure 2.10) comprises typological and global constructive features about the bridge. Particularly, this part includes design data, such as the year (or period) of design, together with the traffic and seismic design categories according to the design reference code. The third part (*Deck*, Figure 2.10) refers to typological and geometrical features of the superstructure and superimposed gravity loads. At this state of development, the spreadsheet suits for hyperstatic (continuous)

and simply-supported (isostatic) girder bridges only.

Piers		Commentary
P01	Pier typology	SC: single column - W: Wall - FR: Portal
P02	Degree of fixity (longitudinal)	X: fixed displacement, R: free displacement. Insert a vector of [RX/R] if HYP, a vector of [RX/R/XX/RR] if ISO. The length of the vector is equal to the number of bents.
P03	Degree of fixity (transverse)	X: fixed displacement, R: free displacement. Insert a vector of [RX/R] if HYP, a vector of [RX/R/XX/RR] if ISO. The length of the vector is equal to the number of bents.
P04	Bearing type (longitudinal)	Type of the fixed bearings - Insert a vector of N: Neoprene or X: Fixed generic
P05	Bearing type (transverse)	Type of the fixed bearings - Insert a vector of N: Neoprene or X: Fixed generic
P06	Cap beam	[m] Dimension of the cap beam. Insert a vector of [B1 - B2 - H1 - H2 - W]
P07	Pier section	Fill in if SC: RECT: Rectangular - CIRC: Circular - Polygonal - Elliptical
		Fill in if W: RECT: Rectangular
		Fill in if P07 is RECT with the dimension parallel to the axis of the bridge
P08	Pier dimensions	Fill in if P07 is RECT with the dimension normal to the axis of the bridge
		[m] Fill in if P07 is CIRC with the diameter
		[m] Fill in with a vector of bearing heights (top of cap beam - bottom of the deck)
P09	Support height	[m] Fill in with a vector of bent heights from the base to top of capbeam
P10	Pier height	[m] Fill in with a vector of bearing distances from the axis of the pier on the capbeam
P11	Distance between supports	[m] Insert the characteristic design strength of concrete (R _{bk} or R _{ck})
P12	Design compressive strength of concrete	Insert the Young's modulus of the steel (E)
P13	Steel bars Young's modulus	Insert the characteristic design strength of steel (R _{ak} or R _{yk})
P14	Design yielding strength of steel bars	Insert the Young's modulus of the concrete (E)
P15	Concrete Young's modulus	
Abutments		Commentary
A01	Degree of fixity (longitudinal)	X: fixed displacement, R: free displacement. Insert a vector of [RX/R] if HYP, a vector of [RX/R/XX/RR] if ISO. The length of the vector is equal to 2.
A02	Degree of fixity (transverse)	X: fixed displacement, R: free displacement. Insert a vector of [RX/R] if HYP, a vector of [RX/R/XX/RR] if ISO. The length of the vector is equal to 2.
A03	Bearing type (longitudinal)	Type of the fixed bearings - Insert a vector of 2 component: Neoprene or X: Fixed generic
A04	Bearing type (transverse)	Type of the fixed bearings - Insert a vector of 2 component: Neoprene or X: Fixed generic
A05	Gap dimension	Dimension of the gap in longitudinal dimension
A06	Width of abutment backwall	[m] Insert the width of the abutment backwall
A07	Height of abutment backwall	[m] Insert the height of the abutment backwall
A08	Stiffness of abutment backwall	[kN/m/m] Insert the stiffness coefficient of the abutment backwall (stiffness per unity of width)
Bearings		Commentary
B01	Bearing height	[m] Height of the bearing device
B02	Bearing stiffness	[kN/m] Fill in if there are NEOPRENE bearings with the stiffness of the single bearing device
		[kN/m] Fill in if there are FIXED bearings with the stiffness of the single bearing device
Materials		Commentary
M01	Compressive strength of concrete	[MPa] Insert the mean strength of concrete (f _c)
M02	Tensile strength of steel	[MPa] Insert the mean strength of concrete (f _y)
Constructive details		Commentary
C01	Number of long bars	Insert the number of long bars, if P07 is RECT, insert a vect of 2 components, if P07 is CIRC insert one number
C02	Diameter of long bars	[m] Diameter of longitudinal bars, RECT: insert a vect of 2 components, if CIRC insert a vector of one component
C03	Step of transv reinf	[m] Step of transverse bars
C04	Diameter of transv reinf	[m] Diameter of transverse reinforcements

Figure 2.11: Spreadsheet for data gathering (Part 2).

The sections designated *Piers* and *Abutments* (Figure 2.11) are aimed at characterising the typological and geometrical features of the piers and abutments, respectively, and the degree of translational/rotational fixity between the superstructure and the substructure members. Some typological features about the bearing devices should be inserted into the following *Bearings* section (Figure 2.11). Finally, the *Materials* and *Constructive details* sections comprise data about concrete and steel strength and steel reinforcements. It is worth noting that design data, such as design concrete and steel strengths and Young's modulus (e.g. from P12 to P15), or structural details such as bearing type

(e.g. P02-P05 or A01-A05 or the data within the *Bearing* section), the deck-abutment gap dimension (A05) or the data required within the *Materials* and *Constructive details* parts are hardly detectable without refined surveys or diagnostic testing. Since the simplified seismic risk assessment algorithm in Chapter 6 is designed to perform a data completion, the unknown field should be left empty.

Note that the spreadsheet is designed for incorporating all the necessary data used by the algorithm to perform the seismic risk assessment of RC girder bridges with single-shaft piers. As the algorithms will be developed, extensions of the spreadsheet could be required. For example, data about multi-column piers or the degradation conditions of the bridge components can be included.

2.3.2. Data acquired on case-study bridges

Eight case-study bridges are selected. The bridges from B1 to B6 are characterised by a medium-level seismic hazard expressed by the Peak Ground Acceleration (PGA) having the 10% probability of occurrence in 50 years (Figure 2.12). Conversely, the bridges B7 and B8 are located in a high (expected PGA exceeds 0.225g) and a low (expected PGA lower than 0.100g) seismic hazard zone, respectively. The seismic hazard is characterised according to the Italian regulations ((Ministero delle Infrastrutture e dei Trasporti 2018)). Information on the soil category is retrieved by the study of Forte et al. (2019). A brief description of the bridges is reported as follows. The spreadsheets, appropriately completed with the case-study data, are extensively reported in Appendix A.

- BRIDGE 1 (B1)

The bridge (Figure 2.13) is located along the provincial road *SP Matera-Grassano* and overpasses a strip of the San Giuliano's lake. The first Google Street View inspection allows identifying the isostatic scheme, the number of spans (5 spans) and the pier typology (single-column piers). However, incomplete Google Street View data are available for this bridge, given the absence of a road underneath or sufficiently close reporting street view data. Therefore, some street view photos are additionally collected during a fast on-site inspection. The pier heights and other geometric characteristics are measured using the digital elevation model

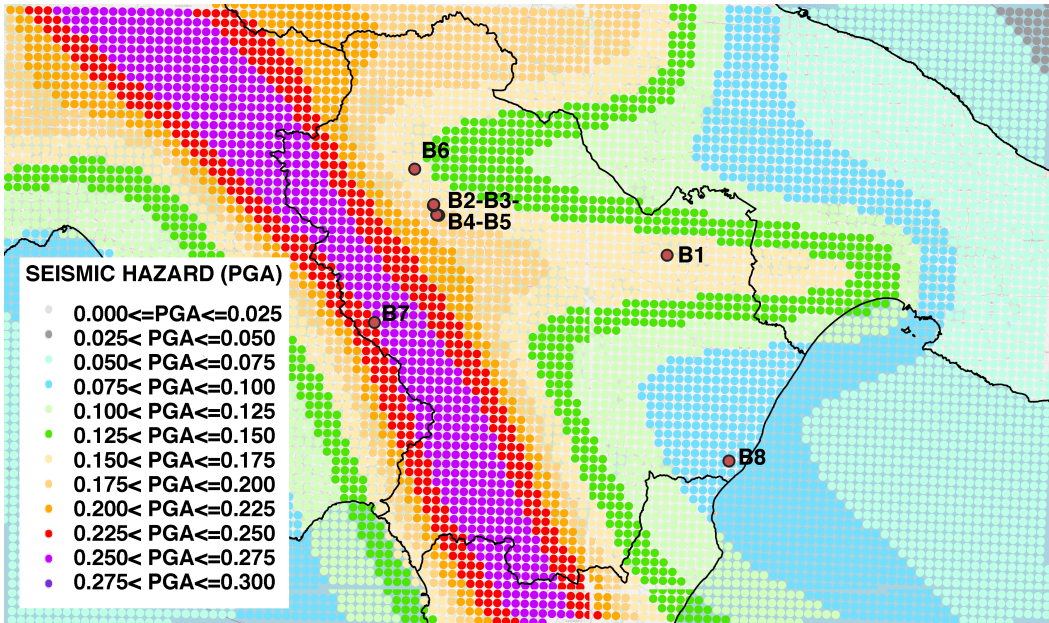


Figure 2.12: Seismic hazard map of the analysed area expressed in PGA [$g = 9.81m/s^2$].

provided by Google Earth and simple photo measurements. It is worth mentioning that also LiDAR data from the *Geoportale Nazionale* suits this purpose. Information on the connection system between the deck and the substructure is not detectable at this stage.

- BRIDGE 2, BRIDGE 3, BRIDGE 4, BRIDGE 5 (B2-B3-B4-B5)

These bridges are part of the national road SS658 and exhibit very similar typological and constructive features (Figures 2.14, 2.15, 2.16, 2.17). Since these bridges overpass some secondary roads from which street view data are collected, an exhaustive amount of knowledge data can be retrieved by Google Street View. All these bridges are isostatic girder bridges with circular cross-section single-column piers. Five precast girders characterise the deck of B2, while four are present in the other bridges in the group. B2, B3 and B5 are three-spans bridges while B4 is four-span. The pier heights are measured using the digital elevation model provided by Google Earth and photo measurements of street view images. The street view images allow characterising the deck-substructure

connection which consists in neoprene bearings. The bridges have shear keys placed at the extreme boards of the pier caps which are aimed to prevent deck unseating in the transverse direction.

- BRIDGE 6 (B6)

The bridge B6 (Figure 2.18) is located along the national road *SS658* and overpasses a secondary provincial road. Street view data collected from the road underneath the bridge allows a comprehensive geometrical and constructive characterisation. The bridge is a three-span isostatic deck bridge with single-column piers having a circular cross-section. The deck is composed of four precast girders. Even in this case, the pier heights are measured using the digital elevation model provided by Google Earth and photo measurements of street view images. The deck-substructure connection typology consists of neoprene bearings with shear keys placed at the extreme boards of the pier caps.

- BRIDGE 7 (B7)

The bridge B7 (Figure 2.19) is located along the national road *SS598* and overpasses a secondary rural road. Street view data collected from the overpassed road is available for exhaustive data gathering. The bridge is a two-span isostatic deck bridge with single-column piers having squared cross-section and spans having a length equal to 33 m. The deck is composed of six precast girders. Even in this case, the pier heights are measured using the digital elevation model provided by Google Earth and photo measurements of street view images. The deck-substructure connection typology consists of neoprene bearings only.

- BRIDGE 8 (B8)

The bridge B8 (Figure 2.20) is located along the national road *E80-SS106* and overpasses a road intersection between secondary suburban roads. Street view data collected from the overpassed road is available for data gathering. The bridge is an isostatic deck bridge with six spans and single-column piers having a circular cross-section. The deck is composed of three precast girders and 40 m-long

spans. Even in this case, the pier heights are measured using the digital elevation model provided by Google Earth and photo measurements of street view images. The deck-substructure connection typology consists of fixed and free bearings.

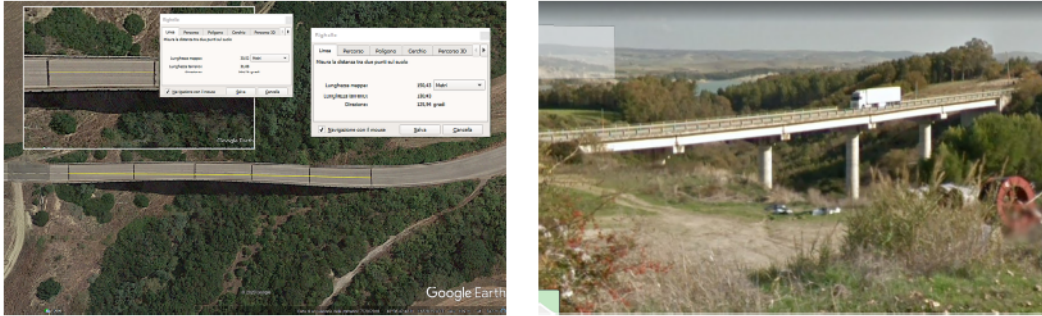


Figure 2.13: Google Earth data on the case-study B1 (top view from Google Earth and Google Street View image)



Figure 2.14: Google Earth data on the case-study B2 (top view from Google Earth and Google Street View image)

2.3.3. Application of RPAS-based survey

2.3.3.1. Data acquisition

Given the lack of suitable street view data to characterize the B1 bridge, an RPAS-based survey is carried out. The adopted drone is a lightweight RPAS quadcopter *DJI (Dà-Jiang Innovations, Shenzhen, China) Mavic 2 Zoom* of about 905g, equipped with a 20mpx RGB-sensor with a focal length varying from 24–48mm but set at 24mm. Two flights



Figure 2.15: Google Earth data on the case-study B3 (top view from Google Earth and Google Street View image)

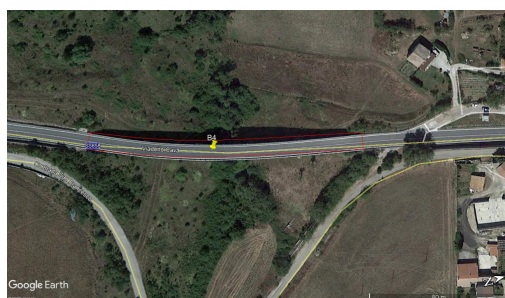


Figure 2.16: Google Earth data on the case-study B4 (top view from Google Earth and Google Street View image)



Figure 2.17: Google Earth data on the case-study B5 (top view from Google Earth and Google Street View image)

at 30m above ground level are planned. The first flight is carried out with a nadiral view of the camera, while the second is carried out with 45° oblique camera in front of each side of the deck. The first flight is performed with a longitudinal overlap and side-lap rate of 80% were, while 75% for the second. A dataset of 97 images along the main axis of the bridge is collected within the first flight in approximately six minutes. The second



Figure 2.18: Google Earth data on the case-study B6 (top view from Google Earth and Google Street View image)



Figure 2.19: Google Earth data on the case-study B7 (top view from Google Earth and Google Street View image)



Figure 2.20: Google Earth data on the case-study B8 (top view from Google Earth and Google Street View image)

flight is completed in 14min approximately collecting 190 symmetrical images. Both of these image datasets are characterised by an average Ground Sampling Distance of 1.68cm/pixel.

To improve the accuracy of the expected results, the geospatial position of eleven artificial targets is materialized. These are homogeneously distributed in the study area.

Nine of these latter are considered as ground control points (GCP) for the georeferencing phase, while the remaining are independent checkpoints (ICP) for the final accuracy verification. These are placed at the joints between the decks of the bridge, varying the side for each span (Figure 2.21). A GCP is also placed at the base of the central pier, while the two ICPs are measured in the middle of the roadway. The position of these targets is measured in network nRTK mode with a *Leica Geosystem GS08 Plus receiver* in a WGS84/UTM zone 33N Reference System, connected to the local permanent station of the *National Dynamic Network (RDN2008)* of the *Continuously Operating Reference Stations*. The accuracy of the measurements is about 2cm along the three axes X, Y and Z (consistently with the limits of the adopted measurement technique). Using the open-source Italian software package *ConveRgo* (Conversioni di coordinate per le Regioni), the altimetric measurements are converted from ellipsoidal to orthometric altitude. Furthermore, a close-range visual inspection is carried out employing another drone, *DJI Phantom 4 Pro quadcopter* with a 20mpx RGB-sensor. This flight has the aim of collecting some close-range images on determined bridge components (e.g. joints and neoprene pads) via a manual flight 2.21 according to the recommendations of Subsection 2.1.3 (Figure 2.22).



Figure 2.21: Dense point cloud model and distribution of (ground/independent) control points



Figure 2.22: Image collection of neoprene bearings in hovering flight mode

2.3.3.2. Data Processing

According to the suggestions of Section 2.2.2, *Agisoft Metashape (v.1.5.4.8885)* is adopted for carrying out photogrammetric operations on the acquired image datasets. Firstly, some parameters are defined to allow the elaborations. The adopted coordinate system is specified, together with the accuracy of the on-board RPAS receiver and the accuracy of the position of the GCP (named markers in the software) when acquired *in-situ* and in the software environment. The self-correction of the camera parameters is performed according to the metadata belonging to each image.

The first step of the process involves the camera alignment, in which the position of the cameras and the collected images are calculated, performing the operating steps reported in Section 2.2.2. The elaboration time usually depends on the number of images, pixel and the size of the sensors. In this case, it lasts around 5min and produces a sparse cloud of 275,687 points with an average Reprojection Error (RE) of 0.744pixels and approximately $23pts/m^2$.

According to Section 2.2.2, this sparse point cloud is subjected to a refining process that involves filtering the points having a RE above 0.40. The refined sparse point cloud is thus composed of 59,086pts, with an average RE of 0.373px.

Moreover, the coordinates of the control points acquired *in-situ* are imported. Each target (both GCPs and ICPs) is selected in each of the images of the dataset and the point cloud model is again adjusted with roto-translation transformation and scaling,

considering the newly imported GCP position. Conversely, the coordinates of the ICPs are used to check the corrected point cloud model at the end of the process. The software evaluates the difference between the ICP position acquired on-site and in the refined model. In this case, a total error of 0.026 m is obtained, which is satisfying for the scope of this study.

Finally, the algorithm for achieving the dense point cloud model allows obtaining a point cloud of 61,933,130pts reported in Figure 2.21 in three hours and 20 minutes.

2.3.3.3. Geometric extraction and storage

Given the dense point cloud, the geometry of the structural components of the bridge is extracted. The spreadsheet described in Section 2.3.1 is filled in with text and numeric variables retrieved by measurements performed on the point cloud model.

Furthermore, a digital model of the bridge is built within a BIM environment utilising the *Autodesk Revit 2020* software package. A manual approach is used for this task, to adequately identify the qualitative and quantitative characteristics of minor size structural components such as the neoprene bearings.

The point cloud model is imported within the software environment and each structural component is visually recognised within the point cloud and converted into a geometric solid block which is assigned to a specific family of elements (Figure 2.23).

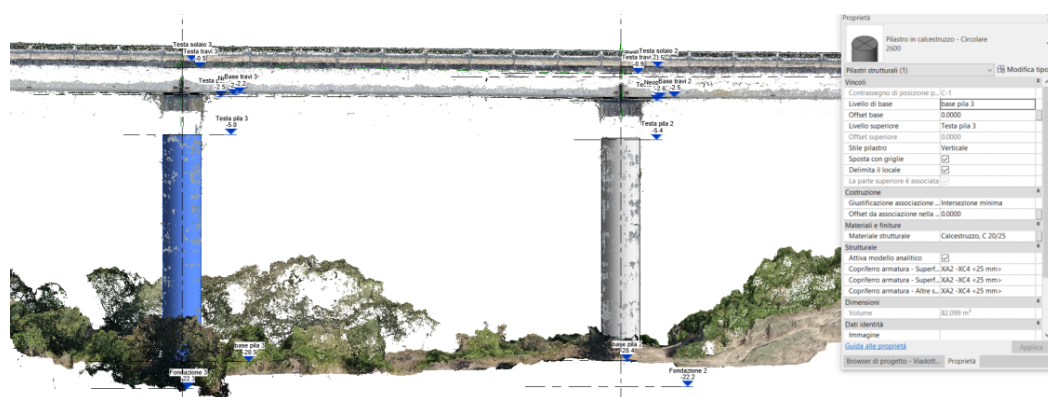


Figure 2.23: Drawing BIM solid blocks from the point cloud

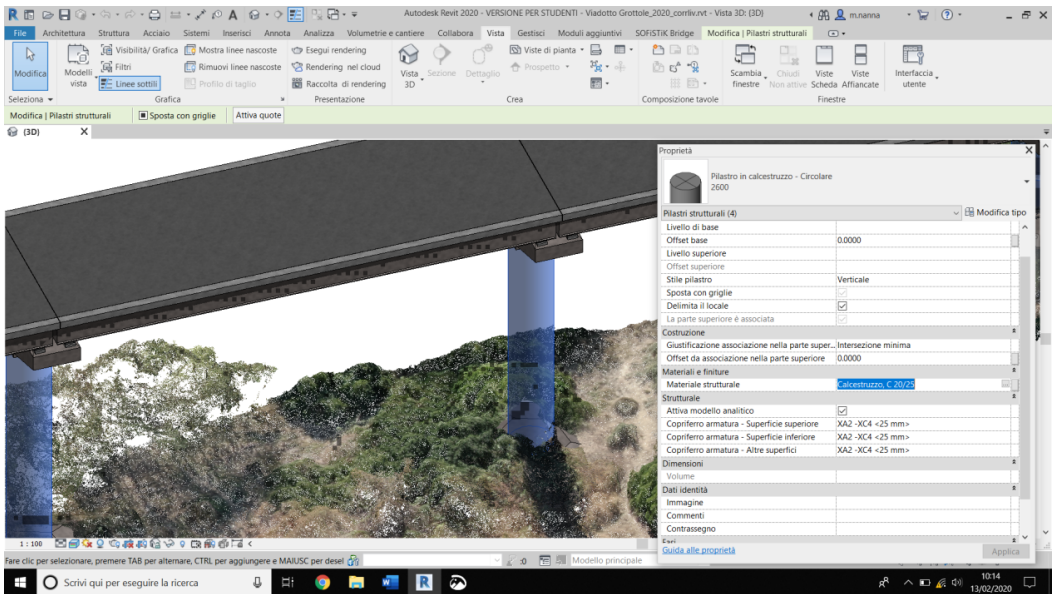


Figure 2.24: Drawing BIM solid blocks from the point cloud

The BIM environment allows for assigning knowledge data to specific components such as material properties, reinforcement amount, damage, degradation together with a wide variety of information sources such as inspection reports and images collected on-site. In this way, each object (and the whole model itself) becomes a container of several types of information. This is a key potential for the adoption of the BIM tool in data storage for the management of existing infrastructure systems.

2.4. Summary

In this Chapter, an overview of multi-source approaches for creating inventory datasets in the framework of structural vulnerability analysis of infrastructure assets is provided. Firstly, the potential of different remote-sensing data sources is described according to an extended literature review. The advantages and shortcomings of using these approaches are specifically described. A special focus on innovative Remotely Piloted Aircraft Systems (RPAS) is provided to the reader, reporting advantages of the employment of RPAS for on-site image gathering and surveys, and describing the fundamentals of a photogrammetric approach for image elaboration.

The described multi-source approach is framed within a multilevel framework that suits

analysing large portfolios of structures, optimising time and cost efforts.

The methodology adopted in this dissertation for retrieving and integrating multi-source data on some case-study bridges, analysed in the following Chapters is described. The case studies are detected by means of street view data within the Basilicata road network. For seven case-study bridges, the street view images allow a satisfying characterisation of the bridges consistently with a medium level knowledge level. One of the case-study, whose street view data are not complete, is surveyed by means of an RPAS-based approach. The images collected are used to perform a photogrammetry process which produces a 3D dense point cloud model. This latter allows for retrieving constructive and geometric data on the analysed case study.

Chapter 3

Effectiveness of the displacement-based seismic performance assessment for continuous RC bridges and proposed extensions

Abstract

The displacement-based assessment (DBA) represents a satisfactory trade-off between simplicity and accuracy for seismic performance assessment of existing bridges. After describing a modal analysis-based DBA procedure proposed in literature, a static analysis-based alternative is proposed in this Chapter, considering its strengths and limitations. Moreover, an extension of the procedure is proposed to derive the force-displacement curve of the investigated bridge (pseudo-pushover capacity curve) which coupled with the capacity spectrum method (CSM) allows for performance displacement calculation. The effectiveness of the DBA is discussed through parametric analyses to address its practical applications. The DBA approaches, both modal and static, is herein adopted for the transverse analysis of a set of 36 reinforced concrete continuous-deck bridges up to six spans, with pier height in the range 8-20m and two different values of the deck transverse stiffness. Additional sensitivity analyses (24 case studies) are conducted to investigate the accuracy of the two approaches considering: 1) the length of the bridge, 2) the amount of longitudinal reinforcement in the piers; 3) different pier typologies. The results are compared to numerical pushover and time-history analyses using three suites of 10 scaled, natural ground motions respectively consistent with low-, medium- and high-hazard sites. For the majority of the case studies, the resulting performance assessments fall within one standard deviation of the results of the time-history analyses. The last part of this Chapter investigates the applicability of the above-mentioned approaches for two real existing case-study bridges.

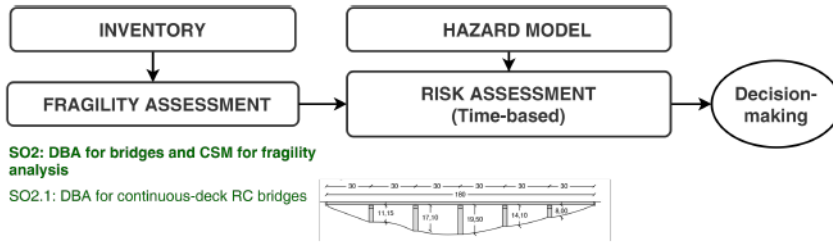


Figure 3.1: Objective of this Chapter (SO2.1) and framing in the flowchart for seismic risk calculation.

3.1. Introduction and motivation

In high earthquake risk countries, the seismic assessment of bridges is particularly important since often such structures represent crucial nodes of the transportation networks and have strategic functions. This is demonstrated by field observations in the aftermath of major earthquakes, e.g. the $M_w = 7.8$, 2016 Kaikoura earthquake (Palermo et al. 2017). Moreover, in many countries (e.g. Italy), many of the existing bridges are designed with non-seismic methods, rather than advanced techniques (Priestley et al. 1996), thus increasing the need for an evaluation of their seismic behaviour.

Nonlinear time-history analysis (NLTHA) is arguably the most refined available tool to perform a seismic performance assessment, provided that significant computational effort is spent, and time/skills are available to set up the numerical model of the bridge and interpret its results. Similar difficulties can arise adopting advanced nonlinear static procedures (NSPs), such as the adaptive pushover. Based on previous work (Elnashai 2001, Gupta & Kunnath 2000), force-based and displacement-based adaptive pushover (FAP and DAP) techniques were proposed (Antoniou & Pinho 2004, Antoniou et al. 2004). These represent improvements of the conventional invariant pushover since they allow to account for the effect that progressive stiffness degradation might have on the distribution of seismic forces. Both the FAP and DAP were tested on reinforced concrete (RC) bridges proving high accuracy (Pinho et al. 2007, Cardone 2014).

Part of the above-mentioned difficulties in nonlinear numerical models is overcome using the Displacement-Based Assessment (DBA), which represents a satisfactory trade-off between simplicity of the analysis and accuracy of the results. Such features render DBA also suitable for the analysis of large portfolios, possibly coupled with simplified methods for the characterisation of structural members (Cosenza et al. 2011, Gentile

et al. 2018a, Gentile & Raffaele 2018).

The DBA derives from its design counterpart (Priestley et al. 2007), which was firstly proposed for bridges by Kowalsky (2002). Extensions to the procedure that include the effects of higher modes in the design were proposed (Adhikari et al. 2010, Kappos et al. 2013). The DBA procedure for bridges was proposed by Şadan et al. (2013) for continuous-deck configurations with pinned abutments and involves the modal analysis of the bridge based on secant stiffness properties for the piers, i.e. the effective modal analysis by Kowalsky (2002). The DBA was extended by Ni et al. (2014) to include soil-structure interaction. Further work by Cardone (2014) aimed at proposing performance displacement profiles correspondent to a limit state in various members of the bridge (i.e. piers, abutments, joints, bearing devices and shear keys). In such cases, the full capacity curve of the bridge is not derived, but rather the performance displacement of the bridge in component-based limit state condition.

After describing the existing DBA procedure based on modal analysis, this Chapter proposes an alternative procedure based on static analysis. Moreover, it is proposed an extension of the DBA procedures, both modal and static, to calculate the full pseudo-pushover capacity curve of bridges. Reference to an open-access application suitable for the above calculations is provided. Since a relatively less-complex model and analysis type are used, the static-based DBA is deemed to be easier in practical applications, for example allowing to utilise an electronic spreadsheet (possibly validated against the provided application) instead of a numerical computer model. Using a static rather than modal analysis is an attempt to render the procedure “practice-oriented” as much as possible, aiming at the adoption of simple mechanical models constructed by the user, while building refined numerical ones only for the final validation (and vice versa). This could potentially reduce (or avoid) the “black-box” effect due to the adoption of highly-refined models.

The above-mentioned modal and static approaches are based on the repeated application of the DBA for increasing values of a control node displacement and are herein called Displacement-Based Pseudo Pushover (DBPP). The concept is similar to what done for RC buildings by proposing the Simple Lateral Mechanism Analysis (SLaMA) method (NZSEE 2017, Gentile, del Vecchio, Pampanin, Raffaele & Uva 2019, Gentile,

Pampanin, Raffaele & Uva 2019a,b,c). The DBPP allows obtaining a pseudo-pushover curve of the bridge, for which the term "pseudo" refers to a series of linear analyses using secant rather than tangent stiffness properties for the members (NZSEE 2017). Using such a curve within a capacity spectrum-based assessment approach allows for calculating a variety of engineering demand parameters (for one or more spectra). This, in turn, allows performing fragility analysis and risk assessment.

The scope of this Chapter is mainly related to the transverse analysis of continuous deck bridges. The longitudinal analysis of such bridges is deemed to be a less-complex application of the proposed solution since it is based on a much simpler static scheme (piers in parallel which are forced to the same top displacement). Moreover, multi-span simply-supported bridges are not considered since in this case each deck-substructure subassembly can be modelled as a Single Degree of Freedom (SDoF) system, both in the transverse and longitudinal directions. An in-depth discussion for isostatic bridges is reported in Chapter 6. Finally, although the main case-study dataset (Section 3.3.1) refers to RC continuous-deck bridges with single-column piers, straightforward modifications in characterising the simplified structural model allow to consider other deck typologies, pier-to-deck connections, and pier typologies (some of which are herein considered in an additional sensitivity analysis).

The effectiveness of the DBPP approach is analysed by means of the application to a dataset composed of 36 RC bridge case studies with continuous deck, comprising wide ranges for the number of spans (2-6), the height distribution of the piers (8-20m), the force-displacement response of the piers and the moment of inertia of the deck (flexure in the transverse direction of the bridge). Firstly, the results are compared with refined numerically-based pushover analyses using two different force profiles. The capacity spectrum method (CSM, Freeman 1998a) is applied using such curves to derive a performance point. The results are critically compared with the average of NLTHA using three suites of 10 scaled, natural ground motions respectively consistent with low-, medium- and high-hazard sites. Finally, additional sensitivity analyses are conducted to investigate the accuracy of both analytical approaches in relation to the bridge length, the amount of longitudinal reinforcement in the piers and different pier typologies. Based on the obtained outcomes, some applicability limits are suggested

to address a practical and appropriate use of these DBA methodologies.

3.2. Description of the DBA for bridges and proposed extensions

The DBA procedure for bridges aims at the identification of their displacement capacity (for a given limit state) expressed in terms of equivalent SDoF properties. The assessment is performed comparing the displacement capacity and demand at the corresponding limit state, which depends on effective structural period and equivalent viscous damping of the SDoF system.

An initial knowledge phase is required to define the geometry and detailing of the investigated bridge. Subsequently, limit displacements (or drifts) should be defined for each member composing the bridge (e.g. piers, abutments, bearings). The DBA allows to identify the displacement profile, and related base shear, associated with the limit displacement/drift for one or more members in the bridge.

3.2.1. Overview of the DBA procedure based on modal analysis

The DBA procedure based on modal analysis (Şadan et al. 2013) is described herein. Firstly, the force-displacement characterisation of the deck-pier and -abutment sub-assemblies should be provided. This means that each subassembly should be represented by the force-displacement curve of an equivalent SDoF system or equivalent cantilever. While an elastic behaviour is often appropriate for the abutments, the non-linear force-displacement curve of the piers is needed. Also, the linear/nonlinear contribution of other significant components (e.g. bearing devices, shear keys), if present, should be included (see Chapter 6). The study in this Chapter considers only the contributions of piers and abutments in the equivalent cantilevers, assuming fixed bearings and non-sacrificial shear keys.

For RC single-column piers, the equivalent cantilever can be calculated based on the study by (Priestley et al. 1996) accounting for the mass distribution along the pier height, the mass of the the pier cap and a tributary portion of the deck. The model choice (with particular reference to the shear span of the pier) can change depending on the boundary conditions at the deck connection (Priestley et al. 1996). The height H of the equivalent cantilever can be calculated according to Equation 3.1, where H_p and H_d are

respectively the height of the pier and the deck centre of mass. The equivalent cantilever mass m involves the mass of pier m_p , the pier cap m_{pc} and the deck portion between two mid-spans m_d . Alternatively, the height of the equivalent cantilever can be set equal to the height of the deck centre of mass. If a high degree of deck torsional restraint is present, a different formulation (Priestley et al. 2007) of the equivalent cantilever height should be chosen.

$$H = \frac{(m_{pc} + 0.3m_p)H_p + m_d H_d}{m} \quad \text{where} \quad m = 0.3m_p + m_{pc} + m_d \quad (3.1)$$

The force-displacement characterisation of each equivalent cantilever requires the (bi-linear) moment-curvature relationship for the base section of the pier. This can be calculated with simplified formulations (Gentile et al. 2018b, Gentile & Raffaele 2018) or numerical approaches such as the computer code CUMBIA (Montejo & Kowalsky 2007). The force-displacement curve can be calculated with Equations 3.2 to 3.7 (Priestley et al. 2007), in which φ_Y and φ_U are the yielding and ultimate curvatures, M_Y and M_U are the yielding and ultimate moments, Δ_Y and Δ_U are the yielding and ultimate displacements. L_{SP} is the strain penetration length, f_y and f_u are the yielding and ultimate steel stresses and d_{bl} is the mean bar diameter in the pier. It is worth mentioning that alternative failure modes should be considered, such as lap-splice (Priestley et al. 1996) or buckling (Berry & Eberhard 2005) of the longitudinal bars or shear failure (Kowalsky & Priestley 2000). If one or more alternative failure modes anticipates (or prevents) the flexural hinging, the force-displacement relationship of the piers should be modified in the pre-processing phase, before using it in the analysis.

$$F_{Y/U} = \frac{M_{Y/U}}{H + L_{SP}} \quad (3.2)$$

$$\Delta_Y = \frac{\varphi_Y(H + L_{SP})^2}{3} \quad (3.3)$$

$$\Delta_U = \Delta_Y + \Delta_P = \Delta_Y + (\varphi_Y - \varphi_U)L_P H \quad (3.4)$$

$$L_{SP} = 0.022 f_y d_{bl} \quad (3.5)$$

$$L_P = kH + L_{SP} \quad (3.6)$$

$$k = 0.2 \left(\frac{f_u}{f_y} - 1 \right) \leq 0.08 \quad (3.7)$$

The so-called structural component modelling approach by Priestley et al. (1996) is used to create a simplified mechanical model of the bridge. For analyses in the transverse direction, such scheme (Figure 3.2) is composed by an elastic beam (the deck) on spring supports (deck-pier and deck-abutment subassemblies, simply quoted as pier or abutments hereafter). In the longitudinal direction, the bridge can be modelled considering springs in parallel which are forced to the same displacement. Each subassembly in multi-span simply-supported bridges is calculated as above.

The DBA procedure based on modal analysis (Figure 3.2) starts with the individuation of the member that controls the considered limit state, which in turn allows to select a "control node" in the structural model of the bridge, and to set its displacement (Δ_c). An initial guess of the displacement shape is scaled in such a way that the displacement of the control node is equal to Δ_c . This allows to calculate the displacement shape Δ_i . The shear force in each pier or abutment (V_i) is derived using the appropriate force-displacement curve, and the secant stiffness (k_i) is calculated according to Equation 3.8. A first modal (eigenvalue) analysis is carried out, deriving the first transverse modal shape (ϕ_i) and its participating mass (M_1^*). The first modal shape is scaled according to Equation 3.9 to derive a new displacement profile (Δ'_i), which is compared to the previous guess (Δ_i). The secant stiffness is updated (Equation 3.8) and a new eigenvalue analysis is performed until the calculated displacement profile stabilises. It is worth mentioning that, using a reasonable value of the tolerance (e.g. 0.001), three or four iterations are usually sufficient.

$$k_i = \frac{V_i}{\Delta_i} \quad (3.8)$$

$$\Delta'_i = \Delta_c \frac{\phi_i}{\phi_c} \quad (3.9)$$

If the participating mass of the first vibration mode is less than a given threshold (e.g. 70%), the effect of higher modes should be taken into account in each iteration. This can be done calculating the Effective Mode Shape (EMS) (Kowalsky 2002), considering a number of vibration modes such that the cumulative participating mass is equal or greater than 90%. The performance displacement for each considered mode j is calculated according to Eq. 3.10, where Γ_j and T_j are the modal participation factor and the period of vibration of mode j . Moreover, $S_d(T_j)$ is the displacement demand calculated with an hazard-specific 5% damped elastic spectrum. The final displacement profile Δ_i is finally obtained with a modal combination method such as the Square Root of the Sum of the Squares (SRSS) or the Complete Quadratic Combination (CQC).

$$\Delta_{i,j} = \phi_{i,j} \Gamma_j S_d(T_j) \quad (3.10)$$

The final step of the procedure is the characterisation of the equivalent (effective) SDoF system of the bridge in limit state condition. This is done consistently with the approach by Priestley et al. (2007). The effective displacement (Δ_{eff}) and effective mass (m_{eff}) are computed according to Equations 3.11 and 3.12. The effective damping of the system is calculated accounting for the contribution of all the bridge members, including their elastic and possible hysteretic contributions. Equations 3.13 and 3.14 allow to calculate it considering 5% elastic damping for the abutments and 2% for the deck. In such equations, Δ_{ab} and V_{ab} are the displacement and shear of one abutment, $\Delta_{pier,k}$ and $V_{pier,k}$ are the displacement and shear of the k^{th} pier and $\mu_k = \Delta_{pier,k} / \Delta_{Y_{pier,k}}$. The seismic assessment can be performed comparing the displacement capacity of the SDoF with the displacement demand calculated on an hazard-compatible displacement spectrum.

$$\Delta_{eff} = \frac{\sum m_i \Delta_i^2}{\sum m_i \Delta_i} \quad (3.11)$$

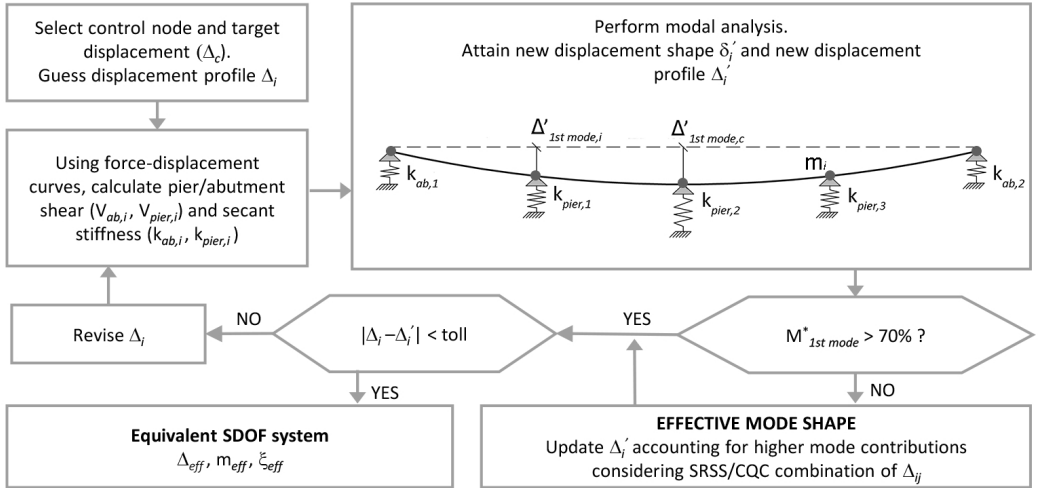


Figure 3.2: DBA procedure based on modal analysis.

$$m_{eff} = \frac{\sum m_i \Delta_i}{\Delta_{eff}} \quad (3.12)$$

$$\xi_{eff} = \frac{\sum 0.05 \Delta_{ab,l} V_{ab,l} + 0.02 \Delta_{eff} (V_{ab,1} + V_{ab,2}) + \sum \xi_{pier,k} \Delta_{pier,k} V_{pier,k}}{\sum 0.05 \Delta_{ab,l} V_{ab,l} + \Delta_{eff} (V_{ab,1} + V_{ab,2}) + \sum \Delta_{pier,k} V_{pier,k}} \quad (3.13)$$

$$\xi_{pier,k} = 0.05 + \frac{0.444(\mu_k - 1)}{\mu_k \pi} \quad (3.14)$$

3.2.2. Proposed alternative DBA procedure based on static analysis

To provide a more practice-oriented tool, an alternative DBA procedure is proposed which is based on static analysis (Figure 3.3). It starts with the definition of a control node, which is related to the subassembly that controls the considered limit state. A guess of the displacement shape is defined and it is scaled in such a way that the displacement of the control node is equal to Δ_c . The displacement of each member (Δ_i) is used to interpolate the force-displacement curve of the sub-structure members and derive the shear (V_i) and, in turn, the secant stiffness (k_i).

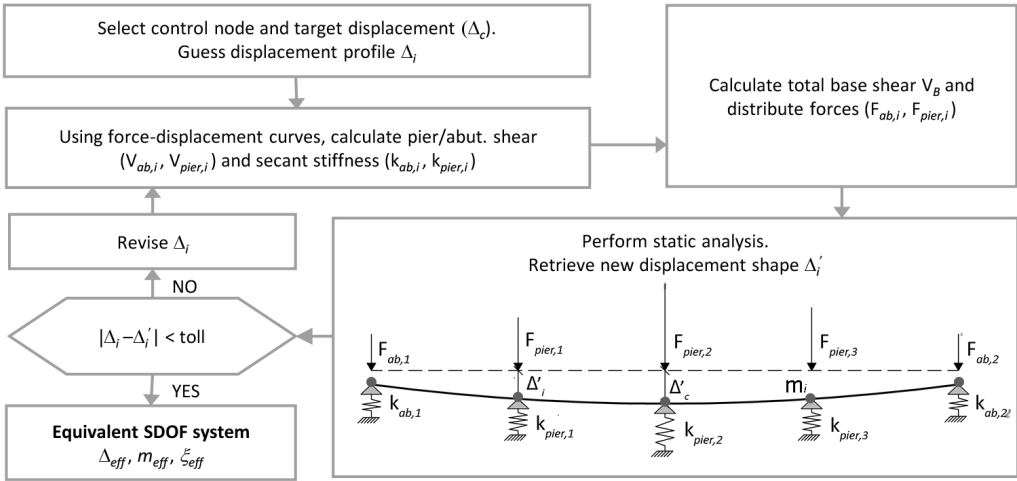


Figure 3.3: Proposed alternative DBA procedure based on static analysis.

The distribution of inertia forces is calculated with Equation 3.15, where V_B is the base shear. A static analysis is performed, and the calculated displacement profile (Δ'_i) is compared with the initial guess to check for convergence. A new static analysis is conducted, after updating all the involved parameters, until the displacement profile stabilises. The characterisation of the SDoF system and the final check against the seismic demand are performed according to the same steps described in Section 3.2.1. The displacement profiles by Priestley et al. (2007) or Cardone (2014) could be adopted to select the initial guess. Nevertheless, a sensitivity analysis in this work demonstrated that the initial guess does not affect the achievement of the convergence for the case studies herein analysed. In fact, regardless of the initial guess, three or four iterations of the analysis are normally sufficient if a tolerance of 1mm is adopted. In the specific case of this study, a parabolic displacement pattern is assumed as initial guess for all the analysed bridges.

$$F_i = \frac{m_i \Delta_i}{\sum m_i \Delta_i} V_B \quad (3.15)$$

3.2.3. Analytical displacement-based pseudo pushover

Both the modal (Section 3.2.1) and the static (Section 3.2.2) DBA procedures are conceptually simple and they can be performed using electronic worksheets or code routines, using analytical static schemes rather than finite element numerical models. Therefore, with the aim of fully exploiting the potentiality of the DBA approaches, it is proposed to extend them to derive the full capacity curve of the bridge. Such process is herein referred as displacement-based pseudo pushover (DBPP). An open access, stand-alone application is provided for these calculations (Gentile 2019). The basic idea is to repeat the modal or static DBA procedure for increasing displacements, allowing to have a thorough information on the behaviour of the analysed bridge with a particularly small increase in computational cost. This allows to calculate, for increasing displacements, the properties of the SDOF system (Δ_{eff} , m_{eff} , ξ_{eff}) and the Engineering Demand Parameters (EDP) for each single member (displacements of the deck, shear in the abutments, shear and base moment of the piers, etc.). Finally, it is possible to plot the base shear vs effective displacement curve.

The capacity curve deriving from this process is based on series of linear analyses (modal or static) of a system whose members are characterised by the secant stiffness compatible with increasing levels of displacement. Such idea is similar to the (more familiar) concept of a pseudo pushover analysis, which refers to a series of linear elastic analyses of a computer model based on secant stiffness. Such approach, also allowed in international seismic guidelines (NZSEE 2017), theoretically allows to achieve the same results of a standard pushover analysis.

Similarly to a numerical analysis, the number of needed steps (or the size of each step) depends on the “smoothness” of the capacity curve required by the user and on the adopted force-displacement relationships of the members (e.g. piers, abutments, bearings, shear keys). If the member capacity curves are multi-linear, $\sum_{i=1}^m b_i$ analysis steps are needed, where m is the number of nonlinear members and b_i is the number of linear branches of the capacity curve of member i . In such case, guidance by Cardone (2014) can be adopted to define the displacement profiles for each analysis step. If the process is implemented in a routine or electronic spreadsheet, it could be less-demanding to run

the analysis for equally-spaced displacement increments (using a sufficiently-small step size) and to derive the relevant limit state displacement profiles by post-processing the results. On the other hand, if smooth capacity curves are adopted for the members (e.g. fibre-based force-displacement analysis for the piers), the latter approach is suggested using a relatively-small step size (e.g. 1 to 5mm).

From the practical point of view, the DBPP starts with the (arbitrary) definition of a control node in the static scheme of the bridge. It is suggested to select the top of a relatively-central pier as control node, although the resulting capacity curve is independent from such choice. The displacement of the control node is set and the modal (Figure 3.2) or static (Figure 3.3) DBA is carried out. The process is repeated for an arbitrary number of times, checking for each step if one or more members in the system have exceeded their displacement capacity. By definition, each analysed step refers to an independent displacement profile and equivalent SDoF system which are compatible with the related secant stiffness, i.e. the procedure is "adaptive". In the context of the DBPPm, if the EMS is needed in the elastic range ($M_1^* < 70\%$), it should be carried out in the non-linear range regardless of the participating mass of the effective first mode (i.e. even if $M_1^* > 70\%$).

Finally, once the DBPP curve is obtained (Figure 3.4), the seismic assessment evaluation can be performed with an Acceleration-Displacement Response Spectrum (ADRS) method such as, the CSM (Freeman 1998a). The defined Performance Point (PP) is compared with the displacement capacity of the system to perform the final assessment.

Apart from the intrinsic simplicity of the method, the adoption of the DB nonlinear curves allows the possibility to investigate the behaviour of the bridge in a "what if" fashion, which can be particularly useful for the design of retrofit options. In other words, by individuating the response of the structure in correspondence of successive performance limits of the members, it is possible to take into account the redundancy of the bridge and/or design redundant retrofit strategies.

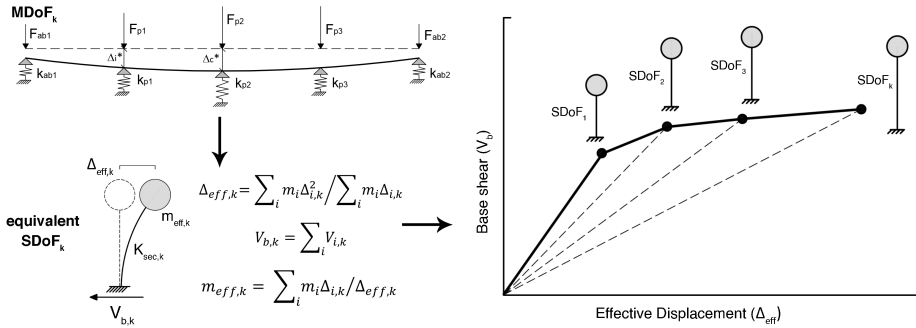


Figure 3.4: Flowchart for calculating the displacement-based pseudo pushover.

3.2.4. Overview of the capacity spectrum method

The CSM aims to identify the performance of a structure under a given seismic input represented by a response spectrum. (ATC 1996) originally proposed three different CSM methodologies (A, B and C). The procedure A is considered the most convenient for simple spreadsheet/programming routine implementation. It is outlined in this section and applied in this study. The CSM requires the computation of a force vs displacement relationship (i.e. pushover curve or the above-mentioned DBPP) for the investigated structure subjected to a monotonic load profile simulating the effect of a dynamic excitation. The pushover curve is converted into a “capacity spectrum” related to an equivalent SDoF system of the structure, expressed in an acceleration vs displacement format. For conventional numerical pushover curve, Equation 3.12, 3.11 should be applied to calculate the equivalent SDoF mass and displacement. For both numerical pushover and DBPP, the conversion in acceleration-displacement space can be simply performed by dividing V_B for m_{eff} .

The CSM involves an iterative graphical procedure aimed to determine the PP in an acceleration-displacement plane through the use of overdamped spectra. First, a tentative performance displacement is assumed. In the conventional CSM approach, a bilinearisation of the capacity spectrum up to the tentative performance displacement is carried out. The equivalent yielding displacement is thus obtained and the ductility demand corresponding to the tentative performance displacement is calculated by simply dividing the target displacement for the yielding one. At this stage, the overdamped

demand corresponding to the tentative performance displacement is computed by multiplying the elastic (5%-damping) demand spectrum ordinates (conventionally a code-based smooth spectrum is used) for a spectral reduction factor (η , Equation 3.16). This latter is derived from the ductility-based equivalent viscous damping coefficient (ξ) which expresses the reduction of the elastic demand given the hysteretic dissipation. In this study, this step (bilinearisation and equivalent viscous damping calculation) is not performed, since the equivalent viscous damping is known for each load step by Equation 3.13. The same formulation can be applied also by using a pushover curve, provided that the displacement profile is calculated for each loading step. This approach is also described by Casarotti & Pinho (2007).

$$\eta = \sqrt{\frac{0.07}{0.05 + \xi}} \quad (3.16)$$

A new target performance displacement is identified at the intersection between the overdamped demand and capacity spectra. If the calculated performance displacement is sufficiently close to the initial guess (within an arbitrary tolerance assumed by the analyst), the algorithm is completed and the performance point is identified. This latter expresses the compatibility between the damping associated to both the overdamped demand and the ductility demand of the structure. Otherwise, the newly calculated performance displacement is used as the new tentative target one, and another iteration is carried out. The process continues until the convergence is achieved.

3.3. Assumptions for the parametric analysis

3.3.1. Description of the case study bridges

The dataset of case studies for this parametric analysis is composed of 36 RC, continuous-deck, straight bridges with pinned deck-pier and deck-abutments connections (Figure 3.5). Two deck typologies are considered. The first (J50) has a moment of inertia (for transverse flexure) equal to $52.5m^4$ and is composed of three V-shaped 1.8m-high pre-cast beams and a 11.5m-wide slab (0.3m-deep). For the second deck typology (J100), the moment of inertia is equal to $104.1m^4$, the number of 1.8m-high beams is equal

to four and the slab width is equal to $14m$. The dimensions of the pier caps related to each deck typology are indicated in Figure 3.5.

For each deck typology, 18 different bridge geometries are considered, with two, four or six $35m$ -long spans. Pier heights of $8m$, $15m$ and $20m$ are adopted to define regular and irregular geometric configurations (Figure 3.5). As an example, the case study labelled as *B132* is a four-span bridge with a $8m$ -, $20m$ - and $15m$ -high piers. The pier cross section, assumed to be equal for all the piers, is circular with $3m$ diameter. The longitudinal reinforcement is composed of $63\phi26$ bars (with ratio $\rho_l = 0.47\%$) while the transverse reinforcement is composed of $100mm$ -spaced $\phi10$ bars (with volumetric ratio $\rho_t = 0.1\%$). The shear strength Kowalsky & Priestley (2000) of the piers is considerably higher than the corresponding flexural one, even for the shortest pier.

The considered unconfined concrete strength is $f_c = 20MPa$ while the steel yield stress is $f_y = 450MPa$. Both the seismic masses and gravity loads (seismic load combination) are calculated based on a concrete density equal to $25kN/m^3$ and a uniform deck load equal to $185kN/m$ ($230kN/m$ for the J100 sub-set) to consider both self weight and superimposed gravity loads.

The elastic dynamic behaviour of the selected bridges is dominated by the first mode. Indeed, the first mode participating mass ranges between 74% and 84%. The elastic (secant-to-yielding) first mode period of the bridges (shown in Figure 3.7) is observed in the range $[0.25s, 1.45s]$. On the other hand, the first mode period of the bridges calculated adopting the secant-to-performance point stiffness (CSM-based) falls within the range $[0.25s, 1.63s]$ (also shown in Figure 3.7).

The regularity of the case-study bridges is measured with the relative stiffness index (Dwairi & Kowalsky 2006) (RS, Eq. 3.17), which quantifies - with a degree of approximation - the ratio between the (elastic) stiffness of the superstructure and the substructure. In such equation, EJ_{deck} and L_{deck} are the transverse flexural stiffness and the total length of the deck, respectively. Greater values of RS indicate high regularity of the bridge and low importance of higher modes (Kappos et al. 2013). The RS is calculated using both the elastic, RS_e , and secant stiffness, RS_{pp} , of the piers (at the CSM-based performance point) to investigate the regularity of the response for increased seismic

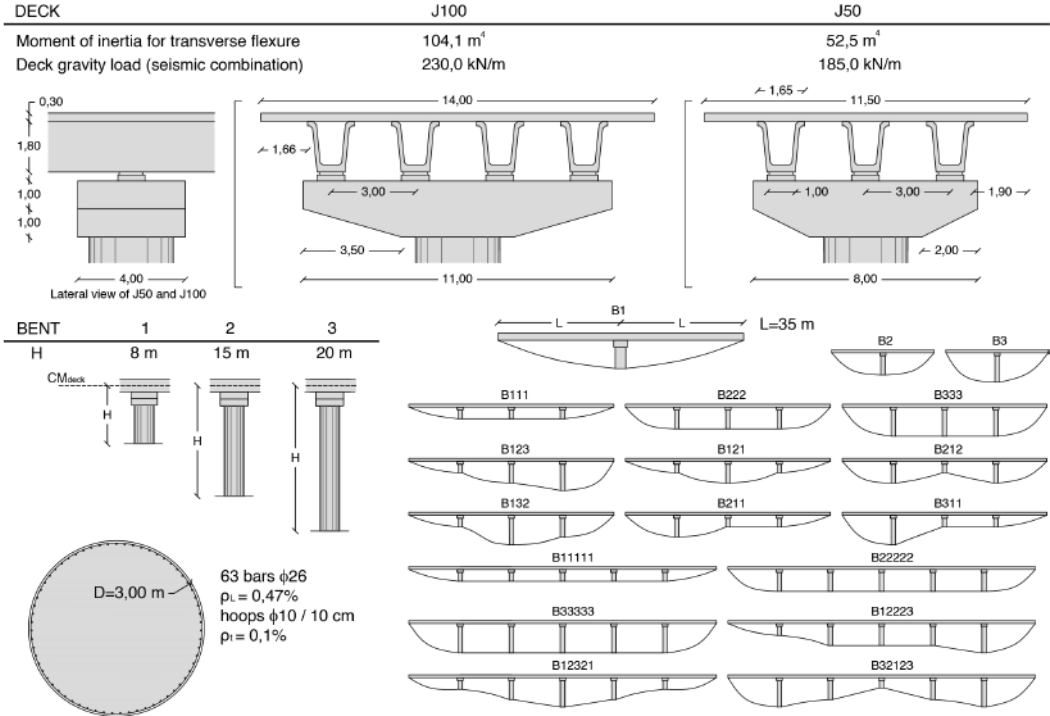


Figure 3.5: Geometrical configuration of the 36 selected case studies. ρ_l, ρ_t : longitudinal and transverse reinforcement ratios.

intensity.

$$RS = \frac{384EJ_{deck}}{5L_{deck}^3 \sum_i k_{pier,i}} \quad (3.17)$$

3.3.2. Assumptions for analytical and numerical analyses

Both nonlinear static procedures (NSPs) and NLTHA are performed in this study. The considered NSPs include: static and modal displacement-based pseudo pushover (DBPPs and DBPPm); numerical pushover analysis considering an invariant force profile proportional to the first vibration mode (PUSHm); uniform force profile pushover (PUSHu). These NSPs are coupled with CSM (subsection 3.2.4) to calculate the PP. For both the analytical and numerical analyses, the bi-linear moment-curvature relationship of the base section of the piers is adopted. This is calculated using the software

CUMBIA (Montejo & Kowalsky 2007). Moment-curvature is carried out adopting the model by Mander et al. (1988) for confined concrete, the model by King et al. (1986) for the steel reinforcement and considering the gravity axial load on the piers. It is worth mentioning that the upper bounds for concrete and steel ultimate strains are set to 0.02 and 0.06, respectively (NZSEE 2017). No strength degradation is considered, since the aim of this work is the analysis of the effectiveness of analytical procedures, rather than capturing strength degradation effects.

The DBPPs and DBPPm procedures are implemented in an ad-hoc Matlab (MATLAB 2018) script, allowing for simple and fast calculations. To this aim, the so-called structural component modelling approach by Priestley et al. (1996) is used, considering the transverse response only. In such analytical model (Figure 3.2), the continuous deck is modelled as an elastic beam while the equivalent cantilevers of piers and the (pinned) abutments are represented by elastic springs. The springs referring to the piers are characterised by a force-displacement curve. This is based on the calculated moment-curvature and adopting Equations 3.2 to 3.7, in which the strain penetration length is neglected. Seismic masses are lumped in the main nodes of the deck, summing the tributary deck mass, the mass of the pier cap and one-third of the pier.

The numerical pushover and NLTHA are performed using the nonlinear finite element software Ruaumoko 3D (Carr 2016). The modelling strategy (Figure 3.6) is based on a lumped plasticity approach in which the deck is an elastic frame member based on uncracked stiffness. In correspondence of each pier, the deck node is part of a body constraint along with mass-less nodes for each girder. Those are connected to the elastic pier cap member through a rigid link and elastic springs representing bearings. Among those, one is modelled as a pinned connection while the others are sliders. A similar approach is adopted for the abutments. Piers are modelled by means of mono-dimensional Giberson elements (Sharpe 1976). The nonlinear behaviour of the (fully-fixed) base section of the piers is set consistently with their bi-linear moment-curvature relationship. The cyclic response of the section is modelled with the revised Takeda model (Saiidi & Sozen 1979), using 0.5 and 0 for the unloading and reloading stiffness factors, respectively. The deck mass is distributed on five nodes for each span. The mass of the piers is assigned to four nodes along their height, while three nodes are

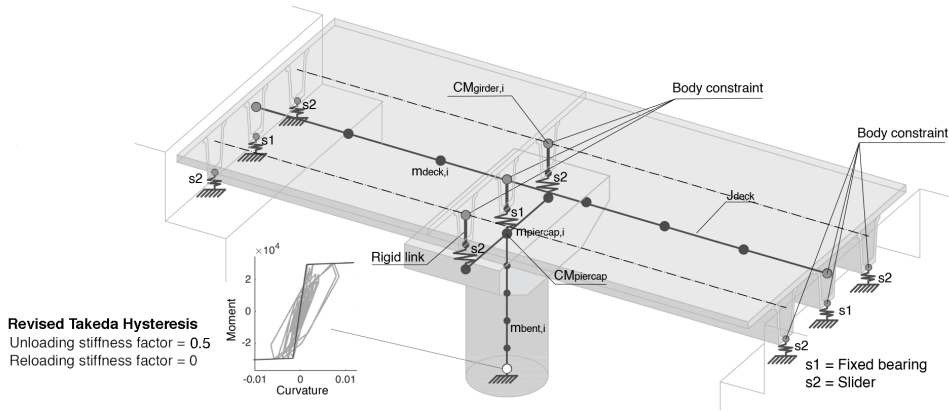


Figure 3.6: Adopted modelling strategy for numerical NLTHA and pushover analyses.

adopted for pier caps. In the pushover analyses (PUSHm and PUSHu), each node assigned with a mass is part of the lateral load pattern. P- Δ effects are considered in both the displacement-control pushover analyses and NLTHA. For the NLTHA, a tangent stiffness proportional damping is selected as suggested by Priestley et al. (2007) and a constant 5% damping is assigned to all the principal modes of the bridges.

3.3.3. Seismic demand

Three ground-motion Intensity Measures (IM) are considered in this study, referring to low-, medium- and high-seismicity zones (Calcata, Montesilvano and Cosenza, Italy). Figure 3.7 shows the related 5%-damped acceleration response spectra provided by the Italian code (Ministero delle Infrastrutture e dei Trasporti 2018), related to a return period equal to 450 years, soil type C (shear wave velocity $V_{s,30} = 180 - 360m/s$) and an importance factor equal to 1.5. The Peak Ground Acceleration (PGA) is respectively equal to 0.25g, 0.32g and 0.42g. Such spectra are adopted to apply the CSM for both the DBPP curves and the numerical pushover ones. The equivalent SDoF conversion related to the numerical pushover curves is applied as per the DBA procedures (Section 3.2.1), for consistency. NLTHA are carried out adopting three suites of 10 natural ground motions selected from the European Strong-motion Database (ESD), using the tool REXEL (Iervolino et al. 2010) (Figure 3.7). Such ground motions are linearly-scaled in amplitude to achieve the compatibility with the above-mentioned target spectra (maxi-

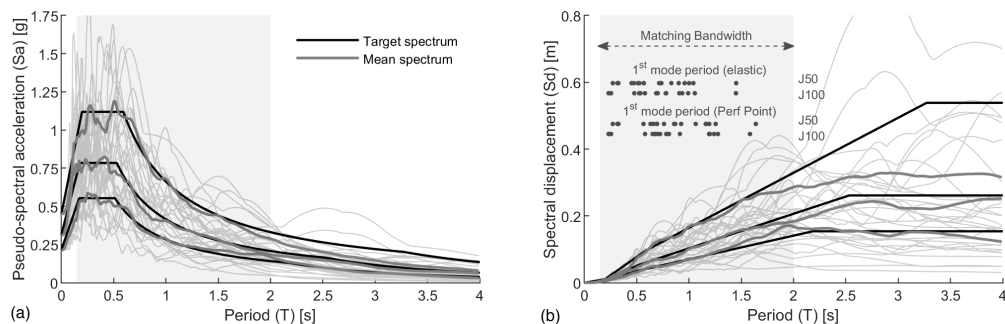


Figure 3.7: Elastic acceleration (a) and displacement (b) spectra of the scaled selected ground motions.

num scale factor equal to 5). Spectrum compatibility is ensured in the bandwidth [0.1 s, 2 s], selected to include the values of elastic (secant-to-yielding) first mode period of the analysed bridges, also shown in Figure 3.7. The observed period shift allows to confirm the appropriateness of the record selection for the NLTHA. Indeed, all the first mode effective periods (secant-to-performance point) fall within the adopted matching bandwidth.

3.4. Results of the parametric analyses

3.4.1. Calculation of the capacity demand ratio and the bridge index

The analysis results for each case-study bridge are represented by two parameters: the Capacity Demand Ratio (CDR) and the Bridge Index (BI). Those respectively refer to the seismic performance of a given bridge with respect to the demand, and to the accuracy of the predicted displacement profile with respect to the NLTHA, herein taken as a benchmark. Similarly, the error on the CDR ($\frac{NSP-TH}{TH}$) is introduced to have a systematic comparison of the parametric analysis results and the evaluation of DBPP procedure.

For all the considered analysis methods, it is assumed that the first pier that reaches the Ultimate Limit State (ULS) causes the bridge ULS. For the NSPs, referring to pushover or DBPP, the CDR is defined by post-processing the results according to Eq. 3.18. The displacement capacity of each pier ($\Delta_{U_{pier,k}}$, where k indicates the piers) is compared to the displacement demand at the performance point ($\Delta_{pier,k}^{PP}$). These refer to the

displacement profile consistent with the performance point calculated with the CSM. To calculate the CDR of the NLTHA for a suite of records (Equation 3.19), the displacement capacity of each pier is compared to the average response for the considered ground motion suite ($\Delta_{pier,k}^{TH}$).

It is worth mentioning that, since no strength degradation is considered in this study, an hardening behaviour is registered in the force-displacement curves after the attainment of the ULS, and this also affects the calculation of the performance point for bridges that do not meet the criterion $CDR \geq 1$. Clearly, other members in the bridge (abutments, bearings, etc.) should be considered in the calculation of the CDR. However, this is outside the scope of this study and only the piers are herein considered.

$$CDR^{NSP} = \min\left(\frac{\Delta_{U_{pier,k}}}{\Delta_{PP}^{pier,k}}\right) \quad (3.18)$$

$$CDR^{TH} = \min\left(\frac{\Delta_{U_{pier,k}}}{\Delta_{pier,k}^{TH}}\right) \quad (3.19)$$

The BI, proposed by Pinho et al. (2007), and adapted by Kohrangi et al. (2015b), is herein adopted as an indicator of the bias of the NSPs with respect to the NLTHA results in terms of deck displacement profile (Δ_i). In particular, the maximum response of each NLTHA run is used to calculate the equivalent SDoF displacement. The average of such displacements for the considered ground-motion suite is calculated (Δ_{SDoF}^{TH}). The corresponding displacement profile (Δ_i^{NSP}) is extracted from the database of a NSP, and the BI is calculated with Eq. 3.20, where N_{sub} is the number of sub-structure members. Clearly, BI values close to one indicate the accuracy of a NSP in approaching the NLTHA results.

$$BI = \frac{1}{N_{sub}} \sum_{i=1}^{N_{sub}} \frac{\Delta_i^{NSP}}{\Delta_i^{TH}} \quad (3.20)$$

3.4.2. Detailed results for selected bridge case studies

This section presents the detailed results of three selected case studies. This allows to better interpret the overall results presented in Section 3.4.3. Note that a complete

extensive collection of results is reported in Appendix B.

The first selected case study is a four-span bridge (J100 B222) showing high regularity in the seismic response ($RS_e = 1.26$, $RS_{pp} = 1.32$). Figure 3.8.a shows the NSP-related curves (PUSHm, PUSHu, DBPPm and DBPPs), representing the effective SDoF displacement versus the total base shear. Both the CSM-based performance points (for the three considered IMs) and the ULS are indicated. Moreover, three indicators show the average response of the NLTHA (10 runs for each considered suite). In particular, the displacement and shear profiles for each ground motion record are enveloped, before taking their average. An SDoF approximation (displacement and base shear) is derived based on such average profiles. To have a measure of the NLTHA response dispersion, the related confidence ellipses are also shown. Those represent the standard deviation of the effective SDoF displacement and the total base shear, including their correlation. Figure 3.8a indicates that the DBPPs curve is particularly similar to the PUSHm, while the DBPPm predicts a slightly-higher base shear (less than 6% over-estimation throughout the entire curve). The worst prediction is provided by the PUSHu, for which a 16% base shear over-estimation at ULS is observed with respect to the PUSHm. In this case, using a uniform force profile introduces a higher shear force directly transferred to the abutments, thus increasing the total base shear. The DBPPs, DBPPm and PUSHm performance points are particularly close to the average NLTHA response, proving the accuracy of the corresponding procedures. For IM3, the error for the displacement is equal to -1.0%, -2.8% and -0.5%, respectively for DBPPs, DBPPm and PUSHm (+8.3%, +5.4% and +9.7% for IM1). However, a slightly-higher over-prediction is observed for the IM2 performance-point displacement (respectively +14.0%, +11.6% and +14.7%). This is possibly related to the damping assumption in the CSM, which may be less accurate in the branch of the capacity curve where the highest stiffness change is registered.

For this case study, the accuracy of the NSPs based on the first modal shape is evident, since the corresponding capacity curves are particularly close to the average NLTHA response for the three analysed IMs, and within the corresponding standard deviation. Moreover, the DBPPs curve is practically identical to the PUSHm one, demonstrating the reliability of the simplified method for first mode-dominated bridges.

The ULS of the system is predicted consistently by using all the NSPs. The CDR based

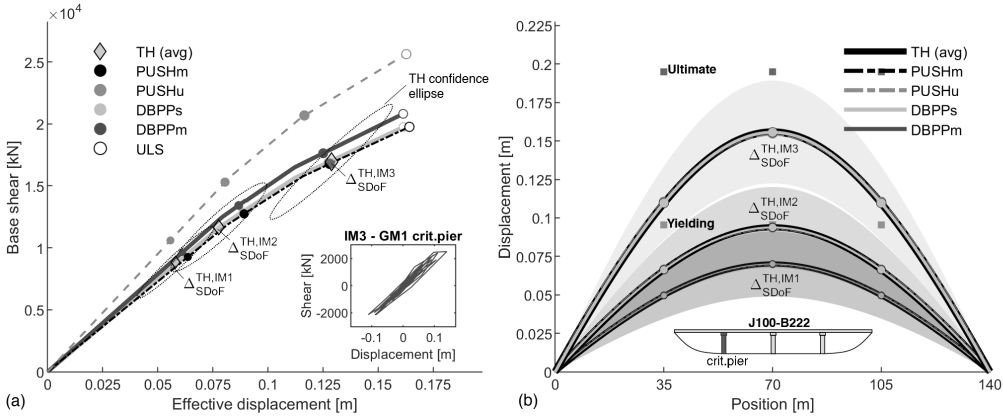


Figure 3.8: J100 B222 bridge: a) capacity curves and NLTHA response, b) displacement profiles calculated at Δ_{SDoF}^{TH} .

on NLTHA is equal to 1.25 at IM3, while its relative error with respect to the NLTHA is equal to +1.1%, +3.1% and +0.7%, respectively for the DBPPs, DBPPm and PUSHm. Considering the simplicity of the proposed methods with respect to the NLTHA, such error trends are deemed to be satisfactory.

Figure 3.8b shows the displacement profiles from the NLTHA (average \pm standard deviation), for each IM. The displacement profiles predicted by each NSP are shown for an SDoF displacement equal to the NLTHA average (Δ_{SDoF}^{TH} defined in Section 3.4.1). It is worth mentioning that a cubic interpolation is adopted herein, to somehow reflect the topology of the elastic deformation of the continuous deck. The yielding and ultimate displacements of each pier are also shown, thus allowing to interpret each stiffness change in the capacity curves. For each IM, the displacement profile of the bridge is effectively captured by all the adopted NSPs (with respect to the NLTHA). This is confirmed by the BI, which is always smaller than 1.001.

The second selected case study is the J50 B12321, whose response is more affected by the piers rather than the deck ($RS_e = 0.05$, $RS_{pp} = 0.11$). Figure 3.9a shows that the DBPPs and DBPPm are affected by a negligible error with respect to the PUSHm, while the PUSHu consistently over-estimates the base shear (max 23% with respect to PUSHm). The CSM performance point is closely matching the average NLTHA response, especially for IM1 and IM3 (e.g. the DBPPs base shear error is respectively equal to +12.0% and -3.0%). A higher error is registered for IM2 (15.9%), although

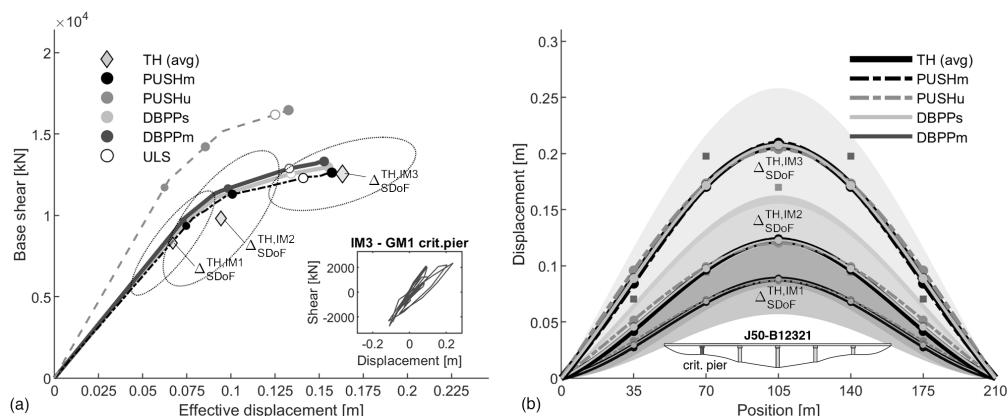


Figure 3.9: J50 B12321 bridge: a) capacity curves and NLTHA response, b) displacement profiles calculated at Δ_{SDoF}^{TH} . For each pier, a light- and dark-grey markers show their yielding and ultimate displacements.

the CSM performance point is within one standard deviation from the NLTHA average. In fact, close to this displacement level, the highest stiffness change is registered in the capacity curve(s), and the record-to-record variability has a higher influence on the NLTHA response (increasing its dispersion). As an example, the yielding of piers 2 and 4 is dependent on the considered ground-motion record (Figure 3.9b). Such results are reflected in the calculation of the CDR. At IM3, this is equal to 0.84, 0.85, 0.87 and 0.79, respectively for DBPPs, DBPPm, PUSHm and NLTHA.

Figure 3.9b shows that the displacement profiles calculated with the NSPs are in good agreement with the average NLTHA results. The BI (IM3) related to the PUSHm is equal to 0.978, while a better performance is observed for the DBPPs and DBPPm (0.999 and 1.002, respectively).

The last selected case study (J100 B1) is a two-span bridge with a 8m-high pier which is clearly dominated by the deck response ($RS_e = 6.44$, $RS_{pp} = 6.44$). It is worth repeating that it is herein chosen to define the ULS of the bridge only according to the piers (not considering bearings, abutments, etc.). For this short bridge, the vast majority of the lateral load is directly carried by the abutments. Therefore, the estimation of the ULS according to the piers (only) leads to particularly high displacement values (outside the limits of the plot in Figure 3.10a). Clearly, this is reflected on the CDR.

The results of the analyses show that the bridge remains in the elastic range for all

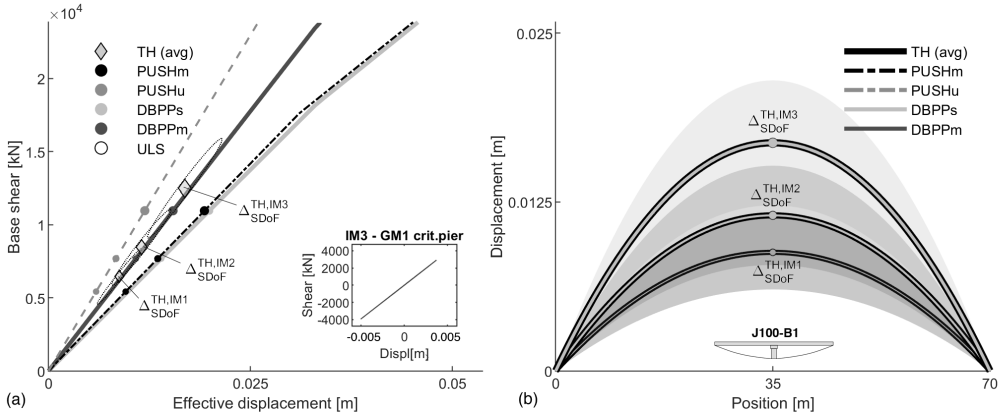


Figure 3.10: J100 B1 bridge: a) capacity curves and NLTHA response, b) displacement profiles calculated at Δ_{SDoF}^{TH} . For each pier, a light- and dark-grey markers show their yielding and ultimate displacements.

the considered ground motion IMs. The DBPPs is practically coincident to the PUSHm, since both are based on a force profile proportional to the first modal shape. Again, this confirms the reliability of the structural component modelling approach. It is worth mentioning that the DBPPm capacity curve is slightly different from the two previously-mentioned approaches since this is based on a shear profile (rather than force profile) proportional to the first modal shape. Indeed, using the response of the structure rather than the applied forces (shear rather than force profile) allows to better consider the influence of the deck, whose properties affect the shear distribution on the piers/abutments. For this reason, the DBPPs provides equivalent accuracy with respect to the PUSHm and the DBPPm better captures the average NLTHA response (displacement error equal to -12.9%, -6.0% and -8.6%, respectively for IM1, IM2 and IM3). The NSPs performance points (for the three IMs) are observed on the plateau of the target spectra. Therefore, the above-mentioned errors are likely caused by the discrepancy between the average ground-motion spectrum and the target one, which is highest in the plateau region (Figure 3.7).

For this case study, and all the two-span case studies, the BI is equal to 1 regardless of the considered method. Indeed, for such simple bridge configurations, the BI depends solely on the maximum displacement of the pier, and does not provide any added value in the interpretation of the results.

3.4.3. Discussion of the results considering the entire dataset

The results for the entire dataset are discussed herein, including the accuracy of the DBPPs and DBPPm. Considering the NLTHA as a benchmark, Figure 3.11 shows the error on the CDR while Figure 3.12 shows the BI. Table 3.1 shows the CDR values for IM3. Finally, Figure 3.13 summarises all the conducted analyses.

Considering RS_e index, the case-study dataset can be split in three groups. Considering the J50 cases, the two-span bridges ($3.24 \leq RS_e \leq 38.20$) are dominated by the deck response; for the six-span bridges ($0.02 \leq RS_e \leq 0.28$), the piers are much more likely to govern the response; the four-span bridges ($0.13 \leq RS_e \leq 1.59$) represent intermediate cases which can be dominated either by the deck or the piers. Clearly, the RS_e for the J100 sub-set are double with respect to the J50 ones. $RS_{pp} = RS_e$ for the two-span bridges (elastic response). For the six-span case studies, the small differences between RS_{pp} and RS_e ($\Delta RS = 0.28$ maximum) indicate that the regularity in their response generally remains unchanged. The response of the four-span case studies is considerably more regular in the inelastic range ($\Delta RS = 0.61$ maximum). Indeed, the stiffness degradation for the piers leads to a deck-dominated behaviour.

Figure 3.11 shows that the DBPPs provides a similar level of accuracy of the DBPPm. In particular, for all the four-spans and six-span case studies, negligible differences in the CDR error are observed. On the other hand, for two-span case studies such differences are higher, indicating a greater accuracy of the DBPPm. This confirms the discussion in Section 3.4.2, including the higher accuracy of the DBPPm with respect to the PUSHm for two-spans bridges. To validate the assumed equivalent cantilever height in the DBPP approaches, the pier bending moment profiles (PUSHm) are used to provide "numerically-based" estimates of their equivalent height. Repeating the DBPPs using these new height estimates leads to negligible differences in the capacity curve, thus proving the low influence of the deck torsional stiffness.

Considering the four- and six-span case studies, the capacity curve estimation by both the DBPPs and DBPPm closely match the results of the PUSHm (Figure 3.13). Moreover, the response of all the case studies is dominated by the first vibration mode. The participating mass is always greater than 74% and therefore the EMS is not necessary (only

the first mode is considered). Slightly higher discrepancies are observed for the most irregular configurations in the dataset, i.e. J50 B32123 ($RS_e = 0.08$, $RS_{pp} = 0.25$), J50 B211 ($RS_e = 0.19$, $RS_e = 0.39$), J50 B311 ($RS_e = 0.20$, $RS_e = 0.81$), where the PUSHm provides the highest base shear, since a non-adaptive approach fails to capture the abrupt stiffness change after the yielding of the shortest piers. The ULS displacement is captured with a relative error (with respect to the PUSHm) equal to 3.3% and 3.4% (average of absolute values), respectively for the DBPPs and DBPPm approaches. On the basis of these results, it can be stated that for a wide range of bridge configurations both the DBPPs and DBPPm allow to estimate capacity curves with a level of accuracy particularly similar to a PUSHm.

The CSM is adopted, in conjunction to the DBPPs and DBPPm curves, to assess the seismic performance of the bridges. The resulting performance points are compared to the analogous values obtained with the PUSHm. The relative DBPPs vs PUSHm error is equal to 1.9% and 2.6% (average of absolute values considering the three IMs), respectively for displacement and base shear. On the other hand, 5.7% and 2.6% average errors are respectively registered for the DBPPm. The relative errors with respect to the average NLTHA are equal to 12.4% and 8.4% for the DBPPs while 10.6% and 9.3% for the DBPPm. This indicates that both methods provide reasonable results when compared to NLTHA analyses, with the DBPPm being slightly better. As shown in Figure 3.13, for the majority of the case studies the DBPPm and DBPPs performance points fall within the confidence ellipses of the NLTHA. For IM3, the coefficient of variation of the NLTHA analyses is reported in the range [16%;33%] for the effective displacement and [7%;30%] for the total base shear.

Figure 3.11 shows the calculated CDR for each analysis approach. It can be firstly stated that, in estimating the seismic performance, the DBPPs provides a similar accuracy if compared to the PUSHm. By referencing to NLTHA, the average CDR error is equal to 11.0% and 8.7% respectively for the DBPPs and the PUSHm. The DBPPm allows for a slightly better accuracy (8.2% average error), since the analyses are based on a shear (rather than force) profile proportional to one or more modal shapes. Finally, the error trends are not sensitive to the moment of inertia of the deck. Indeed, by disaggregating the results for J50 and J100 configurations, a maximum 1% shift in the above-mentioned

average errors is registered. Overall, based on the data in Figure 3.11, it can be further stated that both the DBPPs and DBPPm approaches provide fairly-accurate seismic performance assessments, if compared to NLTHA analyses.

The PUSHu results greatly over-estimate the base shear capacity for all the case studies (Figure 3.13). For this reason, the predicted displacement at the performance point is systematically lower than for the PUSHm, DBPPm and DBPPs. With respect to the other NSPs, this causes a higher estimated CDR for the entire dataset, and therefore a higher relative error with respect to NLTHA. In particular, the CDR error falls within the range [-12.8%; +68.3%]. For some case studies (e.g. J50 B121, B211, B311), the PUSHu CDR error is particularly close to zero. However, this does not correspond to a better accuracy of the PUSHu approach. An example is shown in Figure 3.8 (IM1 and IM2), where the performance point displacement of the PUSHu is particularly similar to the NLTHA one. Although this leads to a low relative error on the CDR, it is clear that the response predicted using the PUSHu is not satisfactory, i.e. the PUSHu performance point falls outside the confidence ellipse of the NLTHA.

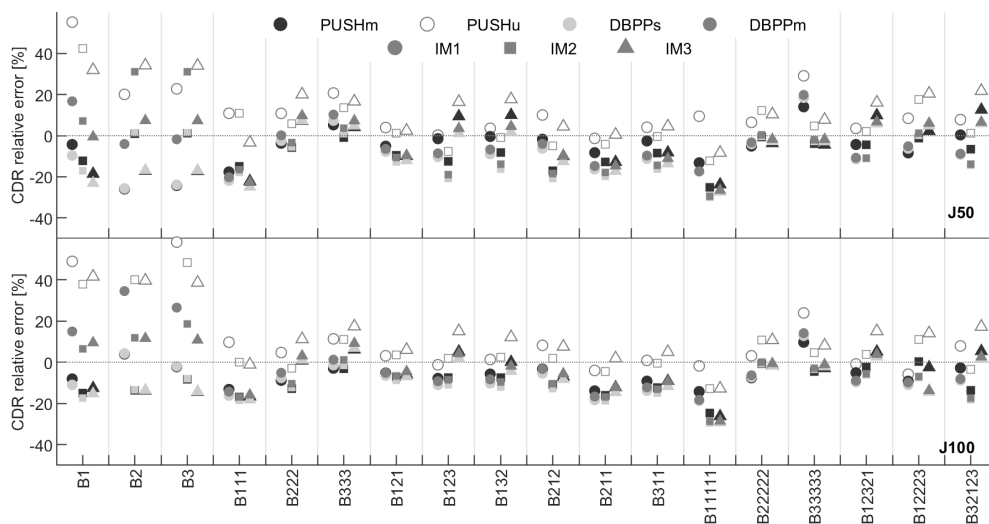


Figure 3.11: Error of the CDR for the entire dataset relatively to NLTHA.

The accuracy in determining the displacement profile is finally measured calculating the BIs, which are shown in Figure 3.12. The BIs for the two-span case studies are practically equal to one, and they are not shown in the figure. It is evident that the DBPPs and

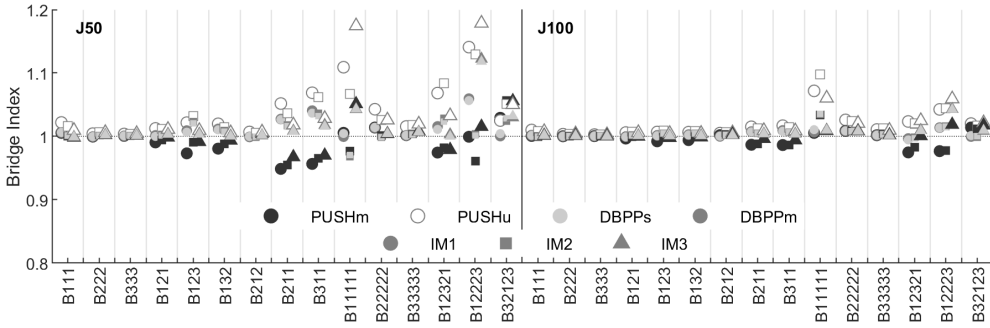


Figure 3.12: BIs for the entire dataset.

DBPPm are equivalently accurate for all the analysed bridges (1.01 average BI for both approaches). For the PUSHm and PUSHu, the observed BIs are generally furthest from 1.00, especially for the less regular bridges (e.g. J50 B211, B311, B12321). This is respectively due to the above-mentioned non-adaptive nature of these approaches and the inadequacy of the uniform force profile. The BIs values are partially governed by the stiffness of the deck, which affects the force redistribution after each stiffness change in the nonlinear static response. Indeed, the J100 BIs are considerably closer to 1.00 and they show less dispersion.

3.4.4. Sensitivity analysis for long bridges

An additional parametric analysis is conducted to investigate the accuracy of the DBPPs and DBPPm for longer bridges (8 or more spans). The adopted analysis approaches are the same of the main parametric analysis. The dataset of case studies is composed of six bridges: four having 8 spans and different pier height distribution along the deck (B2222222, B1223221, B3332211, B2131332); two bridges having 10 and 12 spans with 15m-high piers. The J50 deck configuration is provided for all the cases, yielding to $0.01 < RS_e < 0.035$ for the 8-span bridges and $RS_e < 0.01$ for 10- and 12-span ones. Only the highest seismic intensity is considered (IM3). Given the low RS_e , the seismic response would be likely governed by the piers. This also increases the sensitivity of higher modes (in both linear and nonlinear ranges) to the pier-height distribution.

Figure 3.14a investigates the influence of the bridge length only (for a uniform pier-

Table 3.1: Capacity Demand Ratio (CDR) for the entire case study dataset, calculated at IM3.

	J50			
	DBPPs	DBPPm	PUSHm	PUSHu
B1	2.53	3.27	2.68	4.34
B2	5.10	6.58	5.08	8.23
B3	8.44	10.89	8.40	13.60
B111	0.75	0.77	0.78	0.96
B222	1.19	1.22	1.19	1.33
B333	1.58	1.62	1.57	1.76
B121	0.88	0.91	0.90	1.03
B123	0.78	0.79	0.84	0.89
B132	0.71	0.73	0.77	0.82
B212	0.57	0.58	0.58	0.68
B211	0.66	0.68	0.69	0.80
B311	0.65	0.67	0.69	0.79
B11111	0.62	0.62	0.65	0.78
B22222	0.90	0.91	0.89	1.02
B33333	1.14	1.15	1.12	1.26
B12321	0.84	0.85	0.87	0.92
B12223	0.98	0.99	0.95	1.12
B32123	0.40	0.41	0.43	0.46
	J100			
	DBPPs	DBPPm	PUSHm	PUSHu
B1	3.47	4.49	3.58	5.80
B2	8.00	10.32	7.98	12.91
B3	13.65	17.61	13.61	22.03
B111	0.75	0.77	0.76	0.90
B222	1.27	1.29	1.26	1.39
B333	1.77	1.81	1.76	1.94
B121	0.89	0.92	0.90	1.02
B123	0.79	0.81	0.82	0.90
B132	0.74	0.76	0.77	0.87
B212	0.59	0.61	0.60	0.69
B211	0.67	0.69	0.69	0.80
B311	0.67	0.69	0.69	0.80
B11111	0.58	0.58	0.60	0.71
B22222	0.89	0.90	0.89	1.00
B33333	1.18	1.19	1.17	1.30
B12321	0.76	0.77	0.78	0.85
B12223	0.79	0.80	0.90	0.87
B32123	0.38	0.39	0.40	0.44

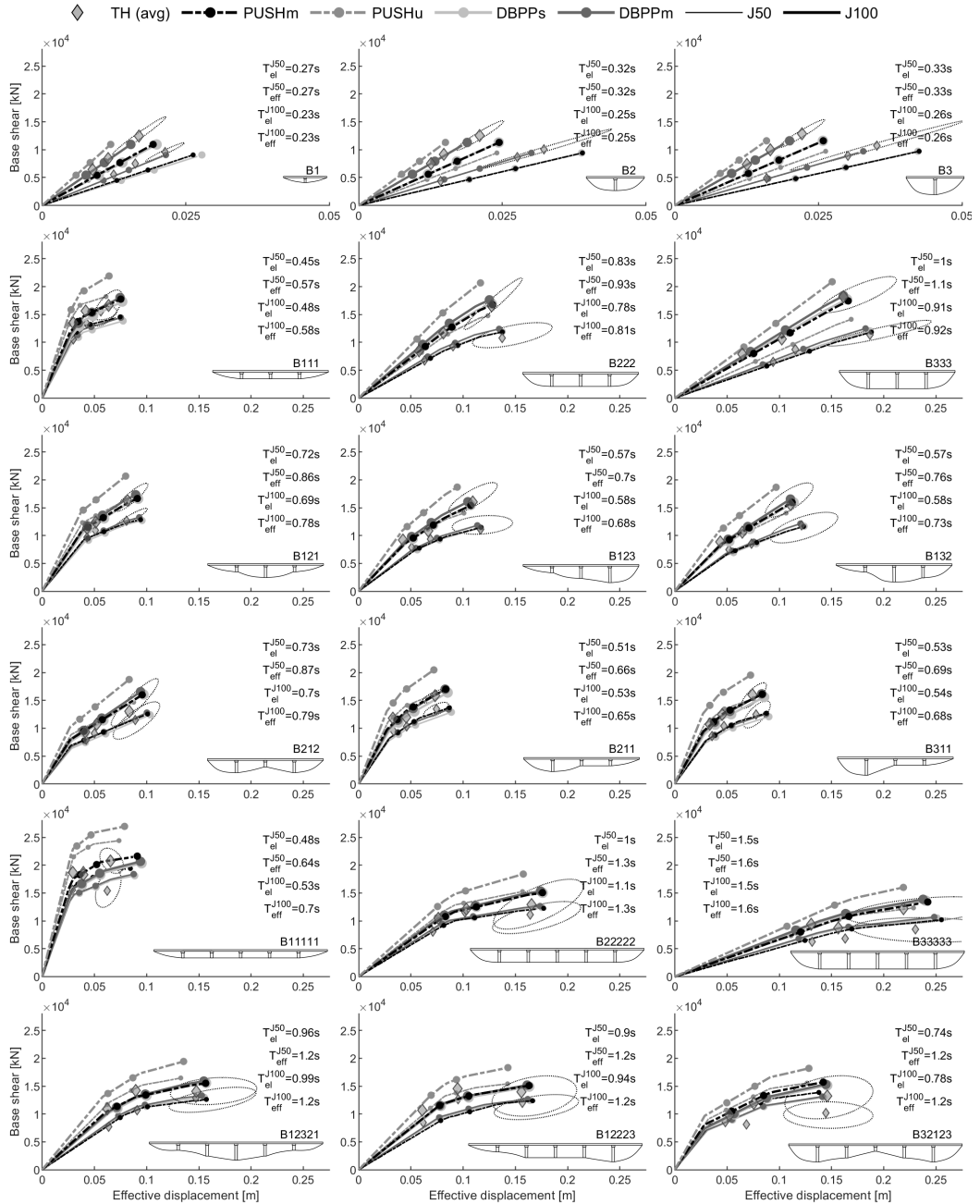


Figure 3.13: Results of the analyses for the entire case study. The thin curves and the small markers are associated to J50 deck, while the thick curves and the big markers refers to J100. First-mode periods, calculated with elastic (secant-to-yielding) and effective (secant-to-performance displacement, CSM-based) stiffness, are indicated.

height distribution), by showing the capacity curves of the bridges having 15m-high piers. Figure 3.14b, instead, shows the influence of pier-height distribution for the 8-spans cases only (B1223221, B3332211 and B2131332). The DBPPs and PUSHm provide similar capacity curves (as for the shorter bridges), while DBPPm diverges considerably, and tends to the PUSHu. This is caused by the EMS calculated in the DBPPm, since the participating mass of the first mode is smaller than 70%. Confirming the results by Pinho et al. (2007), for long bridge case studies, the NSPs based on the first mode only predict a lower total base shear with respect to the NLTHA. The PUSHu and DBPPm respectively show -15.1% and -16.4% average relative errors in terms of base shear. Therefore, they respectively outperform the PUSHm and DBPPs, that yield -38.2% and -40.1% errors. These results are further explained by Figure 3.15, that reports the displacement profiles at Δ_{SDoF}^{TH} for the B2131332 and the 12 span-bridge. In the former case, the PUSHu and DBPPm better mimic the TH-based displacement profile, if compared to the first mode-based analysis techniques (PUSHm and DBPPs). Indeed, the PUSHu and DBPPm provide BIs of 1.10 and 0.96, outperforming the PUSHm and DBPPs respectively (BI equal to 0.67 and 0.71). For the 12-span bridge, the DBPPs and PUSHm fail in capturing the displacement profile ($BI < 0.67$), as reported for the 8-span case studies. Even if it considers a combination of vibration modes, the DBPPm is not able to approximate the NLTHA ($BI = 0.71$). A similar condition is registered for the 10-span case study. Possibly, this relates to the way the significant vibration modes are combined (i.e. SRSS), which may be inappropriate for bridges with 10 spans or more. Further investigations are required to confirm such hypothesis. On the other hand, a better accuracy is given by the PUSHu ($BI = 0.92$), which better mimics the NLTHA response. The CDR for these bridges are generally smaller than 20%, as reported in Figure 3.16 in Section 3.4.5. Although such errors are not excessively high, those mainly refer to the response of the critical pier (on which the CDR is entirely based). Since the accuracy related to the displacement and shear profiles is lower (as demonstrated above), NLTHA is suggested for bridges with 10 spans or more (in conjunction with a nonlinear static approach). Based on this sensitivity analysis, the DBPPs and DBPPm procedures are deemed appropriate for the considered bridges up to six spans (approximately $RS_e > 0.035$). For the considered 8-spans case studies

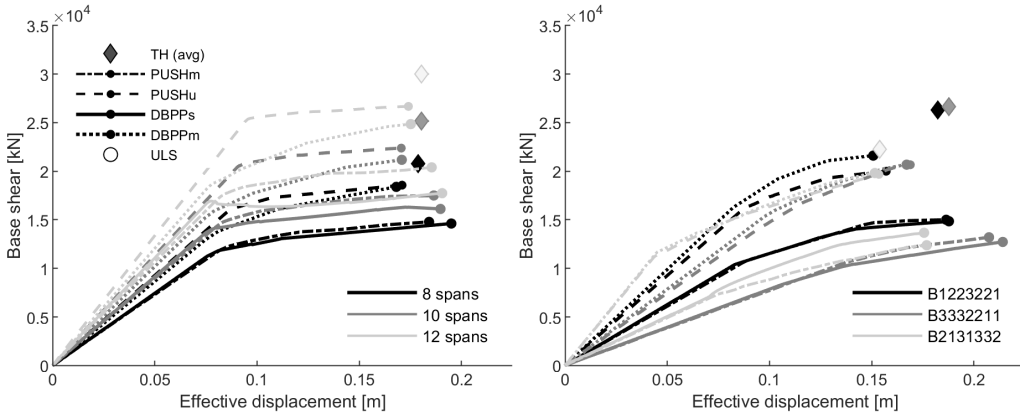


Figure 3.14: Bridge length sensitivity analysis (capacity curves): a) uniform pier height cases; b) irregular pier height cases.

(approximately $RS_e > 0.01$), the DBPPm may still be adopted while the DBPPs is inadequate. For bridges with 10 spans or more (approximately $RS_e < 0.01$), NLTHA is suggested. For practical applications, the applicability of the DBPPs and DBPPm may be based on both the number of spans and RS_e , whichever is most stringent. However, special attention should be given if RS_e is particularly close to the indicated threshold of 0.01.

3.4.5. Further sensitivity analyses

Two sensitivity analyses are conducted to investigate the effectiveness of the displacement-based approaches to: 1) the amount of pier reinforcement; 2) the pier typology. A first dataset of 15 case studies is defined changing the amount of pier longitudinal reinforcement of the J50 B222, B311, B12223, B22222 and B32123 bridges. For each geometrical configuration, the pier reinforcement is set equal to $\rho_l = 0.35\%$ (LR), $\rho_l = 0.47\%$ (MR) and $\rho_l = 0.70\%$ (HR). Only the highest intensity subset of ground motions (IM3) is considered. Figure 3.17.a shows the capacity curves of the B222 bridge, for which the above-mentioned errors (on both displacement and base shear) are in the same order of magnitude, regardless of the pier reinforcement. The relative errors (NSPs vs NLTHA) on the CDRs reported in Figure 3.16 confirm this outcome. It is evident that the discrepancy of the DBPPs and DBPPm with respect to the NLTHA is not sensitive to the

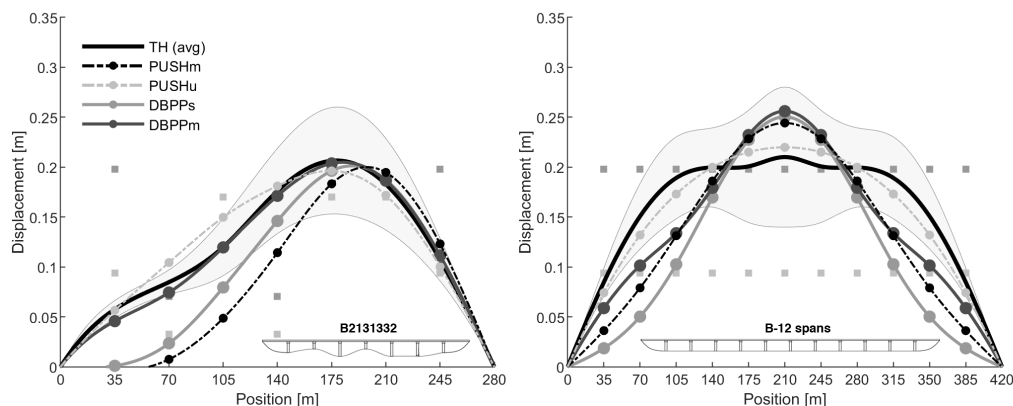


Figure 3.15: Bridge length sensitivity analysis (displacement profiles): a) B2131322 case study; b) 12-span case study. For each pier, a light- and dark-grey markers show their yielding and ultimate displacements.

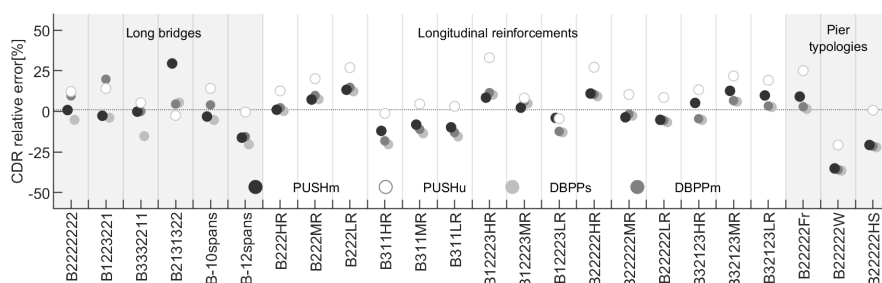


Figure 3.16: Relative errors on the CDRs for the case studies in the sensitivity analyses.

pier longitudinal reinforcement.

For the last sensitivity analysis, three additional case studies are considered, which have six spans and different pier typologies: two-column framed-piers; single-wall piers; and single-column piers with hollow-squared cross section (Figure 3.17b). The force-displacement capacity of such piers is derived analytically according to SLaMA (Gentile, del Vecchio, Pampanin, Raffaele & Uva 2019), and their overall behaviour is flexural. It is worth noting that, shear failures can be likewise considered in the displacement-based procedures by appropriately reducing the displacement capacity of the members and/or modifying their capacity curve accordingly. The PUSHm, DBPPs and DBPPm curves are particularly similar for these case studies, while the PUSHu consistently overestimates the base shear. The capacity curves reported in Figure 3.17b prove that

the pier typology does not affect the consistency between the NSPs (PUSHm, DBPPs and DBPPm) and the NLTHA, which is instead affected by the stiffness of the piers (and consequently a lower accuracy is expected for bridges with low RS). Consistently with the previously-considered parametric analyses, the relative error on the displacement at the performance point with respect to the NLTHA is higher for the case studies with lower RS_e . Considering the DBPPm as an example, the relative errors on the CDRs are equal to +3% for the framed-pier case ($RS_e = 0.07$), -21% for the case study with hollow-squared piers ($RS_e = 0.02$) and -35% for the wall-piers bridge ($RS_e = 0.012$). This error trend agrees with the previously-discussed applicability conditions of the DBPP approaches. Indeed, the higher error for wall-piers bridge is expectable, since its RS_e value is particularly close to the suggested threshold of 0.01.

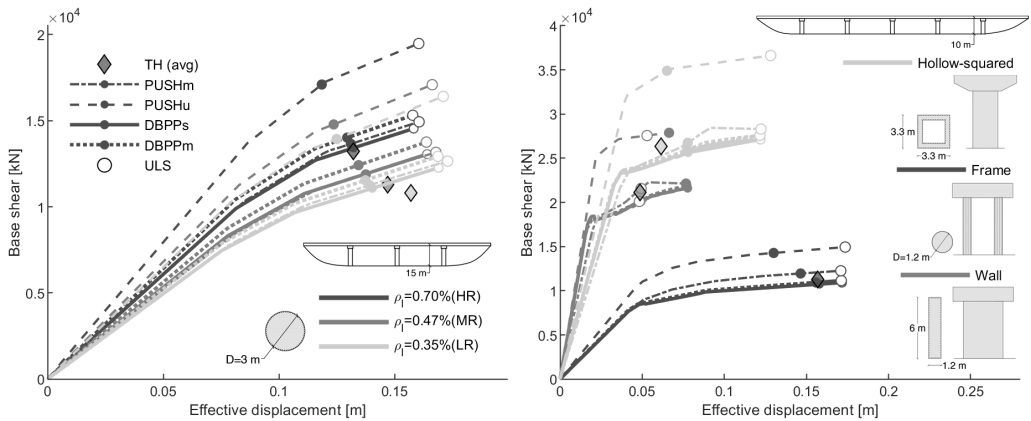


Figure 3.17: a) sensitivity analysis involving the pier longitudinal reinforcement; b) sensitivity analysis involving the pier typology.

3.5. Application to real continuous-deck bridges

To further test pros and cons of the DBPP(s) in the common practice, two real existing continuous deck RC-bridges having different regularity features were selected. The results of the DBPP(s) are again compared with conventional pushover analyses performed with uniform (PUSHu) and modal (PUSHm) invariant load profile and time-history analyses (NLTHA).

3.5.1. Description of the case-study bridges

Both the selected cases are continuous deck straight multi-span bridges, having single column piers and pinned connections between the deck and the substructure. The first case (indicated as Bridge 1) is one of the bridges analysed in the guidelines for existing bridges assessment and retrofit proposed by RELUIS consortium (ReLUIS 2009). It is a relatively short viaduct with 30m-long 6 spans. The deck is composed of two steel girders 1.60m-high and a 0.3m wide-RC slab. The single column piers exhibit a transverse 3m-diameter hollow circular cross section with two layers of $44\phi 26$ longitudinal bars and 200mm-spaced $\phi 12$ hoops. The height of the piers ranges between 8 and 19.50m as shown in Figure 3.18. The second case (indicated as Bridge 2) is a 10-spans viaduct located in Sala Consilina (SA). The external bays measure 38m, while the internal 35m. The deck is composed of 3 precast RC-girders 2m-high linked by a 0.3m wide slab. The piers present an octagonal hollow cross section with two layers of $44\phi 26$ longitudinal bars and 100 mm spaced $\phi 12$ hoops. The horizontal dimensions of the cross section are equal to 3.31m with a 0.5m wall-thickness. The height profile shows that the height of the piers varies between 6.75 and 10m.

3.5.2. Modelling strategy and analysis assumptions

Concerning the DBPP(s), the procedure is performed using the simplified beam analytical model implemented in a MATLAB routine described in Section 3.3.2. The force-displacement laws of the piers are calculated using moment-curvature analysis of the base-section of the piers, performed via the software KSU-RC (Esmaeily & Peterman 2007) which allows for analysing RC members with hollow cross-sections. No strength degradation is considered, and the Ultimate Limit State is identified in the post-processing phase when the first pier reaches its ultimate displacement capacity. Numerical pushover and NLTHA are performed using CSiBridge software (Computer and Structures INC (CSI) 2017). A similar modelling approach to the one proposed in Section 3.3.2 is adopted. The deck and the pier caps are considered via elastic frame with uncracked stiffness, whereas effective stiffness at yielding is assigned to piers modelled as mono-dimensional frames with a fixed base. A lumped-plasticity strategy is used, plastic

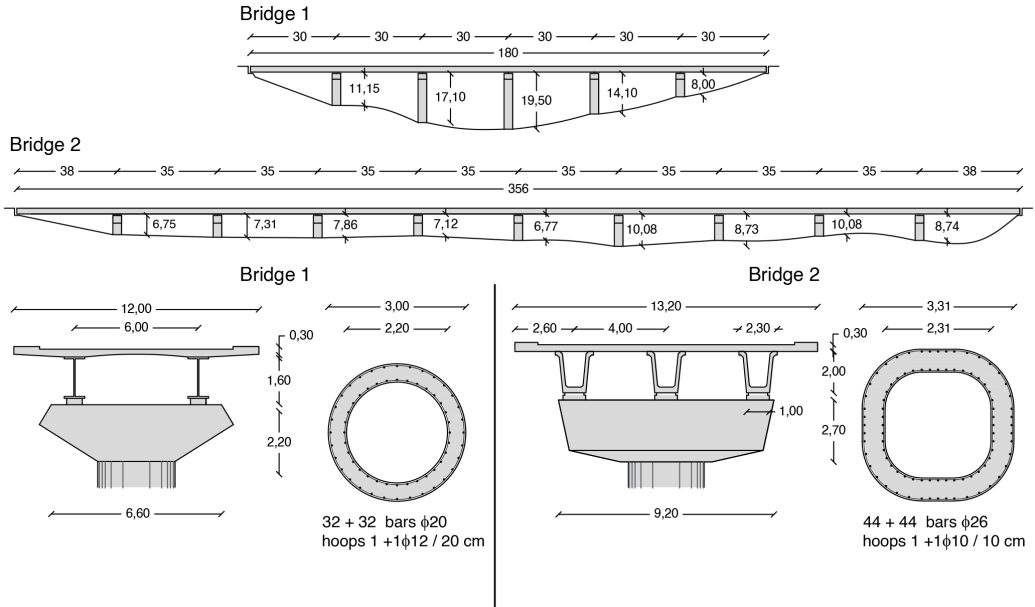


Figure 3.18: Geometrical and constructive features of the existing case studies

hinges are concentrated at the base of the piers equipped with moment-rotation laws and a Takeda hysteresis law (Saiidi & Sozen 1979) for cyclic response. A 3m-refined mass discretization is used for the deck and piers. To be consistent with the assumptions of the simplified model, bearings and abutments are modelled with two-joints links that fix the displacement in the transverse directions, allowing for free relative rotations. A mass-proportional and a first-mode load profile are used for numerical pushover analyses. Even in this case, the assessment is carried out using the CSM strategy in Section 3.3.2 and step-by-step equivalent SDoF systems are characterized, to be consistent with the DBPP. Two different 5%-damped demand spectra are calculated, corresponding to the specific hazard conditions of the selected bridges for a return period of 475 years. Peak Ground Acceleration (PGA) values are 0.34 and 0.43 g for the short and long bridge respectively. NLTHA are carried out with 10 natural scaled ground motions selected from the SIMBAD (Smerzini et al. 2014) database using REXEL (Iervolino et al. 2010). The accelerograms are selected according to the soil-type of the site and scaled in amplitude to satisfy spectrum-compatibility criteria with 10%-lower and 20%-upper bounds in the period range between 0.2-2.0s (Figure 3.19).

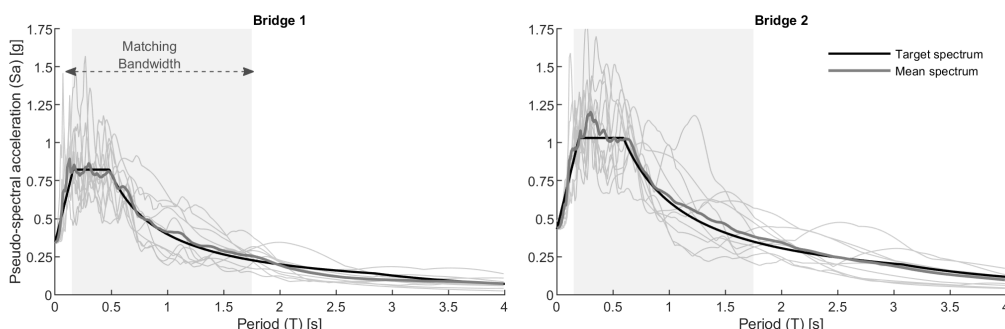


Figure 3.19: Code and mean 5%-damped spectra in terms of spectral acceleration (a) and displacement (b)

3.5.3. Eigenvalue analysis

Eigenvalue analyses (Figure 3.20) are performed to identify the modal properties of the selected cases and to better interpret the results. According to the literature (Priestley et al. 1996, Isakovic 2006), the regularity in the seismic response of a bridge is linked to the influence of higher modes in the undamaged state and it increases proportionally to the ratio between the transverse stiffness of the deck and the total lateral stiffness of the piers. According to this statement, the 6-span bridge exhibits regular behaviour since its dynamic response is governed by the first mode in the transverse direction. About the long bridge, the high lateral stiffness of the short piers concerning the long flexible superstructure induces a strongly irregular dynamic behaviour. The shape of the first transversal mode is determined by the lower stiffness of the piers in the right part with respect to the left shorter columns. Differently, the second mode involves higher displacement in the left part of the bridge. It is expected that both the modes strongly influence the seismic behaviour since the participating mass values are 42% and 34% respectively.

3.5.4. Discussion of the results in transverse direction

The seismic response of the selected bridges is analysed via both the version of DBPP. It is worth noting that the DBPPs considers only the first mode behaviour, while the DBPPm accounts for higher modes when the participating mass of the first mode in the transverse direction is lower than 70%. Consequently, analysing bridge 2, the EMS is

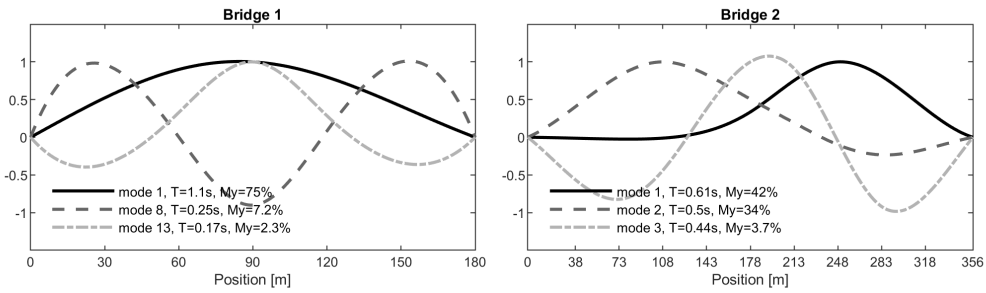


Figure 3.20: Results of modal analysis (a) bridge 1 (b) bridge 2

activated. The results are presented in terms of capacity curves and performance points related to equivalent SDOF systems. With reference to the NLTHA, the equivalent SDOF transformation is executed step-by-step for each ground motion, the maximum effective displacement is calculated, and the corresponding base shear is derived. The average values of effective displacement/base shear of the 10 ground motions are reported as the NLTHA performance point. Moreover, the envelope of the maximum demands in terms of displacement and shear is calculated for each member and the average results of the 10 ground motions are extracted. For bridge 1 (Figure 3.21), the differences between the DBPP and the PUSHm curves are negligible, while the PUSHu predicts higher base shear values. This is due to the higher value of loads applied to the stiffer external part of the bridge, almost entirely transferred to the abutments. Since the predicted response is stiffer, the displacement demands in the piers are underestimated using the uniform load pattern. On the contrary, performance points and performance displacements of the DBPPm, DBPPs and PUSHm are consistent with the average response of the NLTHA. The relative error about performance effective displacement predicted with respect to NLTHA is -4.8%, -4.1% and -3.9% for PUSHm, DBPPm and DBPPs respectively. Generally, the results confirm the above-mentioned accuracy (Section 3.4.3) of a first mode-based nonlinear static method dealing with regular bridges. The results for bridge 2 (3.22) emphasize the inadequacy of using nonlinear static procedures for long irregular bridges. Even though the capacity curves predicted by PUSHm and DBPPs are consistent, these fail in predicting the global base shear, underestimating it with a relative error of 26.8% and 29.0% compared to the NLTHA. The displacement demand

is strongly underestimated in the stiffer part of the bridge. This is because these approaches consider only the first mode influence on the seismic response. Referring to the displacement demand, the PUSHm and DBPPs vs NLTHA average relative error (accounting for all the members) are 49.8% and 39.4%. Higher modes contribution is considered by the DBPPm through the EMS that accounts for the three modes reported in Figure (3.20). Since the modal periods are similar, the complete quadratic combination is used. The DBPPm outperforms the previously discussed modal procedures better predicting the displacement demand of the left side of the bridge, including the second mode contribution. In this case, the average DBPPm-vs-NLTHA relative error is 4.9%. Furthermore, the shear demand is accurately predicted, even if a strong overestimation of the shear absorbed by the right abutment is recognised. It is worth noting that the deformed profile predicted of the DBPPm is not a “real” deformed configuration, but it is calculated through the statistical combination of the contribution of the significant modes. Since the NLTHA-based performance point is related to a specific time step, there is an inconsistency comparing these performance points. Thus, a dummy performance point is associated with the envelope of the NLTHA displacement-shear values. There is good agreement between the DBPPm-based performance point and the latter proving that in this case the former provides accurate predictions. Finally, the PUSHu fails in catching the demand on the left side of the bridge, while yields good results in the most deformable part: the relative error between PUSHu and TH measures an average of 7.9% and 4.9% on the critical pier. This indicates the PUSHu a better solution than PUSHm when dealing with long bridges.

3.5.5. Analysis in longitudinal direction

In this final section, the DBPP procedure is adopted to perform the seismic analysis in the longitudinal direction. This task is deemed to be easier than the transverse direction since, referring to continuous deck multi-span bridges, the deck can be considered axially rigid. Thus, the simplified model is composed of one or more structural member acting in parallel in absorbing inertia forces. Even in this case, the structural members can be modelled with their force-displacement relationship. These latter are different from the force-displacement laws used in the transverse direction since the effective

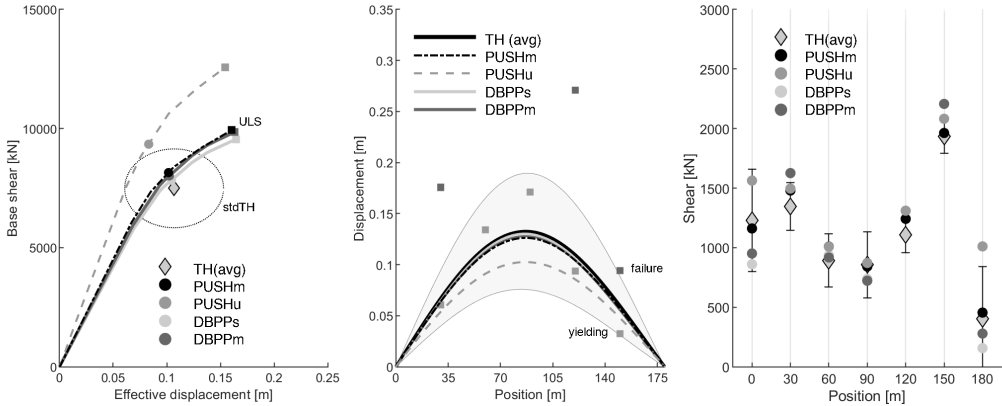


Figure 3.21: Bridge 1 results in terms of capacity curves and performance points, displacement and shear demand for each substructure member

height of the piers changes considering the variation of to the contra-flexure point whose position depends on the degree of fixity at column top. If all the nodes of the deck are constrained to the same longitudinal displacement, the deformed shape is known in advance. Thus, no iterations are needed, and any choice of the control node is equivalent. Given a pre-determined target displacement of a generic node of the deck (the same for all the nodes), the shear stresses in each structural member can be achieved by interpolating the corresponding force-displacement laws and summed up to calculate the global base shear. The equivalent SDoF transformation can be performed and a point is defined on the pseudo-pushover curve. The final capacity curve is the combination of the force-displacement relationships of the shear-bearing members. It is worth specifying that the influence of other factors like abutment-backfill interactions or joint closures are relevant and, generally, should be accounted for. In this case, only the contribution of piers is considered for simplicity in testing the procedure. Both the case studies were analysed under the longitudinal direction assuming fixed bearings or shock transmitters on the piers and free abutments. Capacity curves are presented in Figure 3.23 for DBPP and PUSHm. The comparison proves good accuracy with some differences detected against the NLTHA possibly related to damping contributions.

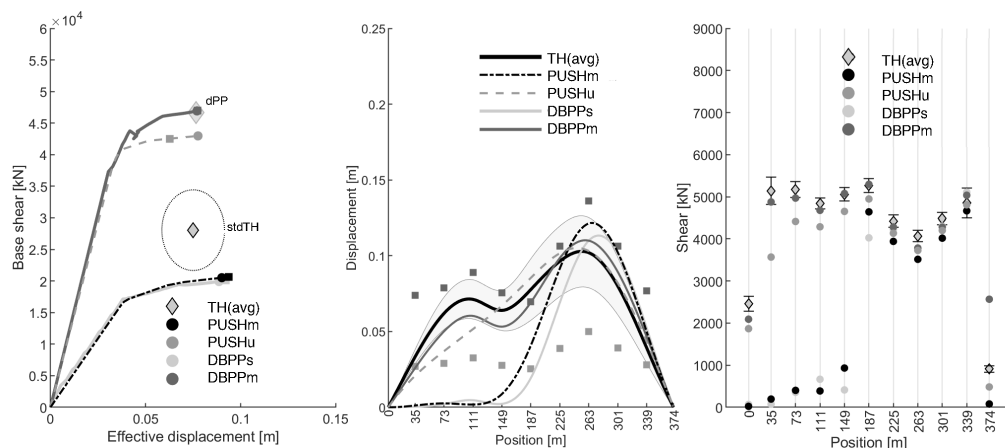


Figure 3.22: Bridge 2 results in terms of capacity curves and performance points, displacement and shear demand for each substructure member

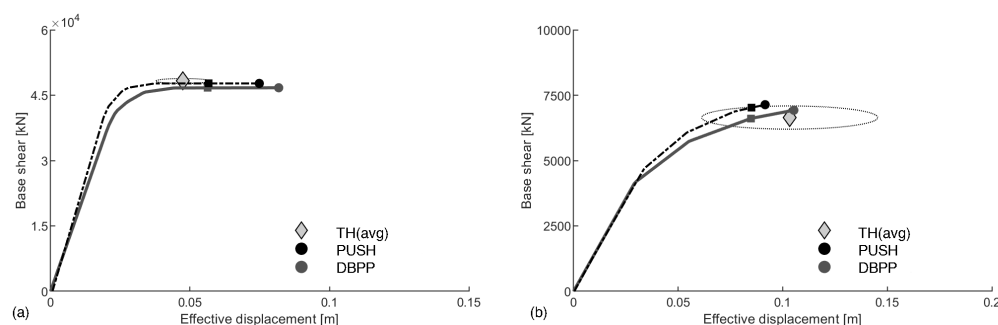


Figure 3.23: Capacity curves along the longitudinal direction and performance points: (a) bridge 1, (b) bridge 2.

3.6. Conclusions

This Chapter deals with the seismic performance assessment of continuous-deck RC bridges using DBA procedures. After describing the modal analysis-based DBA procedure, a static-based alternative is proposed in this study, which is deemed to further increase the simplicity of the DBA approach. Moreover, it is proposed an extension of the DBA procedures, both modal and static, which allows deriving the displacement-based pseudo-pushover curve of the bridge. The basic idea is to repeat the modal or static DBA procedure for increasing displacements, deriving thorough information on the behaviour of the analysed bridge with a particularly small increase in computational

cost. The CSM is finally adopted to assess the bridge performance.

The displacement-based pseudo pushover, both modal (DBPPm) and static (DBPPs), are herein adopted for the transverse analysis of a set of 36 reinforced concrete continuous-deck bridges with two, four or six, 35m-long spans, two values of the deck moment of inertia (transverse direction) and different combinations of 8m-, 15m- and 20m-high single-column piers. The resulting performance assessments are compared with those calculated by means of pushover (with force profile proportional to the first vibration mode, PUSHm, or uniform, PUSHu) and time-history analyses using three suites of 10 scaled, natural ground motions respectively consistent with low-, medium- and high-seismicity sites. Three additional datasets of (24) bridges are adopted to investigate the accuracy of the DBPPs and DBPPm for 1) increasing length of the bridge; 2) amount of pier longitudinal reinforcement; 3) different pier typologies. The results can be summarised as follows:

- For the analysed bridge configurations up to six spans, the DBPPs and DBPPm approaches allow estimating the bridge capacity curve with a level of accuracy particularly similar to the PUSHm. On the other hand, the PUSHu provides a systematic and considerable over-estimation of the base shear;
- Both the DBPPs and DBPPm (coupled with the CSM) provide fairly-accurate seismic performance assessments, measured in terms of capacity-demand ratio (CDR), with the modal approach being slightly better. For the vast majority of the cases up to six spans, the performance points fall within one standard deviation from the average of the time history analyses, both in terms of displacement and base shear of the equivalent SDoF system. The DBPPm allows for better accuracy: the improvement is substantial for two-span bridges and only slight for the four- and six-span ones. The error trends are not sensitive to the moment of inertia of the deck and to the amount of pier longitudinal reinforcement;
- The applicability of the DBPPs and DBPPm may be based on both the number of spans and the relative stiffness index in the elastic range (RS_e), whichever is most stringent. The DBPPs and DBPPm procedures are deemed appropriate for

the considered bridges up to six spans (approximately $RS_e > 0.035$). For the considered 8-spans case studies (approximately $RS_e > 0.01$), the DBPPm may still be adopted while the DBPPs is inadequate. For bridges with 10 spans or more (approximately $RS_e < 0.01$), NLTHA is suggested. However, special attention should be given if the RS_e is particularly close to the indicated threshold of 0.01;

- Additional pier typologies are considered: two-column framed-piers; single-wall piers; and single-column piers with hollow-squared cross-section. The pier typology does not affect the consistency between the NSPs (PUSHm, DBPPs and DBPPm) and the NLTHA;
- Two additional case-study bridges are analysed to confirm the accuracy and the shortcoming observed within the parametric analysis.

Chapter 4

Displacement-based seismic performance assessment for multi-span steel truss bridges

Abstract

The seismic vulnerability of bridge portfolios is of increasing concern for transportation system authorities which need extensive surveys and assessment aimed at risk-based prioritisation. Various research efforts in the last decades were oriented to the development of simplified seismic performance assessment approaches for bridges to be applied for evaluating a large number of structures in short time requiring low computational cost and time. The study presented in this Chapter is aimed at discussing the effectiveness of nonlinear static analysis and analytical displacement-based assessment (DBA) approaches, together with the capacity spectrum method (CSM) for performance displacement assessment, for historical steel truss railway bridges with supporting steel tower. These bridges, although built in the first part of the last century, are currently in-service along the European railway networks and their seismic performance was poorly discussed in the literature. The first part of this study focuses on the seismic performance assessment of steel towers, investigating an effective equivalent viscous damping formulation to be used within the CSM of these structural components. The second part focuses on testing DBA and CSM approaches for steel truss bridges. Six case studies are generated having different substructure regularity and two to four spans. These are analysed via nonlinear static procedures and two direct DBA algorithms. Nonlinear time history analysis is used for benchmarking the accuracy of the simplified approaches.

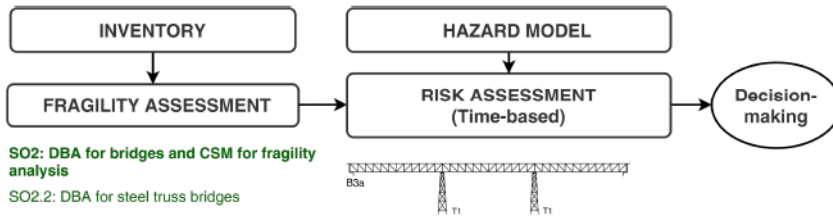


Figure 4.1: Objective of this Chapter (SO2.2) and framing in the flowchart for seismic risk calculation.

4.1. Introduction and motivations

The seismic vulnerability of bridge portfolios is of increasing concern for transportation system authorities. The main issues in this field are related to 1) an expected inadequacy in the seismic response of these critical structures, mostly designed in the past without anti-seismic requirements, and 2) to the high amount of existing structures to be inspected and assessed. In this context, refined modelling and highly accurate analysis methodologies, such as nonlinear time-history analysis (NLTHA), are hardly applicable for their large demand of time and computational effort involved. Various research efforts were oriented to the development and testing of faster simplified seismic analysis approaches which can be applied for evaluating bridge portfolios.

Nonlinear static procedures represent a simplified alternative approach with respect to NLTHA. These are based on the response of the analysed structures under an incremental load pattern in order to achieve a pushover curve relating the total base shear with the displacement of a control node. The pushover curve is converted in an equivalent single-degree-of-freedom (SDoF) capacity spectrum which can be compared to the seismic demand represented by response spectra. Various capacity spectrum-based methodologies can be applied to identify the performance of the equivalent SDoF system. Among these, it is worth mentioning the Capacity Spectrum Method (CSM) (Freeman 1998b) (which is described in section 3.2.4) and the N2 method (Fajfar 1999) which are currently included in guidelines and codes such as the ATC-40 (ATC 1996) and the EC8 part 3 (CEN 2005).

The applicability of several nonlinear static approaches for bridges was widely investigated in the last decades (Isakovic 2006, Isaković et al. 2008, Pinho et al. 2007, 2009, Paraskeva et al. 2006, Paraskeva & Kappos 2010, Perdomo et al. 2017, Kohrangi et al.

2015a). Conventional pushover analysis with an invariant first mode-based load pattern can be successfully applied for regular bridges, according to the outcomes of Chapter 3. For irregular bridges, whose seismic response is typically affected by higher modes or by high variability of modal shapes involved by damaging and inelasticity in the members, some modifications of the conventional algorithm for pushover analysis are proposed in the previously mentioned studies (e.g. multi-modal or adaptive force- or displacement-based load patterns).

Based on early studies about direct displacement-based design and assessment by Priestley et al. (2007), various research efforts focused on proposing displacement-based assessment (DBA) approaches for predicting the displacement profile of bridges under a given seismic action, if coupled with the CSM, or in a given damage state (DS) condition (Şadan et al. 2013, Cardone 2014, Cademartori et al. 2020). In Chapter 3, an alternative static analysis-based algorithm for performing the DBA of continuous girder bridges analysed in the transverse direction is provided and discussed through comparisons with the modal analysis-based algorithm proposed by Şadan et al. (2013) and conventional pushover performed with first mode-based a uniform load patterns. Simplified DBA approaches represent a convenient analysis methodology for the purposes of network-scale analysis of bridge portfolios. As done in Chapter 3 and by Perdomo & Monteiro (2020), these can be applied by resorting to simplified elastic beam modelling and by developing simple programming routines.

However, it is worth noting that all the aforementioned studies focus on the response of RC-girder bridges which is arguably the most spread typology of roadway bridges in the European context. To the author's best knowledge, there are no literature studies which concern testing of these simplified methodologies for steel truss bridges which is a common typology of railway bridges in Europe. These are mainly historical bridges, built during the construction of the transportation network in Europe between the second half of the 19th century and the first decades of the 20th Pipinato (2018). A high number of these old bridges is currently in-service and should be subjected to structural assessment with respect to the current code prescriptions (e.g. traffic and natural hazards) and, if necessary, retrofitted. Most of these bridges are characterised by a considerable historical value which deserves to be preserved.

The guidelines *Seismic retrofitting guidelines for complex steel truss highway bridges* MCEER (2006) provides recommendations for seismic analysis and retrofitting of this bridge typology, referring to the US context. According to the classification reported in this document, this typology includes bridges whose superstructure and (optionally) substructure components are truss structural systems composed of axially-loaded straight steel members connected together forming triangular patterns. The superstructure is commonly composed of two truss girders connected by bracing systems and floor beams supporting stringers and the railroad plane. The truss girders are composed of two longitudinal (upper and lower) chords connected by diagonal and vertical frames (forming triangles). The two truss beams are connected by (secondary) bracing systems in the horizontal planes, resisting seismic and wind loads, and in the vertical ones (in the cross-section of the superstructure) preventing in-plane sway distortions of the truss cross-section.

Multi-span truss bridges are characterised by simply-supported adjacent trusses (i.e. isostatic superstructure) or a continuous (hyperstatic) truss girder superstructure. The truss superstructure is connected via one (for continuous superstructure) or two (for isostatic structural scheme) lines of bearing devices on steel-braced towers or unreinforced masonry/RC wall piers. Steel towers are composed of four steel legs connected by a bracing system consisting of diagonal and horizontal steel elements.

Literature studies on this bridge typology are few and mainly deal with the fatigue response of truss spans characterised by riveted connections. Pipinato et al. (2009, 2011), Silva et al. (2021), Buitrago et al. (2021) described experimental campaigns performed on dismantled steel truss spans, particularly analysing the fatigue response of the systems and, particularly, of the riveted connections under cyclic loading. The study by Pipinato (2018, 2019) discussed strengthening solutions for improving the traffic bearing capacity and extending service life of existing steel truss bridges. To the author's best knowledge, Yilmaz & Çalayan (2018) is the only recent study which investigates the seismic fragility of a multi-span steel truss railway bridges. It analyses a case-study bridge in Turkey, performing fragility analysis via NLTHA discussing the efficiency of different intensity measures. Pollino & Bruneau (2008, 2007) investigates experimentally the performance of steel truss pier retrofitted by using a controlled

rocking approach.

This study focuses on the seismic performance assessment of multi-span steel truss bridges with steel braced towers. An existing case study, an historical bridge of the Valencian (Spain) railway network, is identified as an archetype structure and it is used to perform a typology-based study via a parametric case-study bridge generation.

The first part of this Chapter examines the seismic performance assessment of steel braced towers. It investigates the use of the CSM for carrying out the performance assessment of bridge truss piers.

The second part of this Chapter focuses on testing simple pushover and DBA approaches for continuous-truss bridges. Some case studies are generated having different sub-structure layout and different number of spans. These are analysed with two numerical pushover procedures with a modal (first-mode) and a uniform load pattern and two DBA approaches based on static and modal analysis. NLTHA is used as a benchmark.

4.2. Description of the archetype bridge

A historical steel truss bridge is selected as an archetype structure to introduce the typological study. This is a multi-span truss deck bridge, built between 1913 and 1915, which currently is still in-service within the Spanish railway network.

The superstructure is a continuous truss having 42m-long spans and consisting of two lateral Pratt-type truss girders measuring a height equal to 4m from the top of the bearings to the top of the upper chords. The upper and lower chords exhibit a T-shape built-up cross-section as shown in Figure 4.3. The cross-section of diagonals and verticals is cross-shaped, composed of four angles (i.e. L-shaped cross-section steel frames). Two steel braced towers constitute the substructure system. The first is 18.60m-high and the X-bracing system is arranged in five panels, while the second has a height equal to 11.88m and three panels (Figure 4.3). The diagonals exhibit a T-shaped cross-section composed of coupled angles, while the horizontal braces are battened members, composed of two pairs of coupled-angles with steel plates as battens. At the top of the steel towers, 0.75m-high beams are placed to absorb the gravity loads from the bearings. The legs are battened members: two built-up C-shaped parallel chords are connected by steel plates, one per 0.85m, creating an open-box cross-section. Rivets



Figure 4.2: On-site photographs of riveted steel braced towers

are used to connect the different steel elements in each built-up member and for the connections between the members (e.g. the bracing systems to the gusset plates and legs). At the bottom of the steel towers, steel anchor bolts attach the legs to the masonry foundations. Figure 4.2 reports two photos of the steel braced towers collected on-site. The bearing devices were recently replaced during a recent retrofit intervention. Pot bearings (i.e. confined elastomeric bearings) are placed on the top of the steel towers and the masonry abutments, preventing relative displacement between the deck and the substructure members in the transverse direction. Shock transmitters are also present to ensure the transmission of seismic forces from the deck to the piers. Further information about the analysed case-study are reported in Bertolesi et al. (2021), Buitrago et al. (2021).

4.3. Seismic performance assessment of steel braced towers

In this section, the seismic response of steel braced supporting towers is discussed. The steel towers of the archetype bridge described in the previous section are analysed.

Capacity curves in terms of equivalent SDoF displacement and base shear are calculated by using numerical pushover analysis and a by-hand analytical approach recommended as a simplified seismic analysis methodology in international guidelines.

The effectiveness of the CSM for seismic performance assessment is discussed. Several state-of-the-art approaches for calculating equivalent viscous damping coefficients, which lead to the calculation of overdamped spectra, are compared to NLTHA to identify the most accurate strategy suitable for calculating the seismic demand of steel towers.

4.3.1. Description of the modelling strategy

In this sub-section, the adopted modelling strategy for the steel towers is described. The numerical models of the steel towers are created using the SAP2000 software package (Computer and Structures INC (CSI) 2018). The legs and the top beams are represented by linear frame elements. Fixed restraints are placed at the base of the legs neglecting soil-foundations interactions. The diagonal and horizontal braces are modelled via *two-node nonlinear link* elements.

The tributary seismic mass of the truss deck (i.e. the gravity loads plus a portion of the train loads) is lumped in a node placed on the top of the tower, at the height of the centroid of the truss deck. It is connected to the top nodes of the towers by rigid links. The masses of the members are lumped in their end nodes (i.e. no mass discretisation along the members).

Considering the top beams and the legs, a lumped-plasticity strategy is adopted and plastic hinges are placed at the ends of these members. Plastic hinges equipped with axial load-flexure interaction strength domains are used for the legs, while simple flexural plastic hinges are assigned to the top beams. Also, shear hinges are placed in the middle length of the frames modelling the legs.

Considering the recommendations by Eurocode 3 (EC3)-part 1 (CEN 2009) and by MCEER (2006) and the width-to-thickness ratios of the different plates and angles, the cross-sections of the built-up members can be classified as "compact" (Class 1 of the EC3). This allows for excluding local buckling phenomena which can induce strength reduction during the plastic response until the reaching of the ultimate rotational capacity.

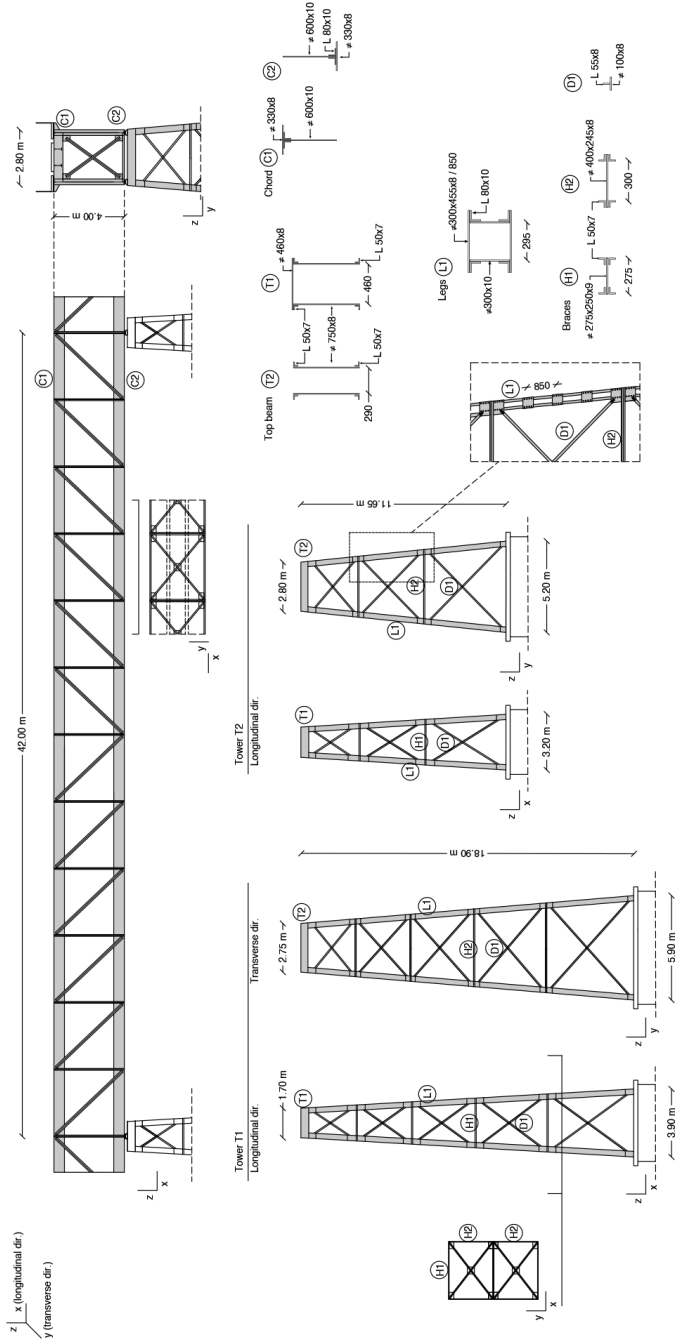


Figure 4.3: Geometric and constructive features of the archetype bridge.

A simplified approach is applied for calculating the axial load-flexure interaction domains for battened members (i.e. the legs) accounting for lateral buckling. The compression strength N_c of the battened members is calculated considering the global buckling and the local buckling of the profiles between the battens. For the former, a value of effective slenderness accounting for the shear flexibility, which is relevant for battened members, is used. The tensile strength N_t is calculated using the net section area (i.e. the gross cross-section area excluding the rivet holes) of the longitudinal profiles only.

Subsequently, the axial load domain is discretised in several intervals $[N_i; N_{i+1}]$ between the maximum (tension, N_t) and minimum (compression, N_c) strength capacity. Varying N_i , the corresponding flexural strength is calculated according to the AISC (2010). For each compressive N_i , the minimum between the moment causing buckling of the single longitudinal C-shaped profile and the plastic moment of the cross-section is used as ultimate strength. This calculation is performed in both the flexure directions of the cross-sections.

The document by MCEER (2006) suggests adopting appropriate limitations for the ultimate ductility capacity of built-up steel members if no experimental tests or refined finite-element modelling plastic analysis are performed. In this study, a maximum rotational ductility equal to 2 is used (i.e. severe damage in MCEER (2006)). This value is linearly reduced, from 2 to 0, for axial load ratio included in $[0.5A_s f_y, A_s f_y]$ where A_s is the gross area of the cross-section, f_y is the steel yielding strength (Lee & Bruneau 2008a,b).

Shear hinges are also modelled considering the minimum between the ultimate plastic shear strength of the whole member and the shear inducing axial buckling or yielding in the battens. For both battens and longitudinal profiles, shear buckling failures are excluded according to the criteria reported in Eurocode 3 (CEN 2009).

It is worth noting that experimental tests on the cyclic response of battened members are reported in literature (Sarkar & Sahoo 2016, Della Corte & Landolfo 2017). However, a general lack of specific capacity models to be used for numerical analyses is evidenced considering the current regulatory codes. In this study, the cyclic response of the legs is neglected (further clarifications are reported in 4.3.3).

A pinned connection between the legs and the bracing members is considered in the

numerical model. An axial load-induced nonlinear response is associated with the diagonal and horizontal bracing members. The compression strength is calculated as the critical buckling load, which is largely lower than the plastic compressive stress, given the high slenderness ratio of the members. The tensile strength is calculated considering the net section. The cyclic response of the bracing members is modelled according to the study by Georgiev et al. (2017) which compare the hysteretic response of steel braces achieved by numerical analyses performed in SAP2000 to experimental tests. The *pivot* hysteresis rule ($\alpha_1 = 100$, $\alpha_2 = 0.1$, $\beta_1 = 0.02$, $\beta_2 = 0.4$, $\eta = 0$) is selected for the *two-nodes-link* modelling the braces.

It is worth mentioning that a more accurate modelling strategy can be adopted as in literature studies related to the cyclic response of concentrically braced systems (Hsiao et al. 2012, Hammad & Moustafa 2020). As an example, a refined modelling approach can be appropriately utilises a fibre-based modelling of the braces with initial out-of-plane geometric imperfections for a refined calculation of the cyclic response of the braces considering buckling. In this case, the nonlinear contribution of the gusset plate, placing rigid end zones in the overlapping parts between the legs and the gusset plate, should be also considered. Such a refined modelling strategy should be adopted within experimental test campaigns, but can considerably burden the assessment process if complex structures, such as truss bridges, are subjected to computational-consuming analysis, such as NLTHA.

It is worth mentioning that a strength-based verification of the critical components, such as the riveted connections between the members or the anchorage devices connecting the legs to the foundation, should be performed to prove the validity of the modelling strategy adopted. This can be performed following the recommendations of MCEER (2006) post-processing the seismic analysis results.

4.3.2. Seismic analysis procedures

The numerical models of the steel towers are subjected to pushover analyses and NLTHA. The pushover analyses are performed using an invariant load pattern tracking the shape of the first vibration mode. A control node on the top of the tower is selected. The NLTHA is performed adopting scaled natural ground-motion records described in the

following subsection. For NLTHA, a tangent-stiffness damping strategy is selected and an elastic damping equal to 3% is assigned to all the vibration modes.

In addition to the numerical pushover analysis, a simplified analytical procedure is also used in this study to validate the pushover results and provide to the users a simple method based on by-hand calculations for achieving capacity curves of steel braced towers. This method does not resort to a nonlinear numerical model and can be applied with fast programming routines. The procedure mimics the steps of the pseudo-pushover analysis proposed in the NZSEE (2017) for the seismic assessment of existing buildings.

This simplified analysis approach is described in the flowchart shown in Figure 4.4. The method is based on a series of linear static analyses performed on an elastic model which is updated during the process. The adopted two-dimensional model represents the front of the tower. The three-dimensional effect is neglected. The model is composed of the legs (fully fixed to the foundations), the top beam, the horizontal and tensile diagonal braces (selected considering the pushing direction), which respond to axial load only (i.e. working as truss or cable members). The compression braces are neglected in the model, due to their low buckling load and expected scarce influence on the total base shear. In this simplified model, all the tributary seismic mass of the system is placed on the top of the tower and it is equal to the tributary mass of the superstructure calculated considering the superimposed gravity loads and, where appropriate, a portion of the total railroad traffic load.

The bracing members are characterised by a bilinear axial stress-displacement backbone, whereas the legs are characterised by bilinear moment-rotation backbones where the yielding moment (i.e. plastic moment) varies depending on the axial load according to the corresponding interaction domain. Only elastic perfectly plastic or positive-hardening backbones can be used in this simplified procedure, neglecting softening effects. In this study, the top beam is considered elastic, given its high flexural strength and its nonlinear response is expected to occur after the reaching of the ultimate tower capacity.

Firstly, the elastic stiffness is assigned to the different members of the model. A static analysis is performed with a force of arbitrary intensity placed at the top simulating the

seismic action. To consider the effect of the eccentricity of the seismic mass of the deck with respect to the top of the tower (if relevant), the force can be coupled with a moment equal to the force multiplied by the distance between the top of the tower and the deck cross-section centroid.

At this stage, the axial/flexural stress of each member can be registered and compared to the corresponding capacity computing a strength-based Capacity Demand Ratio (CDR). In this case, the CDR considers an axial response of the braces (assuming a pinned connection to the gusset plates), and the axial-flexural interaction of the legs. Note that the influence of the gravity loads should be considered by assigning a quarter of the total gravity load to each leg (i.e. half of the total to each two-dimensional model and half of this latter to each leg). Also, the displacement profile of the tower (i.e. top tower displacement and horizontal displacement of all the horizontal braces) which corresponds to the top displacement of each panel $\Delta_{panel,k}$ is extracted.

The member characterised by the minimum of the calculated CDRs is assumed to reach the yielding before the others at the considered analysis step. The total base shear at this step $V_{b,k}$ and $\Delta_{panel,k}$ is calculated by multiplying the counterpart read by the static analysis for the minimum CDR.

If the ultimate capacity of the tower is reached, the analysis stops. In this study, the ultimate capacity condition corresponds to the occurrence of one of the following local conditions:

- reaching of the axial ductility capacity of the tensile bracing member;
- reaching of the flexural ductility capacity of the legs;
- axial buckling of the horizontal braces.

This latter is a fragile mechanism that can induce an important redistribution leading to a loss of global tower strength. Also (considering that the buckling load of the diagonal braces is very prematurely reached), the failure of the horizontal braces implies a large increase in the effective length of the legs reducing its critical buckling load.

If the ultimate capacity is not reached, another step is performed. In this latter case, the model is updated, assigning to the critical member its post-elastic stiffness and

a new static analysis is performed. The newly calculated stresses are added to the stresses calculated in the previous step, the following critical element is identified and, accordingly, another value of $V_{b,k}$ and $\Delta_{panel,k}$ is achieved.

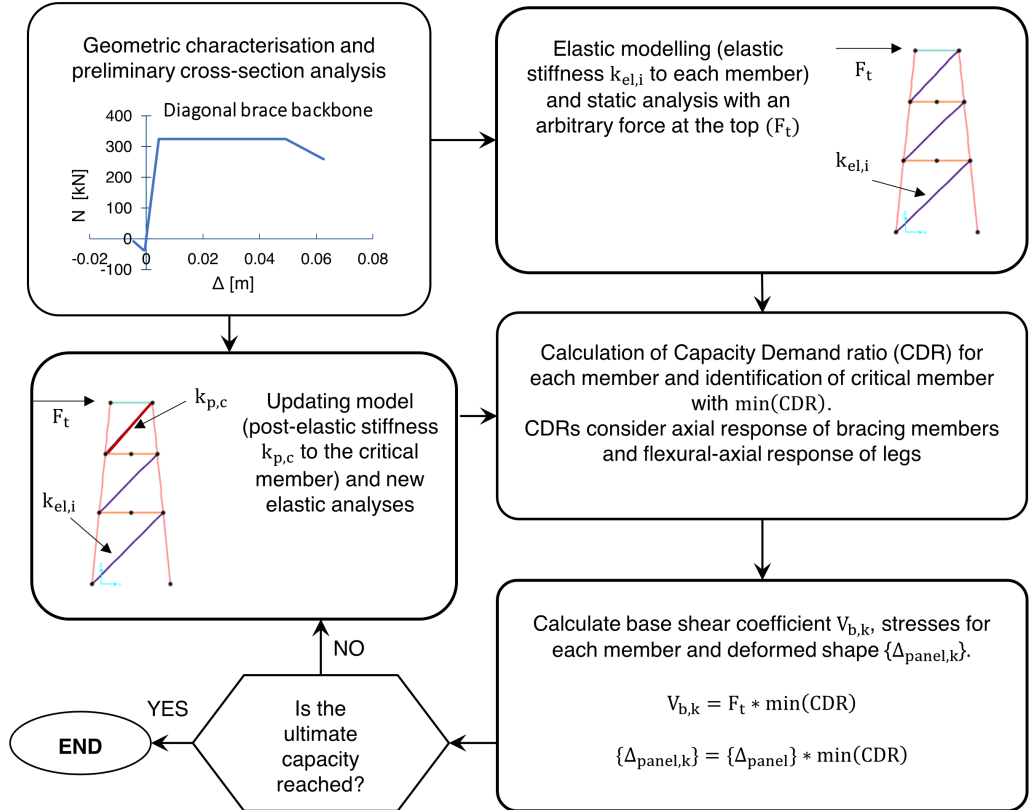


Figure 4.4: Flowchart of the analytical pseudo-pushover for steel towers.

4.3.3. Damage states and seismic response of steel towers under monotonic loading

The seismic response of the analysed towers under an incremental load pattern is discussed in this subsection. Three DS thresholds are identified on the obtained capacity curves following the recommendations of the guidelines by (MCEER 2006) based on

the local nonlinear response of the steel members. The DSs of the steel towers are supposed to determine the global performance level of the bridge. The DS1 corresponds to minimal post-earthquake damages which can slightly affect the bridge serviceability and the global seismic capacity. In this case, the structural repairing, if needed, can involve service limitations. The DS2 includes repairable damages on the steel members, but not affecting the gravity load safety of the tower, keeping an adequate residual capacity to seismic loading. The DS3 reflects a near-collapse condition, with fragile failure modes and severe damages on steel members. The repairing interventions can require large efforts in terms of time and cost. The following Table 4.1 defines the DS adopted in this study. The axial buckling of the compression diagonal braces is not considered to define the tower DS since it occurs in the very first steps of the analysis. Top beam damages are also excluded as stated in Section 4.3.1.

Table 4.1: Damage state descriptions for the steel towers

Damage State	Description
DS1	Yielding of the tensile diagonal braces (minimal damages, $\mu_d \geq 1$) Flexural yielding of the legs (minimal damages, $\mu_l \geq 1$)
DS2	Large plastic rotation of the legs (repairable damages, $\mu_l \geq 1.5$)
DS3	Ultimate flexural ductility on legs (severe damage, $\mu_l \geq 2$) Buckling of a longitudinal profile of the battened legs Shear failure of the legs Axial buckling of horizontal braces

Figure 4.5 shows the capacity curves for the steel towers (named T1 and T2) calculated via the previously described strategies. The consistency between numerical pushover and pseudo-pushover evidences the accuracy of the simplified approach for the analysed cases. This proves the validity of the assumptions of the simplified method (i.e. neglecting compression diagonal bracing members and the three-dimensional effect). The capacity curves related to the longitudinal direction (i.e. longitudinal axis of the bridge) show a ductile response: the yielding of the (at least one) tensile diagonal braces (which determines the DS1) anticipates the nonlinear response of the legs. The plas-

tic rotation at the top of the legs determines the reaching of DS2. No shear failure is detected. The DS3 corresponds also to the ultimate plastic rotation at the top of the legs.

Contrarily, a fragile response is observed in the transverse direction, where the axial buckling of the horizontal braces represents induce a near-collapse DS3, anticipating other ductile failure modes. This is because of the reduced effective length of the horizontal braces with respect to the longitudinal direction, which reduces the critical buckling load.

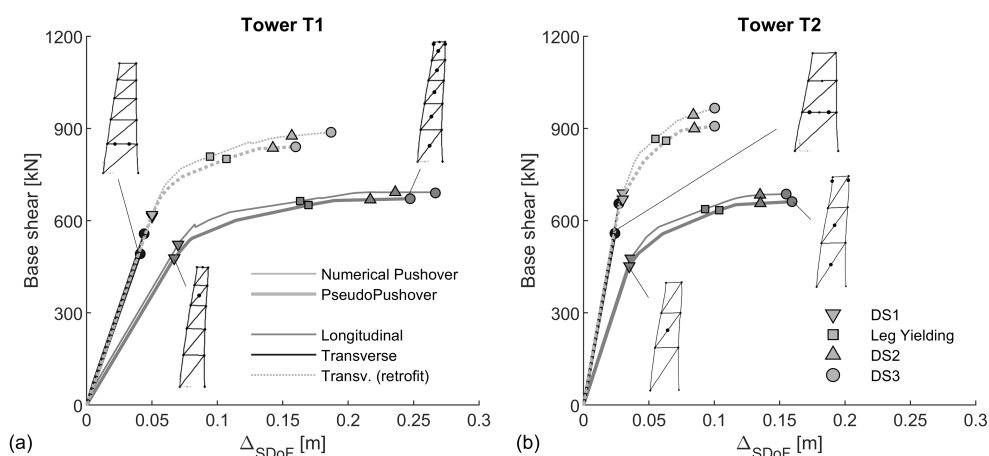


Figure 4.5: Pushover and pseudo-pushover curves of the analysed steel towers.

For studying the nonlinear response in the transverse direction, a retrofitted version of the steel towers is introduced. The cross-section area of the horizontal braces is increased until a ductile response of the tower is activated, simulating a retrofit intervention aimed at increasing the critical buckling load. The capacity curves in Figure 4.5 for the retrofitted cases shows that the hierarchy of strength is consistent with the one observed in the longitudinal direction. In the following sections, the retrofitted towers are indicated as T1r and T2r.

4.3.4. Seismic action

A suite of ten natural spectrum-compatible ground-motion records is selected. The normalised elastic response spectrum proposed by the EC8-part 1 (CEN 2004) Type 1 for site class C (i.e. shear wave velocity $V_{s,30} = 180 - 360m/s$) is adopted. This spectral shape is scaled to a PGA value of 0.4 g and it is used as a target spectrum for the record selection. The records are selected via the MATLAB-based tool REXEL (Iervolino et al. 2010) from the European Strong Motion Database (Ambraseys et al. 2004). This tool allows the analyst for an automatic selection of a suite of ground-motion records which are linearly scaled in amplitude to achieve compatibility with respect to the target spectrum within a given range of period.

In this case, the spectrum compatibility is ensured in the bandwidth [0.15 s, 1.5 s], selected to include the values of elastic (secant-to-yielding) first mode period of the analysed steel towers and (a tentative value of) the period elongation associated to the stiffness degradation during the seismic response. The maximum adopted scale factor is equal to 3.5 avoiding large scaling which can jeopardise the reliability of the record selection.

Finally, the dataset of spectrum-compatible records and target spectrum is again scaled for PGA values corresponding to 0.3 g and 0.2 g obtaining three suites of ground motions having different seismic intensity.

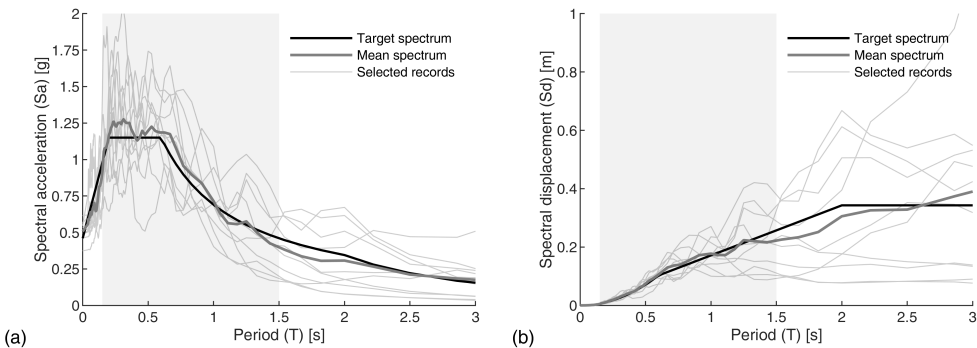


Figure 4.6: Target and mean 5%-damped spectra in terms of spectral acceleration (a) and displacement (b)

4.3.5. Equivalent viscous damping strategies for seismic performance assessment of steel towers

4.3.5.1. Performance assessment and selected strategies for equivalent viscous damping

The CSM is applied to calculate the performance displacement using the numerical pushover and the pseudo-pushover curves under a given seismic action. The CSM algorithm is aimed at identifying the performance point which is the intersection between the capacity spectrum and an over-damped response spectrum accounting for the reduction in the demand given the hysteretic response of the structure. The capacity spectra refer to the relationship between the displacement and acceleration of an equivalent SDoF system of the tower and it is calculated according to the approach by Casarotti & Pinho (2007) and section 3.2.4. Considering the numerical pushover curve, for each pushover load step, the equivalent SDoF displacement, Δ_{eff} , and the acceleration are calculated. The acceleration is obtained by using the effective mass of the tower. The refined mass distribution of the model can be effectively approximated with a mass equal to the tributary seismic mass of the deck placed at the top node of the tower, neglecting the mass of the tower itself. In fact, the total mass of the tower is about 1/20 of the deck mass. Therefore, Δ_{eff} can be approximated as the displacement registered at the top node of the tower. This assumption is also applied in the simplified pseudo-pushover (Section 4.3.1).

The equivalent viscous damping coefficients (identified as ξ_{eff}) are used to calculate spectral reduction factors and reduce the 5%-damping elastic response spectrum. ξ_{eff} is equal to the sum of the elastic ξ_{el} and hysteretic ξ_{hyst} damping which depends on the hysteretic rule.

Several formulations for computing ξ_{eff} calibrated for different structural typologies are proposed in the literature and tested (e.g. (Casarotti et al. 2009)) within a displacement-based assessment framework. However, no recommendations are explicitly reported for steel towers.

Consequently, the effectiveness of several literature formulations for ξ_{eff} is evaluated in this study concerning the seismic performance assessment of steel towers. The

performance points selected via the considered equivalent viscous damping strategies are compared to NLTHA to identify the "best" formulation.

To perform a preliminary literature-based selection of suitable equivalent viscous damping formulations, a qualitative analysis of the cyclic behaviour of steel towers is needed. The steel towers can be studied as concentrically braced structural systems with slender diagonal braces arranged in different panels. The hysteretic dissipation of concentrically braced structural systems is mainly associated with the cyclic nonlinear response of the diagonal braces which are subjected to axial buckling in compression and yielding in tension. This is consistent with the cyclic response of the analysed steel towers which, in the case of a ductile response (Figure 4.5), is governed by the dissipative response of the diagonal bracing systems. In this study, the dissipation of the legs, which yield after the diagonal braces in the analysed cases, is neglected for the following reasons. First, this source of dissipation can not be modelled with the lumped-plasticity numerical modelling strategy adopted which considers axial load-flexure interaction. Instead, it could be modelled using refined fibre-based modelling of the cross section of the legs. Also, the dissipation associated with the legs is supposed to be lower (and also negligible) than the one associated with the bracing systems since 1) the first leg yielding is registered on the last part of the capacity curve, approaching the near-collapse condition (Figure 4.5) and 2) the amount of seismic force absorbed by the legs is negligible with respect to the portion absorbed by the diagonal braces. These hypotheses are assumed in this study. Further research developments can contribute to clarify this issue.

Normally, for steel structures ξ_{el} is fixed at 0.02-0.03. The conventional approach for calculating the hysteretic damping, ξ_{hyst} , is the area-based approach proposed in the study by Jacobsen (1960) (and also quoted by Priestley et al. (2007)) about substitute-structure analysis. It establishes that ξ_{hyst} can be calculated according to Equation 4.1 where A_h is the area measured in a steady-state cycle, F_m and Δ_m are the maximum force and the target displacement. The equivalent viscous damping to be assigned to the substitute structure having linear behaviour and secant-stiffness in target displacement condition is equal to the energy absorbed during a hysteretic steady-state cycle at the

given displacement demand.

$$\xi_{hyst} = \frac{A_h}{2\pi F_m \Delta_m} \quad (4.1)$$

Goggins & Sullivan (2009) proposed a displacement-based design methodology for concentrically braced frame systems. To this purpose, they compared the ξ_{hyst} calculated with the area-based approach based on experimental test results on a concentrically-braced panel, to literature ξ_{hyst} formulations. These are the formulation by Kwan & Billington (2003) and the equivalent viscous damping models by Priestley et al. (2007) calibrated on Flag-Shaped, Ramberg-Osgood and Takeda-Thin hysteresis rules. They stated that the Flag-Shaped ($\beta = 0.35$) relations (Equation 4.2, where $C_{evd} = 0.186$) proposed by Priestley et al. (2007) is consistent to the experimental area-based ξ_{hyst} (steady state response). However, a strong overestimation of the design displacement-demand was detected after comparison with shake table tests and the authors concluded that Equation 4.2 where $C_{evd} = 0.186$ underestimates the hysteretic dissipation. The authors recommended to adopt the Takeda-Thin formulation by Priestley et al. (2007) (Equation 4.2 where $C_{evd} = 0.444$) for calculating the ξ_{hyst} of concentrically-braced structures. This is also consistent with the displacement-based design approach developed by Della Corte & Mazzolani (2008) for concentrically-braced systems.

$$\xi_{hyst} = C_{evd} \frac{\mu - 1}{\pi \mu} \quad (4.2)$$

Besides these studies, Wijesundara et al. (2011) proposed formulations to calculate ξ_{hyst} for the displacement-based design for concentrically-braced frames. Several single-storey frames having decoupled diagonal braces (including a middle column) and X-shaped diagonal braces are analysed. The authors calculated the ξ_{hyst} according to the area-based approach and perform additional calibrations based on NLTHA results (using natural ground motions). They calibrated ξ_{hyst} for varying ductility (from 1 to 7) and non-dimensional slenderness ratio (λ from 0.41 to 0.83) of the diagonal braces and proposed a final analytical equation to support displacement-based design applications. However, the proposed equation is not applicable for very high values of the slender-

ness of the bracing systems which characterise the structural typology analysed in this study.

Given the aforementioned synthetic state-of-the-art, some strategies are selected and tested for computing $\xi_{hyst,p}$ for steel towers. These strategies analyse the dissipation of the single braced panels of the steel towers.

The first follows the fundamentals of the area-based approach by Jacobsen. Several case-study panels having parametric non-dimensional slenderness of diagonal braces are subjected to cyclic pushover analysis to calculate the steady-state response. The $\xi_{hyst,p}$ is calculated according to Equation 4.1 for different values of Δ_m , [2.5 3.5 4.5 5.5], corresponding to ductility equal to [1.5, 2, 2.5, 3, 5, 6.5, 8]. Nonlinear regression with a surface model is performed via the least square method to achieve a synthetic equation (Equation 4.3) relating the $\xi_{hyst,p}$ to μ and λ . The process is described in Figure 4.7.

$$\xi_{hyst} = (\lambda^{0.132} - 1) \frac{\mu - 1}{\mu^{1.5} + 0.5} \tag{4.3}$$

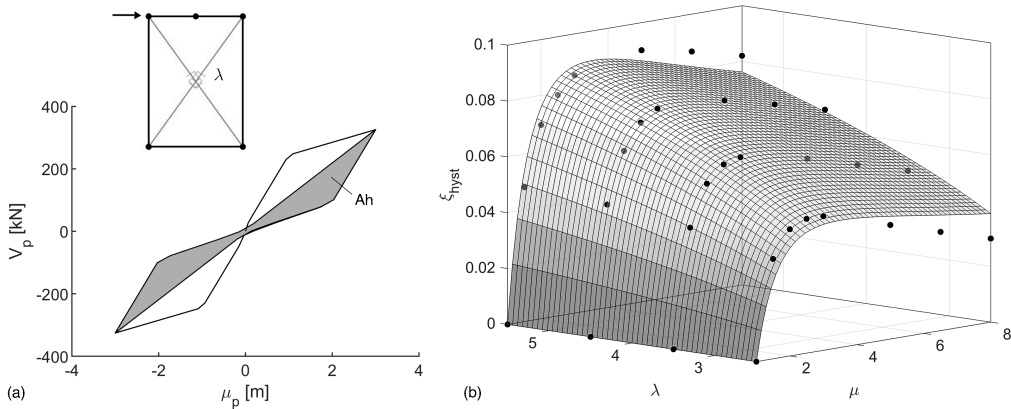


Figure 4.7: Cyclic pushover analysis on the single panel (a) and fitting of the nonlinear surface model (b)

The second strategy considers the outcomes of the study by Wijesundara et al. (2011). It is indicated as X-CBF formulation. The calibrated equivalent viscous damping data which refers to the bracing systems with coupled diagonals are adopted to fit another

nonlinear model via the least square method (Equation 4.4) The dependency on the non-dimensional slenderness is neglected.

$$\xi_{hyst} = 0.218 \frac{\mu - 1}{\mu - 0.76} \quad (4.4)$$

The third and fourth strategies refer to Equation 4.2 using C_{evd} equal to 0.186 and 0.444, according to Goggins & Sullivan (2009) and Della Corte & Mazzolani (2008), respectively.

Finally, the ξ_{eff} related to the tower is computed aggregating the elastic ξ_{el} and the $\xi_{hyst,p}$ of the panels according to the approach proposed by Grande & Rasulo (2013) for multi-storey concentrically braced frames. This latter is tailored for steel towers in Equation 4.5 where E_{hyst} and E_{el} are the hysteretic energy and the elastic energy associated to the response of a linear substitute SDoF system representing the tower in target displacement condition. The numerator of Equation 4.5 can be rewritten using the yielding steel strength f_y , the cross-section area of the tensile brace $A_{d,p}$ and its axial deformation ε_p . The denominator is equal to the product of the top displacement Δ_{top} and the total base shear V_b . This formulation implicitly assumes that all the seismic mass (and seismic force) is placed at the tower top and neglects the mass distribution along the height of the tower. Therefore, the equivalent SDoF of the tower is straightforwardly calculated.

$$\xi_{eff} = \xi_{el} + \xi_{hyst} = \xi_{el} + \frac{E_{hyst}}{4\pi E_{el}} = 0.03 + \frac{\sum_{p=1}^N \xi_{hyst,p} f_y A_{d,p} \varepsilon_p}{\Delta_{top} V_b} \quad (4.5)$$

Figure 4.8 compares the equivalent viscous damping calculated via the selected strategies. Figure 4.8.a refers to the top panel ($\lambda = 3.00$) of the T2r tower parallel to the longitudinal direction (i.e. x direction) of the bridge. It is observed that the Flag-Shaped and Jacobsen's strategies strongly underestimate the $\xi_{hyst,p}$ of the specific panel with respect to the other strategies ($\xi_{hyst,p} \cong 0.05$ at $\mu_p = 7$), the X-CBF provides the maximum value of $\xi_{hyst,p}$ ($\xi_{hyst,p} = 0.21$ at $\mu_p = 7$), while Takeda-Thin provides intermediate results ($\xi_{hyst,p} = 0.13$ at $\mu_p = 7$). The same results are approximately obtained for the other panels (i.e. varying λ). Figure 4.8.b shows the ξ_{eff} aggregating

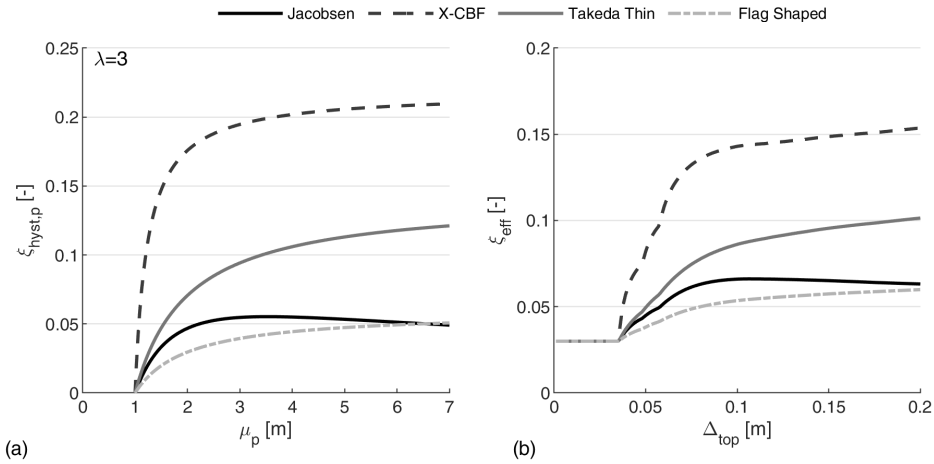


Figure 4.8: Comparison between the equivalent viscous damping strategies associated with a single panel (a) and to the whole system (b) considering the tower T2r analysed in Y direction via numerical pushover analysis.

the ξ_{el} and $\xi_{hyst,p}$ according to Equation 4.5. In this case, the geometry of the tower and the displacement profile calculated for each load step influence the step-by-step value of ξ_{eff} . The ξ_{eff} calculated according to the X-CBF strategy stabilizes around 0.15 for large inelastic demand.

4.3.5.2. Effectiveness of the selected strategies for equivalent viscous damping

The performance displacement calculated according to the CSM adopting the selected four equivalent viscous damping strategies is compared to the NLTHA performance displacement. The relative errors are calculated between the results of the CSM and the NLTHA. These are graphically reported in Figure 4.9 where different markers distinguish the adopted strategies. Also, the numerical results are listed in Table 4.2. The results are calculated for the two steel towers (i.e. T1r and T2r), analysed in both longitudinal and transverse direction (i.e. X dir and Y dir, respectively) using the seismic action described in subsection 4.3.4 by means of the numerical pushover and pseudo-pushover procedures.

The outcomes are particularly consistent with the aforementioned literature studies described in subsection 4.3.5.1. Indeed, the Flag-Shaped and Jacobsen’s area-based

formulations are too conservative and provide a consistent overestimation of the NLTHA performance displacements. The errors increase as the intensity of the seismic action increases. This evidences the need for NLTHA-based calibration if Jacobsen’s approach is adopted for structures where calibrated equivalent viscous damping formulations are not available. The Takeda-Thin formulation provides errors between [+12; +50]% endorsing the outcomes by Della Corte & Mazzolani (2008).

The strategy based on the results by Wijesundara et al. (2011) outperforms the other approaches providing errors generally lower than +10%. The maximum error is equal to +22% and +20% corresponding to the case-study T2r-x analysed via numerical pushover and pseudo-pushover, respectively. It is worth noting that in this case, the effectiveness of the formulation seems to be not sensitive to the intensity of the seismic action.

In conclusion, these results can be used for identifying an accurate equivalent viscous damping formulation to be used for the seismic performance assessment of steel towers. These outcomes can be directly applied for the seismic performance assessment of isostatic steel truss bridges with steel towers, where the Individual Pier Model can be applied (Cardone 2014). Conversely, the proposed formulation can be included in DBA algorithms or can be used within the CSM after pushover analyses if hyperstatic continuous truss bridges are investigated.

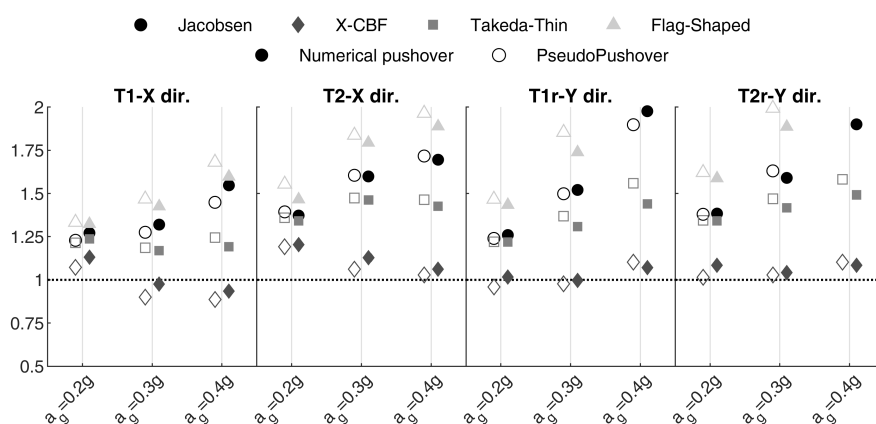


Figure 4.9: Relative error between the performance displacement calculated via the selected equivalent viscous damping strategies and NLTHA.

Table 4.2: Performance displacement calculated via NLTHA and the CSM performed via the selected strategies.

Tower	a_g	Jacobsen			X-CBF		Takeda-Thin		Flag-Shaped	
		NLTHA	Push	Pseudo	Push	Pseudo	Push	Pseudo	Push	Pseudo
T1r	0.2g	0.074	0.094	0.091	0.083	0.079	0.091	0.090	0.098	0.098
x	0.3g	0.113	0.150	0.145	0.111	0.102	0.133	0.135	0.162	0.166
	0.4g	0.157	0.242	0.227	0.146	0.139	0.187	0.195	0.250	0.263
T2r	0.2g	0.032	0.044	0.044	0.038	0.038	0.043	0.043	0.047	0.049
x	0.3g	0.049	0.078	0.078	0.055	0.052	0.071	0.072	0.087	0.089
	0.4g	0.071	0.120	0.121	0.075	0.073	0.101	0.103	0.134	0.139
T1r	0.2g	0.073	0.092	0.090	0.074	0.070	0.089	0.089	0.105	0.107
y	0.3g	0.109	0.165	0.163	0.109	0.106	0.142	0.149	0.189	0.202
	0.4g	0.149	0.295	0.284	0.160	0.165	0.215	0.233	Coll	Coll
T2r	0.2g	0.037	0.051	0.051	0.040	0.038	0.050	0.050	0.059	0.060
y	0.3g	0.057	0.091	0.093	0.060	0.059	0.081	0.084	0.108	0.114
	0.4g	0.084	0.159	Coll	0.091	0.092	0.125	0.133	0.179	Coll

4.4. Displacement-based assessment of continuous truss deck bridges

This Section focuses on the effectiveness of displacement-based assessment (DBA) approaches, applied together with the CSM, for the seismic performance assessment of continuous-truss bridges supported by steel towers. In this Chapter, direct algorithms for performing displacement-based performance assessment are proposed, by combining the conventional DBA approaches and the CSM. These are compared to numerical pushover analyses (together with the CSM) to estimate the seismic performance displacement and NLTHA. The archetype bridge is used to generate six case-study bridges for evaluating the influence of the number of spans (from 2 to 4 spans) and the distribution of the towers on the longitudinal axis on the bridge on the accuracy of the investigated approaches. The DBA algorithms discussed in this section are aimed at analysing the case-study bridges in the transverse direction only. The analysis in longitudinal direction is not performed for the following reasons: 1) the study in Chapter 3 (3.5.5) showed that DBA algorithms in longitudinal direction degenerate in studying the bridge as a parallel system and are not worthy of further validation; 2) the response in trans-

verse direction can be considered the most critical one for continuous-superstructure bridges (Perdomo et al. 2020).

4.4.1. Description of the analysis approaches

The study performed in this Chapter extends the outcomes proposed in Chapter 3, where the effectiveness of two DBA approaches is discussed via comparisons with pushover analyses and NLTHA for continuous-deck RC bridges.

The original version of DBA approach is based on iterative modal (eigenvalue) and was proposed for continuous-deck RC bridges by Şadan et al. (2013) (described in Section 3.2.1). This methodology is slightly modified in Section 3.2.2 by replacing the modal analysis with simpler static analysis. Both the approaches are used for the seismic response analysis of bridge with hyperstatic superstructure in transverse directions where two load paths (i.e. the seismic actions is absorbed by the deck-abutment system and by the piers) combine.

Basically, within both the basic DBA versions, an iterative approach based on an equivalent linear analysis is adopted to calculate the displacement profile of a hyperstatic-superstructure bridge given a pre-determined target displacement (e.g. limit state threshold) of a specific substructure member. Then, the corresponding equivalent SDoF system of the bridge in target displacement condition can be characterised and compared to the demand expressed in terms of over-damped response spectra.

The application of the DBA in the longitudinal direction is straightforward for multi-span bridges whose deck can be assumed axially rigid. The system response can be represented by the parallel actions of the substructure members which absorb the seismic force (i.e. the bearings are longitudinally fixed). No iterations are required to define the displacement profile in target displacement condition.

The basic DBA algorithm is extended in Section 3.2.3 for calculating a displacement-based pseudo pushover (DBPP), enabling the calculation of the displacement demand under a given seismic action via the CSM. In this Chapter, the entire DBPP+CSM procedure is compressed in direct displacement-based seismic performance assessment approaches described as follows. These approaches can be applied to identify, via an iterative procedure, the equivalent SDoF system in performance displacement condition

under a given seismic action. The performance displacement profile can be calculated based on iterative static (DBAs) or modal analysis (DBAm).

The static analysis-based approach is described in Figure 4.10. A tentative displacement profile is defined in the first step. In this study, a parabolic shape is assumed and scaled such that the critical substructure member (which is judgementally identified) reaches the ultimate capacity. It is worth mentioning that an incorrect choice of the control node does not affect the result of the DBA algorithm, but can only involve a slight increase of the required iterations. Subsequently, the shear profile V_i corresponding to the assumed Δ_i is calculated by interpolating the force-displacement relationships of the substructure members. Also the secant-to-target-displacement stiffness ($k_{sec,i} = V_i/\Delta_i$) is assigned to the support of the simplified beam model. At this stage, a static analysis is performed using the force profile F_i indicated in Equation 4.6 and a new displacement profile Δ'_i is calculated which is compared to Δ_i . If the differences of $|\Delta_i - \Delta'_i|$ calculated for each i -th member are minor than a pre-determined tolerance value the convergence is reached, the process continues. If not, another iteration should be performed using Δ'_i as a tentative displacement profile. Assuming that the convergence is reached, the equivalent SDoF system corresponding to the structure in Δ_i condition can be completely characterised in terms of effective displacement Δ_{eff} (Equation 4.7), base shear V_b (Equation 4.8), effective mass m_{eff} , (Equation 4.9), effective period T_{eff} (Equation 4.10). The equivalent viscous damping is calculated via Equation 4.4 and 4.5.

Also, the over-damped displacement demand $S_d^\xi(T_{eff})$ is calculated by multiplying the 5% spectral demand displacement $S_d^{5\%}(T_{eff})$ for the corresponding spectral reduction factor η_{eff} (Equation 4.12). The displacement profile Δ''_{eff} corresponding to a Δ_{eff} equal to $S_d^\xi(T_{eff})$ should be calculated and compared to Δ'_{eff} . At this scope, Δ''_{eff} is calculated via Equation 4.13 where ϕ'_i is obtained by a normalisation of Δ'_i . If Δ''_i does not converge with respect to Δ'_i another iteration is performed where Δ'_i is used as tentative displacement to be stabilised in the first iteration and checked with respect to the corresponding value of spectral reduction factor. A displacement tolerance of 1

mm is suggested to achieve convergence in three or four iterations.

$$F_i = V_b \frac{m_i \Delta_i}{\sum m_i \Delta_i} \quad (4.6)$$

$$\Delta_{eff} = \sum_{i=1}^N \frac{m_i \Delta_i^2}{m_i \Delta_i} \quad (4.7)$$

$$V_b = \sum_{i=1}^N V_i \quad (4.8)$$

$$m_{eff} = \frac{\sum_{i=1}^N m_i \Delta_i}{\Delta_{eff}} \quad (4.9)$$

$$T_{eff} = 2\pi \sqrt{\frac{m_{eff}}{k_{eff}}} \quad \text{where} \quad k_{eff} = \frac{V_b}{\Delta_{eff}} \quad (4.10)$$

$$\xi_{eff} = \frac{0.05\Delta_1 V_1 + 0.05\Delta_N V_N + 0.02\Delta_{eff}(V_1 + V_N) + \sum_{i=2}^N \xi_i \Delta_i V_i}{\Delta_1 V_1 + \Delta_N V_N + \Delta_{eff}(V_1 + V_2) + \sum_{i=2}^N \Delta_i V_i} \quad (4.11)$$

$$\eta_{eff} = \sqrt{\frac{0.07}{0.02 + \xi_{eff}}} \quad (4.12)$$

$$\Delta_i'' = \phi_i' \Gamma S_d^\xi(T_{eff}) \quad (4.13)$$

The DBAm is proposed by proposed by Perdomo & Monteiro (2020). This modal analysis-based DBA is performed according to the following description and Figure 4.11. The first preliminary step is again the calculation of the force-displacement relationships to be assigned to the supports of the equivalent beam model. A first modal analysis is performed assuming a tentative value of the stiffness of the supports $k_{sec,i}$. The secant-to-yielding stiffness can be used as initial assumption. The significant modes, which are deemed to significantly contribute to the performance displacement profile, are selected. It is suggested to select all the modes having more than 5% of participating

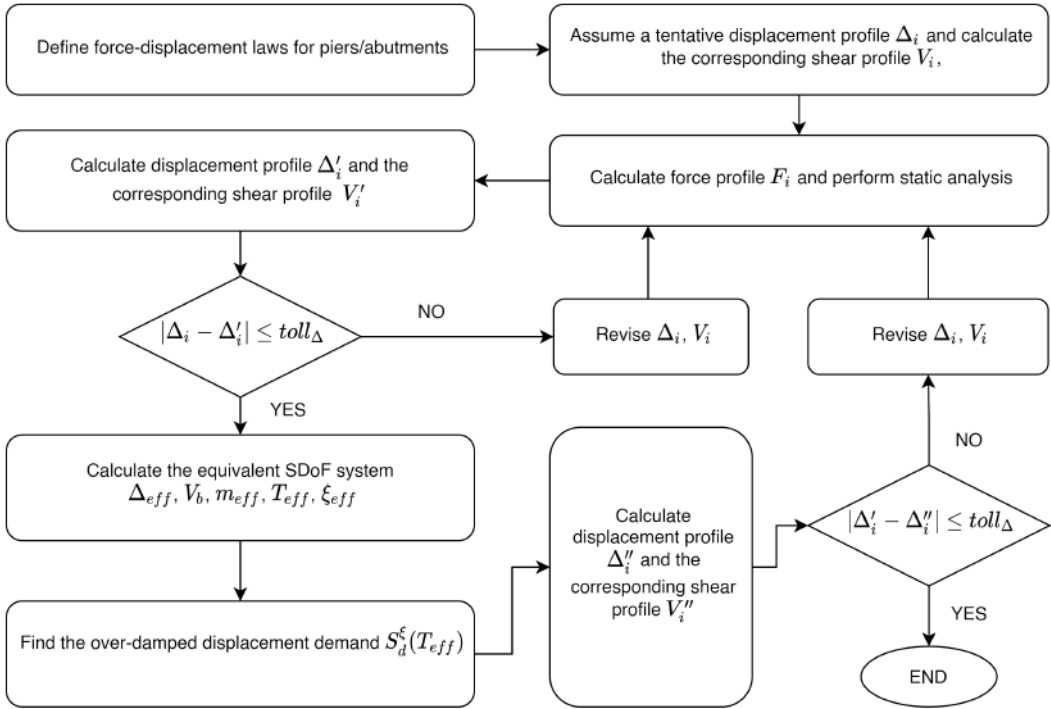


Figure 4.10: Flowchart of the proposed static analysis-based DBA approach

mass. The displacement profiles $\Delta_{i,j}$ calculated for each mode j via Equation 4.14, are used to calculate the corresponding shear profile $V_{i,j}$ associated to the $j - th$ mode. Moreover, the modal superposition is performed via the Complete Quadratic Combination, obtaining the bridge performance displacement Δ_i .

$$\Delta_{i,j} = \Gamma_j S_d^{5\%}(T_j) \phi_{i,j} \quad (4.14)$$

At this stage, the first iteration is carried out. The equivalent SDOF system related to each mode j is calculated in terms of effective displacement $\Delta_{eff,j}$ (Equation 4.7 repeated for each $j - th$ mode), base shear $V_{b,j}$ (Equation 4.8), effective mass $m_{eff,j}$, (Equation 4.9), effective period $T_{eff,j}$ (Equation 4.10). The equivalent viscous damping for each mode j is calculated via Equation 4.11.

The over-damped displacement demand related to each mode $S_d^\xi(T_j)$ is calculated by multiplying the 5% spectral demand displacement $S_d^{5\%}(T_j)$ for the corresponding spectral reduction factor η_j (Equation 4.12). This allows for a recalculation of the per-

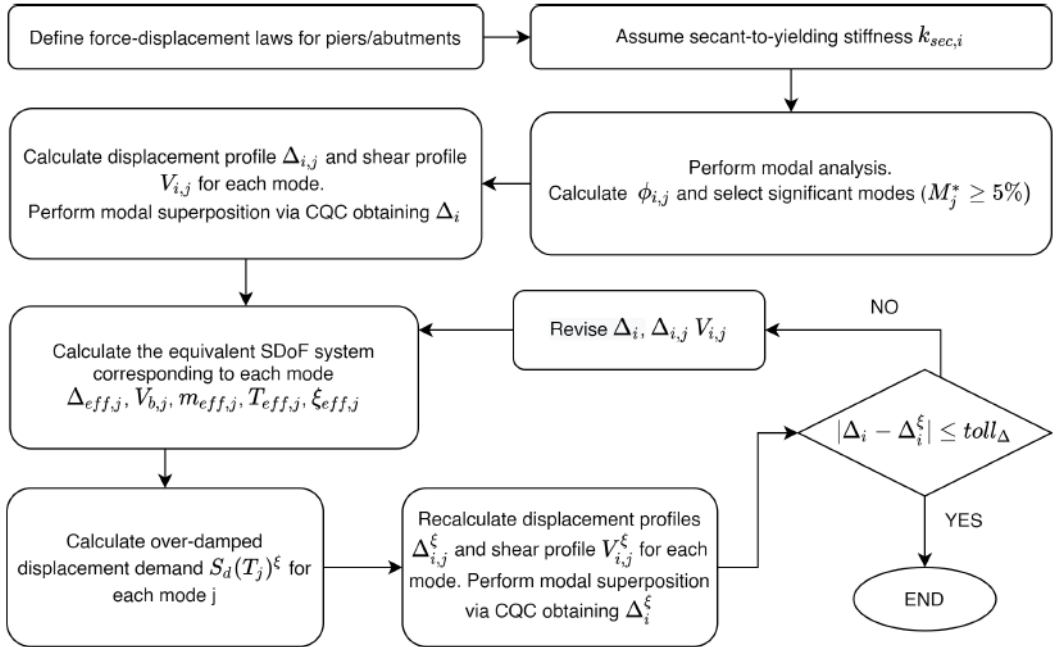


Figure 4.11: Flowchart of the proposed modal analysis-based DBA approach

formance displacement profiles $\Delta_{i,j}^{\xi}$ to be associated with each mode accounting for specific-mode damping. A new global performance displacement profile Δ_i^{ξ} is also obtained by combining $\Delta_{i,j}^{\xi}$ via the CQC combination. This is compared to the first tentative Δ_i , checking the convergence according to a pre-determined value of tolerance. If the convergence is satisfied, the process is completed; if not, other iterations should be performed.

These two analytical DBA methodologies are adopted to analyse continuous-truss multi-span bridges. Additionally, two numerical pushover-based analysis approaches are applied, by using modal (PUSHm) and uniform (PUSHu) load patterns. Within these methodologies, the equivalent SDoF pushover curve of the bridge is calculated and subjected to the CSM to determine the performance point under a given response spectrum, and therefore, the performance displacement profile.

4.4.2. Case study bridges and modelling assumptions

A dataset of six case-study continuous-truss bridges is generated starting from the geometric/constructive features of the archetype bridge (subsection 4.2). The bridges,

shown in Figure 4.12, differentiate in the number of spans and geometric layout of the supporting steel towers. It is assumed that the bearings placed on the substructure members prevent transverse displacements. The nonlinear response of the bearing devices is not considered in the following analysis. The length of the span is 42 m according to the archetype bridge.

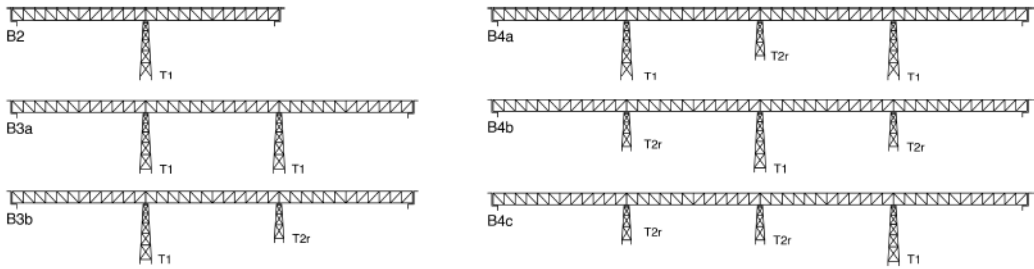


Figure 4.12: Parametric case-study bridges.

The numerical pushover analyses are performed by using the SAP2000 software package (Computer and Structures INC (CSI) 2018) following the strategy presented in Figure 4.13. The steel towers are modelled according to the strategy described in Section 4.3.1, while a spine model is adopted for the longitudinal truss superstructure. At this scope, the superstructure is modelled as an elastic frame whose flexural inertia characteristics are calculated considering a cross-section composed of the upper and lower chords of the truss beams (the contribution of the bracing members of the deck is neglected). The other mechanical characteristics are calculated considering an equivalent rectangular hollow cross-section (CEN 2009), whose thickness is calculated based on the mechanical/geometric features of the bracing system.

The DBAs and DBAm are applied using a simplified modelling strategy where the truss superstructure is modelled as an equivalent beam model and the steel towers are represented by inelastic supports. The mechanical features of the elastic beam are consistent with the spine model in SAP2000. The force-displacement laws calculated by using the pseudo-pushover analysis (sub-section 4.3.2) are assigned to the inelastic supports. Simple programming routines are developed in MATLAB (MATLAB 2018) to apply the DBAs and DBAm with very low modelling/computational effort.

The three ground motion suites shown in sub-section 4.3.4 are used to analyse the

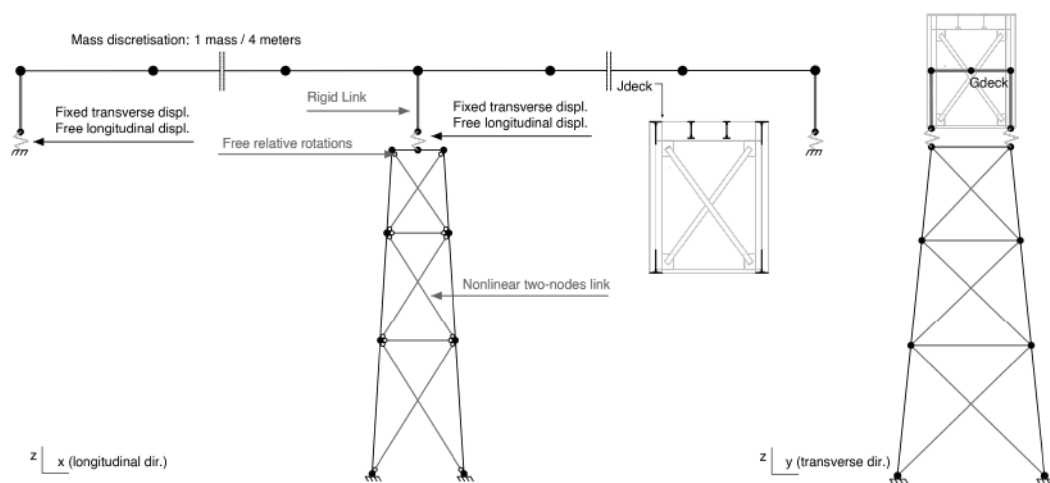


Figure 4.13: Modelling strategy in SAP2000 (Computer and Structures INC (CSI) 2018).

case-study bridges and discuss the accuracy of the procedure described in subsection 4.4.1 with respect to NLTHA.

4.4.3. Results of the parametric analysis

4.4.3.1. Modal analysis and relative stiffness index

A preliminary focus on the regularity in the seismic response in the transverse direction of the case-study bridges is proposed. A regular response means: 1) low influence of higher modes in elastic state and 2) slight modification of the significant modal shapes for increasing nonlinear demand. According to literature studies such as Isakovic (2006), Isaković et al. (2008), Pinho et al. (2007), Kohrangi et al. (2015b), the degree of regularity strongly influences the accuracy of nonlinear static procedures. The regularity indexes adopted are the participating mass of the first mode and the Relative Stiffness index (RS). This latter is calculated with Equation 4.15 and compares the stiffness in the transverse direction of the superstructure and substructure. As evidenced in Chapter 3, the higher is the RS , the higher is the influence of the superstructure in redistributing the seismic action among the substructure members, reducing the variability of the modal shapes for increasing inelastic demands of the substructure

members.

$$RS = \frac{384EJ_{deck}}{5L_{deck}^3} \frac{1}{\sum k_{towers}} \tag{4.15}$$

The results of a preliminary modal analysis are shown in Figure 4.14. All the modal shapes characterised by a participating mass higher than 5% (which are also used in the DBAm calculation) are shown. The RS index is also indicated in this Figure.

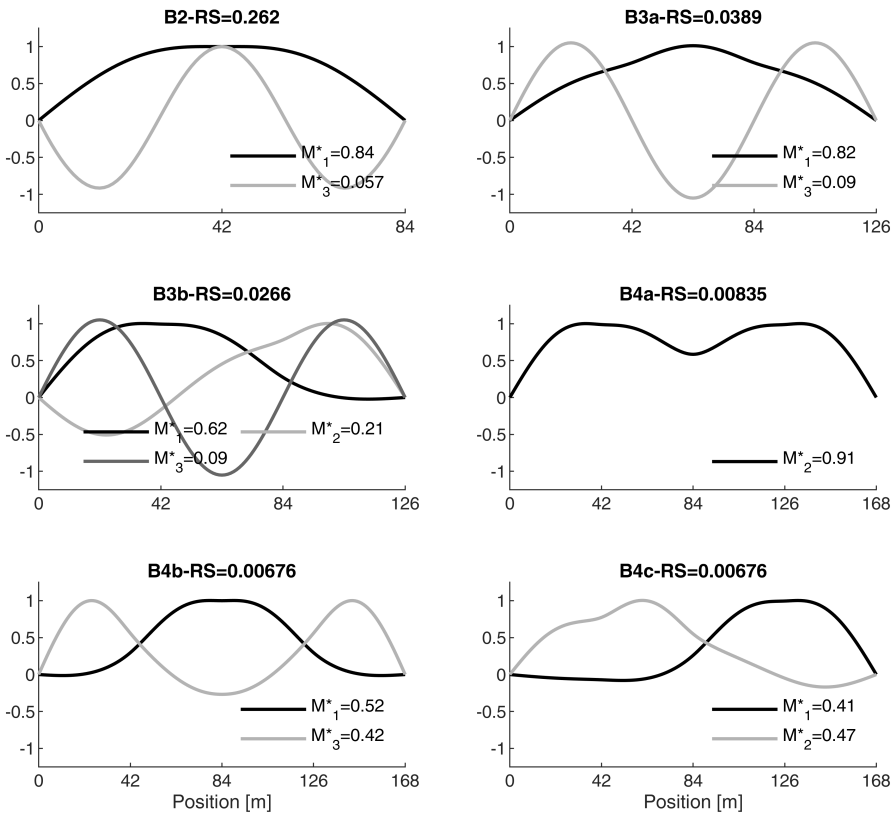


Figure 4.14: Significant modal shapes (participating mass higher than 5%) of the case-study bridges

It is observed that the first modal shape of B2, B3a and B4a (RS equal to 0.262, 0.0389 and 0.00835, respectively) corresponds to a participating mass higher (M^*) than 80%,

which is supposed to govern the seismic response with low higher-mode contributions. Differently than the B3a, the B3b ($RS = 0.0266$), which exhibits an asymmetric layout of the supporting towers, is characterised by an irregular response with M_1^* equal to 0.62. Indeed, the first modal shape slightly differs from the regular "simple beam" vibration mode which means a regular response according to Calvi et al. (1993). Also, the modal shapes of the B4b and B4c are strongly influenced by the presence of short towers (T2r). The first two modes are associated separately with the vibration of the T1r and T2r exciting a participating mass included in the range 41-52%. In these cases, the distribution of stiffness of the towers along the bridge length governs the global deformed shapes rather than the stiffness of the superstructure.

4.4.3.2. Performance displacement evaluation

In this subsection, the accuracy of the considered nonlinear static approaches (PUSHm and PUSHu) and DBA methodologies (DBAs and DBAm) is discussed adopting the same strategy used in Chapter 3. The capacity demand ratio (CDR) and bridge index (BI) are introduced to this purpose. The first is the ratio of displacement-based capacity ($\Delta_{U,t}^p$) and demand (Δ_t^p) related to the critical supporting tower. It is calculated with reference to all the simplified approaches and NLTHA via Equation 4.16 where the index p refers to *PUSHm*, *PUSHu*, *DBAm*, *DBAs*, *NLTHA* and t to the single supporting tower of the analysed bridge. Note that the ultimate displacement capacity differs for analytical (DBA) and numerical methods (PUSH and NLTHA). Indeed, the capacity of the towers ($\Delta_{U,t}^j$) is calculated through the simplified pseudo-pushover within the DBA, while via the (local) numerical pushover for both the global numerical pushover strategies and NLTHA.

$$CDR^j = \min_{t=1}^{N_{tow}} \left(\frac{\Delta_{U,t}^p}{\Delta_t^p} \right) \quad (4.16)$$

Furthermore, the BI is related to the accuracy of each simplified analysis approach in predicting the performance displacement profile concerning NLTHA. It is calculated via Equation 4.17 where N_{tow} is the number of supporting towers. The BI adopted

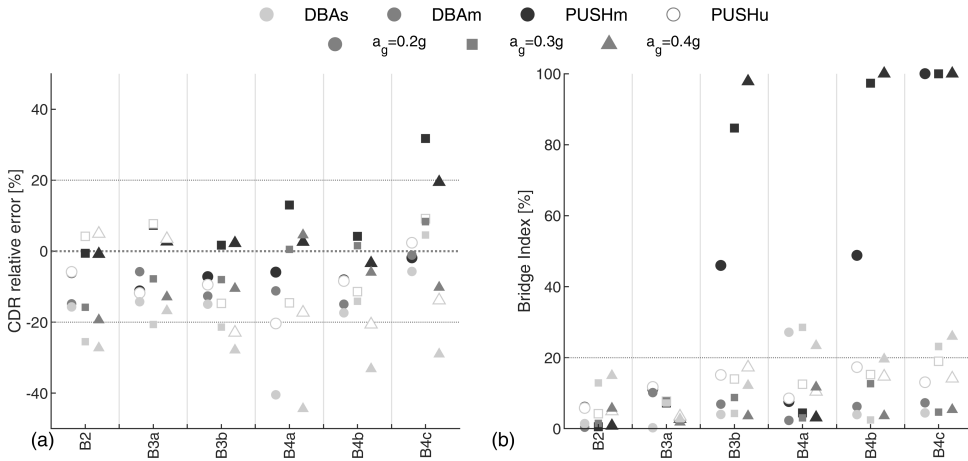


Figure 4.15: CDR and BI for the case-study dataset.

in this Chapter is slightly modified with respect to the BI of Chapter 3 to avoid error compensation due to over/underestimation of displacement demand along the bridge.

$$BI = \frac{1}{N_{tow}} \sum_{t=1}^{N_{tow}} \left| \frac{\Delta_t^{DBA/PUSH}}{\Delta_t^{NLTHA}} - 1 \right| \quad (4.17)$$

Figure 4.15a shows the relative errors of the CDR calculated via the DBA and PUSH to NLTHA, while the BI are reported in Figure 4.15b. To better understand these results, the displacement demand profiles predicted by the considered analysis approaches are shown in Figures 4.16 and 4.17. In these Figures, each column refers to a single case study, while each row corresponds to a different ground motion suite. The results of the NLTHA are shown in both average response and corresponding standard deviation. Considering the "regular" cases indicated in the previous sub-section (i.e. B2a, B3a, B4a), it is observed a general accuracy of all the adopted simplified strategies. Indeed, the corresponding relative errors on the CDR with respect to NLTHA, is included in the range [-20; +20]% and the BI are lower than 20%. However, some inaccuracies are related to the DBAs. Particularly, for case B2, this latter underestimates the CDR calculated with NLTHA, providing errors equal to -26% and 23% for a_g equal to 0.3 and 0.4 g, respectively. This effect is caused by both an overestimation in the displacement demand (Figure 4.16), first column) and an underestimation of the ultimate capacity on the

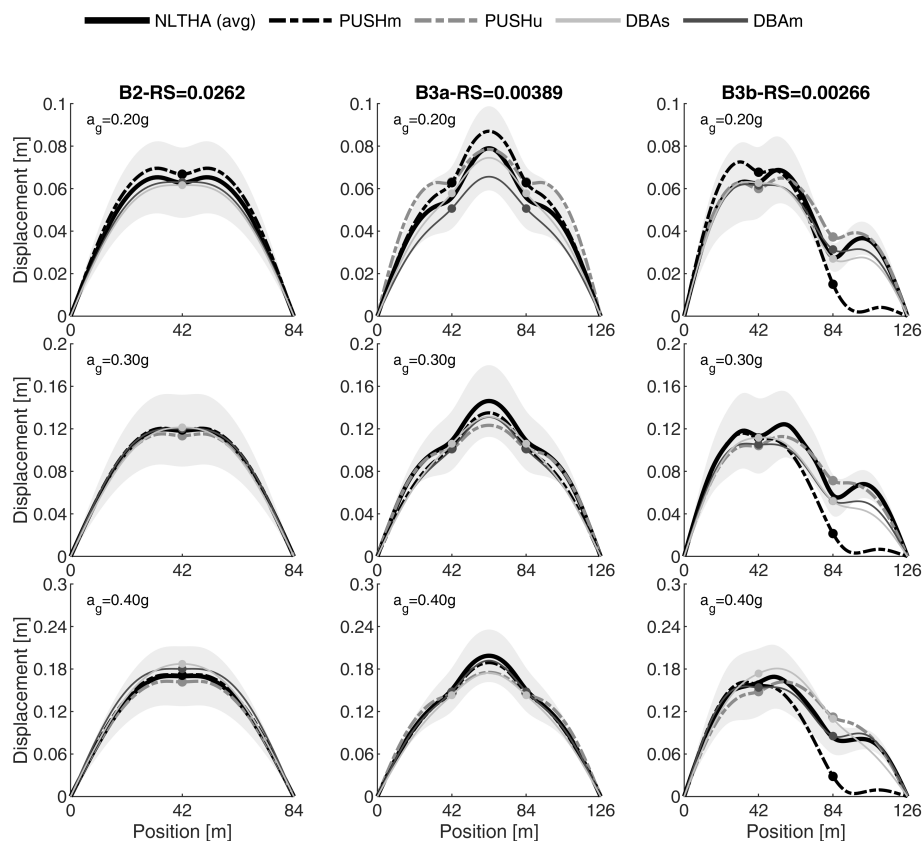


Figure 4.16: Displacement profiles calculated with PUSH, DBA and NLTHA.

tower T1r provided by the simplified pseudo-pushover (Figure 4.5). Moreover, the BIs associated with the DBAs and the case B4a exceed the 40%. This is explained by Figure 4.16 which shows that the DBAs fails in predicting the deformed shape overestimating the demand of the central tower and underestimating it on the lateral towers. This evidences that the DBAs algorithm updates the pushing force profile in a non-consistent way with respect to NLTHA.

The accuracy of the PUSHm and DBAs importantly decreases for the "irregular" cases (i.e. B3b, B4b, B4c). For the bridge B3b and B4b, although the PUSHm and DBAs errors on the CDR are lower than 20% (excluding the DBAs results for $a_g = 0.4g$ on B4b), the BIs exceed the 40%. The plots in the third column of Figure 4.16 show that

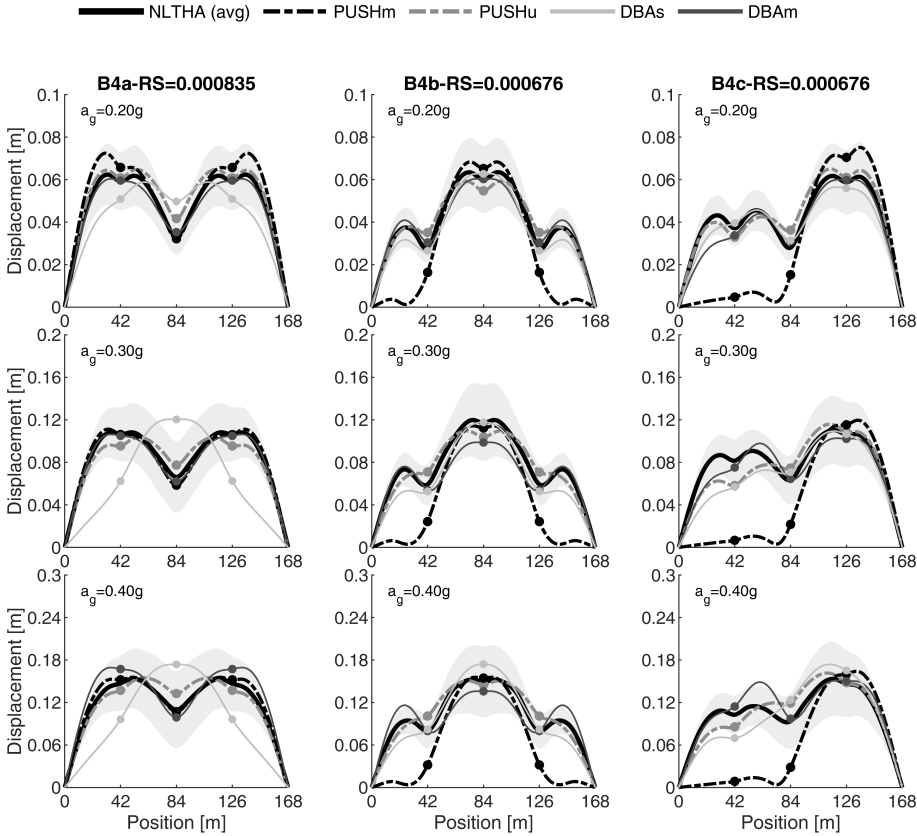


Figure 4.17: Displacement profiles calculated with PUSH, DBA and NLTHA.

PUSHm well-predicts the displacement demand on the tallest tower, which is the critical one, and consequently provides an accurate estimation of the CDR with respect to NLTHA. However, the PUSHm dramatically underestimates the displacement demand on the shortest supporting tower regardless of the intensity of the seismic action. The DBAs provides similar results to the PUSHm for low and medium intensity, while, for the high seismic intensity, it successfully mimics the NLTHA displacement demand providing a BI lower than 20%. This is because the DBAs successfully updates the force and displacement profiles when the short tower reaches its yielding displacement. The inaccuracies of the PUSHm and DBAs are connected to their negligence in considering higher-mode contribution. The same comments can be extended to case B4b. Both the

DBAs or the PUSHm fail in predicting the displacement demand on the short supporting towers of the bridge B4c which is the most "irregular". Indeed, the BI for both DBAs and PUSHm exceeds the 100% regardless of the intensity of the seismic action. Note that these first-mode-based analysis approaches provide inaccuracies, even though the analysed cases are consistent with the limitations for the applicability of DBA and non-linear static approaches for RC bridges.

The PUSHu, thanks to its tendency to envelope the contribution of higher modes with a uniform load profile, outperforms the previously discussed strategies. Particularly, the corresponding error on the CDR is generally less than 20%, while the BIs are included in the range [10;20]%. Also, the DBAm successfully combines higher-mode contribution to predict the NLTHA displacement demand. Indeed, for all the "irregular" analysed cases the DBAm provides an absolute value of the CDR errors lower than 18% and BIs lower than 17%.

The outcomes of this parametric analysis show that the limitations proposed in Chapter 3 for the applicability of nonlinear static procedures and DBA methodologies on RC bridges, can be extended for multi-span steel truss bridges. Generally, since higher mode-contributions can considerably affect the nonlinear response of this bridge typology, DBAm and PUSHu are recommended instead of PUSHm and DBAs. According to Chapter 3, the DBAs can be applied for 2-span steel truss bridges with first-mode-dominant dynamic response. Conversely, the adopted DBAm is particularly promising for steel truss bridges even if values of $RS \leq 0.01$ are observed. It is also suggested to use NLTHA for cases where higher irregularity is expected with respect to the analysed cases (e.g. longer bridges). It is worth noting that these results can guide an analyst in investigating the response of other bridges having high flexibility of the continuous superstructure (e.g. truss bridges supported by masonry/RC wall piers).

4.5. Conclusions

The study proposed in this Chapter is aimed at discussing the effectiveness of nonlinear static procedures and displacement-based assessment (DBA) approaches for the seismic analysis of multi-span steel truss bridges supported by steel towers.

The first part of this study refers to the seismic response of steel towers to identify an ef-

fective equivalent viscous damping formulation to be used within the capacity spectrum method. The results of several equivalent viscous damping strategies proposed in the literature are compared to NLTHA displacement demand. The seismic action is represented by a suite of ten ground-motion excitations which are scaled for three increasing levels of intensity. An accurate equivalent viscous damping strategy is proposed based on the study by Wijesundara et al. (2011) and by Grande & Rasulo (2013).

The second part focuses on testing these approaches for the seismic performance prediction of hyperstatic multi-span steel truss bridges. Six case-study bridges are generated via a parametric analysis, having different substructure layout and two to four spans. These are analysed via two pushover analysis approaches, adopting a first mode-based and uniform load profile, coupled with the CSM, and two direct DBA algorithms for performance displacement prediction based on equivalent modal and static analysis. Nonlinear time history analysis is used for benchmarking the above-mentioned methodologies. The effectiveness of the considered analysis approaches is discussed adopting two indexes: the capacity demand ratio and the bridge index, which refers to the performance of the critical substructure members and the whole performance displacement of the bridge. The results evidence that the higher-mode contribution to the seismic response is significant. Consequently, the modal version of the DBA approach and the pushover analysis with a uniform load profile should be used for this bridge typology with a limited number of spans. Conversely, the first-mode-based methodologies, even though result accurate in predicting the performance of the critical tower, present an unsatisfying bias in estimating the demand on all the substructure members.

Chapter 5

Cloud-CSM: including record-to-record variability in fragility analysis using the capacity spectrum method

Abstract

This Chapter investigates the use of the capacity spectrum method (CSM) in fragility analysis of structures. As opposed to code-based conventional spectra, the CSM is applied with real (i.e., recorded) ground-motion spectra to explicitly consider record-to-record variability in fragility analysis. The study focuses on single-degree-of-freedom systems, which is a modelling strategy commonly adopted for the performance prediction within the framework of displacement-based or conventional nonlinear static procedures (see Chapters 3, and 4). This study is aimed at providing an essential basis for future multi-degree-of-freedom system applications. A case-study database of 2160 inelastic oscillators is defined through parametric backbones with different elastic periods, (yield) base shear coefficients, values of the ductility at peak strength, hardening ratios, residual strength values and hysteresis rules. The considered parametric case studies are representative of bridge components, but also other structural typologies. These case studies are analysed using 100 real ground motions.

An efficient algorithm to perform the CSM with real spectra is proposed, combined with a cloud-based approach (Cloud-CSM) to derive fragility relationships. Simple criteria to solve the issue of multiple CSM solutions (i.e., two or more points on the backbone satisfying the CSM procedure) are proposed and tested. It is demonstrated that the performance point selection can be performed based on a particularly efficient intensity measure detected via optimal intensity measure analysis. The effectiveness of the proposed Cloud-CSM in fragility analysis is discussed through extensive comparisons with nonlinear time-history analyses, the code-based N2 method, and a simple method involving an intensity measure as a direct proxy for the performance displacement. The

Cloud-CSM provides errors lower than $\pm 20\%$ in predicting the median fragility in most of the analysed cases, and outperforms the other considered methodologies in calculating the dispersion.

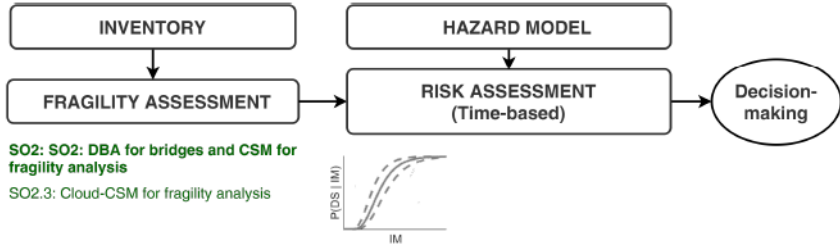


Figure 5.1: Objective of this Chapter (SO2.3) and framing in the flowchart for seismic risk calculation.

5.1. Introduction and motivation

In seismic vulnerability modelling and probabilistic risk assessment applications, fragility relationships for a considered structure or structural type report the probability of violating a damage state (DS) given a value of the earthquake ground-shaking intensity. Numerical (or analytical) methodologies to derive fragility relationships are currently widespread and preferred to empirical approaches because of the scarcity of post-earthquake damage data for various earthquake-prone regions. Such numerical approaches generally are based on a probabilistic seismic demand model (PSDM) calibrated on a dataset of engineering demand parameter (EDP) vs earthquake-induced shaking intensity measure (IM) pairs. Various EDPs of interest can be calculated via refined nonlinear dynamic or simplified nonlinear static analysis methodologies. Nonlinear dynamic approaches enable the prediction of structure- or structural component-specific EDPs for an appropriately selected (and eventually modified) suite of ground-motion records through nonlinear time history analyses (NLTHA) of a numerical structural model. Contrarily, nonlinear static procedures (NSPs) analyse the structural capacity of an equivalent single-degree-of-freedom (SDoF) system of a structure case-study under incremental load patterns, enabling the prediction of the seismic performance (in terms of EDPs) through demand-spectrum-based approaches. The former approach is the most advanced/accurate but generally requires high modelling efforts, apart from

being more computational-demanding than NSPs. The latter approach is simpler, but it generally results in biased EDP estimates due to the various assumptions in the method, such as the selection of an appropriate load pattern representative of the effects of a dynamic excitation or the definition of an equivalent SDoF system (Silva et al. 2014). The analysis approaches used in Chapter 3 and 4 belong to this second category.

Dealing with regional-scale applications (e.g. evaluating the seismic performance or the risk of bridge portfolios in a network), an analyst should find a trade-off between computational efforts and assessment accuracy, for instance concerning the adopted number of archetype structures to represent structural class and the considered seismic analysis approach Silva et al. (2019). For example, depending on the availability of computational and modelling time and skills, an analyst may consider a large population of structures analysed through NSPs, trying to capture the class variability (Gentile & Galasso 2020); or 2) few archetype structures to be analysed via nonlinear dynamic procedures.

NSPs involve approximate approaches for the nonlinear performance displacement prediction of SDoF systems and can be divided into two groups. The first includes methods which estimate the inelastic demand by modifying the displacement demand of an equivalent secant-to-yielding-period linear system. As an example, the N2 method (Fajfar & Gašperšič 1996, Fajfar 1999) uses an elastic-perfectly plastic SDoF transformation of refined pushover curves (in terms of global base shear and displacement of a control node) which is consequently used to calculate the nonlinear equivalent SDoF performance displacement. In the N2 original version, the nonlinear performance displacement is calculated via NLTHA of the equivalent SDoF. Currently, a code-based simplified approach (Eurocode 8 part 3 CEN (2005)) adopts a simplified strategy using ductility-based modification factors and demand-spectra.

The second group refers to methods that calculate the performance displacement of nonlinear systems as the over-damped response of elastic SDoF systems having secant-to-target-displacement stiffness. The Capacity Spectrum Method (CSM) Freeman (1998a), which is applied in this dissertation, belongs to this category. It was implemented in different guidelines (e.g. ATC (1996), Federal Emergency Management Agency (FEMA) (2012)). It is conceptually based on overdamped spectra calculated through equivalent

viscous damping coefficients expressing the reduction of seismic demands caused by the inelastic response of the structure under investigation. Starting from a bilinear idealisation of pushover curves, aimed at identifying a global yielding displacement, the CSM involves an iterative procedure to identify a performance point (PP) corresponding to the equivalent SDoF target displacement of the structure.

Several studies carried out in the last decades proposed formulations which can improve the estimation of equivalent SDoF target displacement within both the categories (e.g. Ruiz-García & Miranda (2003), Lin & Chang (2003), Ruiz-García & Miranda (2007), Lin & Miranda (2008)).

According to Silva et al. (2019), NSPs usually do not account for record-to-record variability since the seismic demand is represented by conventional smooth code-based design spectra. This approach is, indeed, used in Chapter 3 and 4. In this way, only a central value of the fragility relationship can be estimated (e.g., the IM associated to a 50% probability of reaching/exceeding a DS of interest, if a lognormal model is used). In this case, conventional values of variance, calibrated for different structural types, can be usually introduced for describing the lognormal probabilistic model (Silva et al. 2019).

Hybrid methodologies based on pushover analysis of MDoF systems together with NLTHA performed on sets of equivalent SDoF systems were recently proposed (Dolšek 2012, Rossetto et al. 2016). Vamvatsikos & Cornell (2006) proposed a semi-empirical analytical approach for approximating (16%, 50% and 84% fractiles of) incremental dynamic analysis curves based on multi-linear backbones of equivalent SDoF systems. This study is aimed at analysing the use of NSPs and, particularly the CSM, with real (i.e. unsmoothed, record-specific) response spectra for estimating record-to-record variability in fragility analysis explicitly. To the authors' knowledge, only a few studies in the literature analysed the application of NSPs with real response spectra to predict non-linear seismic performance. In the Global Earthquake Model guidelines D'Ayala et al. (2013), an approach to derive a PSDM using the N2 method is described for fragility analysis of low/mid-rise buildings. Silva et al. (2014) investigated the effectiveness of several NSPs applied with real response spectra for fragility analysis and risk/loss estimations for a class of typical Turkish RC-framed buildings. A stripe-based approach is

used in Gentile, Galasso & Pampanin (2020) for estimating fragility relationships via the CSM for existing reinforced concrete (RC) frames. No literature study on this topic refers to bridges. Although this dissertation specifically focuses on the seismic response of bridges, this Chapter focuses on simple inelastic SDoF systems representative of various structural types (including bridges). This study is considered the basis for more elaborated algorithms for bridge application, which are illustrated in the following Chapter 6. A database of 2160 case-study systems defined through parametric multi-linear backbones and several hysteresis rules is defined. Also, a suite of 100 ground motions selected from the Selected Input Motions for displacement Based Assessment and Design (SIMBAD) database (Smerzini et al. 2014) is adopted.

Findings from this study can also directly support fragility analysis applications where the SDoF idealisation (in secant-to-yielding or target displacement state) of the analysed structures is performed such as the displacement-based approaches illustrated in Chapter 3 and 4.

In the first part of this study, the effectiveness and shortcomings of the CSM applied with real spectra is discussed. An algorithm to effectively adapt the CSM for application with specific-record spectra is described. Different strategies to select the PP in multiple-solution cases are proposed, based on simplistic assumptions or efficient IM parameters. These are identified via an optimal IM analysis. Moreover, a cloud-based approach to compute PSDMs via the CSM (and other NSPs) is described. In the second part of this study, the effectiveness of the afore mentioned strategies is discussed with reference to both single ground-motion record and fragility analysis. In the final part, the accuracy of the Cloud Capacity Spectrum Method (Cloud-CSM) for fragility analysis is investigated. To this aim, the main parameters of the fragility curves calculated by means of the Cloud-CSM are compared to the results related to the N2 method applied with real spectra, a simple method involving an intensity measure as a direct proxy for the performance displacement, and NLTHA.

5.2. Methodology

In this section, the case-study database of inelastic SDoF systems and the ground-motion suite is described. Also, the proposed CSM algorithm suitable for the use with

real spectra is presented. Moreover, to select the PP when multiple CSM solutions are retrieved, different strategies are defined. The strategies are based on both simplistic assumptions and on a particularly efficient IM parameter which is identified via an optimal IM analysis. Also, other NSP-based methodologies used for benchmarking the Cloud-CSM are described. Finally, an overview of the cloud-based methodology to perform fragility analysis through NSPs is illustrated.

5.2.1. Considered SDoF case-study database and seismic action

The database of case-study includes simple inelastic SDoF oscillators with different non-linear (monotonic and cyclic) behaviour, represented by a multi-linear backbone curve (in pseudo acceleration-displacement format) and several hysteresis rule. The adopted hysteresis rules are selected with the aim to simulate the seismic response of different structural types. Two different types of Modified Takeda hysteresis rules (Priestley et al. 2007, Otani 1974) are used (Figure 5.2a). The “thin” version (hereafter MTt) is appropriate for the cyclic behaviour of structures subjected to high axial stress (such as bridge piers, structural walls, or masonry structures), while the “fat” type (hereafter MTf) is used in the case of ductile RC frames (Priestley et al. 2007). Particularly, the MTt is adopted in Chapter 3 and 6 to simulating the cyclic response of RC single-column piers.

Moreover, a bilinear (BIL) and an elastic-perfectly-plastic (EPP) hysteresis laws (Figure 5.2b) are used to represent the cyclic flexural response of steel structures (neglecting the Bauschinger effect in the members) or seismic isolated structures (such as elastomeric bearings or friction pendulum systems). As an example, an EPP hysteresis rule is, indeed, adopted in the following Chapter 6 for the cyclic response of old neoprene bearings.

A flag-shaped (FS) law is adopted (Figure 5.2c), for the cyclic behaviour of hybrid prestressed structures. The parameters defining the backbones are listed in Figure 5.2 and are the elastic period T_{el} (related to the secant-to-yielding stiffness K_{el}), the base shear coefficient F_y (yield base shear strength normalised by the total weight), the ductility at peak strength μ , the hardening ratio r and the normalised residual strength F_r . The assumed values related to each varying parameter are listed in Table 5.1. Note that the

softening and residual strength branches are not considered within the FS subgroup since no strength degradation may be considered for low-damage structures. In this case, μ is only used to define the DS thresholds. In the case of BIL, EPP and FS no cyclic stiffness degradation is adopted (kinematic hardening behaviour). In summary, 720 (i.e., eight values of T_{el} \times five of F_y \times three of μ \times three of r \times two F_r) oscillators are associated to the MTt, MTf; 240 correspond to the BIL subgroup (where $r = 10\%$) and for the EPP (where $r = 0\%$ by definition); a total of 240 oscillators are associated to the FS subgroup.

The 2160 SDoF oscillators are subjected to a suite of 100 unscaled ground motions selected from the SIMBAD database. This latter includes 467 tri-directional records related to 130 worldwide seismic events (shallow crustal earthquakes) with moment magnitudes between 5 to 7.3 and epicentral distance lower than 35 km. In this study, 100 records are selected by first ranking the 467 records in terms of their PGA values (by using the geometric mean of the two horizontal components) and then keeping the component with the largest PGA value. This record selection strategy is compatible with the adopted cloud-based approach for fragility analysis. This latter approach is suitable when a large number of structures is analysed since it does not require a hazard-specific record selection. Clearly, the lack of specific record selection considering the hazard of the site can create a bias in the analysis results, which, however, may be mitigated after running the response analysis (Haselton et al. 2011). The peak ground accelerations of the selected ground-motion records range between 0.29g and 1.77g.

In summary, a total of 216000 NLTHA (100 records \times 2160 SDoF systems) is performed using the nonlinear finite element software RUAUMOKO3D (Carr 2016) using nonlinear spring models equipped with appropriate multi-linear backbones and cyclic behaviour. As suggested by Priestley et al. (2007), a constant 5% tangent stiffness proportional damping is selected for all the frequencies.

5.2.2. Proposed CSM algorithm for real spectrum application

The CSM aims to identify the performance of a structure under a given seismic input represented by a response spectrum. (ATC 1996) originally proposed three different CSM methodologies (A, B and C). The procedure A is considered the most convenient

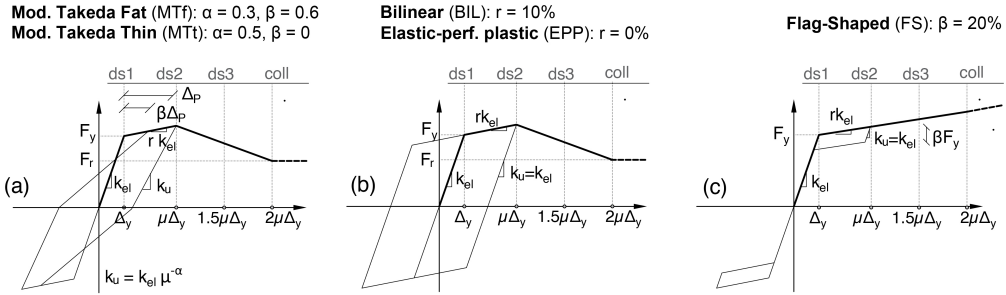


Figure 5.2: Parametric backbones and selected hysteresis rules

Table 5.1: Values adopted for each backbone parameters

	MTt	MTf	BIL	EPP	FS
T_{el}		0.25-0.5-0.75-1.00-1.25-1.50-1.75-2.00 s			
F_y			0.1-0.2-0.3-0.4-0.5		
μ			1.5-3.0-4.5		
F_r		$0.6F_y-0.3F_y$			No softening
r	0-5-10%		10%	0%	0-5-10%

for simple spreadsheet/programming routine implementation and it is outlined in this section. The CSM requires the computation of a force vs displacement relationship (i.e. pushover curve) for the investigated structure subjected to a monotonic load profile simulating the effect of a dynamic excitation (i.e. pushover analysis). The pushover curve is converted into a “capacity spectrum” related to an equivalent SDOF system of the structure, expressed in an acceleration vs displacement format. The CSM involves an iterative graphical procedure aimed to determine the PP in an acceleration-displacement plane through the use of overdamped spectra. First, a tentative performance displacement is assumed and a bilinearisation of the capacity spectrum up to the tentative performance displacement is carried out. The equivalent yielding displacement is thus obtained and the ductility demand corresponding to the tentative performance displacement is calculated by simply dividing the target displacement for the yielding one. At this stage, the overdamped demand corresponding to the tentative performance displacement is computed by multiplying the elastic (5%-damping) demand spectrum ordinates (conventionally a code-based smooth spectrum is used) for a spectral reduction factor (η).

This latter is derived from a ductility-based equivalent viscous damping coefficient (ξ) which expresses the reduction of the elastic demand given the hysteretic dissipation. A new target performance displacement is identified at the intersection between the overdamped demand and capacity spectra. If the calculated performance displacement is sufficiently close to the initial guess (within an arbitrary tolerance assumed by the analyst), the algorithm is completed and the PP is identified. The PP expresses the compatibility between the damping associated to both the overdamped demand and the ductility demand of the structure. Otherwise, the newly calculated performance displacement is used as the new tentative target one, and another iteration is carried out. The process continues until the convergence is achieved.

In this study, the CSM algorithm is slightly modified for the use with real demand spectra. Note that multiple solutions could be obtained when using real spectra (Federal Emergency Management Agency (FEMA) 2012, Casarotti & Pinho 2007, Chopra & Goel 1999). Obviously, multiple solutions have not a physical meaning since the PP represents the response of the structure under a given earthquake-induced shaking. Thus, to adapt the CSM for the use with real spectra, a final additional step to select the PP, in case of multiple solutions. Note that such an iterative process could be unstable in case of multiple solutions (Chopra & Goel 1999). Consequently, an alternative algorithm is herein proposed to easily identify the candidate solution(s). It is graphically represented in Figure 5.3. It is worth mentioning that other non-iterative approaches for performing the CSM were proposed. As an example, the algorithm proposed by Lin & Miranda (2008) is based on a direct closed-form estimation of the secant-to-target period, which avoids multiple-solution. The secant-to-target-period depends on the strength ratio between an equivalent elastic response and the actual one. However, this approach is developed for EPP hysteretic response only and, to the authors' best knowledge, have not been tested for other hysteresis rules, which are deemed to influence the intensity of the period elongation and consequently affect the accuracy of the approach.

In the proposed algorithm, a preliminary task is the identification of the yielding point of the capacity spectrum of the structure by means of an equivalent bilinear or multi-linear relationship. De Luca et al. (2013) provide recommendations to perform the bi- or multi-linearisation. Obviously, if the 5%-damping spectrum intersects the elastic

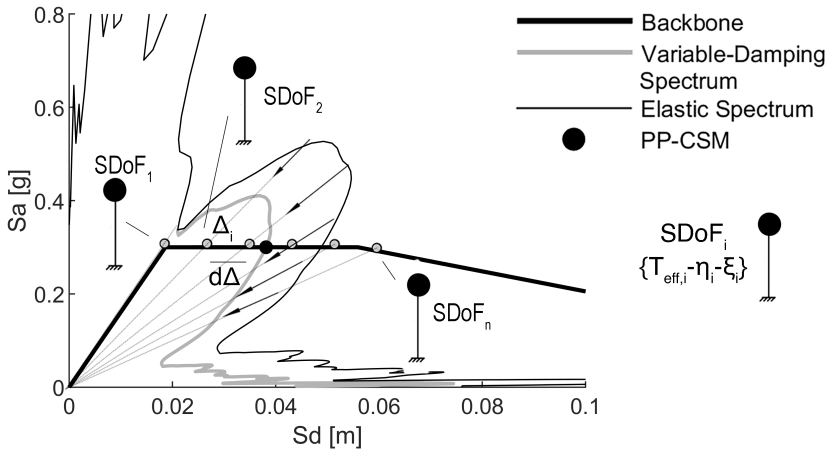


Figure 5.3: Graphical representation of the proposed CSM algorithm

branch of the capacity spectrum, an elastic response of the SDoF system is registered, and the PP can be straightforwardly identified. If no elastic solutions are detected, the capacity spectrum is discretized in displacement intervals Δ_i of small amplitude $d\Delta$ from the yielding point to the ultimate displacement capacity. Each Δ_i corresponds to a different damping level (ξ_i). The amplitude of $d\Delta$ is arbitrarily selected by the analyst and corresponds to the accuracy of the final result (in this study $d\Delta = 0.001m$). An equivalent elastic SDoF oscillator can be associated with each Δ_i , characterised by an effective period ($T_{eff,i}$), an equivalent viscous damping (ξ_i) and a spectral reduction factor (η_i). $T_{eff,i}$ is calculated via Equation 5.1 where μ_i is the ductility demand at Δ_i . There is an extended research literature on the approaches for the calculation of ξ and η , adapted for various specific structural typologies (Ceballos C & Sullivan 2012, Khan et al. 2016, Pennucci et al. 2011). In this study, the approach proposed by Priestley et al. (2007) is used, which is suitable for displacement-based design and is based on simple ductility-based formulations calibrated for different hysteretic behaviour (Equations 5.2 and 5.3). The adopted coefficients C_{evd} vary depending on the considered hysteresis rule and are reported in Table 5.2.

For each i – th equivalent SDoF system, the acceleration-displacement components of the elastic demand at the corresponding effective period $T_{eff,i}$ are retrieved by linear in-

terpolation and are multiplied by η_i , generating the overdamped demand at $T_{eff,i}$. Thus, a “variable-damping spectra” is obtained by collecting the acceleration-displacement pairs of the overdamped demand calculated for each value of $T_{eff,i}$ and η_i . The CSM solution(s) are the intersections between the capacity spectrum and the variable-damping spectra. If no intersections are found, the structure is unable to sustain the applied seismic input. Figure 5.4 presents three sample ground motions selected for illustrative purposes. The ground-motion records #3 and #6 produce one solution (elastic and inelastic, respectively), while the record #10 leads to multiple solutions.

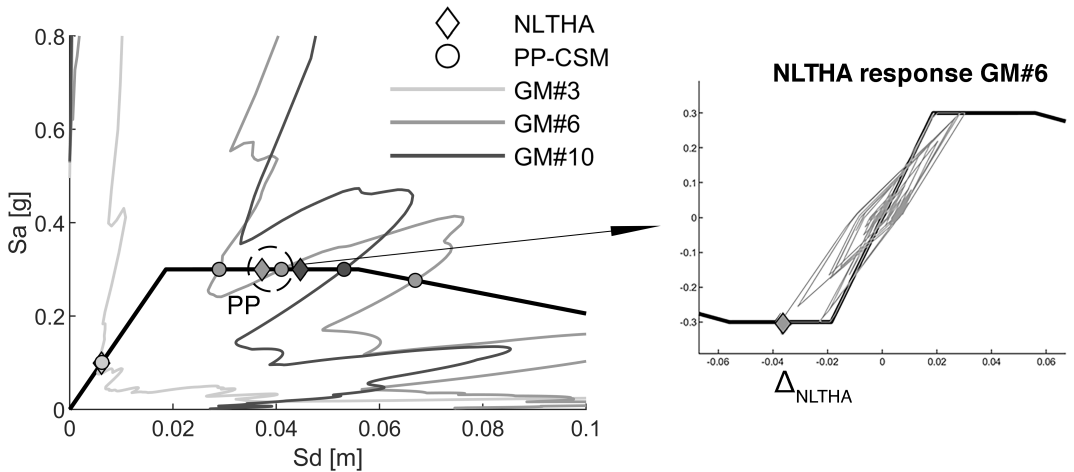


Figure 5.4: Graphical representation of single- and multiple-solution cases

$$T_{eff,i} = \sqrt{\frac{\mu_i}{1 + r(\mu_i - 1)}} \tag{5.1}$$

$$\xi_i = 0.05 + C_{evd} \frac{\mu_i - 1}{\pi \mu_i} \tag{5.2}$$

$$\eta_i = \sqrt{\frac{7}{2 + \xi_i}} \tag{5.3}$$

Table 5.2: Values of C_{evd} related to adopted hysteresis rules

	MTt	MTf	BIL	EPP	FS
C_{evd}	0.444	0.565	0.519	0.670	0.186

5.2.3. Optimal IM analysis for PP selection

The efficiency of an IM parameters is related to its relevance for indicating damage potentials and it is measured by the correlation to the EDPs of interest (such as the ductility demand or target displacement). The optimal IM analysis performed in this subsection discusses the efficiency of different IM parameters. The efficient IM(s) are used to define strategies for selecting the PP in multiple-solutions CSM cases. Only spectral shape-dependent IMs, that can be easily extracted by the response spectrum within the CSM algorithm, are considered. Integral IM (e.g. duration-based) are neglected since can not be used in the CSM process.

The candidate IMs are listed as follows. The first is the spectral displacement at the elastic period, $Sd(T_{el})$. The second candidate IM is the displacement demand at corner period ($Sd(T_D)$), corresponding to 90% of the maximum displacement demand, according to Calvi et al. (2018). It is well-recognized in the literature that efficient spectral shape-based IMs should consider the spectral demand in the period elongation range, when an inelastic response is required. According to this statement, the third IM is a displacement-based version of the IM proposed by Cordova et al. (2001) (Sd^C), calculated via Equation 5.4 which considers the ratio of the spectral demands calculated at the elongated (cT_{el}) and at the elastic periods. Cordova et al. (2001) recommend a value of $c = 2$. Recent studies (Minas & Galasso 2019, Kohrangi et al. 2016) investigated the efficiency of IMs based on the geometric average of the spectral accelerations over an appropriate range of periods (usually named $AvgSa$). In this study, since the displacements are of interest, an IM based on the geometric average of the spectral displacements is added in the candidate IM dataset. This latter is calculated via Equation 5.5) by defining appropriate value of period elongation kT_{el} . Values of period lower than T_{el} which are associated with higher modes in dynamic response of MDoF structures, are not considered in Equation 5.5, since this study focuses on SDoF systems. Katsanos & Sextos (2015) analyse the period elongation of SDoF systems and evidence

that kT_{el} ranges from 120% to 250% of T_{el} , being strongly affected by the ratio between the yielding displacement with respect to the elastic displacement demand at the first period. Therefore, two versions of $AvgSd$ are considered, setting k equal to 1.5 and 2 (respectively indicated as $AvgSd_{1.5}$ and $AvgSd_2$ hereafter). Finally, another version of $AvgSd$ is proposed ($AvgSd_k$), defining a more advanced strategy for period elongation. The range of significant periods affecting the inelastic response is defined on a specific-record basis and is related to a proxy of the likely ductility demand expressed in Equation 5.6 (Mehanny 2009). Ten equally spaced periods are used to compute $AvgSd$ Minas & Galasso (2019).

$$Sd^c = Sd(T_{el}) \sqrt{\frac{Sd(cT_{el})}{Sd(T_{el})}} \quad (5.4)$$

$$AvgSd(T_{el} - kT_{el}) = \left(\prod_{i=1}^N Sd(T_i) \right)^{\frac{1}{N}} \quad \text{with} \quad T_i \in [T_{el}; kT_{el}] \quad (5.5)$$

$$k = \sqrt{\frac{Sd(T_{el})}{\Delta_y}} \quad (5.6)$$

The optimal IM analysis is performed with reference to the results of NLTHA which leads to an inelastic response. Indeed, in case of an elastic response, no multiple solutions can be retrieved via the CSM, and the displacement demand and $Sd(T_{el})$ coincides as shown in Figure 5.4.

Considering the NLTHA maximum displacement of the SDOF system, a power-law model ($EDP = aIM^b$) is fitted to the “cloud data” in the transformed $\log IM - \log EDP$ plane (Jalayer et al. 2017). The parameters a and b are estimated through regression analysis resorting to the least square method. As confirmed by Minas & Galasso (2019), an inverse proportionality relationship exists between the efficiency of the IM and the standard deviation (σ) of the observed $edp_{gm} - im_{gm}$ pairs in their transformed state with respect to the linear statistical model. This logarithmic standard deviation (or dis-

person) is quantified via Equation 5.7 where N is the number of ground motions.

$$\sigma = \sqrt{\frac{\sum_{gm=1}^N (\ln edp_{gm} - \ln a \cdot im_{gm}^b)^2}{N - 2}} \quad (5.7)$$

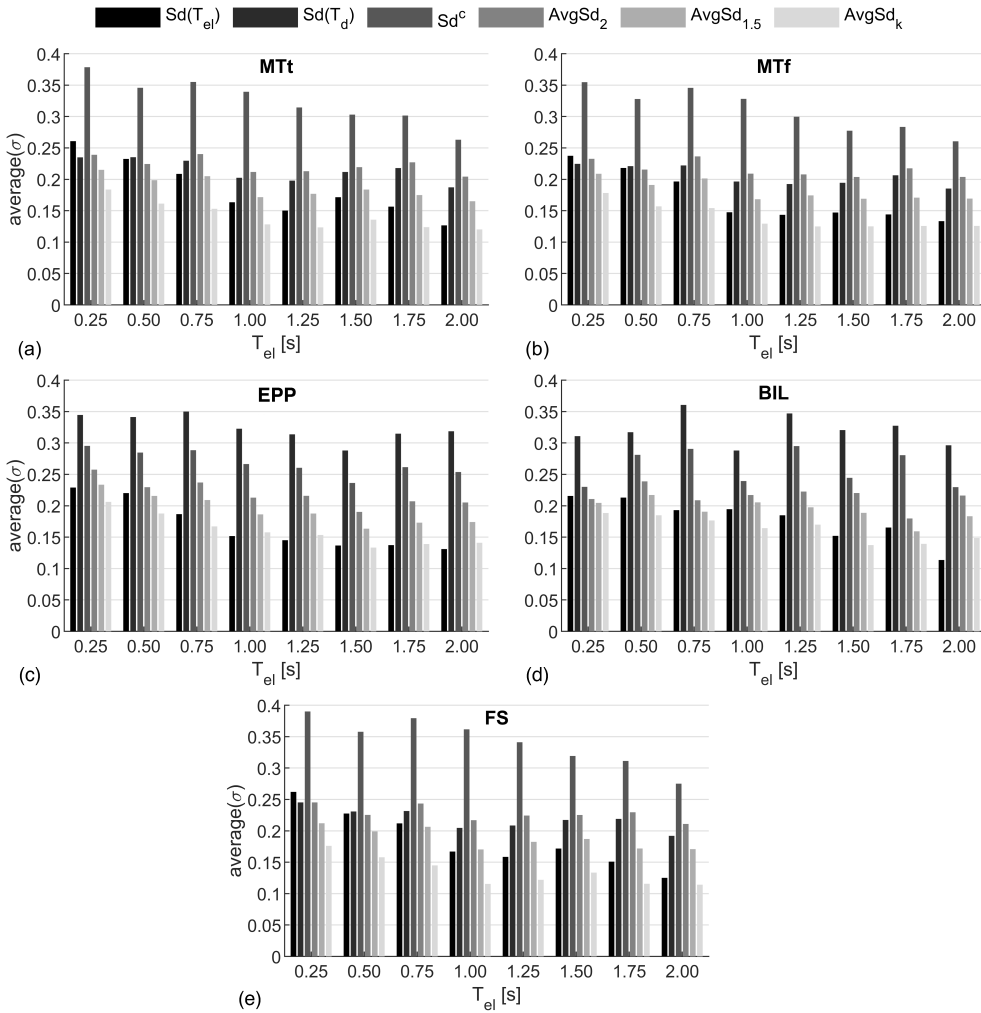


Figure 5.5: Results of the optimal IM analysis

To systematically analyse the results, all the SDoF systems are grouped by T_{el} and hysteretic behaviour; the average value of σ is estimated for each subgroup and for each

candidate IM. Figure 5.5 shows the results for all the hysteresis subgroups. $Sd(T_d)$ is the least efficient IM being totally independent of structure-specific dynamic features. $Sd(T_{el})$ is a particularly efficient for high-period oscillators that exhibit a low nonlinear demand such as high-period cases. $AvgSd_{1.5}$ provides a low average(σ) for low-period SDoF systems, where a strong inelastic demand is usually registered and the influence of the spectral shape in the period elongation range is significant. Noticeably, $AvgSd_{1.5}$ outperforms $AvgSd_2$ proving that $k = 1.5$ is likely a better choice than $k = 2$ with reference to the average features of these case studies. Sd^c provides comparable efficiency to the results of $AvgSd_2$. The most efficient IM is $AvgSd_k$ which exhibits the lowest average(σ) for all the considered subgroups. This advanced IM adapts the period elongation range depending on the spectral shape joining the advantages of $AvgSd$ and $Sd(T_{el})$. The comparison between the several adopted hysteresis rules in Figure 5.5 evidences that these results are weakly affected by the cyclic dissipation. Further analyses could be carried out to appropriately calibrate the discretisation of the period range in which $AvgSd$ is calculated (Minas & Galasso 2019, Kazantzi & Vamvatsikos 2015) or the c parameter for Sd^c , possibly with reference to a narrower subgrouping of the case-study dataset (e.g., grouped using the base shear coefficient). However, this task is deemed not consistent with the purposes of this study.

5.2.4. Candidate strategies for PP selection

Six candidate strategies are defined to select the PP handling multiple-solution cases. To this purpose, it is assumed that these strategies should be simple enough to enable a fast, possibly automatized, selection of the PP within a fragility analysis framework dealing with a high number of ground motions.

- The first strategy (S1) is the most refined one. A preliminary regression analysis is performed to provide a simple relation between the NLTHA-based ductility demand, μ_{TH} and two predictors linked to both the ground-motion spectrum and the SDoF backbone parameters. These are the ratio between $AvgSd_k$ and the yielding displacement of the specific SDoF, Δ_y , and the elastic period T_{el} . The pairs of ground motion-SDoF system characterised by inelastic demand are used

to perform the nonlinear regression according to the power model proposed in Equation 5.8 via the least square method. The values of the parameters [a,b,c,d], calculated for the different hysteresis subgroups, together with the corresponding coefficient of determination R^2 are presented in Table 5.3. According to this strategy, the PP is the CSM solution whose ductility demand best agrees with the results of the proposed regression model.

$$\mu_{TH} = (aT_{el} + b) \cdot \left(\frac{AvgSd_k}{\Delta_y} \right)^{cT_{el}+d} \tag{5.8}$$

- The second strategy (S2) assumes that, for a specific ground motion, the PP is the solution that minimizes $|AvgSd_k - \Delta_{PP}|$.
- The third (S3) and fourth (S4) strategies assume that the first and the last solutions, respectively, on the backbones are the PP. These strategies are proposed to evaluate if it is worth performing a more accurate selection according to S1 and S2.
- The last strategy (S5) foresees that the record-specific displacement performance can be approximated by the arithmetic average of the displacements provided by the various solutions.

Table 5.3: Parameters for the power model in Equation 5.8 depending on the hysteresis rule

	MTt	MTf	BIL	EPP	FS
<i>a</i>	-0.03	-0.028	-0.021	-0.036	-0.055
<i>b</i>	1.059	1.033	1.098	1.082	1.095
<i>c</i>	0.023	0.034	0.017	0.017	0.056
<i>d</i>	0.86	0.831	0.876	0.751	0.685
R^2	0.8156	0.8275	0.8643	0.7487	0.8008

5.2.5. N2 method for application with real spectra and proposed IM-based approach

In this Chapter, other NSPs are introduced to discuss the effectiveness of the CSM. The first is the widespread code-based version of the N2 method as included in Eurocode

8 part 3 (CEN 2005) and modified in D'Ayala et al. (2013) for its application with real spectra to compute fragility functions. The N2 method is a pushover-based methodology like the CSM. It is based on capacity spectra and, differently from the CSM, exploits displacement modification factors for approximating the inelastic SDOF displacement, corresponding to the PP on the capacity spectrum.

Within the N2 method, the capacity spectrum is simplified in an elastic-perfectly plastic law to determine T_{el} and Δ_y of the investigated structure. The PP is estimated depending on the relation between the T_{el} and the corner period of the adopted elastic (usually code-based) spectrum (T_c) which is the period at the end of the constant-acceleration part. If T_{el} is higher than T_c , the equal-displacement rule is applied, and the target displacement (Δ_{PP}) is equal to the spectral displacement at the elastic period $Sd(T_{el})$. On the other hand, if T_{el} is lower T_c , two conditions may occur. If the spectral acceleration is lower than the yielding acceleration capacity of the system, an elastic response is expected, and the $Sd(T_{el})$ equals the Δ_{PP} , again. In contrast, the formulation by Vidic et al. (1994) is applied, and the target displacement is calculated with Equation 5.9 where q_u is the ratio between the spectral acceleration at the elastic period and the yielding acceleration. Note that k of Equation 5.6 is a displacement-based version of q_u .

$$\Delta_{PP} = \frac{Sd(T_{el})}{q_u} \left(1 + (q_u - 1) \frac{T_c}{T_{el}} \right) \geq Sd(T_{el}) \quad (5.9)$$

This methodology is usually applied with smooth code-based spectra, where the interval of periods related to the constant acceleration section of the spectrum, from T_b to T_c (which are the upper and lower limits of the constant acceleration part), is known. Since this interval is not defined for real unsmoothed spectra, the strategy proposed by Calvi et al. (2018) for the calculation of T_c of real spectra is adopted. T_c can be identified in the spectral acceleration vs period plane, at the intersection between an horizontal line at 90% of the maximum spectral acceleration and the response spectrum ordinates. If more than one intersection occurs, the lowest period should be chosen. It is worth mentioning that, in this study, the simplified code-based N2 method is applied to calculate the performance of multi-linear SDOF systems in which the elastic branch is known.

Therefore, the MDoF-SDoF conversion strategy is not applied and the bilinearisation is directly carried out neglecting the hardening and the softening.

Finally, to further benchmark the CSM, another NSP-based methodology is proposed. This approach is identified herein as IM-based method. It is used to select the performance displacement dealing with record-specific spectra and it is based on the results of the optimal IM analysis. It foresees that the performance displacement of an SDof system under a given ground-motion input is simply equal to the value of $AvgSd_k$ calculated through Equation 5.5 and 5.6. This approach requires the knowledge of the T_{el} and the k -factor calculated with Equation 5.6.

It is worth noting that both the N2 and IM-based methods are less computational-demanding than the CSM. The comparison among these methodologies is aimed at evaluating whether it is worth performing a more accurate and computationally demanding CSM algorithm.

5.2.6. Cloud-based approach for fragility analysis

A cloud of EDP vs IM points is obtained for each specific SDof system using NLTHA, the CSM, the N2 method and the proposed IM-based approach for performance displacement prediction. The adopted reference IM for fragility analysis is the geometric average of the spectral accelerations $AvgSa$, whose efficiency is previously discussed in subsection 5.2.3 for the case-study database. Also, desirable IM properties such as efficiency, sufficiency and hazard computability of $AvgSa$ are extensively evaluated in recent literature studies for fragility analysis of various structural types. Given the optimal IM analysis, $AvgSa$ is computed in the interval between T_{el} and $1.5T_{el}$ and it can be calculated via Equation 5.5, by replacing $Sd(T_i)$ with $Sa(T_i)$ and $k = 1.5$.

Three ductility-based DS thresholds (indicated in Figure 5.2) are defined, corresponding to the yielding point ($\mu_{ds1} = 1$), the peak strength point ($\mu_{ds2} = \mu$) and at the middle of the softening branch ($\mu_{ds3} = 1.5\mu$).

The cloud data are initially divided into “collapse” and “no-collapse” categories. Collapse herein corresponds to a global dynamic instability within NLTHA or at the exceedance of a conventional displacement threshold for the NSPs. This latter threshold

is equal to the reaching of the residual strength branch ($\mu_{collapse} = 2\mu$).

$$\begin{aligned}
 P(EDP \geq edp_{ds}|IM) &= P(EDP \geq edp_{ds}|IM, NoC)(1 - P(C|IM)) + \\
 &P(EDP \geq edp_{ds}|IM, C)P(C|IM) = \\
 &(1 - \phi\left(\frac{\ln edp_{ds} - \ln aim^b}{\sigma_{NoC}}\right))(1 - P(C|IM)) + P(C|IM)
 \end{aligned} \tag{5.10}$$

Equation 5.10 shows the generic analytical form used in this study for a given fragility relationship, where the probability of violating a given DS threshold, $P(EDP \geq edp_{ds}|IM)$, is calculated by applying the total probability theorem. This equation aggregates the probability of reaching or exceeding the DS for the non-collapse cases, $P(EDP \geq edp_{ds}|IM, NoC)$, and the probability that the collapse occurs, $P(C|IM)$ (Jalayer et al. 2017).

Note that since all the collapse cases certainly exceed the DS threshold, $P(EDP \geq edp_{DS}|IM, C)$ is equal to 1. The fragility model related to the non-collapse cases only is expressed by the normal cumulative distribution function $\phi(\cdot)$ based on the power model-based PSDM for non-collapse cases. The coefficients a , b and the dispersion σ are calculated as described in subsection 5.2.3. A logistic regression model is fitted to "no collapse-collapse" data to calculate the $P(C|IM)$. The PSDM represents the median EDP (having the 50% probability of being reached, edp^{50}) given IM and it can be calculated with Equation 5.11.

$$edp^{50} = a \cdot im^b \exp\left(\sigma_{NoC} \left[\frac{0.5}{1 - P(C|IM)}\right]\right) \tag{5.11}$$

For analysing the results, $P(EDP \geq edp_{ds}|IM)$ is approximated with a lognormal cumulative distribution function, whose median (α) and dispersion (β) are adopted for comparing the large number of SDoF fragility curves calculated for all the SDoF dataset (four ds x 2160 SDoF systems).

α represents the value of IM corresponding to a 50% probability to be reached or exceeded of a given edp_{ds} and it is calculated via Equation 5.10 by setting $P(EDP \geq$

$edp_{ds}|IM)$ equal to 0.5. β expresses the “slope” of the fragility curve and is approximated as half of the difference between the logarithmic values of IM corresponding to the 84% and 16% exceedance probability ($P(EDP \geq edp_{ds}|IM)$ equal to 0.84 and 0.16).

5.3. Discussion on selection strategies for multiple CSM solutions

This Section discusses how to handle multiple CSM solution. The effectiveness of the previously described strategies to identify the PP is assessed. Therefore, the influence of the percentage of multiple-solution cases detected within the NLTHA database for a given case-study on the fragility analysis is evaluated.

5.3.1. Effectiveness of the proposed strategies for PP selection

In this section, only the combinations of SDoF oscillator-record for which multiple CSM solutions are detected are considered. In these cases, the PP is selected considering the various strategies (from S1 to S5). The accuracy of the single strategy is assessed comparing the chosen PP with a benchmark strategy, named S0, that implies the manual selection of the PP, which best mimics the NLTHA result. This is assumed as the theoretically best solution (benchmark PP). Note that the cases in which the benchmark PP is a collapse case are excluded. Moreover, the cases characterised by multiple solutions, which are all detected beyond the collapse threshold are excluded and directly considered as collapse cases (rather than multiple solution cases).

A preliminary discussion about the influence of significant backbone parameters and expected equivalent viscous damping on the occurrence of multiple solutions is needed to understand the following outcomes.

Figure 5.6 relates the percentage of multiple-solution cases (calculated as the number of SDoF-record pairs producing multiple solutions divided by the total number of the corresponding subgroup) varying T_{el} , μ and F_y for the considered hysteresis subgroups (representative of high- and low-dissipation). The results of Figure 5.6 are related to the oscillators having F_r and r equal to and $0.6F_y$ and 0% respectively (selected for illustrative purposes). It is worth mentioning that the outcomes shown in Figure 5.6 could be influenced to the amplitude and frequency content of the specific ground motions

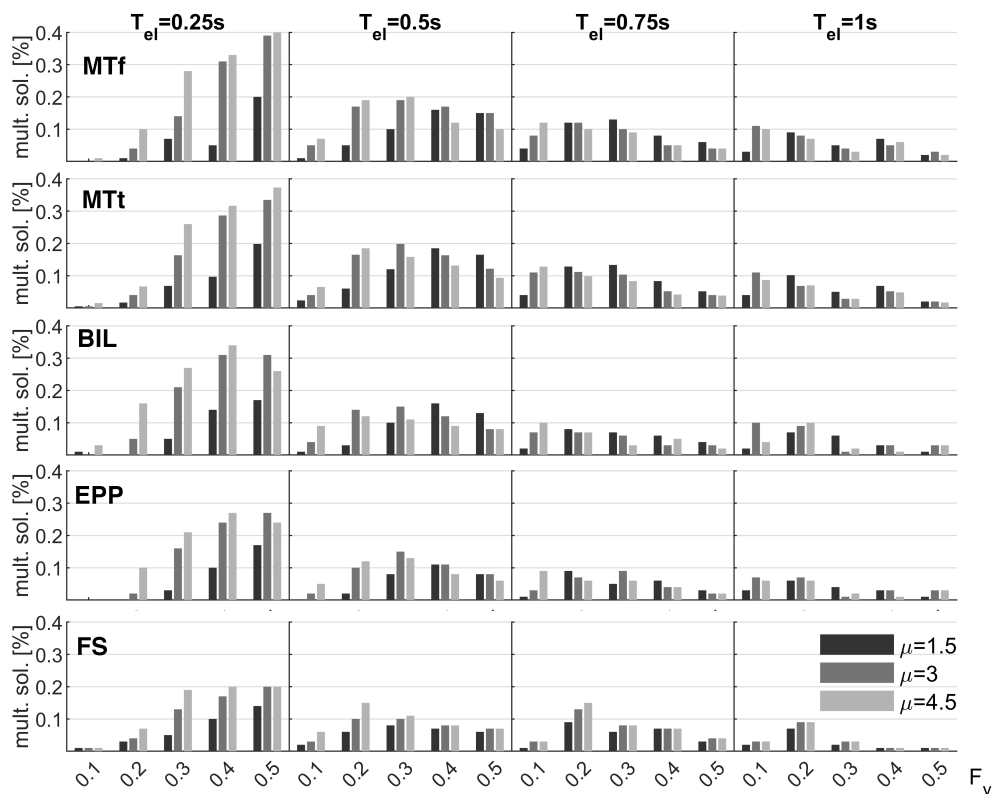


Figure 5.6: Percentage of multiple-solution cases on varying significant backbone parameters for the adopted hysteresis rule subgroups ($F_r = 0.6F_y$ and $r = 0\%$).

adopted in this study. Thus, these could not be valid for other studies if other ground motion suites are adopted.

It is evident that the number of multiple solutions decreases as the elastic period increases. This outcome is influenced by the higher number of elastic responses detected for increasing periods. The cases having T_{el} higher than 1.00 s are not considered in the figure since they exhibit a negligible number of multiple solutions (less than 5%). It is shown that the 0.25 s-period cases exhibit the highest percentage of multiple solutions. This percentage increases as F_y and μ increase, with a maximum of 39% for F_y equal to 0.5 and μ of 4.5 for MTf. For the FS, the number of multiple-solution cases strongly decreases within the $T_{el} = 0.25s$ subgroup, with a maximum of 15% for the case with F_y equal to 0.5 and $\mu = 3$. In this case, the number of intersections between the

variable-damping spectra and the backbone decreases. This may be caused by the low cyclic dissipation capacity and the absence of the softening branch which induce a low number of intersections between the capacity and demand spectra. For the $T_{el} = 0.50s$ subgroup the maximum is 20% for the case MTt with $F_y = 0.3$ and $\mu = 2$. For the groups having 0.75 s the percentage of multiple-solution cases is generally lower than 15%, while for the and 1.00 s (and higher) is lower than 10% regardless on the strength and ductility at peak strength.

It is worth mentioning that the results are only slightly sensitive to the hardening and residual-strength values (variations less than 5% within each $T_{el}-F_y-\mu$ subgroup are registered).

To discuss the effectiveness of the proposed strategies in selecting the PP for a single ground-motion response, the results are grouped by elastic period and hysteretic behaviour. The effectiveness of each strategy is evaluated introducing the \hat{R} index, which is the mean of the ratios between Δ_j^{S0} and Δ_j^{Si} which are the performance displacements respectively corresponding to the benchmark S0 and the generic $i - th$ strategy, for the $j - th$ record-SDoF pair showing multiple solutions. \hat{R} is calculated through Equation 5.12 where N_{ms} measures the total amount of multiple-solution cases for a determined T_{el} -hysteresis subgroup of oscillators. The effectiveness of the $i - th$ strategy increases as the corresponding \hat{R} approaches one.

$$\hat{R}_{Si} = \frac{1}{N_{ms}} \sum_{j=1}^{N_{ms}} \frac{\Delta_j^{Si}}{\Delta_j^{S0}} \tag{5.12}$$

Figure 5.7 synthetically shows the indexes \hat{R} for all considered subgroups. Different marker shapes differentiate the strategies, while the variation of colours corresponds to different hysteresis rules. The effectiveness of S1 is evidenced by the corresponding \hat{R} which is included in the range $[0.94;1.08]$, demonstrating the accuracy of the regression models described in Section 5.2.4. The accuracy of S2 is particularly evident for low/medium-period ($T_{el} \leq 1.25s$) oscillators ($0.99 \leq \hat{R} \leq 1.04$), while a loss of effectiveness is registered for high-period cases ($T_{el} \geq 1.50s$) having EPP or BIL hysteresis rule ($\hat{R} \geq 1.08$). Although its simplicity, S3, which implies the selection of the solution associated to the lowest performance displacement, provides a satisfactory

accuracy with respect to S0: an overestimation of the performance displacement in the range [2%; 14%] ($0.86 \leq \hat{R} \leq 0.98$) is observed, with the maximum error registered for EPP at $T_{el} = 0.50s$. Contrarily, if the last PP (largest displacement) is chosen (i.e. S4), an important bias is registered and a displacement overestimation higher than 50% ($\hat{R} \geq 1.50$) is generally expected regardless of the elastic period and hysteresis rule. The strategy S5 leads to values of \hat{R} included in the range [1.2;1.4] for the FS subgroup and higher for other hysteresis rules. Particularly, S5 provides \hat{R} higher than 1.5 for low-period cases ($T_{el} \leq 0.75s$) for MTt, MTf, EPP and BIL hysteresis rules.

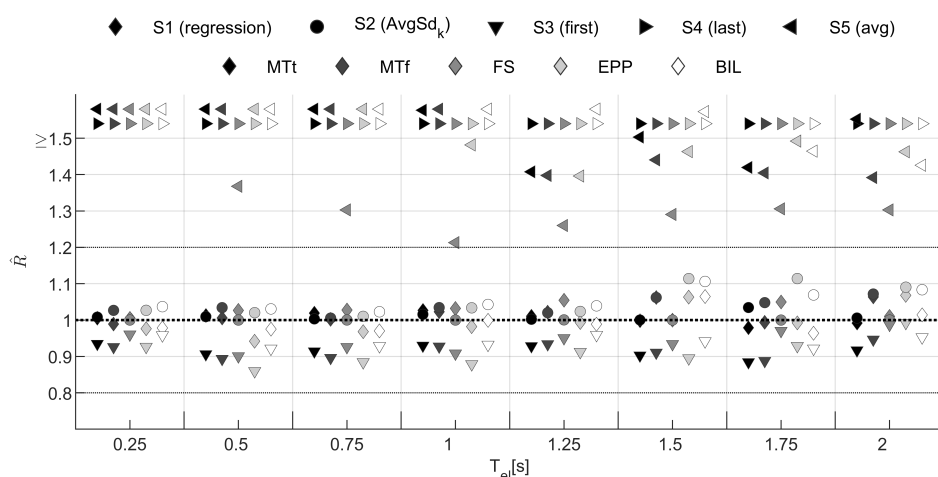


Figure 5.7: \hat{R} of the candidate PP selection strategies for all the period-hysteresis subgroups.

5.3.2. Effect of multiple-solution cases in fragility analysis

The discussion of the previous sub-section is limited to single ground-motion response analysis. Therefore, further tests are needed to definitively assess the accuracy of the different strategies in fragility analysis which is the main target of this study.

The fragility relationships for DS1, DS2 and DS3 are computed for all the considered SDoF systems in the database according to the procedure outlined in subsection 5.2.6, selecting the PP according to the previously described strategies. It is worth mentioning that if the selected PP exceeds the collapse threshold, it is classified as collapse within the PSDM calculation. The strategy S0 is again taken as a benchmark. Note that the

oscillators characterised by at least one ground-motion record producing multiple solutions are selected to perform this task (approximately 75% of the SDoF systems; only extremely high-period high-strength cases are excluded). Figure 5.8 helps the reader in understanding the expected effect of the multiple-solution records in the fragility analysis. It shows the cloud data ($\Delta_{PP} - AvgSa$ where the collapse cases are indicated with squared markers beyond the collapse threshold) and the PSDM modified power-law model of two sample cases having T_{el} equal to 0.25 s and 0.75 s with 45% and 13% of multiple solutions, respectively. The medians of the fragility curves are the $AvgSa$ values corresponding to the intersections between the PSDM and the horizontal line at the DS thresholds. Only the results for the candidate strategies S2, S3, S4 and S0 are reported. In both cases, it is evident that the pair of $\Delta_{PP} - AvgSa$ chosen according to S2 and S3 generally overlap with the corresponding one estimated by S0, so that the associated power-law models are similar, with increasing differences approaching the DS3 threshold. In Figure 5.8a, several of the $\Delta_{PP} - AvgSa$ points associated with S4 differ with respect to the other strategies producing different estimations of the power-law models. Since in this case, S4 overestimates the Δ_{PP} , it provides lower values of the median fragility at all the three DSs. As expected, this effect is less evident in the case shown in Figure 5.8b, where the percentage of multiple solutions is lower than the previous one.

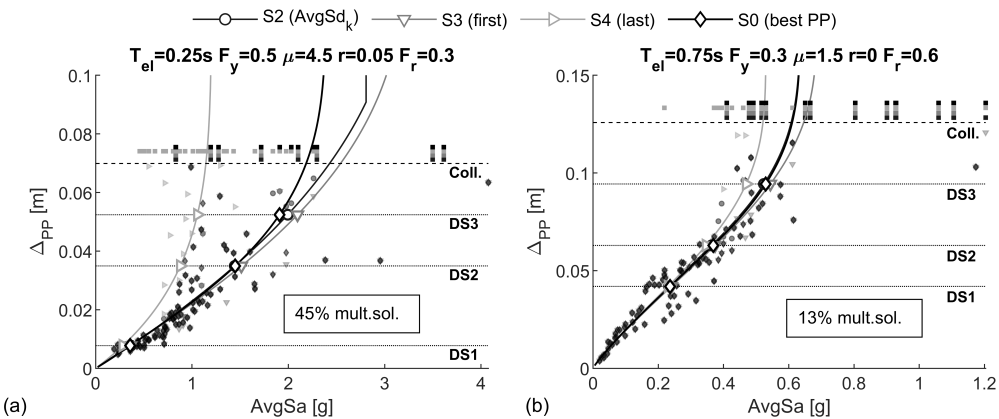


Figure 5.8: CSM-based probabilistic seismic demand models for two sample SDoF cases (MTt subgroup) having different amount of multiple-solution records

To systematically investigate the effectiveness of the different selection strategies, the relative error between the median fragility (α) and the dispersion (β) estimated by means of the i -th strategy (S_i) and S_0 is calculated for each SDoF oscillator. Each calculated error is related to the percentage of multiple solutions detected for the corresponding case. Therefore, the error data are grouped in intervals depending on the associated percentage of multiple-solution (each interval has 10% amplitude), and piece-wise trend lines are calculated (through the least square method).

The results are discussed in terms of relative error vs percentage of multiple solutions within the 100 ground motions in Figure 5.9 which shows the error trend lines together with the error data, indicated with markers having different shades of grey with reference to DS1 (first column) and DS3 (second column).

For DS1, S_1 , S_2 and S_3 provide errors lower than 10% regardless of the percentage of the multiple solutions and the adopted hysteresis rule. In contrast, the deficiencies of S_4 and S_5 strongly increase with the number of multiple solutions leading to average errors higher than 30%, tending to a percentage of multiple solutions equal to 40%. This is valid for all the adopted hysteresis rule, but the FS hysteresis rule. In this last case, the number of multiple solutions are lower than the other hysteresis rules (as discussed in the previous subsection) and the trend lines are calculated for a maximum of 20% percentage of multiple-solution cases.

For DS3, S_2 and S_1 are the most accurate strategies. As an example, these strategies produce errors lower than +5 and +8%, respectively for MTf. S_5 is the worst strategy providing errors which increase from -18% to -35% for 30% to 40% percentage of multiple solutions. It is worth noting that S_3 , although its simplicity, provides errors lower than +10% with a negligible increase for increasing percentages of multiple-solution cases. For FS, the low number of multiple solutions implies that the average expected error is lower than 15% independently of the selection criterion.

Finally, Figure 5.10 reports the relative errors in terms of dispersion β for DS3. Differences between the other DS are negligible as explained in the following Section 5.4.1. It is evident that S_4 considerably overestimates the dispersion from 10% to 50% approaching 40% of multiple solutions for all the hysteresis rule subgroups but FS. Differently, S_1 , S_2 and S_3 provide 5% errors on average.

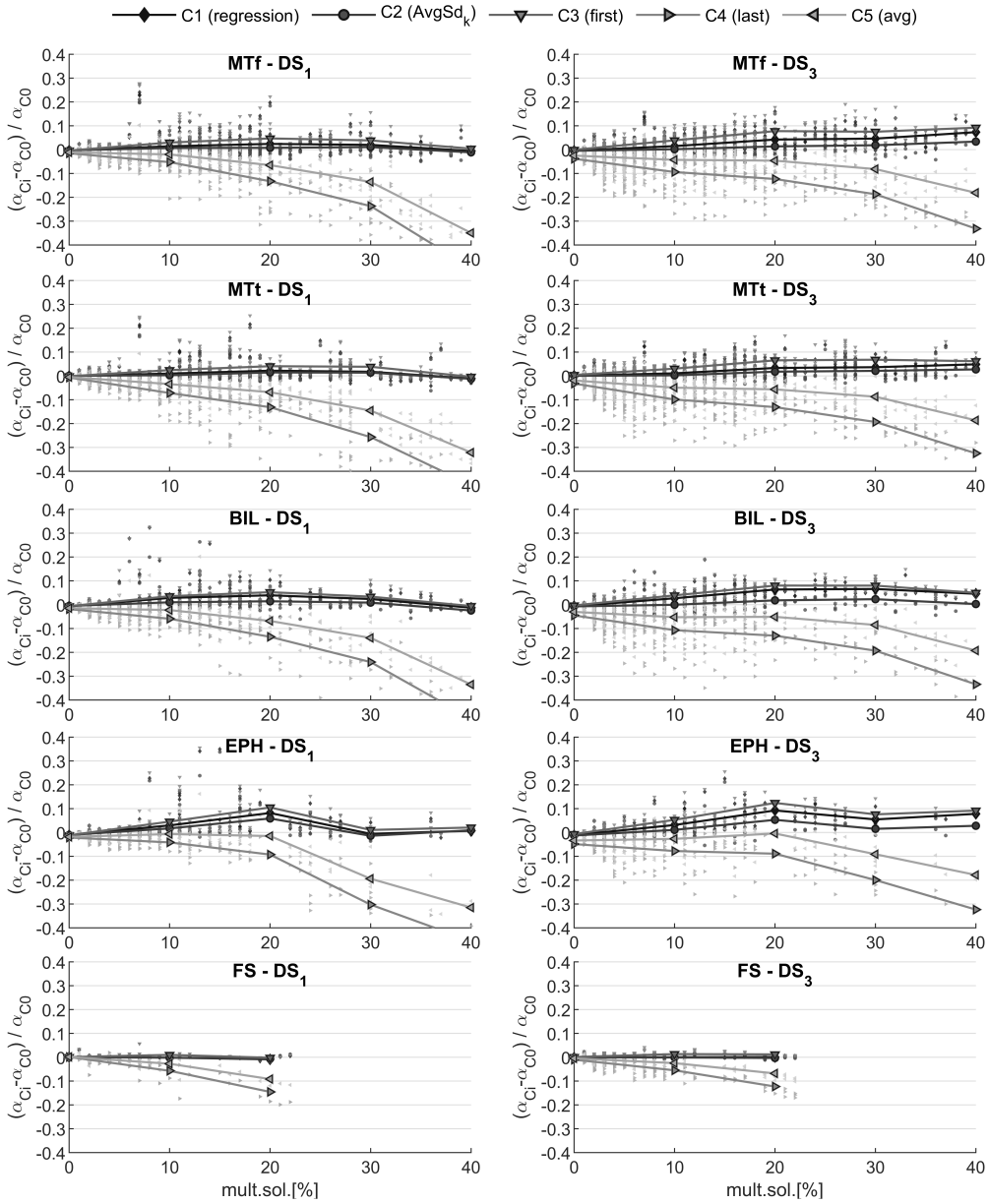


Figure 5.9: Errors on fragility medians (DS1 and DS3) depending on the adopted strategy for PP selection.

These outcomes extend the recommendations by Casarotti & Pinho (2007) suggesting to select the PP corresponding to the largest displacement (i.e. S4 in this study) in

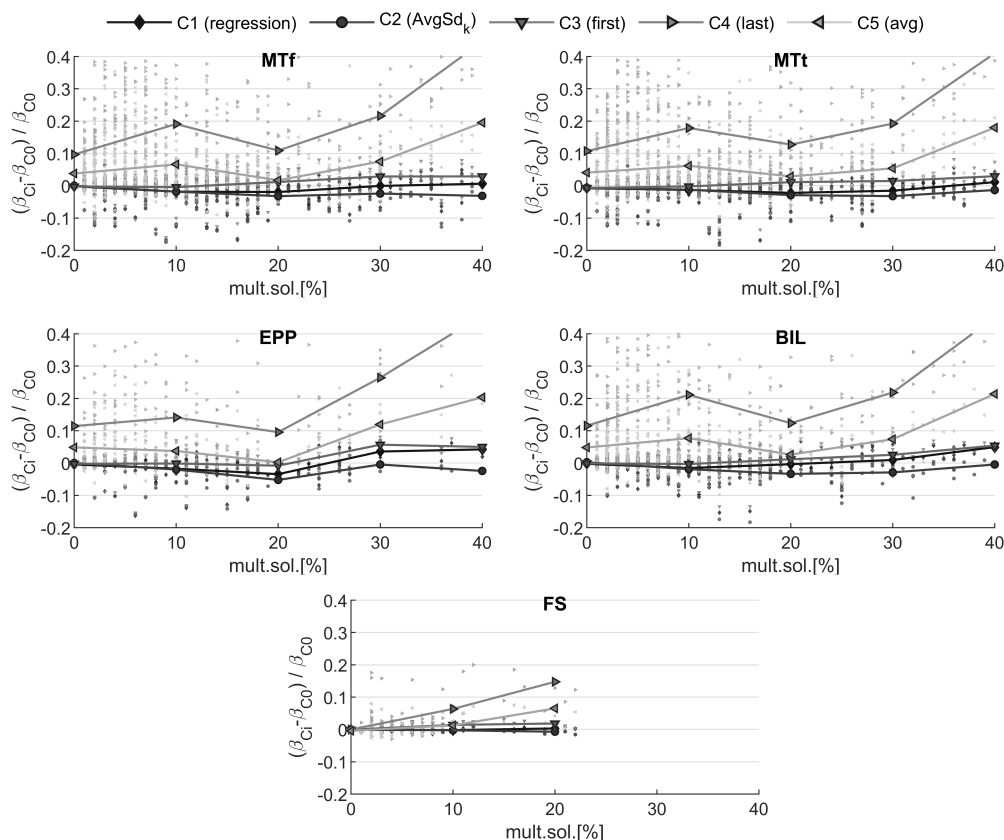


Figure 5.10: Errors on fragility dispersion depending on the adopted strategy for PP selection.

multiple-solution cases as a conservative choice. It is shown that S4 (and also S5) may considerably overestimate the fragility of the investigated structure with a noticeable bias depending on the percentage of multiple solutions. Conversely, S1, S2 and S3 can consistently reduce the bias induced by the multiple solutions. However, although providing a satisfying accuracy, S1 is the most demanding in terms of calculation effort and does not involve consistent improvements with respect to S2 and S3. S3 is also accurate, but its results could be not conservative. In conclusion, S2 is identified herein as the best strategy, allowing a quick and accurate selection of the PP.

5.4. Cloud-CSM for fragility analysis: Discussion of results

This Section discusses the results of the fragility analysis performed for each SDoF system by using the performance displacements calculated via the proposed algorithm for the CSM (Section 5.2.2), the N2 method, the IM-based method (Section 5.2.5) and NLTHA. The S2 strategy, which involves the selection of the nearest solution to the proposed $AvgSd_k$ is used to select the PP in case of multiple solutions of the CSM algorithm. The fragility analysis follows the cloud-based approach in Section 5.2.6. The median (α) and the dispersion (β) are used to systematically compare the differences in fragility functions calculated with the different approaches. To efficiently discuss the results, the oscillators are grouped based on significant backbone parameters and hysteresis rules and the outcomes are discussed according to the flowchart presented in Figure 5.11.

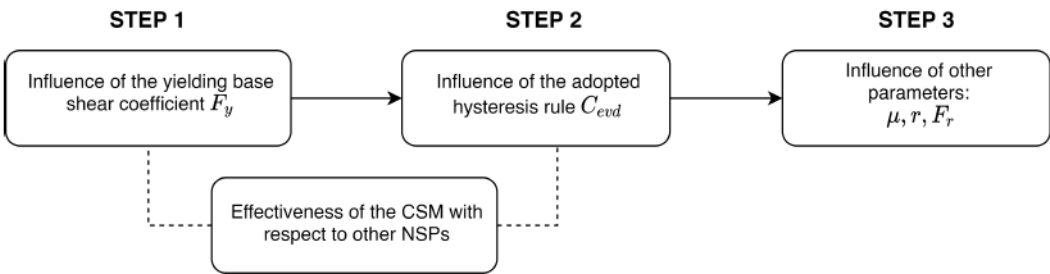


Figure 5.11: Steps of the analysis of results about the effectiveness of the CSM in fragility analysis.

5.4.1. Influence of the base shear coefficient and comparison with other nonlinear static approaches

This sub-section discusses the sensitivity of the effectiveness of the Cloud-CSM with respect to the yield base shear coefficient F_y , which can be considered the most critical backbone parameter affecting the inelastic response. For clarity, the results for the SDoF systems having a medium value of ductility ($\mu = 3$), a maximum value of residual strength ($F_r = 0.6F_y$), no hardening ($r = 0\%$) and MTt hysteresis rule (representative of moderate hysteretic dissipation) are selected for illustrative purposes. Note that an extensive collection of the fragility curves is also reported in Appendix C.

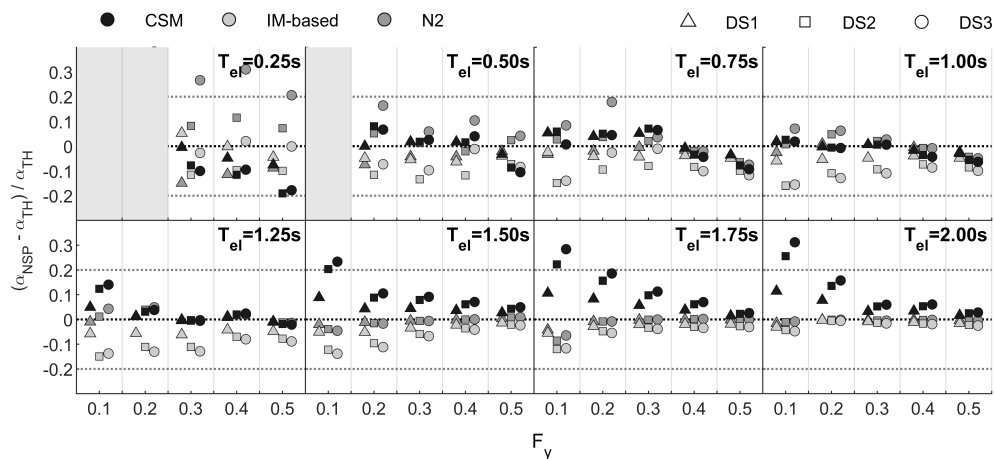


Figure 5.12: Errors between NSPs and NLTHA on the median fragility (α) for the SDOF subgroup with MTt hysteresis rule, $\mu = 3$, $F_r = 0.6F_y$, $r = 0\%$.

Figure 5.12 shows the relative errors on the median fragility α between the considered NSPs and NLTHA $((NSP - NLTHA)/NLTHA)$ calculated at the reaching of the three DSs (indicated with different markers) for all the considered oscillators grouped by period. Figure 5.13 reports the PSDMs related to four sample cases, appropriately selected to better understand the results of Figure 5.12. In Figure 5.13, the cloud data are graphically differentiated in collapse (squared markers) and non-collapse cases (circular markers). The median values of the fragility curves are the abscissa-components of the empty markers at the intersections between the modified power-law models and the dotted horizontal lines which indicate the DS thresholds. As evidenced in Figure 5.12, the cases with $T_{el} = 0.25s$ and $F_y \leq 0.2$, together with those with $T_{el} = 0.50s$ and $F_y \leq 0.1$ are excluded from the result database, since more than half of the cloud data exceed the collapse thresholds, thus obstructing a robust fitting of the PSDM according to Jalayer et al. (2017).

In the remaining 0.25 s-period cases, the CSM and IM-based method lead to errors included in the range $[-20;10]\%$, while the N2 method provides errors higher than $+20\%$ at DS3. Indeed, Figure 5.13a reports a short-period high-strength oscillator in which the CSM-based displacement demands overestimates the NLTHA resulting in lower values of α with errors equal to -19% and -20% for DS2 and DS3, respectively. Contrarily, the N2 method underestimates the NLTHA for the entire range of IM, thus resulting in

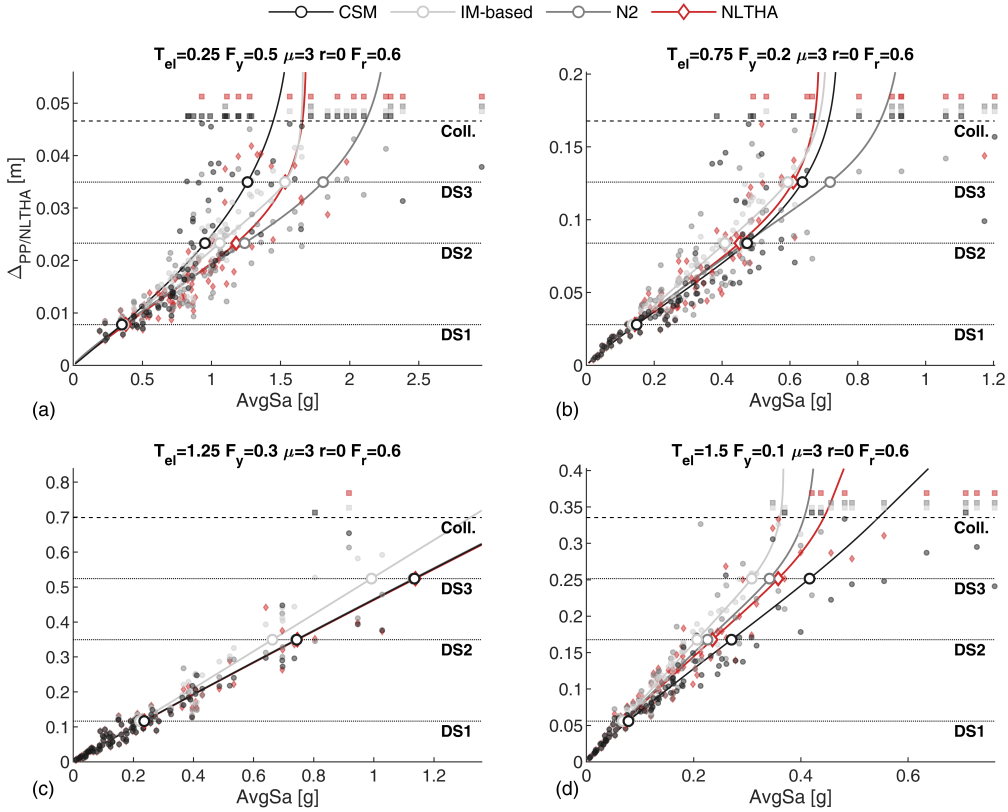


Figure 5.13: NLTHA- and NSP-based cloud data and probabilistic seismic demand models for four SDoF case-studies (MTt subgroup) selected for illustrative purposes

an error on the median fragility equal to +20% for DS3. Furthermore, the IM-based method outperforms the N2 (the maximum error with respect to NLTHA is -10% for DS2) proving (again) that in this case $AvgSd_k$ is a better proxy (higher efficiency) for the inelastic response of the considered oscillators with respect to the simpler $Sd(T_{el})$, accounting for the spectral demand in the range of period elongation.

In the majority of the cases with medium secant-to-yielding period, $0.50s \leq T_{el} \leq 1.00s$, the CSM provides good accuracy, with errors included in the range [-10;10]%, outperforming the other methods. To better understand these results, Figure 5.13b reports the cloud data and PSDMs for the oscillator having $T_{el} = 0.75s$ and $F_y = 0.2$. It is observed that the CSM-based modified power-law model nearly matches with the

NLTHA-based one, providing a maximum error of 4% on α at DS3. The IM-based method underestimates α with a maximum error equal to -9% at DS2, whereas for the DS3 and collapse thresholds, the PSDM estimated by the N2 strongly diverges from the other methods. This further evidences that $Sd(T_{el})$ is less representative of the displacement demand when strong inelasticity is required. This is also confirmed by the lower number of collapse cases (7) predicted by this method with respect to the CSM (11) and NLTHA (13).

According to Figure 5.12, the accuracy of the N2 and IM-based methods increase with increasing values of F_y and the resultant decreasing inelastic demand. This is also evidenced by the results of high-period ($T_{el} \geq 1.25s$) cases, where the N2 outperforms the other considered CSM. Figure 5.13c and d represents the PSDMs of long-period oscillators. The first exhibits period equal to a $1.25s$ and $F_y = 0.3$, while the second oscillator has a long period ($T_{el} = 1.50s$) and low strength ($F_y = 0.1$). In this cases, N2 provides the best accuracy with negligible errors with respect to the NLTHA-based results. In Figure 5.13c, the accuracy of the CSM is comparable to the N2 method, while the IM-based method overestimates the NLTHA-based displacement demand, underestimating the median fragility α . This outcome repeats for most of the analysed cases and proves that the α associated to the IM-based method are on the safe side with respect to NLTHA with errors lower than -20% regardless on the backbone parameters. These errors decreases as the nonlinear demand decreases (i.e. yield base shear increases). Conversely, in Figure 5.13d, The CSM significantly underestimates the displacement demands for higher values of the considered IM, overestimating the value of α with errors equal to +10%, +20% and +22% at DS1, DS2 and DS3 respectively. As shown by Figure 5.12, a significant bias of the CSM is generally observed for all the oscillators having $T_{el} \geq 1.25s$ and $F_y = 0.1$. However, the accuracy of the CSM consistently increases for a higher value of yield base shear strength, producing errors lower than 20% when $F_y \geq 0.2$. Also in this case, the IM-based method underestimates α with a maximum error equal to -14% at DS3.

To further evaluate the divergences in the fragility analyses related to the NSPs and NLTHA, the differences in the dispersion β are shown in Figure 5.14. According to the procedure described in Section 5.2.6, the global dispersion for a given DS accounts

for the contribution of the lognormal cumulative distribution function and the logistic function modelling the probability of occurrence of collapse/no collapse. It is proved in this study that the former term, which is linked to the residual errors of the cloud data with respect to the power-law model and thus is by-definition constant among the different damage states (D'Ayala et al. 2013), is the most significant contribution to β . Consequently, slight differences are registered among the dispersions calculated at the different DSs. For instance, with reference to the cases shown in Figure 5.13, β_{ds1} and β_{ds3} are 0.26 - 0.24, 0.24 - 0.20 and 0.18 - 0.17 for the first (a), second (b) and fourth (d) case, respectively (no collapses are registered for the third case). Therefore, the following discussion is addressed to DS3 only.

Figure 5.14a shows the values of β calculated assuming $AvgSa$ as an IM. It is observed that the differences in calculating the dispersion using the different approaches become negligible with increasing F_y and T_{el} . Particularly, in short-period cases, the CSM overestimates the NLTHA-based dispersion. The results show that in these cases the N2 outperforms the CSM providing negligible errors with respect to the NLTHA. The dispersion provided by the IM-based method is always lower than 0.2 underestimating the one calculated by means of NLTHA. On the other hand, Figure 5.14b refers to the fragility analysis carried out using $Sa(T_{el})$ as an IM. In this case, N2 produces a very low dispersion compared to the NLTHA, while higher accuracy is evident for the IM-based method. This low value of β is due to an increasing correlation between EDP and IM. Indeed, when the equal-displacement rule is applied, the performance displacement provided by the N2 is equal to $Sd(T_{el})$, which is perfectly correlated to the $Sa(T_{el})$ used as IM ($Sa(T_{el}) = (2\pi/T)^2 Sd(T_{el})$). It is observed that β of the N2 method gradually decreases for increasing elastic periods and increasing relevance of the equal-displacement rule in the calculation of the cloud data. Similarly, the low dispersion of the IM-based method when the $AvgSa$ is used as IM can be explained by an increasing correlation between EDP and IM. This happens even though a different range of periods is adopted to calculate $AvgSa$ and $AvgSd_k$. This outcome shows that NSPs which calculate the seismic performance of the investigated structure based on simple spectral ordinates, can strongly underestimate the effect of record-to-record variability in the dispersion of fragility curves. It is worth noting that an underestimation

of the dispersion means an underestimation of the probability of damaging for IM values lower than the median fragility and an overestimation for higher IM. Since the Eads et al. (2013) proved that, within a seismic risk assessment process, the mean annual frequency of exceeding a given DS, is more affected by the probability of damaging calculated at low IM values, than at high IM values. Therefore, an underestimation of β can result in potential underestimation of the seismic risk.

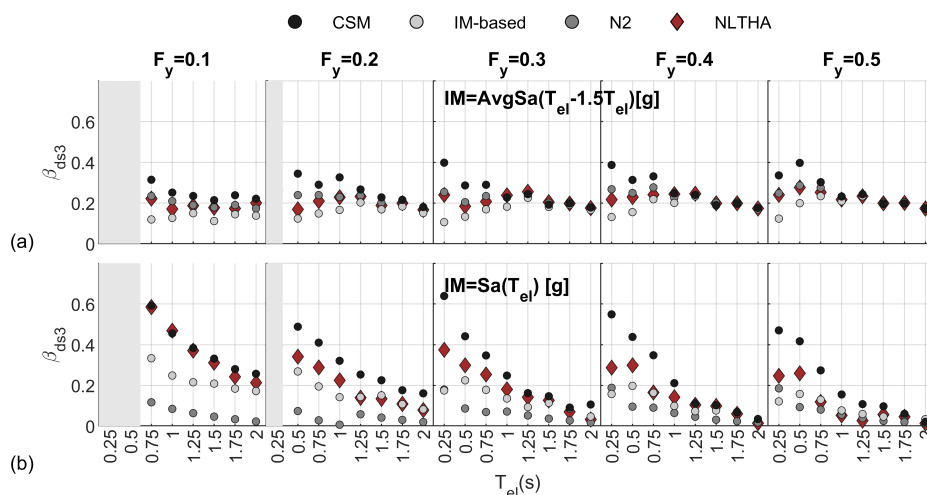


Figure 5.14: Dispersion (β) of the fragility curves calculated via the NSPs and NLTHA for the SDoF subgroup with MTt hysteresis rule, $\mu = 3$, $F_r = 0.6F_y$, $r = 0\%$.

Conversely, the CSM-based performance displacement is not dependent on the adopted IM type since this method resort to over-damped spectra to calculate the performance displacement. Figure 5.14 illustrates a general overestimation of the NLTHA-based dispersion by the CSM, both if $Sa(T_{el})$ or $AvgSa$ are used as IM. Particularly, with reference to Figure 5.14a, the registered overestimation decreases as F_y and T_{el} increase (decreasing average inelastic demand within the analysis database). The errors with respect to NLTHA are emphasized if a less efficient IM is adopted (such as $Sa(T_{el})$) in cases for which a considerable period elongation is expected. Note that, as explained before, an increasing dispersion is on the safe side with reference to seismic risk calculation. Consequently, this error can be considered an acceptable trade-off for the reduction in computational effort involved by the CSM with respect to NLTHA.

5.4.2. Influence of the hysteresis rule

The sensitivity of the effectiveness of the Cloud-CSM to the hysteretic behaviour is discussed in this sub-section. The evaluation of the influence of the adopted hysteresis rule is directly reflected in an evaluation of the accuracy in predicting the NLTHA-based results of the different equivalent viscous damping coefficients (C_{evd} , Table 5.2). To synthetically address this discussion, the results herein analysed refers to the oscillators having the intermediate value of ductility ($\mu = 3$), the maximum residual strength ($F_r = 0.6F_y$) and 0% hardening (except for the BIL subgroup where a hardening equal to 10% is considered). Note that, differently than the CSM, the N2 and IM-based methods do not account for modifications in the seismic performance due to different hysteresis rules, thus providing the same target displacement regardless of the cyclic response: the fragility curves calculated via these methods do not change among the considered hysteresis subgroups. In this section, the results are synthetically discussed, while a complete collection a fragility curves is reported in Appendix C.

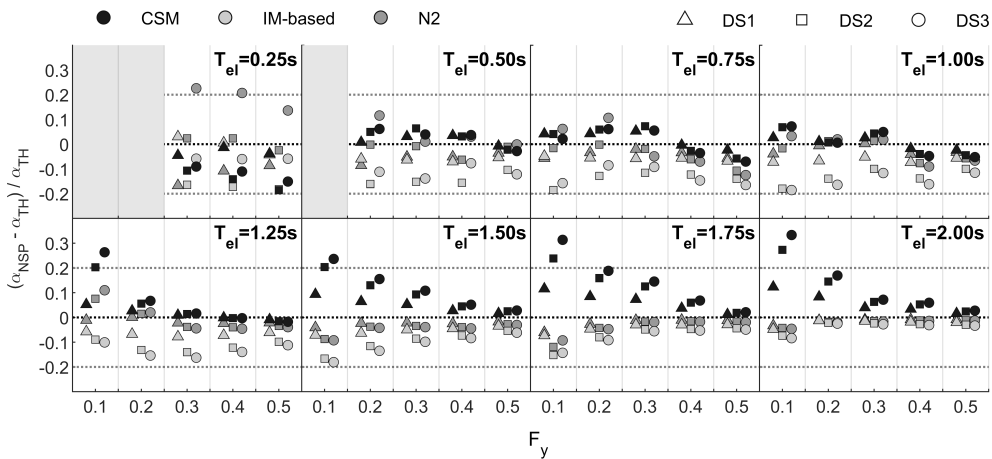


Figure 5.15: Errors between NSPs and NLTHA on the median fragility (α) for the SDoF subgroup with MTF hysteresis rule, $\mu = 3$, $F_r = 0.6F_y$, $r = 0\%$

Figure 5.15 and 5.16 reports the results for the MTF and BIL subgroups (which exhibit comparable values of C_{evd}) and shows that the CSM generally provides good accuracy for the cases with a short-medium elastic period leading to errors on α lower than 20%. Furthermore, in these cases, a loss of accuracy is registered for low-strength cases with

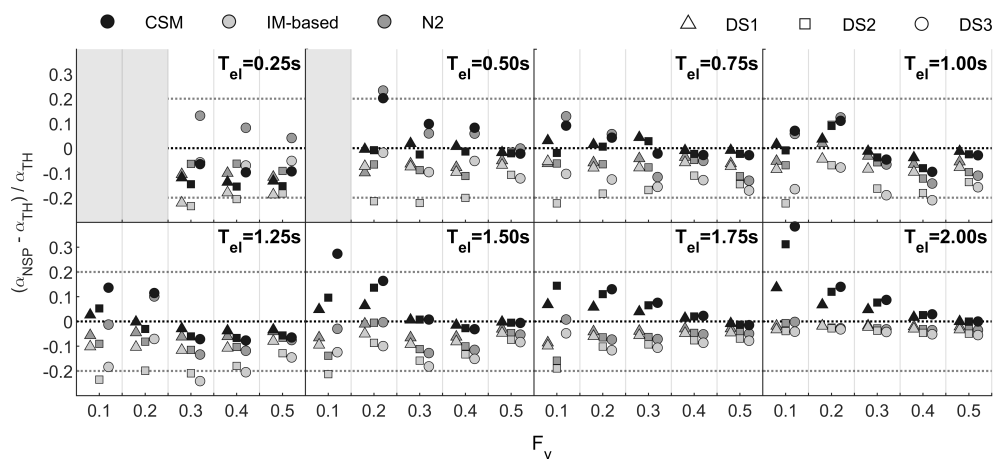


Figure 5.16: Errors between NSPs and NLTHA on the median fragility (α) for the SDoF subgroup with BIL hysteresis rule, $\mu = 3$, $F_r = 0.6F_y$, $r = 0\%$

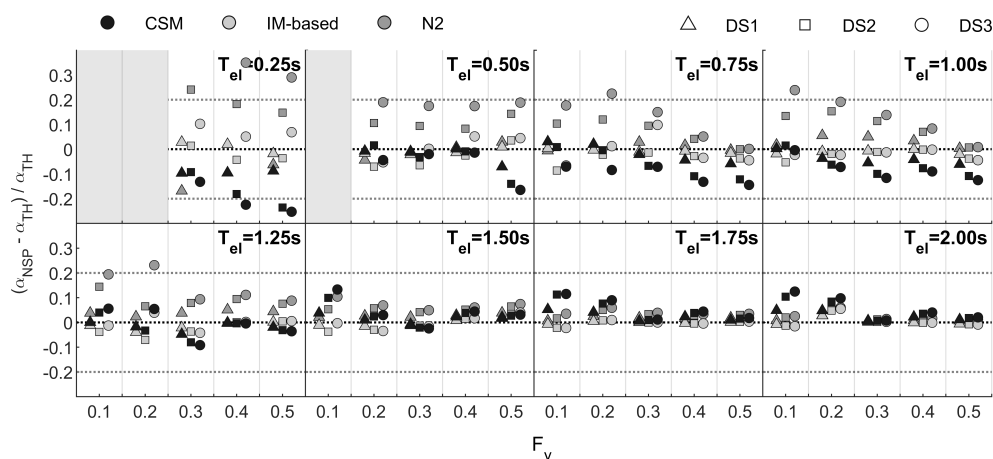


Figure 5.17: Errors between NSPs and NLTHA on the median fragility (α) for the SDoF subgroup with FS hysteresis rule, $\mu = 3$, $F_r = 0.6F_y$, $r = 0\%$

high elastic periods. As an example, for the oscillator having $T_{el} = 1.50s$ and $F_y = 0.1$, the CSM provides errors for DS3 equal to 22% and 27% for MTf and BIL, respectively. These outcomes are consistent with the outcomes related to MTt (Figure 5.12, since the hysteretic dissipation associated with MTf and BIL slightly differ to MTt (see Table 5.2). This also implies that the accuracy of the N2 and IM-based methods (not sensitive to the hysteresis rules) registered for the MTt subgroup is generally confirmed for MTf

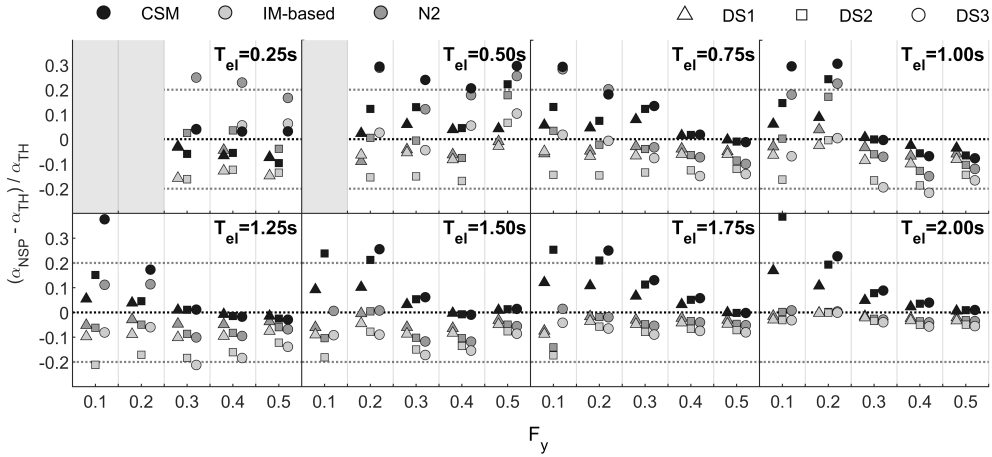


Figure 5.18: Errors between NSPs and NLTH on the median fragility (α) for the SDoF subgroup with EPP hysteresis rule, $\mu = 3$, $F_r = 0.6F_y$, $r = 0\%$

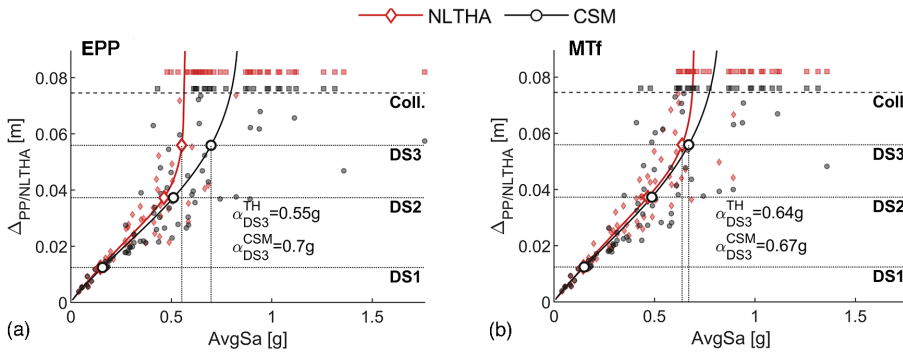


Figure 5.19: NLTHA- and NSP-based cloud data and probabilistic seismic demand models for two selected SDoF case-studies having EPP and MTF subgroup selected for illustrative purposes

and BIL.

Figure 5.17 and 5.18 reports the errors on α for the FS and EPP, which are characterised by a considerably different hysteretic behaviour with respect to the cases previously analysed. Referring to the FS, higher values of the CSM performance displacements are expected given the low hysteretic dissipation ($C_{evd} = 0.186$). In this case, Figure 5.17 evidences that the CSM accurately predicts (errors included in the range $[-18;12]\%$) the NLTHA-based α for cases with $T_{el} \geq 0.50s$. In contrast, the N2 systematically overestimates it, with the error increasing for strong inelasticity. This evidences the general accuracy of the equivalent viscous damping proposed by Priestley et al. (2007)

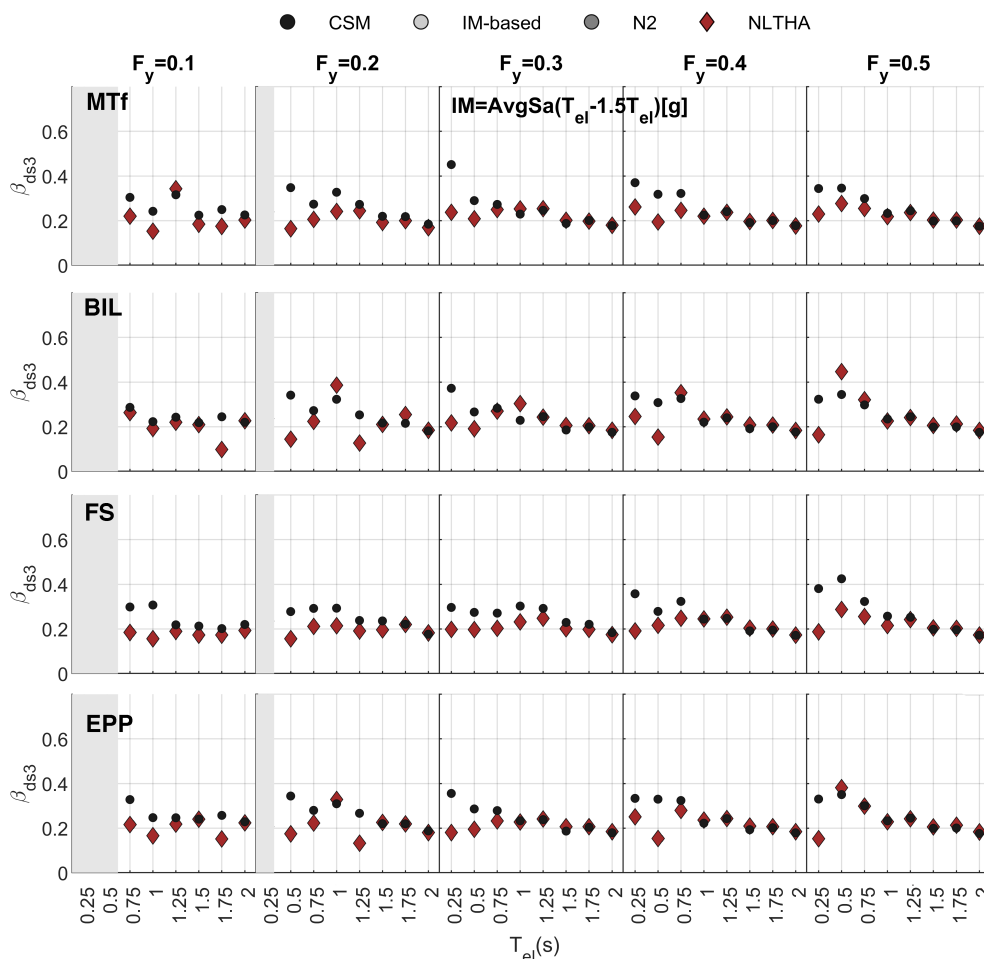


Figure 5.20: Dispersion (β) of the fragility curves calculated via the NSPs and NLTHA for the SDoF subgroup with EPP hysteresis rule, $\mu = 3$, $F_r = 0.6F_y$, $r = 0\%$.

for a FS hysteresis rule and the low reliability of the N2 method in using $Sd(T_{el})$ in estimating the seismic performance of low-dissipation structures. Note that the IM-based method provides high accuracy in predicting the median fragility of this type of structures.

On the other hand, lower values of the CSM target displacements are expected for EPP, because of the high value of C_{evd} associated ($C_{evd} = 0.670$). Figure 5.18 shows that for $T_{el} = 0.50s$, the CSM generally overestimates the NLTHA-based α , since it provides lower performance displacements with respect to the NLTHA. This can be

caused by a too-high value of the EPP-based C_{evd} or by the high sensitivity to the record duration of the response of SDoF systems characterised by an EPP hysteretic behaviour. Further information about this latter phenomenon is reported in Priestley et al. (2007), stating that long-duration ground motions could involve “crawling” displacement for EPP systems. For instance, the PSDMs of the SDoF systems having T_{el} and F_y equal to 0.50 s and 0.2 respectively, can be observed (Figure 5.19).

In this case, the NLTHA-based α for DS3 is equal to 0.55 g and 0.64 g if EPP or MTf are respectively used. The higher fragility detected in the first case contrasts with the corresponding higher value of C_{evd} which is a proxy of larger dissipation (implying lower ductility demand) with respect to the MTf hysteretic behaviour. This explains the loss of accuracy of the CSM in this case, which provides α equal to 0.7 g and 0.67 g respectively for DS3.

For the sake of completeness, Figure 5.20 reports the values of the β for DS3 calculated through the NSPs and NLTHA for the MTf and FS subgroups adopting $AvgSa$ as IM. The results of the N2 and IM-based methods are not shown in the figure for the reasons explained in the previous sub-section. Consistently with the MTt, it is evident that the employment of the CSM induces an overestimation in the dispersion, which is higher for a high inelastic response (for example caused by a low base shear coefficient). Moreover, higher CSM-vs-NLTHA differences in β_{DS3} corresponds to cases where the accuracy CSM concerning the fragility medians decreases. This can be easily observed for the oscillators having an elastic period equal to 0.25 s for all the hysteresis subgroups.

5.4.3. Influence of other backbone parameters

The sensitivity of the effectiveness of the Cloud-CSM to the variation of significant backbone parameters is discussed in this sub-section. Figure 5.21 reports the errors on the median fragility (α) at different DSs of the CSM with respect to the NLTHA for different values of the ductility at DS2 (μ), the residual strength after the softening branch (F_r) and the hardening ratio (r). For illustrative purpose, various subgroups of oscillators are considered, which are identified in the legends of the subplots. Firstly, Figure 5.21a, b and c aim to discuss the influence of varying μ , comparing the errors on α for subgroups

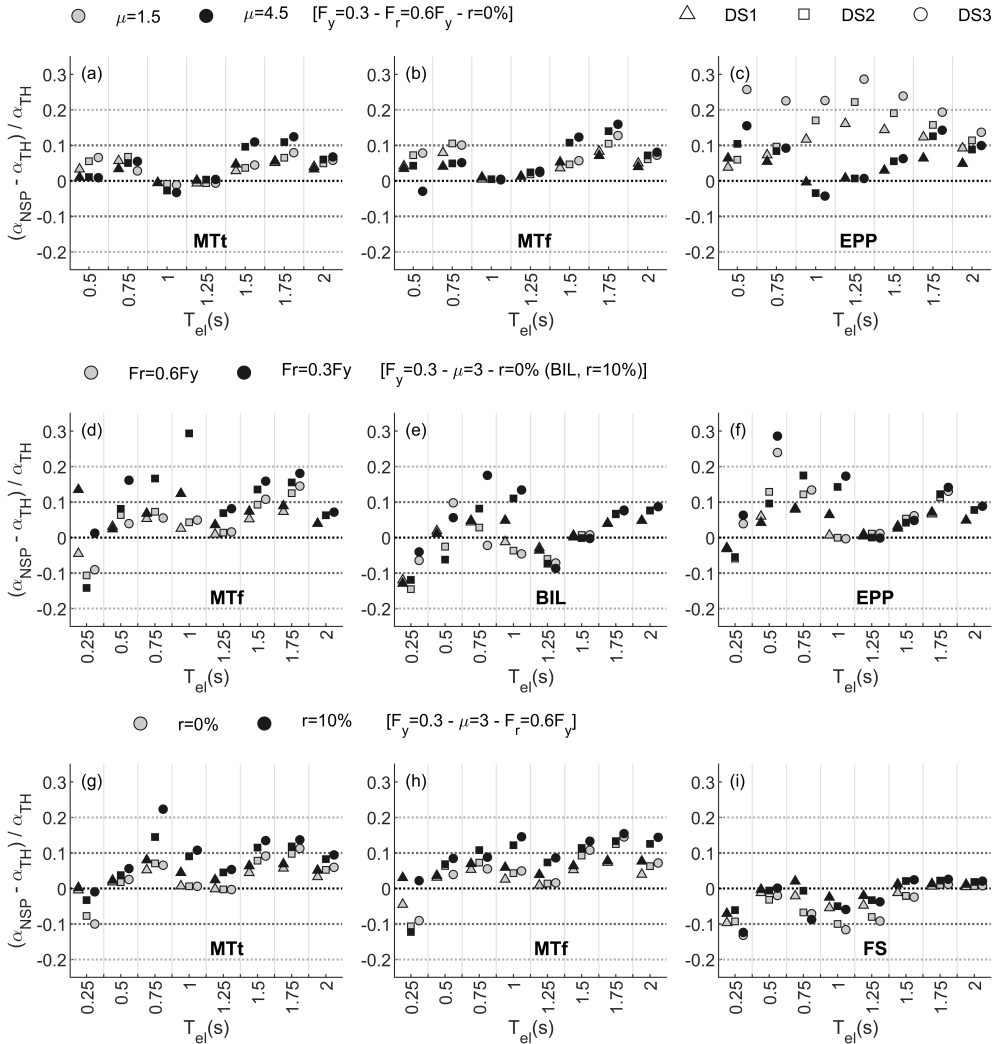


Figure 5.21: Errors between NSPs and NLTHA on the median (α) for variable ductility (a-c), residual strength (d-e) and hardening ratio (g-i).

of oscillators having μ equal to 1.5 and 4.5 ($T_{el} = [0.50 - 2.00]s$, $F_y = 0.3$, $F_r = 0.6F_y$, $r = 0\%$). Again, the results of the SDoF system having a period equal to 0.25 s are excluded (Section 5.4.1). These outcomes evidence a low influence of the ductility capacity on the results of the Cloud-CSM within the Modified Takeda subgroups. This means that the C_{evd} adopted for the Takeda subgroup is efficient, providing a stable accuracy even though the inelastic demand increases (increasing μ implies increasing

DS thresholds). In this case, the maximum difference is detected for the SDoF with $T_{el} = 1.50s$ and MTf where the errors for the DS3 fragility median raise from 5% to 12%. In this case, the PSDMs related to $\mu = 1.5$ and $\mu = 4.5$ are very similar since the backbones are practically identical and until the reaching of DS2 and therefore the cloud data almost match: only the 6% of the ground motions push the former case (low ductility) beyond the DS2 threshold. This means that the difference in the errors is only linked to the propagation of the divergences between the NLTHA- and CSM-based power-law models approaching the DS2 and DS3 thresholds which in the high-ductility cases correspond to high inelastic response with respect to the low-ductility one. Figure 5.21c shows that the sensitivity of the CSM to the variation of the parameter μ increases for the EPP rule. In this case, if the ductility capacity is low, the softening branch is prematurely reached, and therefore, the inaccuracies discussed in the previous section are emphasized.

Figure 5.21d, e and f show the sensitivity of the CSM-induced relative errors on α with respect to NLTHA for SDoF systems with variable residual strength at collapse (F_r equal to $0.6F_y$ and $0.3F_y$) for MTf, BIL and EPP hysteresis rules. Note that again the results corresponding to MTf are comparable to MTt. The decreasing F_r induces increasing error in the cases with a short-to-medium elastic period where a significant number of ground-motion records pushes the SDoF beyond the DS3 threshold. This inaccuracy of the CSM is caused by a likely inadequacy of the C_{evd} coefficients which, being originally calibrated to serve Displacement-based Design approaches, may be less reliable in considering the decreasing hysteretic dissipation in the softening and residual strength branches. For this reason, when a consistent number of ground motions requires a performance displacement higher than the displacement at DS2, the CSM underestimates the NLTHA-based target displacement, overestimating α at the different DSs. For instance, for MTf the errors at DS3 are 42% and 38% (out of bounds in the plot) for the oscillators with T_{el} equal to 0.75 and 1.00 s (Figure 5.21d).

Figure 5.21g, h and i discuss the accuracy of the CSM on varying values of hardening ratio (r equal to 0% and 10%) for MTt, MTf and FS subgroups. Note that an increasing hardening ratio implies a decreasing hysteretic dissipation which is not considered by the ductility-based equivalent viscous damping formulations. In other words, the CSM

predicts the same displacement demand, neglecting the hardening ratio. Accordingly, Figure 5.21g and h (MTf and MTt) indicate that, for hardening equal to 10%, the CSM increasingly overestimates the median estimated by NLTHA with respect to hardening equal to 0%. As an example, for the oscillator of $T_{el} = 0.75s$ and MTt, the error at DS3 increases from 9% to 21%.

5.4.4. Influence of cyclic strength degradation

The cyclic strength degradation is neglected in the hysteretic behaviour of the oscillators described in Section 5.2.1. However, a cyclic reduction of strength, which can affect the seismic response of non-seismically designed structures, implies a reduction in the hysteresis dissipation with the increasing of the load cycles. To evaluate the influence of this effect in the effectiveness of the Cloud-CSM, an additional subset of SDoF systems is generated. In this subset, only the MTt and MTf hysteresis rules are considered, the adopted backbone parameters are those described in Section 5.2.1, whereas a 20% cyclic strength degradation is fixed.

The effect of strength degradation is supposed to increase the NLTHA-based displacement demand with respect to the CSM-based one that neglects this effect accounting only for the spectral shape in performance displacement demand prediction. Figure 5.22 reports the results for MTt (a) and MTf (b) for a subgroup of SDoF oscillators having $F_y = 0.3$, $\mu = 3$, $F_r = 0.6F_y$ and $r = 0\%$. It proves that the influence of the cyclic strength degradation is low for MTt in all the cases having elastic period equal or higher than 0.5. For the MTf subgroup, the errors increases for the cases with period equal to 0.25-0.75 s. For instance, for the 0.75 s-period case the errors at DS3 reaches 17% if 20%-cyclic dissipation is adopted, while a 5% is attributed to 0%-cyclic degradation. For higher periods, the inelastic demand is lower, therefore the effect of cyclic degradation is negligible.

5.5. Conclusions

In this Chapter, the effectiveness of the Capacity Spectrum Method in performing probabilistic seismic assessment considering record-to-record variability is discussed with application to a case-study database of 2160 SDoF systems and 100 natural recorded

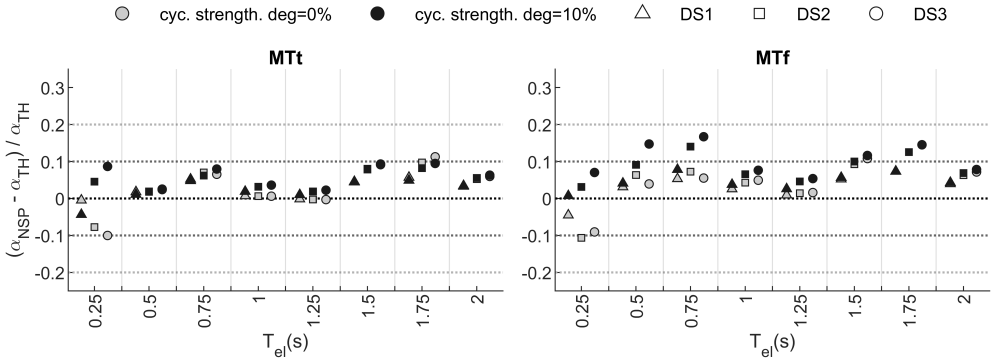


Figure 5.22: Errors between NSPs and NLTHA on the median (α) for variable cyclic strength degradation (MTt (a), MTf (b), $\mu = 3$, $F_r = 0.6F_y$, $r = 0\%$).

ground motions. The SDoF systems are represented by multi-linear parametric backbone curves with variable elastic period, yield base shear coefficient, ductility at peak strength, hardening ratio, residual strength. Five types of hysteresis rules are also adopted: Modified Takeda Fat, Modified Takeda Thin, Elastic-Perfectly Plastic, Bilinear and Flag-Shaped. An efficient algorithm to perform the CSM with real, as-recorded spectra is proposed, combined with a cloud-based approach (Cloud-CSM) to derive fragility relationships. Simple strategies to select the Performance Point (PP), if multiple CSM solutions are calculated, are proposed and tested. The effectiveness of the Cloud-CSM in fragility analysis is discussed by means of comparisons with more refined nonlinear time history analyses (NLTHA), the N2 method and a proposed simple method involving an intensity measure, the geometric average of spectral displacement within a given period range, as a direct proxy for the performance displacement. The results of this study can be summarised as follows:

- The CSM applied with real spectra may produce multiple solutions which are not physics-based. The effectiveness of different criteria (based on simplistic assumption or efficient intensity measures) in selecting the performance point is analysed. It is demonstrated that in multiple-solution cases the PP can be identified as the solution whose associated displacement best mimics the geometric average of the spectral displacements calculated in an appropriate range of periods.

- It is demonstrated that an incorrect choice of the PP may imply errors on the median fragility and dispersion higher than 20% if the percentage of multiple-solution ground motions is higher than 20% of the total number of adopted records. The adoption of an appropriate strategy for PP selection, involves a strong reduction of the errors (lower than 5%) regardless of the number of multiple solutions.
- The Cloud-CSM provides errors lower than $\pm 20\%$ in predicting the median fragility. Its accuracy reduces for cases with particularly low strength and long period or if an elastic-perfectly plastic hysteresis rule is adopted (errors higher than 20%).
- The CSM and the proposed intensity measure-based method outperform the N2 method in predicting the median fragility for short-period oscillators. Moreover, the N2 can provide large inaccuracies (errors higher than 20%) if flag-shaped or elastic-perfectly plastic hysteretic behaviour is adopted.
- The N2 and the proposed intensity measure-based method for performance displacement identification can strongly underestimate the dispersion in fragility curves depending on the adopted intensity measure. Contrarily, the Cloud-CSM can be applied regardless of the selected intensity measure. This latter implies an increasing dispersion in the fragility relationships with respect to NLTHA, depending on the efficiency of the adopted intensity measure.

Given the low computational effort required, the Cloud-CSM can accurately support applications where a large number of analyses is generally involved, such as regional-scale assessment of portfolios of structures for modelling epistemic uncertainties in archetype structures. This method is adopted in Chapter 6 for applications on common roadway bridges.

Chapter 6

Seismic risk assessment of roadway bridges accounting for knowledge-based uncertainty

Abstract

The prediction of the seismic vulnerability of bridges is a challenging task for road managers which need to include structural risk prioritisation schemes in their Bridge Management Systems to improve the resilience of road networks. The large number of bridges designed without anti-seismic requirements and the uncertainties linked to the lack of knowledge data, such as design documents and blueprints, strongly affect the feasibility of this process. A simplified approach for performing fragility analysis considering knowledge-based uncertainties is described. The approach is based on the statistical generation of a population of index-bridges, which are analysed by means of a simplified modelling approach and simplified analytical methods providing capacity curves. The capacity spectrum method is used to evaluate the performance of the index-bridges under a specific earthquake record. The fragility of the main bridge is calculated aggregating the fragility curves of the index-bridge populations. The proposed approach is applied on a dataset of eight simply-supported bridges of the Basilicata national road network. The influence of knowledge-based uncertainty on both the fragility and the seismic risk is discussed depending on the bridge constructive features. Finally, a validation of the proposed approach is carried out by means of a comparison with refined modelling approach and nonlinear dynamic analyses.

6.1. Introduction and motivations

In the aftermath of strong earthquakes, an inadequate seismic response of railway and roadway bridges could provoke direct and indirect losses, such as structural damages, economic losses, casualties or issues in managing the post-event emergency. In most

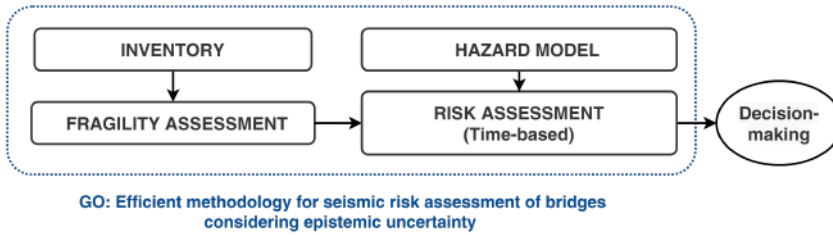


Figure 6.1: Objective of this Chapter (GO) and framing in the workflow for seismic risk calculation.

of the developed countries, many bridges were built in the past decades, when the old regulatory codes did not require an adequate anti-seismic design. As an example, in Italy a high amount of bridges were built during the 60s and 70s Pinto & Franchin (2010) when the majority of the Italian territory was not considered earthquake-prone. Consequently, transportation authorities deal with the risk prioritization of a large number of bridges.

Many literature studies investigated the extension of typological approaches, already consolidated for regional-scale assessment of buildings, to assess the seismic vulnerability of bridge portfolios (Choi et al. 2004, Avşar et al. 2011, Moschonas et al. 2009, Nielson 2005, Monteiro et al. 2019). These simplified methodologies are based on a typological classification, according to proposed taxonomies (Zelaschi & Monteiro 2017, Hancilar & Taucer 2013), and assume that the performance of bridges belonging to the same class is similar. One or more index-structures, representative of each typological class, are identified and analysed to achieve class-fragility curves. These express the probability to reach or exceed a determined limit state for a given earthquake intensity of a bridge belonging to a given class. Class fragility curves could be calculated analytically accounting for geometric and material variability within the class. The accuracy of these approaches is strictly linked to the classification scheme adopted, usually defined on a judgemental-empirical basis, that could be not directly related to the expected seismic performance (Mangalathu et al. 2017). Furthermore, as evidenced by Stefanidou & Kappos (2019), typological approaches neglect the contribution of structure-specific components and geometrical features that could be crucial in the vulnerability of bridges belonging to the same class.

On the other hand, recent studies turn to simplified structure-specific approaches. The

study by Şadan et al. (2013) extended the displacement-based assessment procedure for SDoF systems by Priestley et al. (2007) to multi-span continuous girder RC bridges via the approach presented in 3. Cardone (2014) analysed the effectiveness of displacement-based seismic assessment, i.e. simplified rational assumptions and numerical nonlinear static approaches, for common Italian bridge typologies. Displacement limits for different structural components are proposed and fragility analysis via a simplified capacity spectrum-based methodology is also carried out. Both of these were extended by Cademartori et al. (2020) for considering the contribution of different bearing devices on the superstructure-substructure connection and to achieve analytical fragility functions. Stefanidou & Kappos (2017) presented a hybrid methodology for bridge-specific fragility analysis to be used for both bridge portfolio, using simplified elastic analysis, or refined single-bridge applications, via nonlinear time history analysis (NLTHA) in a multi-stripe approach. Differently, Borzi et al. (2014), after proposing a comprehensive database layout to store bridge data, developed an automated tool aimed at building refined finite element models and performing multi-stripe analysis for calculating fragility curves dealing with a high number of bridges.

Generally, within both a typological or structure-specific probabilistic seismic assessment, aleatory and epistemic uncertainties should be considered. The aleatory uncertainties are commonly related to the random nature of the variable to be modelled and can not be reduced by the analyst. The epistemic uncertainties are related to a knowledge limit about some properties e.g. structural (geometric and material) properties, modelling assumptions or adopted capacity models. Epistemic uncertainties are modelled as random variables characterised by appropriate statistical distributions modelling their variability. Their consideration in the probabilistic seismic assessment requires statistical sampling techniques and burden considerably the process, especially if refined modelling and analysis techniques are used. A preliminary adequate knowledge level of the structure(s) being analysed could beneficially limit the influence of epistemic uncertainties. However, such a refined data collection phase may be unaffordable, since a common inadequate and not homogeneous knowledge about these structures is evidenced by roadway and railway authorities. Currently, bridge databases are lacking design data and blueprints which mostly were lost by management authorities or stored

in inaccessible archives. Moreover, *in-situ* inspections with accurate diagnostic testing may help the analysts, even though these require a high amount of time and economic resources.

If the knowledge process is lacking, the necessary modelling effort and the required number of analysis for considering the amount of epistemic uncertainties increases. In this context, refined numerical models and analysis techniques are not a practical solution. This implies the need for simplified fragility analysis methodologies to account for both aleatory and epistemic uncertainties. In this study, a bridge-specific fragility analysis approach accounting for aleatory and epistemic uncertainties via statistical sampling, and based on a simplified mechanics-based assessment, is proposed. Simplified mechanical models and displacement-based assessment analytical procedures are used within a cloud approach for fragility analysis. The methodology results in "bundles" of fragility curves which are used for simplified seismic risk calculations, quantifying the effect of knowledge-based uncertainties.

This approach could be applied for the quick risk assessment of bridges within portfolio analysis to identify bridges exposed to high seismic risk which should be retrofitted. It can also be used for detecting the critical assets where the uncertainty mostly affect the seismic risk, where refined inspections should be addressed to improve the knowledge degree of the seismic risk of the network.

A refined description of the procedure, adapted to typical bridge structural schemes, is reported in Section 6.2. In Section 6.3, the procedure is applied to eight existing simply-supported RC bridges, part of the national road network of the Basilicata geographical region. The influence of the knowledge-based uncertainty on both the fragility and the risk of the investigated bridges is quantified and discussed with reference to the characteristics of the analysed bridges.

The case studies described in the previous Chapter 2 whose knowledge data are collected based on street-view surveys are analysed via the proposed methodology. The results are discussed analysing the influence of epistemic uncertainty on fragility and risk. For one of the case-study the procedure is applied again after a more refined RPAS-based data collection 2.3.3 which reduces the influence of epistemic uncertainty. This last case is used to perform a validation of the simplified methodology for fragility anal-

ysis using the results of refined numerical models analysed via NLTHA as a benchmark.

6.2. Description of the methodology

The simplified methodology to perform probabilistic seismic assessment of bridges considering aleatory and epistemic uncertainties is described in this section and Figure 6.2. A population of index-models is generated to consider the epistemic uncertainties, while the aleatory ones are represented by an appropriate suite of ground motions. A fragility curve is calculated resorting to a cloud approach for each index-model, leading to a population of fragility curves representing the fragility of the main bridge.

6.2.1. Modelling uncertainties in fragility analysis

Aleatory and epistemic uncertainties should be considered in the probabilistic seismic assessment. The former are linked to inherently random processes and, in this study, only the uncertainty in the seismic ground shaking is included in this group. This so-called record-to-record variability is captured with an appropriate selection of ground motions representative of the seismicity of the site. Epistemic uncertainties (indicated also as knowledge-based hereafter), in this study, include geometry and mechanical properties of the materials or structural details which can not be assumed as “deterministic”. The knowledge-based uncertainties can be represented by random variables and appropriate statistical distributions. Zelaschi et al. (2016) and Nielson & DesRoches (2007) proposed sets of statistical distributions to appropriately model the geometric parameters and the material properties of highway bridges, respectively for Italy and the US. Within the probabilistic seismic assessment process, the epistemic uncertainties are usually accounted for by means of the random generation of a population of index-models (i.e. samples) characterised by variables retrieved from the corresponding statistical distributions. In this process, statistical sampling techniques, such as the standard or Latin Hypercube Sampling (LHS) Monte Carlo methodology, can be used. The LHS (Olsson et al. 2003) is widely used in literature for the probabilistic seismic analysis of both single or portfolios of bridges. As an example, Padgett et al. (2008) and Tavares et al. (2012) resort to this methodology to model uncertainty of geometric and constructive parameters within classes of typical US bridges. Monteiro (2016) ad-

addresses various issues of the employment of LHS for probabilistic bridge assessment, such as the evaluation of a robust sampling size evaluating the variability of the outcomes. The LHS is usually preferred over the standard Monte Carlo technique since it requires a lower number of samples and thus involving lower computational effort by using stratification. In the LHS framework, the cumulative distributions of the generic random variables X_j are divided into N equal-probability intervals, where N is the target number of realizations. Then, a single value is randomly extracted from each interval. The output samples are N vectors having a size equal to the number of uncertain vari-

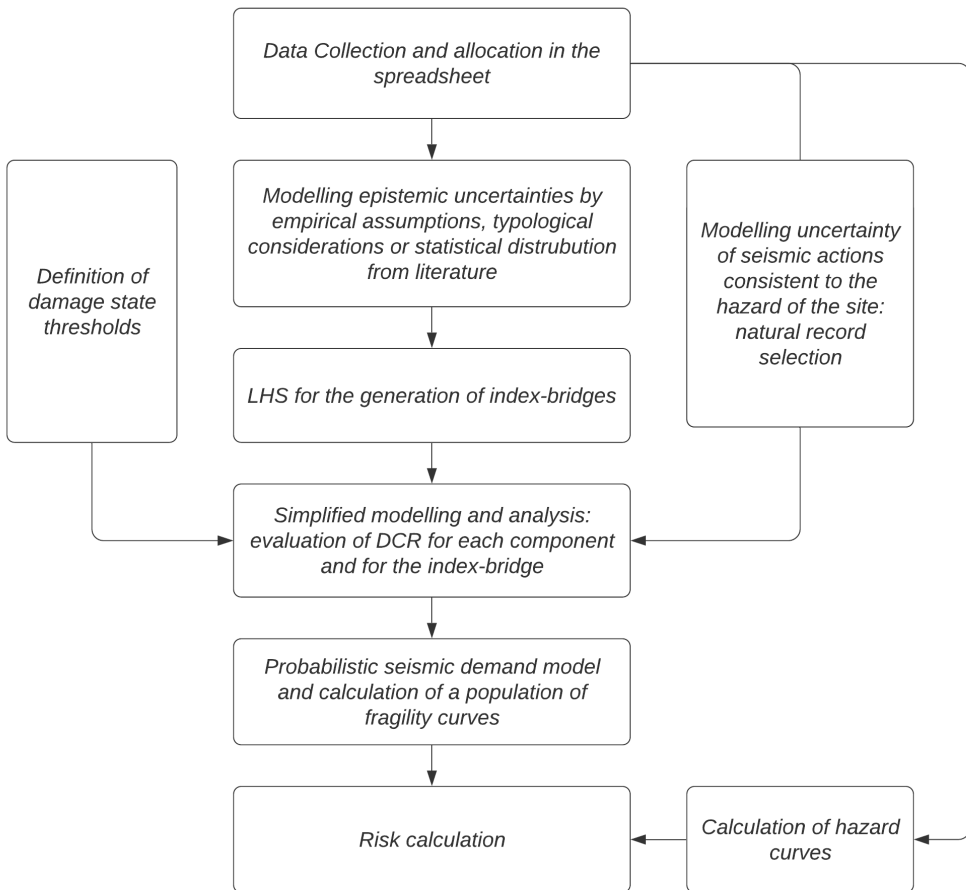


Figure 6.2: Flowchart of the proposed procedure.

ables. Each vector is composed of values randomly paired under the assumption that these belong to different intervals (i.e. in the process of sampling each interval is taken only once). At the end of the simulation process, a set composed of N bridge realisations (or index-models) is obtained. Each realisation is “deterministically” characterised and can be analysed directly.

6.2.2. Damage states

The response of a bridge subjected to earthquake-induced ground shaking can be categorized in performance levels (or limit states) depending on the damage of the structural components (e.g. piers and bearings). The DS thresholds are defined in terms of appropriate engineering demand parameters (EDP) that measure the seismic demand of each bridge component. In this study, three global DS levels are assumed, according to Cardone (2014) and Cademartori et al. (2020), that propose DS thresholds tailored for displacement-based assessment approaches.

- The DS1 is related to light damages that require minor repairs with no service interruption. No significant variation in the stiffness and strength of the members is expected.
- The DS2 identifies extensive damages that require expensive interventions and traffic interruption. However, the structure retains adequate safety with respect to structural collapse for seismic actions.
- The DS3 is related to a near-collapse limit state with severe damages that could prevent the reparability of the structure. The structure should guarantee an adequate gravity load-bearing capacity, whereas some aftershocks could cause partial or total collapse.

In this study, the global DS is related to the “local” DS thresholds of the different components which are listed in Table 6.1. Further information on the process adopted for defining the global DS based on local DS is described in Section 6.2.4.

Table 6.1: Damage state thresholds for typical bridge components

Component type	DS1	DS2	DS3	Note
RC Piers (flexural) (Priestley et al. 2007)	Δ_y	$\Delta_y + 2/3(\Delta_u - \Delta_y)$	Δ_u	Δ_y and Δ_u are the yielding and ultimate displacement of the pier in flexural response.
RC Piers (shear) (Priestley et al. 1996)	-	Δ_{sh}	$1.1\Delta_{sh}$	Δ_{sh} is the displacement corresponding to shear failure
Steel towers (ductile) Chapter X	Δ_y	$\Delta_y + 2/3(\Delta_u - \Delta_y)$	Δ_u	Δ_y is the displacement at tensile strength attainment of a diagonal brace or at buckling of an horizontal brace
Steel towers (fragile) Chapter X	-	-	Δ_u	Δ_u is the displacement at the reaching of the fragile mechanism (e.g. local or global column buckling, brittle failures of connections)
Unbolted neoprene bearings (friction/slipping) (Cardone 2014)	Δ_{fr}	Δ_{pad}	Δ_{uns}	$\Delta_{fr} = (\mu P/A)$ is the displacement corresponding to friction strength attainment. μ is the friction coefficient usually assumed as 0.4 for rubber-concrete surfaces
Unbolted neoprene bearings (roll-over) (Cardone 2014)	$\Delta_{pad/3}$	Δ_{pad}	Δ_{uns}	A is the area of the neoprene pad and P is the tributary compressive load of the bearing device. Δ_{pad} is the dimension of the bearing device in the considered direction
Bolted neoprene pads (Cardone 2014)	$1.5t_b$	$3t_b$	Δ_{uns}	t_b is the thickness of the bearing device
Fixed bearings (Cardone 2014)	-	$\Delta_{fix} + 2/3(\Delta_{uns} - \Delta_{fix})$	Δ_{uns}	Δ_{fix} is the displacement at maximum strength of the bearing device.
Sliding bearings (Cardone 2014)	Δ_{sl}	$\Delta_{sl} + 2/3(\Delta_{uns} - \Delta_{sl})$	Δ_{uns}	Δ_{sl} is the displacement capacity of the bearing device
Shear keys (Megally et al. 2002, Han et al. 2017)	Δ_{gap}	$\Delta_{u,sk}$	-	Δ_{gap} is the gap size $\Delta_{u,sk}$ is the displacement capacity of the shear key
Abutment (Sextos et al. 2008, Caltrans 2013)	Δ_{gap}	Δ_{bw}	$1.1\Delta_{bw}$	Δ_{bw} is the displacement at the reaching of the passive backfill pressure calculated from the ratio between $P_{bw} = hwp_s(h/1.7)$ and $k_{bw} = k_2w(h/1.7)$, where h and w are the height and width of the abutment backwall, k_2 is equal to $11.5(k_2N/mm^2)/m$ and p_2 is $239kPa$.

6.2.3. Simplified methodology for seismic demand evaluation

In the following sub-section, the simplified methodologies to calculate the performance of the index-models of the generated population, under a specific ground-motion shaking, is described. According to the basis of nonlinear static procedures (NSPs), equivalent single-degree-of-freedom (SDoF) pushover curves of the analysed bridge are obtained analytically in both longitudinal and transverse direction. These are subjected to a capacity spectrum-based approach performed with real (un-smoothed) response spectra to calculate the performance under a given ground motion.

The calculation of the pushover curves is based on simplified modelling approaches adapted for typical Italian bridge structural schemes. Only the nonlinear response of the substructure components (i.e. piers and abutments) and of the deck-substructure connection systems are considered, while the deck is supposed to exhibit an elastic response during the earthquake (Priestley et al. 1996). Also the nonlinear response of the foundation systems is not considered, assuming fixed base condition for piers and abutments. In fact, in past Italian design practice of bridges, the foundations were generally conservatively designed as stated by (Calvi et al. 2013). In bridges designed in the last decades, a premature failure of the substructure members or of the deck-substructure connections with respect to the foundation components is expected. This limits the shear forces transmitted to the foundations, preventing their damages (Borzi et al. 2014). However, the proposed procedure can be extended to account for soil-structure interactions following the methodology by Ni et al. (2014). Two different algorithms to calculate capacity curves can be adopted for simply supported bridges and continuous-deck bridge structural schemes.

6.2.3.1. Simplified seismic demand calculation for simply supported bridges

According to Pinto & Franchin (2010), the Individual Pier Model (IPM) is a simplified strategy to calculate the seismic performance of simply supported bridges with independent adjacent decks. In this methodology, each structural subassembly composed by the sub-structure member and the connection system of this latter to the deck can be isolated and analysed separately. The equivalent SDoF pushover curve of each sub-

assembly is calculated by combining the force-displacement relationships of the connection system (e.g. bearing devices, shear keys) and of the pier/abutment that are assumed to act as a series system. For RC bridges, the force-displacement behaviour of single-shaft piers should be calculated according to the formulation proposed in Chapter 3. For this task, a moment-curvature analysis is necessary and can be performed via programming routines such as CUMBIA (Montejo & Kowalsky 2007) or surrogate meta-models (Gentile et al. 2018*b,a*). The force-displacement relationship of RC framed (i.e. multi-column) piers with high flexural stiffness of the pier cap can be commonly calculated aggregating the force-displacement relations of the columns working as a parallel system (i.e. assuming a shear-type behaviour). A more accurate evaluation can be performed utilising the Simple Lateral Mechanism Analysis (SLaMA) described in the NZSEE guidelines (NZSEE 2017) or the study by Gentile, del Vecchio, Pampanin, Raffaele & Uva (2019). The force-displacement relationship of steel-truss piers can be calculated according to Chapter 4.

The force-displacement relationship of the connection system between the deck and the substructure is composed by the force-displacement response of the bearings or shear-keys, if present. As an example, in most of the existing simply-supported bridges, usually fixed bearing devices (e.g. steel hinges or pin bearings) are not seismically designed and could experience brittle shear failures under strong seismic shaking and displacement demand, followed by a pure friction (concrete-to-concrete) behaviour until deck unseating. Differently, rubber bearings (e.g. simple neoprene pads), which were widely used in Italy between 1960 and 1990, considerably affect the seismic response of bridge subassemblies with their high flexibility (Tortolini et al. 2011). Indeed, the shear strength of unbolted neoprene pads is governed only by friction between rubber and concrete and likely affects the hierarchy of strengths in the subassembly. The force-displacement relationship of the deck-pier connection system can be computed by aggregating the contribution of the bearing devices acting in parallel. If present, the contribution of shear keys should be also considered. Multilinear force-displacement laws for the mechanical characterisation of bearing devices and shear keys are reported in (Cardone 2014).

According to the IPM framework, the pushover curve of the equivalent SDoF represen-

tative of each subassembly can be calculated in a simplified way, assuming that all the mass (and the seismic force) is entirely lumped in the centre of mass of the deck. Once the pushover curve of the subassembly is characterised, its performance displacement under a given ground-motion record can be conveniently approximated adopting one of the NSPs mentioned in Chapter 5. In this study, the adoption of a capacity spectrum method (CSM) approach with real unscaled response spectra is proposed, exploiting the non-iterative methodology described in Chapter 5.

Referring to a subassembly composed by the pier and its connection system to the deck composed of bearing devices only, for a given value of the base shear (V_b), the effective displacement of the equivalent SDoF system (Δ_{eff}) is given by the sum of the displacements of the pier (Δ_{pier}) and the connection system (Δ_{bear}), obtained interpolating the respective constitutive laws at V_b (Figure 6.3). The equivalent viscous damping of the pier and the connection system, subjected to a given displacement, is calculated through the ductility-based formulation proposed by Priestley et al. (2007) reported in Equation 6.1 where a 5% elastic damping is assumed and C_{evd} depends on the cyclic response of the component. It can be defined as 0.444 for piers with Takeda Thin-type hysteretic response and as 0.565 for neoprene bearing devices characterised by an elastic-perfectly plastic cyclic response. Other coefficients C_{evd} can be computed according to the procedure proposed in Priestley et al. (2007). The equivalent viscous damping of the subassembly for a given Δ_{sub} is computed by Equation 6.2 which assumes that the effective damping of each component is proportional to the work carried out during the seismic response, and consequently (since the shear is equal between the components in the series system) to its displacement.

$$\xi = 0.05 + C_{evd} \left(\frac{\mu - 1}{\pi \mu} \right) \quad (6.1)$$

$$\xi_{sub} = \frac{\Delta_{pier} \xi_{pier} V_{pier} + \Delta_{bear} \xi_{bear} V_{bear}}{\Delta_{pier} V_{pier} + \Delta_{bear} V_{bear}} = \frac{\Delta_{pier} \xi_{pier} + \Delta_{bear} \xi_{bear}}{\Delta_{sub}} \quad (6.2)$$

For increasing values of base shear, the effective displacement and the equivalent viscous damping of the subassembly is calculated, until the deck-substructure connection or the pier reach the ultimate displacement capacity. If very high-stiffness bearings are

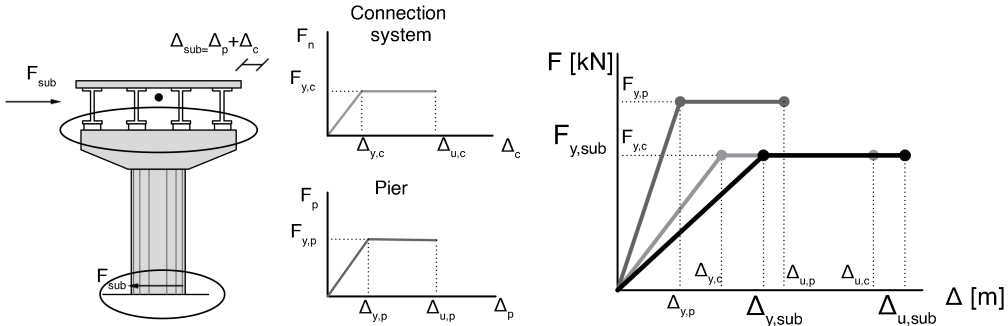


Figure 6.3: Simplified calculation of force-displacement curve for deck-pier subassemblies

present, only the force-displacement behaviour of the pier/abutment is considered in the subassembly pushover curve whose ultimate capacity should appropriately consider the maximum strength of the bearings. The same process should be accomplished for the characterization of the deck-abutment subassemblies. In this case, if fixed abutments are assumed, the force-displacement relationship of the equivalent SDoF is represented by the connection system only.

At this stage, a set of equivalent SDoF pushover curves is associated with the different subassemblies of the analysed bridge. According to the IPM approach, each of the equivalent SDoF pushover curves is converted in a capacity spectrum (in terms of acceleration-displacement) by dividing the base shear for the corresponding effective mass which is equal to the tributary seismic mass of the subassembly. Using the CSM algorithm described in Chapter 5, the seismic performance under a given ground-motion record is calculated for each subassembly and is compared to the corresponding capacity. The displacement profile of the bridge under the considered seismic actions is composed of the performance displacement of each subassembly.

As anticipated, this approach can be adopted for analysing the seismic response of simply-supported bridges characterised by an isostatic scheme in the transverse direction, if relative rotations between adjacent decks are allowed by the deck-substructure connection systems. Cardone (2014) also claims that the IPM methods can be reliably used when there is weak interaction (i.e. unlikely impacts) between the adjacent decks and a global regular response of the bridge (i.e. high participating mass). These conditions occur when the ratio of the effective periods of the adjacent deck-pier sub-

assemblies is included between 0.50s and 2.00s. The average values of the periods should also be included in the range [0.65; 1.50]s. It is worth noting that the IPM can not be applied for analysing skewed bridges (skew angle higher than 15°). It is worth noting that, in this study, the approach is described for subassemblies in which the pier mass is negligible (lower than 10% Priestley et al. (1996)) with respect to the tributary mass of the deck. If this condition is not satisfied, a two-mass model can be used to characterise each subassembly, composed by the mass of the deck (lumped at the height of the deck centre of mass) and the mass of the pier cap plus a portion of the mass of the pier (placed at the centre of mass of the pier cap).

In the longitudinal direction, the IPM can be used depending on the width of the expansion joints between adjacent decks. Under seismic shaking, each pier responds independently until the closure of the joints is reached and impacts between adjacent decks occur. The tributary seismic mass of each subassembly depends on the fixity conditions of bearing devices (i.e. fixed or free) and their capacity to transfer shear forces. If the expansion joints between the decks are seismically designed, their width is adequate to avoid impacts and usually, the IPM approach could be applied for the response in the longitudinal direction. On the contrary, for bridges with joints designed considering the thermal deformations only, the premature closure of joints under seismic action generates a parallel system, in which the deck-pier and deck-abutment subassemblies resist the seismic shear forces depending on the proper stiffness 6.4. This also occurs when shock transmitters are placed on the piers. When the closure of the deck-abutment joints is likely to occur, the abutment-backfill interaction should be appropriately modelled, since it strongly affects the longitudinal seismic behaviour (Shamsabadi & Kapuskar 2010) and fragility. Guidelines for the modelling of the abutment-backfill interaction are reported in Sextos et al. (2008) and Caltrans (2013).

If a parallel system composed of the different subassemblies is likely to be activated. The capacity curve of the equivalent SDoF of the bridge could be calculated by aggregating the force-displacement laws of each subassembly, assuming that these are subjected to the same deck displacement. Given a pre-determined target displacement of a generic node of the deck, the shear forces in each subassembly can be obtained by interpolating the corresponding force-displacement laws and can be summed up for cal-

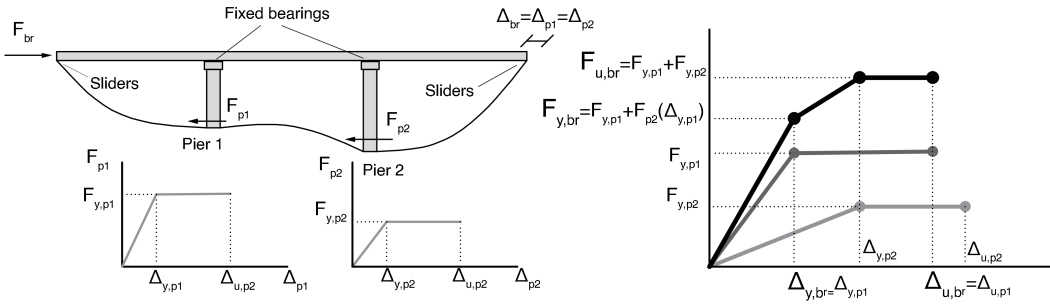


Figure 6.4: Simplified calculation of force-displacement curve for bridges in longitudinal direction acting as a parallel system (fixed bearings on the piers only are considered)

culating the total base shear. Repeating this process for incremental deck displacement, the equivalent SDoF capacity curve is achieved. For each step, the equivalent viscous damping of the equivalent SDoF system is calculated via Equation 6.3. The capacity curve can thus be subjected to the CSM algorithm to calculate the performance point.

$$\xi_{eff} = \sum_{j=1}^N \frac{\xi_{sub,j} V_{sub,j}}{V_{sub,j}} \quad (6.3)$$

6.2.3.2. Simplified seismic demand calculation for continuous-deck bridges

The seismic behaviour of continuous-deck (hyperstatic) bridges in the transverse direction is characterized by the coexistence of two load paths since a portion of the total seismic loads is directly transferred by the deck to the abutments, while the remaining part is resisted by the piers. The tributary seismic load related to the different load path depends on the ratio between the stiffness of the deck and the piers for transverse seismic action.

To calculate the capacity curve of this bridge typology, the process described in subsection 6.2.3.1 for the characterization of single subassemblies is nested in the procedure proposed by Şadan et al. (2013), Perdomo & Monteiro (2020) and extended by the author and other colleagues in Gentile, Nettis & Raffaele (2020). This latter is extensively described in Chapter 3. It resorts to simplified mechanical modelling and

analysis which are consistent with the purposes of regional-scale analyses. The model of the bridge is a simple elastic beam with an appropriate transverse moment of inertia, placed on elastic springs equipped with effective stiffness in target displacement condition which represent the deck-pier and deck-abutment subassemblies. The effective masses are lumped in the main nodes of the deck corresponding to the substructure members. The analysis approach is composed of a series of progressive iterative linear (modal or static) analyses performed for incremental values of control node displacement. The stiffness of the supports is updated step-by-step according to the increasing ductility demand.

In the longitudinal direction, the capacity curve of the bridge is the aggregation of the force-displacement laws of the subassemblies that absorb the seismic action. In existing bridges, a common old design strategy was based on the definition of a “fixed” pier designed to resist the full seismic load, whereas the others were released from the deck through roller bearings or sliders. In this case, the capacity curve of the bridge coincides with the force-displacement relationship of the “fixed” subassembly. Contrarily, if more subassemblies are designed to resist the seismic actions, the force-displacement laws of these subassemblies should be aggregated as a parallel system (see sub-section 6.2.3.1).

6.2.4. Adopted methodology for fragility analysis

This section explains the cloud approach adopted for fragility analysis. It consists in an extension of the Cloud-CSM approach presented in Chapter 5 dealing with (simply supported girders) bridges. Fragility analysis of complex structural systems composed by several members, like bridges, is not a straightforward task. Indeed, the global DS of the bridge is related to the DS of different components. Commonly, fragility relationships of bridges are calculated through a detailed probabilistic approach, involving an appropriate correlation of the component-specific fragility functions (Choi et al. 2004, Stefanidou & Kappos 2017, Tavares et al. 2012), or via a simplified approach in which the bridge is seen as a series system where the “weakest” member (i.e. the most damaged component) determines the DS of the bridge at a given seismic intensity (Borzi et al. 2014). This latter approach is considered suitable for simplified regional-scale

analysis and is used in this study. The EDP which expresses the performance of a generic bridge component subjected to a given ($j - th$) ground-motion shaking with respect to a given DS (DS_k), is a Demand Capacity Ratio (DCR) (Equation 6.4).

$$DCR_{ij}^{DS_k} = \frac{\Delta_{ij}}{\Delta_i^{DS_k}} \tag{6.4}$$

The global DCR for the analysed ground-motion record is the maximum of the DCRs of the different components. As an example, if only the piers, the bearings and the abutments are considered in the determination of the bridge DS, the global DCR is given by Equation 6.5 where the p,b and ab subscripts indicate piers, bearing devices and abutments respectively.

$$DCR_j^{DS_k} = max(DCR_{p1,j}^{DS_k}, \dots, DCR_{pN,j}^{DS_k}, DCR_{b1,j}^{DS_k}, \dots, DCR_{bN,j}^{DS_k}, DCR_{ab1,j}^{DS_k}, DCR_{ab2,j}^{DS_k}) \tag{6.5}$$

In this study, the fragility relationships express the probability of the bridge to reach or exceed a unitary DCR^{DS} for a given shaking intensity measure (IM).

Various literature studies focus on the definition of optimal IMs for probabilistic seismic analysis of bridges. Particularly, the adopted IM should be chosen depending on its efficiency, sufficiency, practicality and hazard computability (D’Ayala et al. 2013). A wide description of these characteristics is proposed by Padgett et al. (2008). The efficiency is a particularly important factor for fragility analysis since it expresses the correlation between the IM and the EDP and it is measured by the amount of variation in EDP for a given IM within a probabilistic seismic demand model. Padgett et al. (2008) identified the Peak Ground Acceleration (PGA) as an adequate IM for fragility analysis of bridge portfolios. Contrarily, dealing with isolated structures, IMs calculated based on spectral pseudo accelerations/displacements corresponding to the modal period/s of the investigated structure outperform PGA in terms of efficiency (Minas & Galasso 2019, Monteiro et al. 2019) As an example, it is commonly expected that the PGA, which is not related to the vibration modes of the investigated structure, can be less efficient

than the spectral acceleration at first mode.

Recently, O'Reilly et al. (2019) investigated the efficiency of $AvgSa$, defined as the geometric mean of the spectral accelerations within a determined period range (also used in Chapter 5). $AvgSa$ can be successfully adopted for fragility analysis of specific structures considering the period elongation during the seismic response, or higher-mode contributions. Moreover, $AvgSa$ suits for class fragility analysis if the period range is calibrated depending on the modal properties of the structures within the class. Fragility curves are calculated based on regression-based probabilistic seismic demand models as proposed within the cloud analysis approach by Jalayer et al. (2017) and adapted in the Cloud-CSM in Section 5. The results of the previous analyses are organized in couples of [EDP, IM], where the EDP is the DCR_j^{DS} and the IM is the $AvgSa_j$ which refers to each ground motion j (i.e. the "cloud data"). The probabilistic seismic demand model is represented by a power-law model ($DCR = aAvgSa^b$) which describes the relationship between the median value of DCR (α_{DCR}), and $AvgSa$. The parameters $[a, b]$ are estimated by fitting a linear model to the cloud data transposed in the natural logarithmic space (Equation 6.6), via the Least Square Regression Method.

$$E[\ln(DCR)|AvgSa] = \ln(\alpha_{DCR|AvgSa}) = \ln(a) + b \ln(AvgSa) \quad (6.6)$$

The dispersion of the demand around the median value estimated with the regression model is assumed constant varying the value of $AvgSa$ and is given by Equation (Equation 6.6) where M is the number of ground motion records.

$$\beta_{DCR|AvgSa} = \sqrt{\frac{\sum_{j=1}^M \ln(DCR_j) - \ln(aAvgSa^b)}{M - 2}} \quad (6.7)$$

Finally, the fragility function is represented by the probability of exceedance of the DS given an IM value, $P(DCR^{DS} = 1|AvgSa)$, and can be calculated by Equation 6.8 where $\Phi(\cdot)$ is the standard cumulative distribution function.

$$P(DCR > 1|AvgSa) = \Phi\left(\frac{\ln \alpha_{DCR|AvgSa}}{\beta_{DCR|AvgSa}}\right) = \Phi\left(\frac{\ln aAvgSa^b}{\beta_{DCR|AvgSa}}\right) \quad (6.8)$$

Within this approach, the seismic action should be modelled by a suite of natural ground motions, representative of the seismic hazard condition of the site. Unscaled ground motions can be adopted, although some limited amplitude-scaling could be required to improve the robustness in fitting the power-law model. This approach is largely utilised for the analysis of portfolios of structures, where a specific-structure record selection is not convenient.

By using this procedure, several fragility curves (i.e. one for each DS) can be associated with each index-bridge, reporting its probabilistic response considering record-to-record variability only.

To evaluate the influence of knowledge-based uncertainty on the main bridge at a given DS, all the fragility curves calculated for the index-models can be analysed in a stack of fragility curves which can be, in turn, resumed by significant percentiles (e.g. 10th, 50th, 90th) (Bradley 2010).

A synthetic fragility curve, expressing the probability to reach a DS, comprehensive of both aleatory and epistemic uncertainty can be defined calculating the median ($\alpha_{DS,bridge}$) with Equation 6.9, being equal to the 50th percentiles of the population of the medians of the index-bridges. N is the number of index-bridges of the population and $\alpha_{DS,k}$ is the median fragility related to the $k - th$ index-bridge for a generic DS. The overall dispersion ($\beta_{DS,bridge}$) should account for both the dispersion of the fragility curves of each index-model ($\beta_{DS,k}$) and the dispersion around the medians. These contributions are combined with the SRSS rule (Equation 6.10).

$$\ln \alpha_{DS,bridge} = \left(\sum_{k=1}^N \ln \alpha_{DS,k} \right) / N \tag{6.9}$$

$$\beta_{DS,bridge} = \sqrt{\left(\frac{1}{N} \sum_{k=1}^N \beta_{DS,k} \right)^2 + \frac{1}{N} \left(\sum_{k=1}^N \ln \alpha_{DS,k} - \ln \alpha_{DS,bridge} \right)^2} \tag{6.10}$$

6.2.5. Risk quantification

The approach for quantifying the seismic risk is described in this sub-section. For this purpose, hazard curves that express the mean annual frequency of exceedance of a ground-motion IM for a given location are needed. These are calculated via probabilistic seismic hazard analysis of the site of interest. Since, to calculate the seismic risk, the integration between hazard and fragility should be performed, the adopted IM for hazard curves should be consistent with the one used for fragility analysis. The suitability of an IM to perform probabilistic seismic hazard analysis is expressed by the so-called hazard computability which measures the amount of effort required to perform the probabilistic seismic hazard analysis (Giovenale et al. 2004). PGA is a good choice in terms of hazard computability, since it is used for proposing a wide variety of seismic hazard maps, it is used in the codes and to develop ground motion prediction equations. It is worth mentioning that ground-motion prediction models with low uncertainty are available for "simple" IM, such as PGV or pseudo-spectral accelerations at given periods (Campbell & Bozorgnia 2008). Recently, Kohrangi et al. (2018) proposed empirical ground-motion prediction models also for $AvgSa$, estimating the seismic hazard with low uncertainty. In this study, the seismic risk is calculated in terms of mean annual frequency of exceeding a determined DS and it is indicated with λ_{DS} . It can be estimated by Equation 6.11, where the first term, $P(DS|IM)$, is the fragility relationship, while the second term $H(IM)$ is the hazard curve. In the second format of Equation 6.11, $\left| \frac{dH(IM)}{dIM} \right|$ expresses the slope of the hazard curve.

$$\lambda_{DS} = \int_0^{+\infty} P(DS|IM) \cdot |dH(IM)| = \int_0^{+\infty} P(DS|IM) \cdot \left| \frac{dH(IM)}{dIM} \right| dIM \quad (6.11)$$

Numerical approaches can be used to solve Equation 6.11. The approach used in this study is described by Eads et al. (2013) and is expressed via Equation 6.12. If the fragility and the slope of the hazard curves are divided in a high number of small intervals (with amplitude ΔIM), the Equation 6.11 can be re-written as in Equation 6.12. The contribution to the risk of the i -th interval $[IM_i, IM_i + \Delta IM]$ is calculated as the

product of the amplitude of ΔIM multiplied by the average probability of reaching the DS and (the absolute value of) the slope of the hazard curve in the considered interval. The λ_{DS} is equal to the sum of the contributions of all the intervals.

$$\lambda_{DS} = \sum_{i=1}^{+\infty} P(DS|IM_i) \cdot \left| \frac{dH(IM_i)}{dIM} \right| \Delta IM_i \quad (6.12)$$

An alternative simplified methodology to calculate the risk, by approximating the integral in a closed-form formulation, is proposed by (Cornell et al. 2002).

In the proposed procedure, the λ_{DS} is calculated using the fragility curves corresponding to the 10th, 50th and 90th percentiles with the aim to quantify the influence of knowledge-based uncertainties in the determination of the seismic risk. The larger is the range, the higher is the influence of epistemic uncertainty associated with the bridge. The variation of seismic risk, if calculated for a consistent number of bridges initially characterised depending on the proper knowledge level, suits for addressing refined inspections only towards bridges where such a process could involve a significant improvement in risk estimates.

6.3. Application of the framework on case-study bridges

The seismic risk assessment methodology described in Section 6.2 is applied to the case-study bridges, part of the Basilicata National road network, described in Chapter 2. The case studies belong to the same typology, i.e. simply-supported girder RC bridges with single-shaft piers, and are selected to test the applicability of the proposed procedure within the same bridge class. As stated by Cardone et al. (2011), this is the most spread typology of bridges in Italy.

The knowledge data on these bridges are collected via the "desk" approach (i.e. without *in-situ* surveys), the knowledge-based uncertainties are characterized after the data collection process and a simulation of the incomplete data is performed. First, fragility curves are calculated using *AvgSa* as IM. The robustness of the adopted statistical method to generate the index-bridge population is checked varying the variation of the outcomes for different sampling and different sizes of the dataset of generated population. Furthermore, a discussion on the influence of the epistemic uncertainty within

fragility analysis is reported.

Then, the simplified procedure for risk assessment accounting knowledge-based uncertainties is applied. For this latter task, PGA is used as IM since hazard curves in terms of PGA are easily retrievable in practical application.

Subsequently, a more refined data collection is addressed to one of these bridges and the sensitivity of the fragility curves and risk to the different amount of the knowledge-based uncertainty between the two knowledge levels is discussed. This latter case study is also analysed by means of NLTHA in order to evaluate the approximations introduced by the simplified methodology for the seismic performance assessment.

6.3.1. Data collection and modelling uncertainty for data completion

A description of the data collection approach performed for selecting the case studies is described in Chapter 2. The described data form (2.3.1), suitable to allocate the geometry and constructive data, is connected to an Excel-based spreadsheet which is used as input for an appropriately developed MATLAB-based routine that performs the risk calculation according to the proposed approach. The filled-in spreadsheets are reported in A.

The main features of the case-study bridges (e.g. number and length of spans, height and typology of the piers, connection system between the deck and the substructure members) are reported in Figure 6.5.

Table 6.2 lists the uncertainties associated to the case studies which were defined in terms of statistical distribution derived from literature studies (Nielson 2005, Nielson & DesRoches 2007, Cardone et al. 2011, Zelaschi et al. 2016, Tavares et al. 2012, Monteiro 2016, Soleimani 2020). If the statistical distributions are not available, uniform distributions (continuous and discrete) defined only by the lower and upper bounds, are used for simulating the maximum uncertainty as suggested by Celik & Ellingwood (2010). Note that, in this study, statistical distributions defined by analysing bridge portfolios from different geographical contexts are used. It is expected that more data about Italian highway and railway bridges will be available in future, improving the reliability of the proposed assessment process.

It is worth specifying that for the B1 bridge the typology of the deck-substructure con-

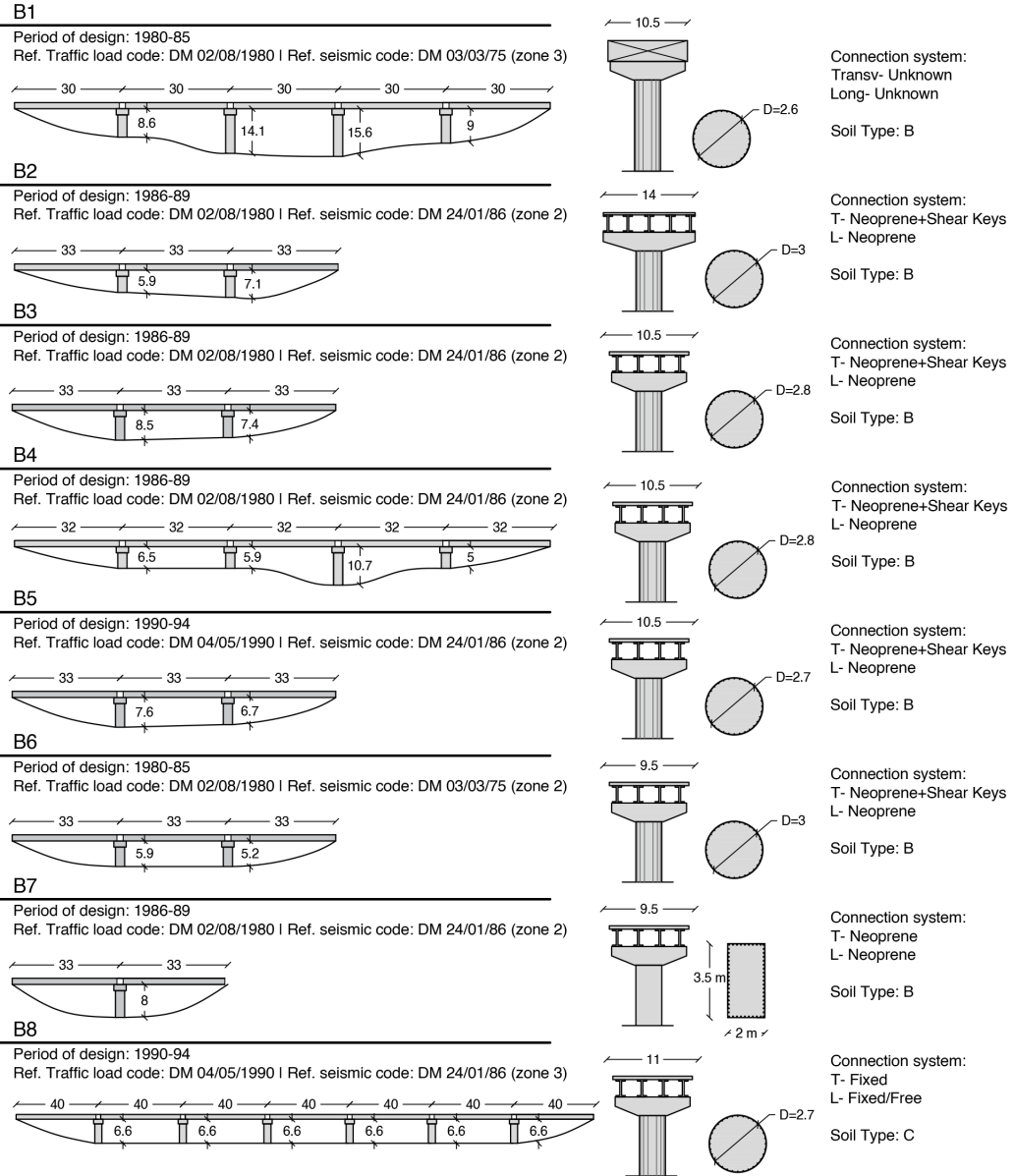


Figure 6.5: Geometry and constructive characteristics of the case studies

nection system is unknown. Thus, a discrete categorical variability is assumed to vary between two configurations: with fixed/free bearings and with neoprene rubber bearings as done in Borzi et al. (2014). In the first configuration, the bearings are assumed to be fixed in the transverse direction, while a fixed and movable bearing line is placed on the

Table 6.2: Statistical characteristics of epistemic uncertainty parameters

Parameter	Distribution	Parameters/Values	
Characteristic compressive strength of concrete (f_{ck})	Uniform (Discrete)	[25 – 30 – 35]	MPa
Characteristic tensile strength of steel (f_{yk})	Uniform (Discrete)	[375 – 440]	MPa
Mean concrete compressive strength (f_c)	Normal	$\mu = 1, \sigma = 0.18$	Factor
Mean steel Tensile Strength (f_y)	Normal	$\mu = 1, \sigma = 0.09$	Factor
Transverse reinforcement volumetric ratio (ρ_t)	Uniform (Discrete)	0.05 – 0.1	%
Abutment gap size ¹	Normal	$\mu = 24.5, \sigma = 5$	mm
Shear modulus of neoprene bearings (G_{neop})	Uniform	$l = 0.8, u = 1.2$	MPa
Thickness of neoprene bearings ² (t_b)	Uniform	$l = 40, u = 70$	mm
Abutment passive stiffness	Uniform	$l = 0.5, u = 1.5$	Factor
Mass variability (G1 + G2)	Uniform	$l = 0.9, u = 1.1$	Factor

¹the gap size of B9 was measured (150 mm), no variability is assumed

²the height of the neoprene bearing is fixed as 30 mm for B7

top of each pier in the longitudinal direction. In this way, the tributary seismic mass of each pier is equal to the mass of a single span. This was a common old design strategy in the Italian context.

Furthermore, since the cross-section of the deck is unknown, variability between three and four devices per bearing line is empirically assumed by observing the other bridges in the dataset having similar deck width. As shown in Table 6.2, since no original design blueprints are retrieved, variability in the design class of the materials (f_{ck} and f_{yk}) is assumed for all the bridges. The mean and dispersion of the mean strength values (f_{cm} and f_{ym}) are calculated depending on the characteristic values as suggested by Borzi et al. (2008), assuming a coefficient of variation of 0.09 and 0.18 for steel and concrete respectively (Monteiro 2016).

It is recognized that the mechanical properties of the materials are strongly influenced by preparation and manufacturing issues and are expected to vary depending on the constructive methodology of the geographical context. In this case, no experimental

values are available for the Basilicata region, and the values adopted are calibrated for the Italian context.

The LHS is performed for each case-study bridge to generate a population of index-models. All index-models are grouped for couples of design concrete and steel strengths and the longitudinal reinforcement are calculated by means of a simulated design procedure. An appropriate MATLAB routine is developed to perform the simulated design of single-shaft piers according to Italian old regulatory codes for bridges. The procedure automatically neglects the couples of design concrete and steel classes which yield an incompatible design with respect to the old reference code. Furthermore, it is recognized that, in the '70-'90 decades, the design of transverse reinforcements of bridge columns was dictated by constructive needs rather than mechanical because of the low seismic design actions. Consequently, the volumetric ratio of the transverse reinforcement ρ_t is modelled with a uniform distribution, as indicated in Table 6.2, and not calculated via the simulated design. The minimum and maximum values are retrieved by the study of Cardone et al. (2011). In Figure 6.5, the reference design codes are specified for all the case studies. It is worth mentioning that the prescribed design seismic action was very similar for the bridges from B2 to B8, considering that these are located in a medium-level seismic zone, according to the old seismic classification. In fact, the *Decreto Ministro dei Lavori Pubblici (DM) 3 marzo 1975 -Approvazione delle norme tecniche per le costruzioni in zone sismiche.* (1975) and *Decreto Ministro dei Lavori Pubblici (DM) 24 gennaio 1986 - Norme tecniche relative alle costruzioni antisismiche.* (1986) stated that the seismic design force is proportional to the seismic mass multiplied by a coefficient related to the seismic hazard zone. In addition to the previous *Decreto Ministro dei Lavori Pubblici (DM) 3 marzo 1975 -Approvazione delle norme tecniche per le costruzioni in zone sismiche.* (1975), the *Decreto Ministro dei Lavori Pubblici (DM) 24 gennaio 1986 - Norme tecniche relative alle costruzioni antisismiche.* (1986) added another coefficient to the seismic design force which considers the importance of the designed structure.

Differently, the B1 is located in a low-level seismic zone, thus probably it is designed with a lower level of seismic actions. It is worth mentioning that the B9 bridge is the only one in which a seismically designed gap between the deck and abutments is recognized.

In the other cases, since the width of the gap is very low and not measurable without an in-situ inspection, it is assumed to vary as suggested by Tavares et al. (2012), Nielson & DesRoches (2007) and as confirmed by Cademartori et al. (2020)] for not-seismically designed Italian bridges.

The record-to-record variability is considered in fragility analysis through an appropriate ground motions suite. To this aim, a suite of 100 natural ground motions is selected from the SIMBAD database (Selected Input Motions for displacement-Based Assessment and Design, Smerzini et al. (2014)) consistently with the characteristic of soil type, magnitude and distance of expected earthquakes in the investigated region. The magnitude and distance de-aggregation is achieved using the software Rexel (Iervolino et al. 2010) for all the bridges of the dataset. The soil type is collected thanks to the study by Forte et al. (2019) and it is indicated in Figure 6.5. All the bridges are characterised by a soil type B, but the B8 whose soil type C. A preliminary dataset of 176 ground motions compatible with the average required values of magnitude and distance within the analysed bridge dataset and for soil type B is collected from the considered database. Then, the 100 records with the highest PGA are selected to perform the fragility analysis. The PGA of the selected record varies between 1.77 and 0.16 g. The criteria proposed by Jalayer et al. (2017) for the record selection to be used within a cloud approach were also considered.

6.3.2. Warning Class definition according to the Italian guidelines on existing bridges

A preliminary evaluation the Seismic Warning Class as suggested by the Ministero delle Infrastrutture e dei Trasporti (2020) is performed. The Seismic Warning Class expresses a proxy of the risk associated to the single structure and it is defined according to the hazard class, vulnerability class and exposure class. Both the final Seismic Warning Class and the specific hazard/vulnerability/exposure classes are categorised as High-Medium High-Medium-Medium Low and Low according to some structural/non-structural parameters. For the whole procedure, the reader is referred to the guidelines presented by Ministero delle Infrastrutture e dei Trasporti (2020). The calculation of the above-mentioned classes for the case-study bridges is presented in Table 6.3.

The hazard class is computed by using the PGA on rigid soil prescribed by the Italian

Code (Ministero delle Infrastrutture e dei Trasporti 2018) having 10% probability to be exceeded in 50 years (return period equal to 475 years), the topographic class and soil type. According to Table 6.3, the bridges B2, B3 and B7 are associated to the highest hazard class. The vulnerability class is associated to structural features determining the response of the structure under the seismic action. It is defined based on: material of the superstructure, static scheme, number of spans, maximum span length, presence of critical components/features (e.g single-column piers, irregular height distribution of the piers along the bridge length, skewed/curved bridges) and degradation condition of the structure. This latter parameter is defined as a degradation index and requires an on-site inspection based on the observation and judgemental evaluation of existing defects or damages. In this study, it is neglected since the results of the on-site inspection are not available. As shown in Table 6.3, all the case studies are characterised by a high vulnerability class. Finally, the exposure class is based on the service loads (i.e. mean annual traffic in terms of number of ordinary and commercial vehicles per day), the maximum span length, the presence of alternative routes in case of bridge inaccessibility, the use class of the obstacle which is overpassed by the bridge and the importance of the bridge for emergency use (i.e. if the road/bridge is recognised as a strategic structure within emergency management plans). In this case, the traffic frequency information is not available and it is neglected in the evaluation. All the case-study bridges, part of the national road network, are characterised by medium-high or high exposure, while the bridge B8 (associated to the provincial road network) corresponds to a medium-low exposure class.

Because of the high vulnerability class, the Seismic Warning Class of the analysed bridges results to be high. Therefore, according to the Italian guidelines (Ministero delle Infrastrutture e dei Trasporti 2020), all the case studies are associated to the same degree of seismic risk and can be defined as "high priority" bridges in road authority's bridge management systems.

6.3.3. Modelling and analysis assumptions

The seismic assessment is performed according to the CSM-based procedure described in Section 6.2.3.1 for simply supported bridges. To this aim, the moment-curvature

Table 6.3: Definition of the Warning Class according to Ministero delle Infrastrutture e dei Trasporti (2020)

	B1	B2	B3	B4	B5	B6	B7	B8
PGA	$0.10g \leq$ $PGA <$ $0.15g$	$PGA \geq$ $0.25g$	$PGA \geq$ $0.25g$	$0.15g \leq$ $PGA <$ $0.25g$	$0.15g \leq$ $PGA <$ $0.25g$	$0.15g \leq$ $PGA <$ $0.25g$	$PGA \geq$ $0.25g$	$0.10g \leq$ $PGA <$ $0.15g$
Topographic class	T1	T1	T1	T1	T1	T1	T1	T1
Soil Class	B	B	B	B	B	B	B	C
Hazard Class	MEDIUM	HIGH	HIGH	MEDIUM-HIGH	MEDIUM-HIGH	MEDIUM-HIGH	HIGH	MEDIUM-HIGH
Deck material	Prestr. Conc.	Prestr. Conc.	Prestr. Conc.	Prestr. Conc.	Prestr. Conc.	Prestr. Conc.	Prestr. Conc.	Prestr. Conc.
Static scheme	Isostatic	Isostatic	Isostatic	Isostatic	Isostatic	Isostatic	Isostatic	Isostatic
Num. Spans	Multi-span	Multi-span	Multi-span	Multi-span	Multi-span	Multi-span	Multi-span	Multi-span
Max span length	High	High	High	High	High	High	High	High
Critical elements	Single-col. piers	Single-col. piers	Single-col. piers	Single-col. piers	Single-col. piers	Single-col. piers	Single-col. piers	Single-col. piers
Seismic Design	Seismic	Seismic	Seismic	Seismic	Seismic	Seismic	Seismic	Seismic
Degradation index	-	-	-	-	-	-	-	-
Vulnerability Class	HIGH	HIGH	HIGH	HIGH	HIGH	HIGH	HIGH	HIGH
Traffic	-	-	-	-	-	-	-	-
Max span length	Medium	Medium	Medium	Medium	Medium	Medium	Medium	Medium
Alternative routes	No	No	No	No	No	No	No	Yes
Overpassed feature	Low	Low	Medium	Low	Low	Medium	Low	Low
Strategic	Yes	Yes	Yes	Yes	Yes	Yes	Yes	No
Exposure class	MEDIUM-HIGH	MEDIUM-HIGH	HIGH	MEDIUM-HIGH	MEDIUM-HIGH	HIGH	MEDIUM-HIGH	MEDIUM-LOW
Warning class	HIGH	HIGH	HIGH	HIGH	HIGH	HIGH	HIGH	HIGH

laws of the piers are calculated using the MATLAB routine CUMBIA (Montejo & Kowalsky 2007). The mechanical behaviour of the different connection system typologies is modelled as follows. An elastic perfectly-plastic behaviour is assigned to the neoprene bearings, assuming a slipping failure between the neoprene and the concrete surfaces. This failure mechanism is described by Cardone (2014) for low-thickness neoprene bearings. The stiffness of neoprene bearings is equal to $k_b = GA/t_b$ (Table 6.2) and the yielding displacement $\Delta_{y,b}$ is equal to the 150% of the thickness of the pad. When the neoprene bearings are present together with shear keys, the parallel contribution of this component should be calculated and the hierarchy of strength should be checked. In these cases, it is assumed that the maximum strength of the piers is reached before the connection systems and the contribution of the flexibility of the connection system to the subassembly top displacement is neglected. The same consideration is applied for subassemblies having fixed bearings. Finally, The abutment-backfill interaction for seat type abutments is calculated as proposed in Caltrans (2013), Sextos et al. (2008). The proposed approach provides for calculating a population of fragility curves to be associated with the main bridges to capture the variability in seismic performance depending on the specific uncertainties. To this aim, $AvgSa$ is used as IM which is calculated within a period range calibrated considering the vibration modes of the analysed bridges. A preliminary modal analysis of all the bridges is performed considering a single model characterised by average values of the uncertainties. Two average models are associated with B1 considering neoprene and fixed bearings. The results show that the secant-to-yielding period of the first mode in longitudinal direction ranges between 0.7 and 1.5 s. In the transverse direction, the elastic periods of the subassemblies range within a minimum of 0.5 s, (e.g. piers with fixed bearing or abutments with neoprene bearings) and a maximum of 1.6s for the tallest piers (which is 20m-high pier of the B1 bridge with neoprene bearings). Given this outcome, $AvgSa$ is calculated for each ground-motion record using a lower bound of 0.5 s, since higher modes with lower periods are not accounted for in the simplified procedure, and an upper bound of 1.6 s, expecting that the period elongation would affect mostly the subassemblies with high stiffness (i.e. low elastic period).

6.3.4. Sample size calibration

A preliminary step to provide for robustness in the LHS-based model generation is performed. The aim of this step is to define a sample size that is a compromise between computational effort and representativeness of the generated population. For this task, only the B1 bridge is considered, which is deemed to be the case study with higher influence of uncertainty, according to Table 6.2. First, a population of 500 index-models is generated, the set of fragility curves is derived and the 10th, 50th and 90th percentiles of the median fragility calculated at DS3, α_{DS3} , are extracted and assumed as optimal estimations. Then, the process is repeated several times reducing the sampling size. The stability of the outcomes reducing the sampling size is evaluated with respect to the optimal values, calculating the relative errors between the percentiles calculated using the reduced sampling size α_{DS3} and the optimal estimate. The results are reported in 6.6, which shows that errors within a range of $\pm 10\%$ are achieved when a sample size of 50 realisations is fixed in both longitudinal and transverse direction analysis.

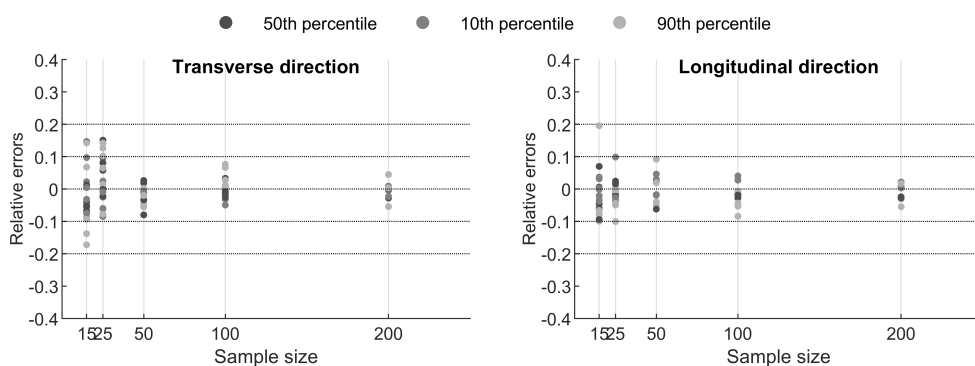


Figure 6.6: Errors on the 10th, 50th and 90th percentiles of the median fragility for B1 and DS3 varying the sampling size for B1.

6.3.5. Discussion on fragility analysis

Figure 6.7 shows the population of fragility curves at DS1 and DS3 for all the case studies analysed in transverse direction. The IM adopted for fragility analysis is *AvgSa*. The critical component which determines the reaching of a DS is extracted from all the single analysis performed with a specific record and the most recurring one is identified

for each index-bridge. In the Figure, the pattern of the single fragility curve reflects the most recurring critical component selected among pier, deck-pier connection and deck-abutment connection (as indicated in the legend).

As expected, the population of fragility curves of the B1 bridge shows considerably more variation than the other cases since the connection system between the deck and the substructure is modelled considering a fixed/free condition of the bearings or neoprene bearings. As an example, the median at DS3 varies in a range [0.45-1.40]g. In this case, at DS1 the population of the index-bridges can be divided in two groups corresponding to different bearing systems. When the fixed/free bearings are present, the median fragility is registered at $AvgSa$ lower than 0.25 g. On the contrary, if there are neoprene bearings, the DS1 is postponed beyond $AvgSa$ equal to 0.25 g and the deck-abutment connection in most of the cases represents the critical component. This is because in these cases, the flexibility of the subassembly increases, the DS threshold is postponed when the slipping between concrete and neoprene surfaces occurs. This allows relative displacements between the deck and the piers and prevents the yielding of the piers since the shear strength of the whole bearing system is generally lower than the shear strength of the pier.

Clearly, the piers (flexural response) determine the reaching of both DS1 and DS3, for the bridges where a failure of the connection system between the deck and the substructure is prevented by the shear keys. The population of fragility curves assigned to B7 shows that the DS1 can be reached for both slipping of the neoprene bearings placed on the abutments and yielding of the pier, depending on the mechanical properties of these components. Also, DS3 can be reached for both a deck-unseating mechanism at the abutments or ultimate displacement capacity of the piers. In this case, neoprene bearings imply a particularly beneficial effect on the median fragility at DS3 with respect to the other cases. This is also enhanced by the lower seismic mass of the deck with respect to the other cases.

Figure 6.8 shows the population of fragility curves calculated for the case studies analysed in longitudinal direction. The response of the bridges from B1 to B7 is governed by the abutment-backfill system that absorbs most of the seismic actions when a displacement of the deck equal to the gap width is reached. The abutment-backwall system

prematurely reaches all the damage states with respect to the other subassemblies. Differently, in the B8 bridge the piers are the critical members since the gap width is major (i.e. seismically designed) and the impact between the deck and the abutment is anticipated by the ultimate displacement of the piers. These outcomes underline the need to model accurately the abutment behaviour dealing with seismic response assessment of existing bridges. Indeed, as reported by Shamsabadi & Kapuskar (2010), the embankment failure represents a common damage mechanism that involves traffic closure in the post-earthquake phase. This failure mode is typical of the '70-'80 Italian bridges whose deck-abutment gap is not adequately designed as observed by Moschonas et al. (2009), Cardone et al. (2011), Cademartori et al. (2020).

Figure 6.9 and 6.10 reports in a synthetic way the values of α_{DS} and $\beta_{DS,i}$ calculated by means of the simplified fragility analysis. Particularly, the values corresponding to the 10th, 50th and 90th percentiles of the fragility population of each single case study are shown. It is evident in Figure 6.9 that in the bridges in which the abutment-backfill system is critical (i.e. the gap size on the abutment is not-seismically designed) the longitudinal direction is weaker than the transverse with a lower value of median fragility. Indeed, for bridges from B1 to B7, the values of the 50th percentile of α_{DS3} in the longitudinal direction range between 0.25 g and 0.48 g and are lower than α_{DS3} calculated in the transverse direction (0.62g and 1.45g). On the contrary, for bridge B8, whose gap size is higher with respect to the other cases, similar values of α_{DS} are estimated in the transverse and longitudinal direction.

The 10th and 90th percentiles of the population of fragility curves are indicated in the Figures by error bars to represent the range of variability due to the knowledge-based uncertainties. Numerical values are also reported in Tables 6.4 and 6.4, where the parameters $var\alpha_{DS}^{10th}$ and $var\alpha_{DS}^{90th}$ represent the variability around the 50th percentiles and are calculated as the relative difference between the 50th percentiles and the 10th/90th percentiles. The variability of α_{DS} increases according to the number of uncertainties characterising the critical component. As previously mentioned, in the transverse direction, the variability of α_{DS} for the bridge B1 is higher than the other cases given the higher amount of uncertainties linked to the unknown bearing typology which induce strong variations in the force-displacement relationships of the subassemblies. As an

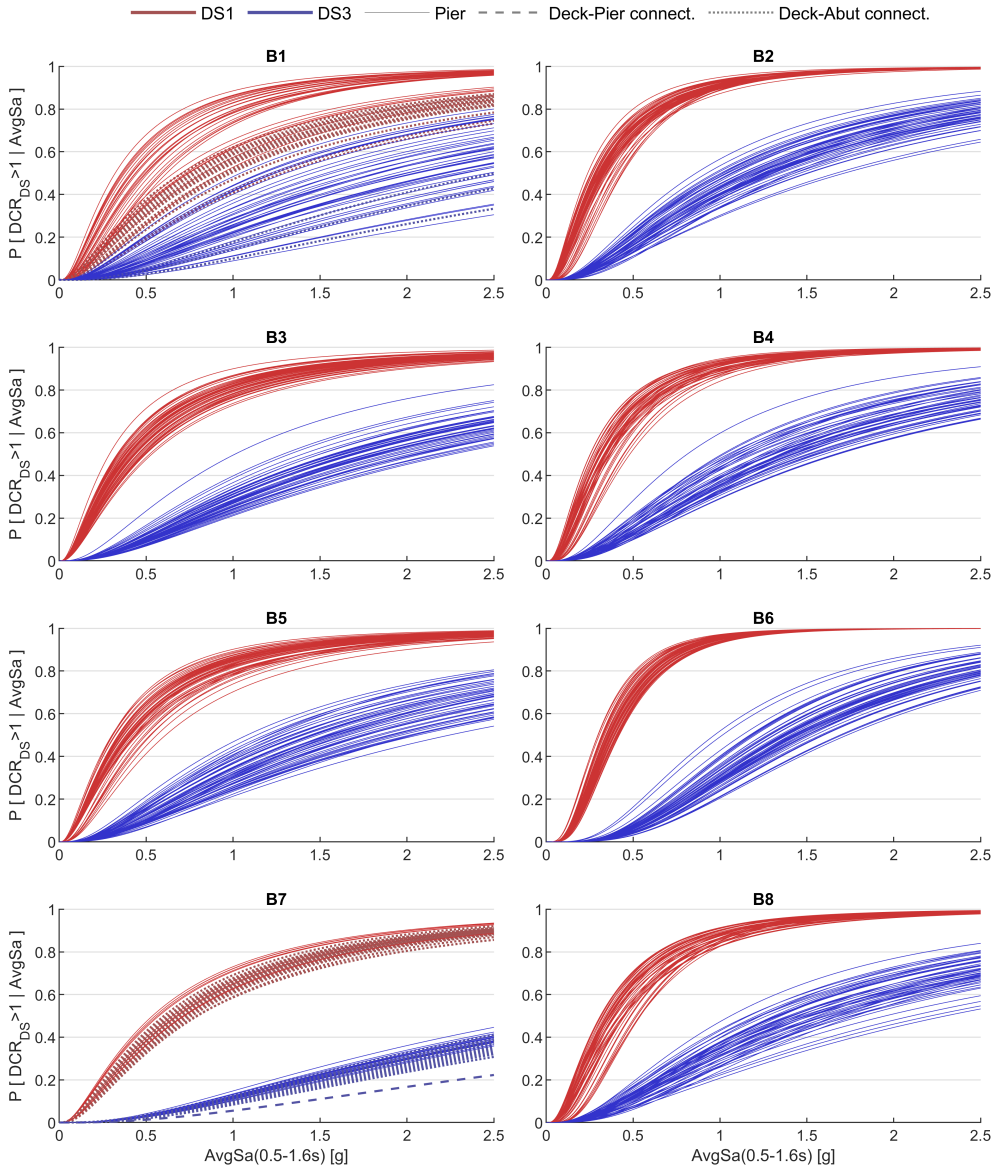


Figure 6.7: Populations of fragility curves in transverse direction. Different patterns of the fragility curves indicate the most recurring critical component among all the records.

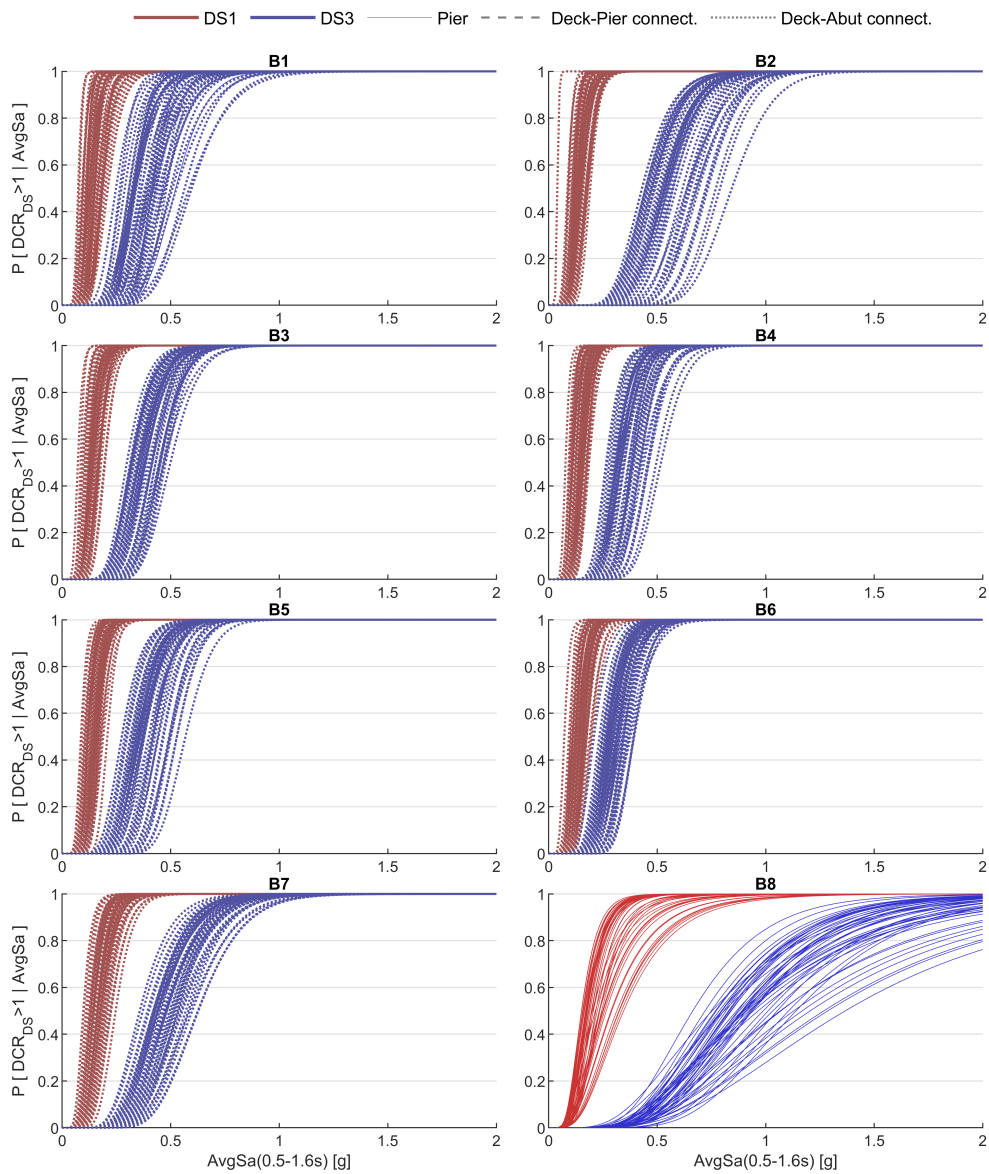


Figure 6.8: Populations of fragility curves in longitudinal direction. Different patterns of the fragility curves indicate the most recurring critical component among all the records.

example, the 10th and 90th percentiles of the median fragility of bridge B1 correspond to the [-40; +39]% and [-37; +44]% of the central value (i.e. 50th percentile) at DS1 and DS3 respectively. Considering the other bridges, the variation of the 10th and 90th percentiles with respect to the 50th is generally lower than [-20; +20]% regardless of the damage state. For instance, for the bridge B6 the variation is [-16; +15]% and [-16; +18]% at DS1 and DS3, respectively.

The response of the B7 is governed by the neoprene bearings which are the critical components. The beneficial effect of the neoprene bearings to the bridge fragility is evident since the 50th percentiles of the median fragility is registered at 1.45 g and it is higher with respect to the other cases. The variability expressed by the 10th and 90th percentiles is lower than the other cases: [-8; +17]% at DS3 and lower than 5% at DS1 and DS2.

The results of Figure 6.9 for the bridges from B1 to B7 in longitudinal direction allow for measuring the influence of the uncertainties of the abutment-backfill system in fragility analysis. For bridge B1, the variability of α_{DS} expressed by the 10th and 90th percentiles is included in the ranges [-36; +28]% and [-21; +30]% at DS1 and DS3, respectively. Similar values are registered for the other bridges from B2 to B7. Contrarily, the global damage states of B8 in the longitudinal direction are governed by the damage state thresholds of the deck-pier subassemblies which vary depending mostly on the mechanical uncertainties of the concrete and steel (no neoprene bearings are present) and the detailing. In this case, the variability registered by analysing the 10th and 90th percentiles is [-20; +55]% [-14; 27]% because its global damage states are governed by the damage states of the deck-piers subassemblies that, in turn, are considerably affected by uncertainties on material properties and detailing.

The values of the dispersion β_{DS} , reported in Figure 6.10, are affected by the correlation between the adopted IM and the minimum DCR related to the critical components detected varying the seismic actions. Note that within the cloud-based approach for fragility analysis of deterministically characterised structures, the dispersion is calculated with reference to the fitted power-law model and it is assumed constant among the different DS. In this study, this is valid in the cases where a low variability of the critical component is detected where DCRs calculated at the different DS are equal to

the same EDPs, scaled by different DS displacement threshold. For example, in the longitudinal direction analysis, the abutment backfill system is critical for the bridge from B1 to B7 and the global DCRs are equal to the demand displacements of this component divided for the three DS thresholds of the abutment-backfill subassembly. This is registered also for bridge B8 analysed in the longitudinal direction.

The results registered in transverse direction analysis shows that if the critical member changes depending on the considered damage state, the logarithmic dispersion slightly varies among the performance levels.

Figure 6.10 shows that β_{DS} is generally lower than 0.3, if the response is governed by the abutment-backfill interaction. Note that the effective periods of the case-study bridges when the abutment-backfill interaction is activated vary between 0.55 s and 0.65 s. Considering a period elongation of 100%, these period values are consistent with the considered period range for $AvgSa$.

β_{DS} slightly increases for B8 in the longitudinal direction where the DS is reached for the ultimate capacity of the piers. In the transverse direction, β_{DS} generally ranges between 0.2 and 0.4. The maximum value of β_{DS} is registered for B6 analysed in the transverse direction and it means a lower efficiency of the $AvgSa$ with respect to the other cases.

However, generally, these results confirm the efficiency of $AvgSa$ and, particularly, the adequacy of the period range in which it is calculated for this bridge dataset. These results agree with the conclusions by O'Reilly & Monteiro (2019) that evidence the efficiency of $AvgSa$ for the fragility analysis of RC continuous deck bridges in the transverse direction.

Even if a good efficiency of $AvgSa$ is evidenced for the case studies herein analysed, more refined analysis (i.e. NLTHA) should be performed to investigate the efficiency of $AvgSa$ for simply-supported bridges, possibly with comparisons with other spectral shape-based IMs.

6.3.6. Simplified risk assessment

The procedure for the seismic risk assessment, expressed as the mean annual frequency of exceeding a given limit state, is applied to all the case studies. Hazard curves

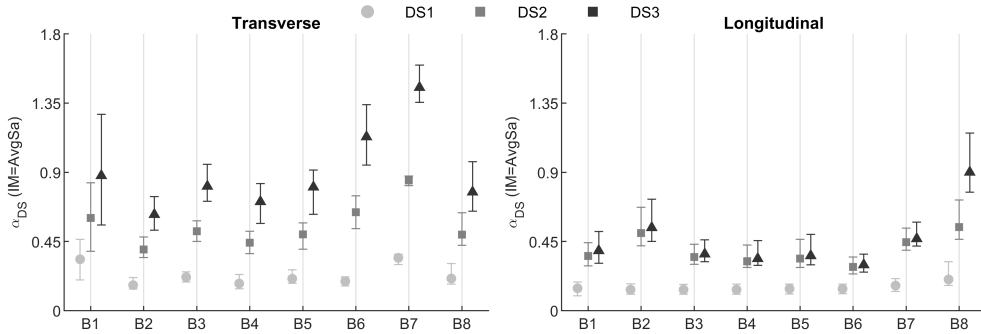


Figure 6.9: Median of the fragility curve population: 50th percentile and corresponding range of variation (10th-90th percentiles).

that report the mean annual frequency of exceedance of a given PGA are derived for all the locations of the case-study bridges and used to compute the seismic risk with the approach reported in Section 6.2.5. The hazard curves are retrieved by means of the REASSESS platform proposed by Chioccarelli et al. (2019) applying the source model by Meletti et al. (2008). It is worth noting that, according to Table 6.3, although the investigated bridges are part of the same road network, B1 and B8 are located in a medium-level seismic hazard area, while B2 to B7 are situated in a medium-high- or high-level one with reference to the Italian guidelines on existing bridges (Ministero delle Infrastrutture e dei Trasporti 2020). The seismic hazard curves are reported in Figure 6.11. Note that, the hazard curves for the bridges B2 to B6 are very similar since these

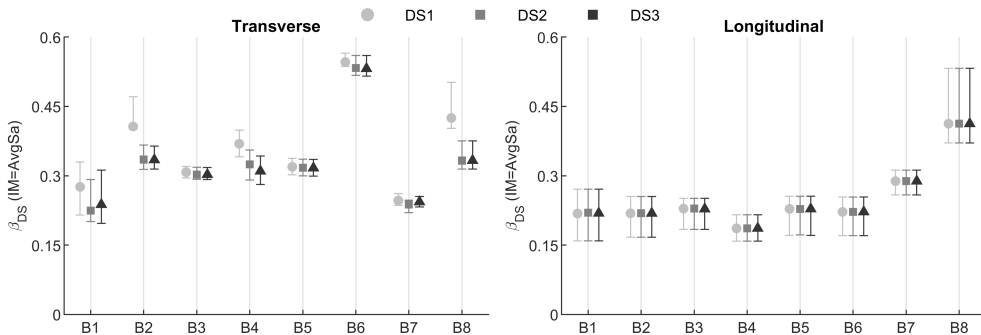


Figure 6.10: Logarithmic dispersion of the fragility curve population: 50th percentile and corresponding range of variation (10th-90th percentiles).

Table 6.4: Median fragility and corresponding variation (transverse direction).

	α_{DS1}^{50th}	$var\alpha_{DS1}^{10th}$	$var\alpha_{DS1}^{90th}$	α_{DS2}^{50th}	$var\alpha_{DS2}^{10th}$	$var\alpha_{DS2}^{90th}$	α_{DS3}^{50th}	$var\alpha_{DS3}^{10th}$	$var\alpha_{DS3}^{90th}$
	[g]	[%]	[%]	[g]	[%]	[%]	[g]	[%]	[%]
B1	0.33	-40.39	39.02	0.60	-36.06	37.91	0.88	-36.53	45.36
B2	0.17	-15.22	29.48	0.40	-13.07	20.45	0.62	-16.21	18.73
B3	0.22	-14.10	16.30	0.52	-12.89	13.12	0.81	-12.15	17.69
B4	0.18	-19.75	33.27	0.44	-16.29	16.84	0.71	-20.04	16.52
B5	0.21	-14.19	27.93	0.50	-19.29	15.25	0.80	-21.94	13.87
B6	0.19	-16.34	15.42	0.64	-16.57	16.82	1.13	-16.20	18.57
B7	0.34	-12.96	7.00	0.85	-4.06	3.48	1.45	-6.69	10.04
B8	0.21	-17.20	46.56	0.49	-14.03	28.83	0.77	-16.14	25.69

Table 6.5: Median fragility and corresponding variation (longitudinal direction).

	α_{DS1}^{50th}	$var\alpha_{DS1}^{10th}$	$var\alpha_{DS1}^{90th}$	α_{DS2}^{50th}	$var\alpha_{DS2}^{10th}$	$var\alpha_{DS2}^{90th}$	α_{DS3}^{50th}	$var\alpha_{DS3}^{10th}$	$var\alpha_{DS3}^{90th}$
	[g]	[%]	[%]	[g]	[%]	[%]	[g]	[%]	[%]
B1	0.15	-33.48	27.51	0.36	-17.97	24.25	0.39	-20.87	32.23
B2	0.14	-21.62	27.78	0.50	-16.48	33.21	0.54	-16.67	34.39
B3	0.14	-22.40	25.78	0.35	-13.55	23.46	0.37	-13.36	25.03
B4	0.14	-22.38	26.02	0.32	-12.56	32.41	0.34	-12.69	34.72
B5	0.14	-24.27	20.88	0.34	-16.78	37.50	0.36	-16.46	39.10
B6	0.14	-22.83	21.89	0.28	-16.30	22.28	0.30	-16.10	23.49
B7	0.16	-23.55	27.72	0.44	-11.77	20.74	0.47	-10.27	22.98
B8	0.20	-19.34	56.99	0.54	-14.84	32.32	0.90	-14.41	28.21

are geographically close. The highest PGA registered with a return period of 475 years is 0.38g for the B7 bridge.

Fragility curves are computed for all the case studies using PGA as IM, which is deemed to be more practical and user-friendly than *AvgSa*. Figure 6.12 shows the 50th percentiles of the median fragility within the populations and the corresponding variation. Comparing these results with Figure 6.9, it is clear the beneficial effect of *AvgSa* in reflecting the probability of exceedance with lower bias with respect to PGA when epistemic uncertainties are considered. As an example, for B1 analysed in transverse direction, the variability of α_{DS} expressed by the 10th and 90th percentiles is included in the range [-41; +50]% at DS3 and it is slightly higher than the values reported in sub-section 6.3.5. The median fragility values of the bridges B7 in transverse direction

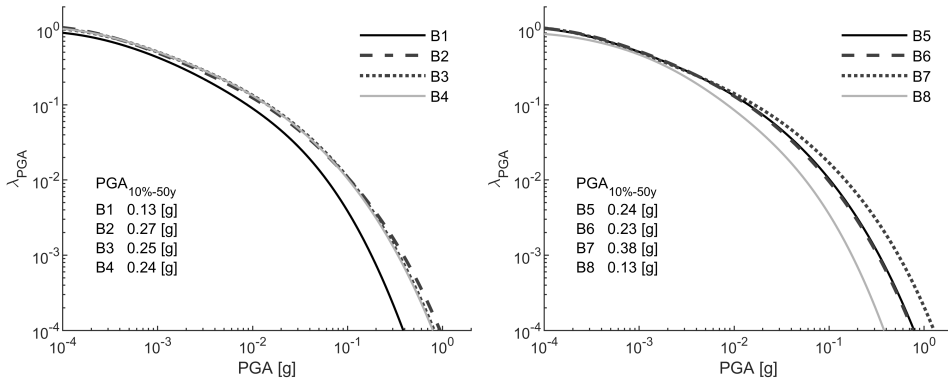


Figure 6.11: Hazard curves for the case studies.

are particularly higher than the other cases and confirm the outcomes by Borzi et al. (2014) who evidenced the low seismic vulnerability of bridges with neoprene bearings. In these cases, the neoprene bearings prevent damaging of the piers and allow relative displacement between the deck and substructure over the friction shear. The collapse (i.e. DS3) occurs for deck-unseating and the corresponding DS displacement threshold depends only on the support length on the pier cap.

Figure 6.13 reports the values of the 10th, 50th and 90th percentiles of the logarithmic dispersion β_{DS} of the population of fragility curves. It is shown that the 50th percentiles of β_{DS} are included in the range 0.9-1.1 for both transverse and longitudinal direction analysis, strongly exceeding the β_{DS} associated to $AvgSa$. As stated by Minas & Galasso (2019), the logarithmic dispersion is an index of efficiency of the adopted IM. As expected, this result demonstrates that PGA is less efficient than $AvgSa$ in correlating the considered EDP to the intensity of the adopted ground-motion shaking.

The outcomes of this new fragility analysis are reported in Figures 6.14 and 6.15. It is worth specifying that the fragility curves reported in these Figures are calculated as the 10th, 50th and 90th percentiles of the probability of exceedance of the three considered DS described by the whole fragility populations. These do not exactly correspond to the cumulative probability distribution functions (although being very similar) using the values of α_{DS} and β_{DS} reported in Figures 6.12 and 6.13.

Each fragility curve of the population related to each bridge is numerically integrated

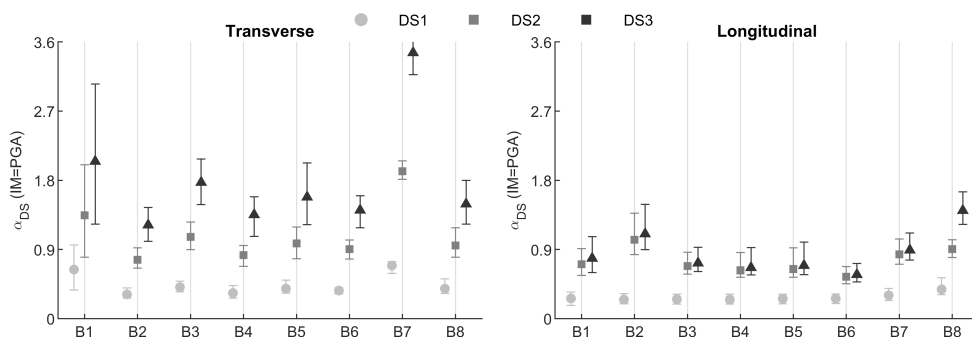


Figure 6.12: Median of the fragility curve population using PGA as IM: 50th percentile and corresponding range of variation (10th-90th percentiles).

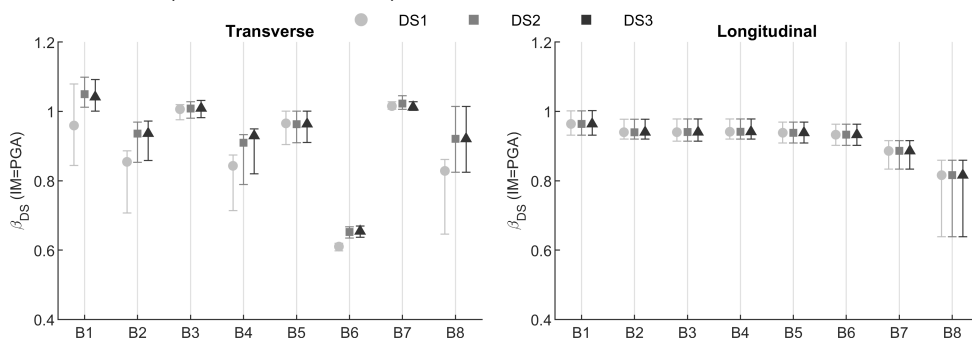


Figure 6.13: Logarithmic dispersion of the fragility curve population using PGA as IM: 50th percentile and corresponding range of variation (10th-90th percentiles).

with the corresponding hazard curve to calculate a population of mean annual frequency of exceedance of a DS, λ_{DS} , which are adopted in this study, to express the seismic risk. The λ_{DS} corresponding to the 10th, 50th and 90th percentiles are computed and graphically shown in Figure 6.16. Furthermore, Tables 6.6 and 6.7 numerically list the 50th percentile of λ_{DS} and report the corresponding variation, $var\lambda_{DS}$ computed as the relative percentage error of the 50th percentile with respect to the 10th and 90th ones. $var\lambda_{DS}$ measures how much a refined data collection can change the seismic risk evaluation. It is worth mentioning that the seismic risk calculation can be also carried out directly using the 10th-, 50th- and 90th-percentile fragility curves (in place of the whole population) increasing the practicality of the procedure with a lower number of numerical integrations.

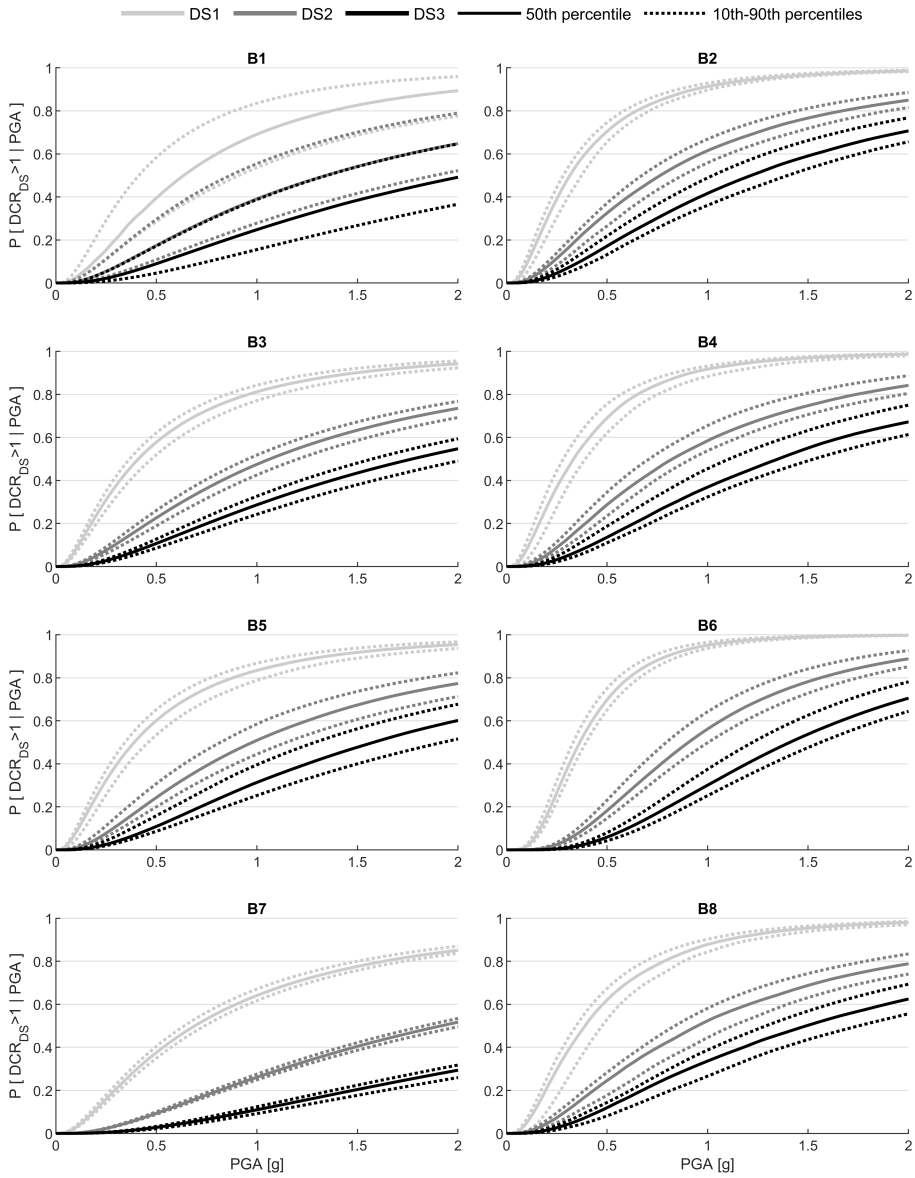


Figure 6.14: Fragility curves in transverse direction (10th-50th-90th of the population).

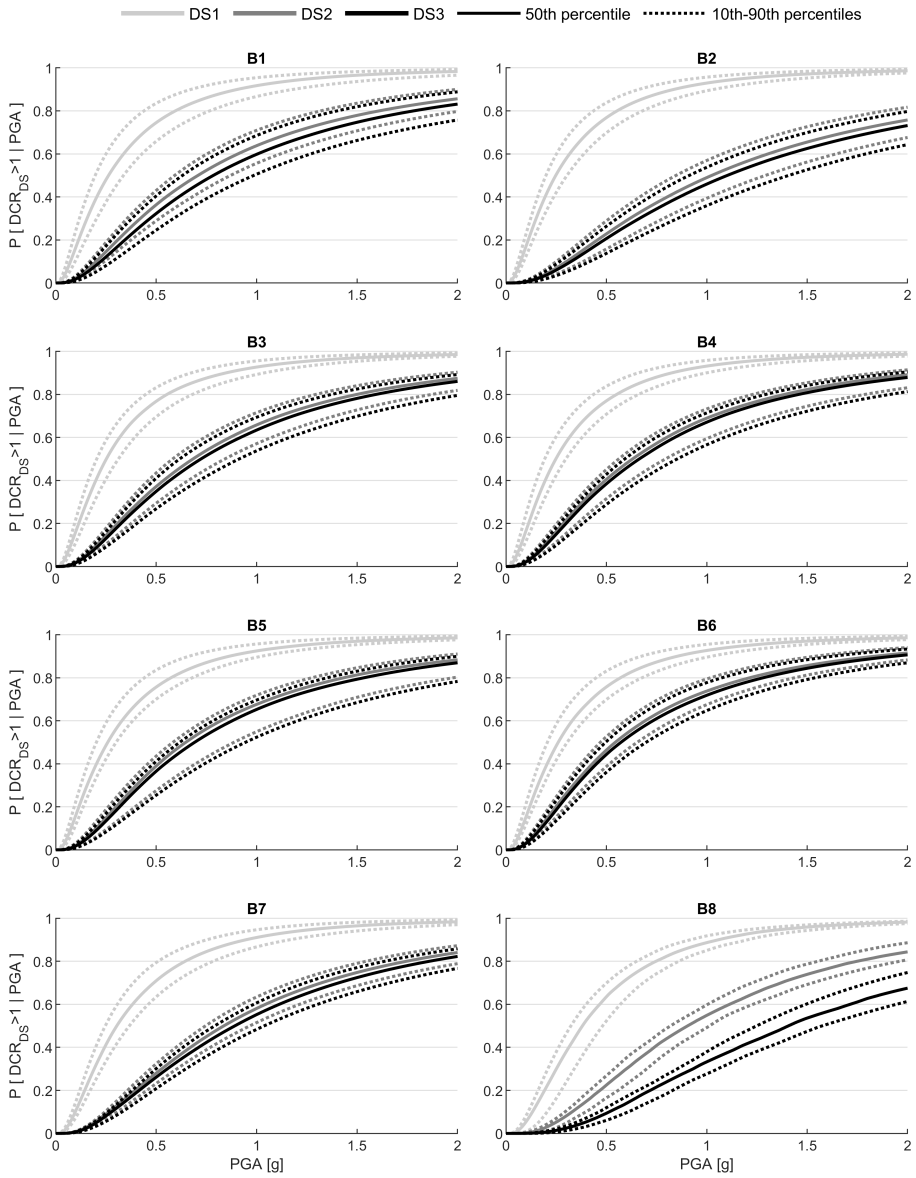


Figure 6.15: Fragility curves in transverse direction (10th-50th-90th of the population).

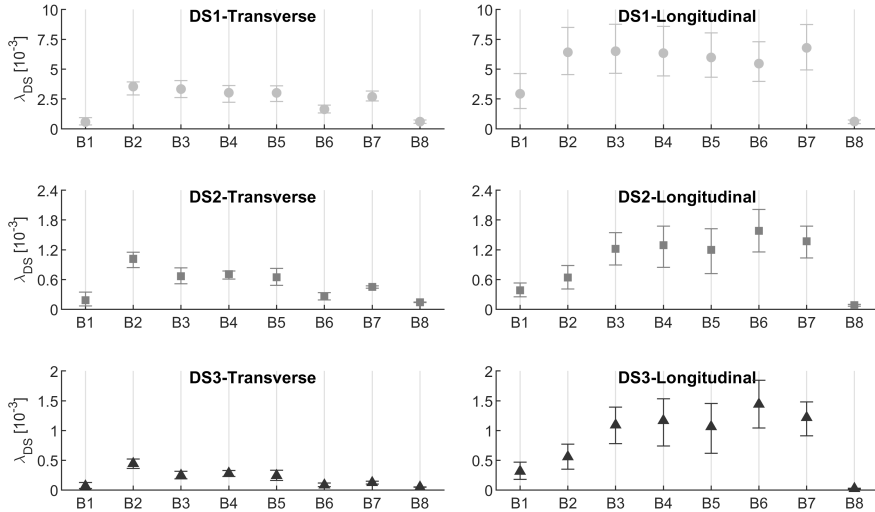


Figure 6.16: Seismic risk (mean annual frequency of exceeding a given limit state) calculated for all the bridges with the corresponding 10th-90th variability

These results allow discussing the influence of knowledge-based uncertainties on seismic risk and showing how the simplified approach proposed can be of support in risk mitigation strategies. Also, it is evident that this approach can be used to perform a refined risk-based prioritisation respect to the Warning Class adopted by the Italian Guidelines on existing bridges (Ministero delle Infrastrutture e dei Trasporti 2020) (see sub-section 6.3.2).

Another clarification is needed. In this study, for the sake of simplicity, the fragility is calculated by decoupling the transverse and longitudinal responses. It is suggested that the risk calculated for the "weakest" direction (i.e. the direction which the highest λ_{DS} is associated to) is critical and the corresponding λ_{DS} can be adopted to indicate the global risk of the bridge.

If the nonlinear response under bidirectional ground-motion records is of interest, more refined numerical modelling and analysis techniques should be adopted strongly increasing the effort demand to the analyst. This could jeopardise a fast application of the procedure for analysing large bridge portfolios.

Table 6.6: Seismic risk and corresponding variation (transverse direction).

	λ_{DS1}^{50th}	$var\lambda_{DS1}^{10th}$	$var\lambda_{DS1}^{90th}$	λ_{DS2}^{50th}	$var\lambda_{DS2}^{10th}$	$var\lambda_{DS2}^{90th}$	λ_{DS3}^{50th}	$var\lambda_{DS3}^{10th}$	$var\lambda_{DS3}^{90th}$
	[10^{-3}]	[%]	[%]	[10^{-3}]	[%]	[%]	[10^{-3}]	[%]	[%]
B1	0.56	-44.44	64.37	0.18	-62.51	90.03	0.07	-64.30	93.25
B2	3.54	-20.02	11.24	1.02	-17.58	12.68	0.44	-18.54	16.83
B3	3.33	-21.16	21.06	0.67	-23.48	24.98	0.25	-23.91	26.85
B4	3.02	-26.08	20.01	0.71	-14.18	8.69	0.28	-19.97	15.74
B5	3.01	-24.02	19.46	0.64	-25.12	27.86	0.24	-33.80	36.69
B6	1.63	-18.76	21.30	0.26	-25.85	30.90	0.08	-30.72	38.98
B7	2.68	-12.93	18.26	0.45	-5.46	5.43	0.12	-19.40	17.87
B8	0.60	-24.50	22.19	0.14	-3.61	2.76	0.05	-4.05	4.83

Table 6.7: Seismic risk and corresponding variation (longitudinal direction).

	λ_{DS1}^{50th}	$var\lambda_{DS1}^{10th}$	$var\lambda_{DS1}^{90th}$	λ_{DS2}^{50th}	$var\lambda_{DS2}^{10th}$	$var\lambda_{DS2}^{90th}$	λ_{DS3}^{50th}	$var\lambda_{DS3}^{10th}$	$var\lambda_{DS3}^{90th}$
	[10^{-3}]	[%]	[%]	[10^{-3}]	[%]	[%]	[10^{-3}]	[%]	[%]
B1	2.93	-42.10	58.17	0.38	-34.41	38.15	0.31	-43.40	48.82
B2	6.41	-29.23	32.55	0.64	-36.27	37.25	0.56	-37.52	38.14
B3	6.50	-28.48	34.60	1.22	-26.92	26.55	1.09	-28.68	27.52
B4	6.34	-30.09	35.45	1.29	-34.34	29.97	1.17	-36.59	31.29
B5	5.98	-27.64	34.45	1.20	-40.19	35.16	1.06	-41.81	36.70
B6	5.46	-27.37	33.37	1.58	-26.79	27.40	1.44	-27.76	27.95
B7	6.78	-27.43	28.91	1.37	-24.56	22.00	1.22	-25.25	21.75
B8	0.61	-30.86	21.03	0.08	-29.05	20.50	0.02	-34.98	28.34

Figure 6.16 allows for a direct comparison on the λ_{DS} associated with the different case studies. Firstly, as expected, it is evident that the risk calculated with transverse seismic action is lower with respect to the longitudinal direction for the bridge with not-seismically designed deck-abutment gaps.

It is observed that the lowest λ_{DS} is registered for B1 and B8, because of the lower hazard of their geographical location. Although presenting a strongly higher α_{DS} with respect to the other cases, the bridge B7 is characterised by a comparable value of λ_{DS} considering the different DS. Tables 6.6 and 6.7 register a high influence of epistemic uncertainty associated to the B1, due to the lack of knowledge data λ_{DS} . Indeed, the variability measured by the 10th and 90th percentiles is included in [-42.10; 58.17]%, [-34.41; 38.15]% and [-43.30; 48.82]% for DS1, DS2 and DS3, respectively. How-

ever, Figure 6.16 shows that a refined data collection aimed at reducing this bias would not change a risk prioritisation scheme since the bridges B3 to B7 would be anyway characterised by higher λ_{DS} , meaning a high retrofit priority.

Consequently, the influence of epistemic uncertainty on B1 is negligible within a decision-making framework based on risk prioritisation. Similar outcomes are related to B2: the effect of epistemic uncertainties are supposed to be relevant for prioritising risk considering DS1, but less important at DS2 and DS3, resulting in lower λ_{DS} even if considering a refining knowledge process of the bridge.

The bridges from B3 to B7 exhibit the highest λ_{DS} within the bridge dataset. It is observed that a refined knowledge process can be useful to reduce the bias due to the epistemic uncertainty and to accurately define a risk priority hierarchy.

6.3.7. Fragility analysis with a refined knowledge level and validation

A refined data collection (named second-level data collection) is performed for the B1 bridge by means of a refined UAV-based inspection to appropriately reduce the knowledge-based uncertainties. This process is deeply described in 2.3.3.

The objectives of this last section are: 1) illustrating the reduction of the uncertainty-based bias in fragility analysis consequent to a refined data collection and 2) evaluating the approximation introduced by the proposed simplified mechanic-based assessment methodology with respect to refined NLTHA.

With respect to the knowledge data listed in sub-section 6.3.1 (identified as first-level data collection in this sub-section), further data about this case-study bridge are retrieved: the connection system between the deck and the substructure is simply composed of four neoprene bearings per line, having 4 cm-thickness; the gap size between the deck and abutments is fixed at 2.5 cm. Negligible geometric variations with respect to the geometry acquired with first-level data collection are registered. This case study is analysed via the proposed methodology for fragility analysis and by means of NLTHA performed in Opensees McKenna (2011) based on a refined numerical model. The knowledge-based uncertainties linked to the concrete and steel design classes, concrete and steel mean strengths and shear modulus of the neoprene are modelled again as reported in Table 6.2. The lumped-plasticity modelling strategy for NLTHA is adopted

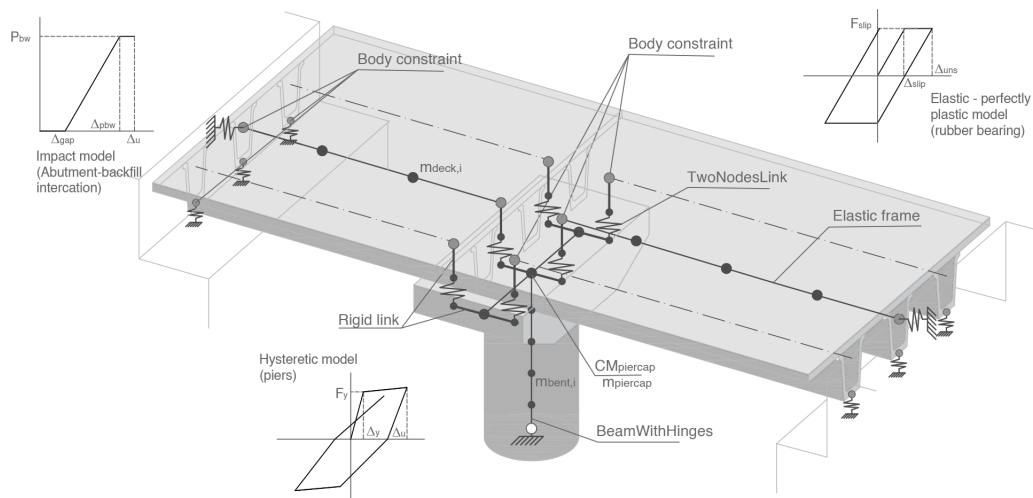


Figure 6.17: Adopted modelling strategy in OpenSees for performing nonlinear time-history analysis

and described in Figure 6.17.

The piers are modelled with *BeamWithHinges* elements composed by an internal elastic part and a nonlinear hinge at the base. The *hysteretic* material is used to model the nonlinear cyclic behaviour of the plastic hinges expressed by means of a sectional moment-curvature law. The deck and the pier caps are modelled with elastic beam elements. *TwoNodesLink* elements are aimed at modelling the nonlinear response of the bearing devices and the abutment-backfill interactions. As suggested by Nielson (2005), the neoprene bearings are modelled with an elastic-perfectly plastic behaviour, while an *impact* model is used for the longitudinal response of the abutments. A tangent stiffness proportional damping is defined for NLTHA as suggested by Priestley et al. (2007). Moreover, a 5% Rayleigh damping model is assigned.

Once the population of index-models is generated by means of the LHS, the performance of each model is evaluated by means of the simplified CSM approach (sub-section 6.2.3.1) and NLTHA using the entire suite of ground motions. The EDPs are extracted for each component and local and global DCRs are computed with Equation 6.4 and 6.5. The fragility curves are obtained by means of the Cloud-CSM described in Section 6.2.4 using the DCRs calculated via both the analysis strategies. The fragility curves are calculated assuming $AvgSa$ as IM. These are reported in Figure 6.18 for the transverse and longitudinal direction and all the damage states. $B1_{1,CSM}$ refers to first data col-

lection and CSM approach, $B_{1,2,CSM}$ and $B_{1,2,TH}$ refer to second-level data collection and CSM or NLTHA approach, respectively. These outcomes are reported numerically in Tables 6.8 and 6.7.

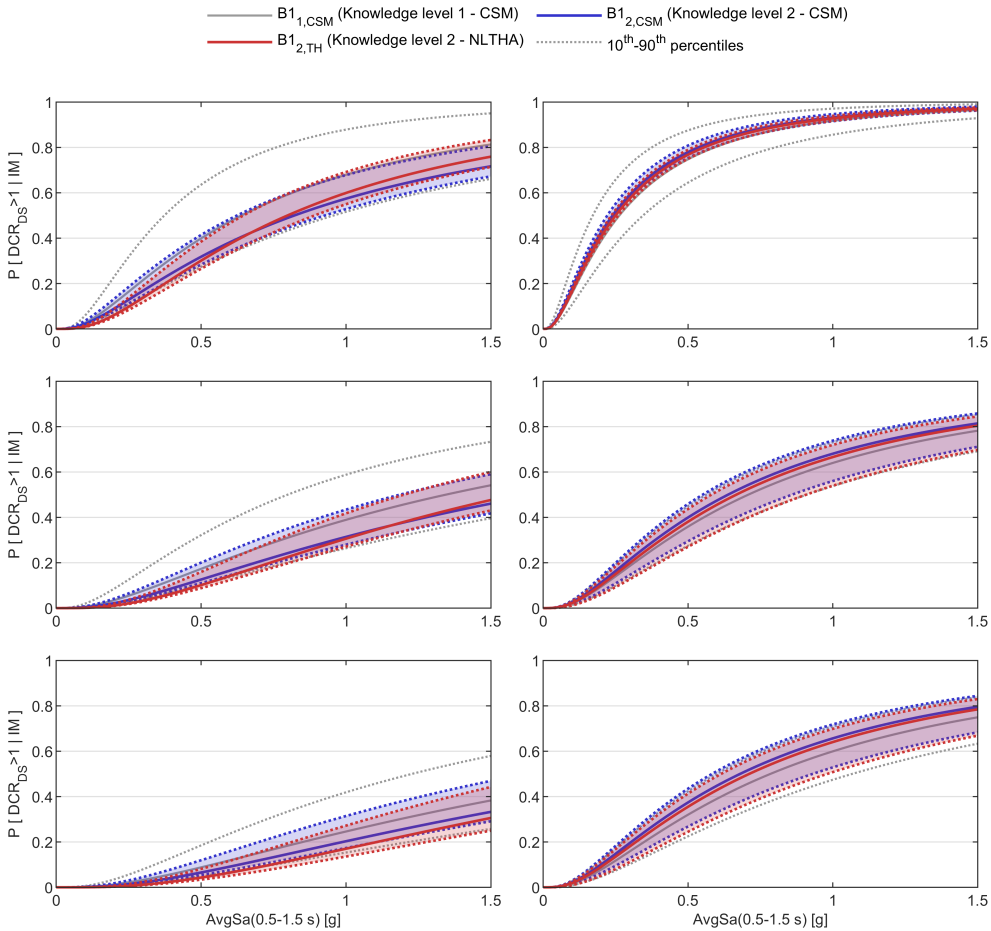


Figure 6.18: Fragility curves for the bridge B1, calculated via the simplified CSM-based approach ($B_{1,1,CSM}$ and $B_{1,2,CSM}$ for the first- and second-level data collection, respectively) and via NLTHA (only second -level data collection, $B_{1,2,TH}$).

The comparison between the fragility functions calculated with first- and second-level data collection approach shows that the influence of uncertainties (again quantified by

the 10th and 90th percentiles of the probability of exceedance of a given DS conditioned to $AvgSa$), is strongly reduced with this refined data collection as shown in Tables 6.8 and 6.9. This effect is noticeable for the transverse direction, while it is slighter for the longitudinal. In fact, in this latter case, the reaching a DS is governed by the abutment-backfill interaction, whose uncertainties are not reduced by the second-level data collection approach. Contrarily, the second-level inspection allows for detecting the presence of neoprene bearings which induces a beneficial effect on the fragility of the bridge in transverse direction. In this case, the median fragility (at the 10th and 50th percentiles) increase with respect to the previous one for all the damage states. As an example, the 50th percentile of the median fragility increases by 16% at DS3. Figure 6.18 shows that there are some approximations related to the CSM-based simplified procedure with respect of the NLTHA. However, these are on the safe side in terms of fragility for this case study. Particularly, in the transverse direction (Table 6.8), the relative errors between the two approaches are higher than the longitudinal one (Table 6.9) and increase with the inelastic demand of the bridge and more severe damage states. The highest relative error $((CSM - NLTHA)/NLTHA)$ on the median fragility 50th percentile is registered at DS3 and is equal to -13.6%. This is probably caused by the simplifying assumptions of the IPM that neglects the interactions between the subassemblies and the bias produced by the adopted formulations for the equivalent viscous damping. The inaccuracies of the simplified approaches propagate with the rising of the nonlinear displacement demand.

Considering the high reduction in terms of computational effort of the proposed procedure with respect to the refined NLTHA, the calculated errors are considered acceptable. Moreover, it is deemed that applying the proposed procedure on bridge portfolios, the systematic error linked to the approximations of the simplified procedure does not affect the effectiveness in defining a reliable risk prioritisation scheme. However, it is worth noting that the simplified CSM-based approach is accurate in predicting the amplitude of the range of variability of the median fragility. A maximum difference of 3.6% is noted for DS3 in longitudinal directions. This evidences that, in this case, the simplified approach well-quantifies the contribution of the uncertainty and provides a positive insight for the application of this approach for portfolio analysis, selecting the bridges when the

uncertainty influences more the seismic risk.

Table 6.8: Median fragility (50th, 10th and 90th percentiles) for seismic action in the transverse direction ($IM = AvgSa$). $B_{1,CSM}$ refers to first data collection and CSM approach, $B_{12,CSM}$ and $B_{12,TH}$ refer to second-level data collection and CSM or NLTHA approach, respectively.

	α_{DS1}^{50th}	α_{DS1}^{10th}	α_{DS1}^{90th}	α_{DS2}^{50th}	α_{DS2}^{10th}	α_{DS2}^{90th}	α_{DS3}^{50th}	α_{DS3}^{10th}	α_{DS3}^{90th}	
$B_{1,CSM}$	0.29	-41.84	41.08	0.54	-37.32	39.67	0.79	-37.60	47.97	[g]
$B_{12,CSM}$	0.34	-20.24	11.26	0.66	-24.68	8.56	0.95	-26.35	13.36	[g]
$B_{12,TH}$	0.37	-18.09	13.69	0.75	-22.01	7.90	1.10	-23.03	15.99	[g]

Table 6.9: Median fragility (50th, 10th and 90th percentiles) for seismic action in longitudinal direction ($IM = AvgSa$).

	α_{DS1}^{50th}	$var\alpha_{DS1}^{10th}$	$var\alpha_{DS1}^{90th}$	α_{DS2}^{50th}	$var\alpha_{DS2}^{10th}$	$var\alpha_{DS2}^{90th}$	α_{DS3}^{50th}	$var\alpha_{DS3}^{10th}$	$var\alpha_{DS3}^{90th}$	
$B_{1,CSM}$	0.12	-34.96	29.13	0.31	-18.93	25.14	0.34	-21.86	34.28	[g]
$B_{12,CSM}$	0.11	-5.76	4.30	0.28	-13.34	29.72	0.30	-13.85	31.17	[g]
$B_{12,TH}$	0.11	-4.23	3.50	0.29	-11.73	33.89	0.31	-12.17	34.69	[g]

6.4. Final remarks

In this Chapter, a simplified methodology to perform fragility analysis of bridges directly accounting for aleatory and epistemic uncertainties is described. The methodology is feasible for the seismic risk assessment of bridges in case of lacking knowledge input data. The uncertainties linked to the seismic actions are accounted for by a suite of natural ground-motion record, whereas knowledge-based ones are modelled by means of the statistical generation of a population of index-bridges. The seismic performance analysis of the index-bridges is based on simplified modelling approaches, adapted for different bridge structural schemes, and nonlinear static analysis methods. A capacity spectrum method is used to evaluate the performance of index-bridges under a specific ground-motion record. The performance of the single index-bridge is synthesized by a set of Demand-Capacity ratios which is used to fit probabilistic seismic demand models and compute fragility curves. The fragility of the main bridge is represented by a population of fragility curves. The influence of the knowledge-based uncertainty on the fragility of the main bridge can be quantified by analysing the variability of the fragility

curves around the central value. If hazard curves are integrated with the fragility curves, the mean annual frequency of exceeding a damage state (both the central value and its variability) can be also quantified. In this study, the 10th and 90th percentiles of the fragility curve population are adopted for this scope.

This methodology can be of support for addressing risk prioritisation schemes for large bridges portfolios, since it can be applied based on fast data collection processes. Also, it can be used to perform a more refined risk-based prioritisation with respect to the procedure based on a Warning Class adopted by the Italian Guidelines on existing bridges (Ministero delle Infrastrutture e dei Trasporti 2020). The methodology is applied on a dataset of eight reinforced-concrete case-study bridges described in Chapter 2 which are "surveyed" by a "desk" approach using open data. After the simplified data collection is carried out, the knowledge-based uncertainties are modelled with statistical distributions retrieved by the literature. The analysed uncertainties concern the mechanical properties in concrete and steel, constructive details in the piers, bearing typology and mechanical properties, gap size and abutment-backfill system.

After defining an appropriate sample size to generate a representative population of index-bridges, the fragility analysis is carried out for all the case studies and the results are critically discussed. A first set of fragility curves is calculated by using the geometrical average of the spectral accelerations within a given period range as intensity measure. The efficiency of this typology of intensity measure, already evidenced in other literature studies for buildings and continuous deck bridges, is preliminary confirmed for simply-supported bridges. However, further studies are needed to confirm this outcome and address recommendations to fix the significant period range with an appropriate discretization interval. It is observed that the response in the longitudinal direction can be critical for the damage state of bridges whose deck-abutment gap size is not seismically designed. In this case, the abutment-backfill system determines the reaching of the damage states. Consequently, the employment of typological approaches that neglect this component could involve severe inaccuracies in fragility estimations of bridge portfolios. In the transverse direction, the bearing typology could considerably affect the hierarchy of the strength between the substructure and the deck-substructure connection system and affects the fragility of the investigated bridge. Particularly, a

beneficial effect on the fragility in the transverse direction is registered for the bridges whose neoprene bearings enhance the ductility capacity of the subassemblies.

The variability in fragility analysis due to the knowledge-based uncertainties is quantified. In the cases where the bearing typology is known, the variation between the 50th percentile of the median fragility and the corresponding 10th-90th percentiles is, generally, lower than $\pm 20\%$ in transverse direction regardless of the considered damage state. For the bridge whose bearing typology is unknown, this uncertainty is modelled with fixed-free/neoprene bearing systems. In this case, the influence of the uncertainties reaches the $\pm 45\%$. In the longitudinal direction, the variation between the 50th percentiles and the 10th/90th ones of the median fragility arises at $\pm 30 - 40\%$, but it is mainly related to the uncertainty of the properties of the abutment-backfill system.

A second set of fragility curves is calculated using the peak ground acceleration as IM and it is used for computing the mean annual frequency of exceeding a damage state which is commonly used as a seismic risk index. This latter is used to provide an example of how the proposed approach can be used within the definition of a risk prioritisation scheme, to identify the bridges to be retrofitted first and also the bridges where a detailed in-situ survey can provide a more accurate evaluation of the seismic risk.

Finally, one of the selected case studies is subjected to a more accurate data collection and the effect of the reduction of epistemic uncertainties is evaluated on the fragility analysis. Moreover, the approximations introduced by the simplified methodology are briefly evaluated by means of comparisons with non-linear time history analysis performed on a refined numerical model. The errors involved by the simplifications in the modelling approach and the analysis reach a maximum of 13% in terms of median fragility. These are deemed to be acceptable if the procedure is used within the risk prioritisation framework given the strong benefits involved in terms of computational efforts. Moreover, a maximum difference of 3% is detected comparing the variability with respect to the 50th percentile of the median fragility calculated by means of the simplified and refined approaches.

Chapter 7

Conclusion

7.1. Overall conclusion and key findings

The structural safety of bridges and viaducts has a key role in ensuring the serviceability of transportation infrastructure systems on the occurrence of earthquake events. In seismic hazard-prone countries, existing bridges can induce important direct or indirect losses if subjected to severe seismic ground shaking. In developed countries, such as Italy, these structures were mostly designed in the past without appropriate anti-seismic regulations. Therefore, transportation managers need methodologies for extensive seismic risk assessment of existing bridges, in order to address refined inspections or specific retrofit interventions. The main challenges in this process are related to the large number of existing structures to be inspected and the limited available time and financial resources.

This dissertation investigates procedures for an efficient seismic risk assessment of bridge portfolios based on low effort-demanding data collection and analytical seismic assessment procedures.

- Chapter 2 describes a methodology for collecting and integrate multi-source data for creating inventory datasets in the framework of structural vulnerability analysis of infrastructure assets. Firstly, the potential of different remote-sensing data sources is described according to an extended literature review, highlighting specific advantages and shortcomings. A special focus on innovative Remotely Piloted Aircraft Systems (i.e. drones) for bridge inspection is provided to the reader. A framework for the use of drones for on-site image gathering and use of photogrammetric approaches for image elaboration and 3D modelling is described. The described multi-source data collection/integration approaches are framed within a multilevel framework that suits analysing bridge portfolios. These data

collection methodologies are applied on eight case-study bridges. The knowledge data are detected by means of street view data within the Basilicata road network. For seven case-study bridges, the street view images allow a satisfying characterisation of the bridges consistently with a medium level knowledge level. One of the case-study, whose street view data are not complete, is surveyed by means of a drone equipped with optical RGB sensors. The images collected are used to perform a photogrammetry elaboration which produces a 3D dense point cloud model. This latter allows retrieving constructive and geometric data on the analysed case study with high (centimetric) accuracy.

- Chapter 3 deals with the seismic performance assessment of continuous-deck RC bridges using displacement-based assessment (DBA) procedures and the capacity spectrum method (CSM). Starting from a state-of-the-art modal analysis-based DBA procedure, an additional static-based alternative is proposed, which is deemed to further increase the simplicity of the DBA approach. An extension of the DBA procedures, both modal and static, is proposed, to derive the displacement-based pseudo-pushover curve of the bridge with a particularly small increase in computational cost. The displacement-based pseudo pushover is herein adopted for the transverse analysis of a set of 36 reinforced concrete continuous-deck bridges with two, four or six, 35m-long spans, two values of the deck moment of inertia (transverse direction) and different combinations of 8m-, 15m- and 20m-high single-column piers. Additional datasets of bridges are analysed to investigate the accuracy of the DBA for relatively long bridges (8 to 12 spans), different pier longitudinal reinforcements and pier typologies. The resulting performance assessments are compared with those calculated by means of numerical pushover (with force profile proportional to the first vibration mode or uniform) and nonlinear time-history analyses (NLTHA) using three suites of 10 scaled natural ground motions. The CSM is used to identify the seismic performance on the numerical pushover and displacement-based pseudo pushover curves. For the analysed bridge configurations up to six spans, the DBA approaches allow estimating the bridge capacity curve with a level of ac-

curacy particularly similar to the first-mode-based pushover analysis. On the other hand, the uniform-load pushover provides a systematic and considerable overestimation of the base shear. The DBA approaches (coupled with the CSM) provide satisfying accuracy in seismic performance assessment, measured in terms of capacity-demand ratio. For the vast majority of the cases up to six spans, the performance points fall within one standard deviation from the average of the time history analyses, both in terms of displacement and base shear of the equivalent SDoF system. The error trends are not sensitive to the moment of inertia of the deck and to the amount of pier longitudinal reinforcement. The outcomes show that the applicability of the DBA should be based on both the number of spans and a so-called relative stiffness index proposed in the literature (RS_e), whichever is most stringent. The static and modal analysis-based DBA procedures are deemed appropriate for the considered bridges up to six spans (approximately $RS_e > 0.035$). For the considered eight-spans case studies (approximately $RS_e > 0.01$), the modal DBA may still be adopted while the static DBA is inadequate. For bridges with 10 spans or more (approximately $RS_e < 0.01$), NLTHA is suggested.

- Chapter 4 discusses the effectiveness of DBA approaches and the CSM for the seismic analysis of multi-span steel truss railway bridges supported by steel towers. A steel truss bridge, part of the Valencian railway network, is used as an archetype case study. The first part of this Chapter tests an analytical pseudo-pushover procedure for two case-study truss steel towers and discusses the effectiveness of several equivalent viscous damping formulations to be used within capacity spectrum-based assessment. The results of several equivalent viscous damping strategies (to be used in the CSM) proposed in the literature are compared to NLTHA-based displacement demand. The seismic action is represented by a suite of ten ground-motion excitations which are scaled for three increasing levels of intensity. An equivalent viscous damping strategy of fair accuracy is proposed based on the study by Wijesundara et al. (2011) and by Grande & Rasulo (2013). The second part applies the DBA and nonlinear static approaches for the

seismic performance prediction on a set of six hyperstatic multi-span steel truss bridges generated parametrically varying the number of spans and substructure layout. These are analysed via two pushover analysis approaches, adopting a first mode-based and uniform load profile, two direct DBA+CSM algorithms (a synthetic version of DBA coupled with CSM) based on equivalent modal and static analysis, and NLTHA. The outcomes evidence that the higher-mode contribution to the seismic response is significant for such a bridge typology. Therefore, the modal version of the DBA approach and the pushover analysis with a uniform load profile should be used for this bridge typology with a limited number of spans. Conversely, the first-mode-based methodologies, even though result fairly accurate in predicting the performance of the critical tower, present an unsatisfying bias in estimating the demand on all the substructure members.

- Chapter 5 studies the effectiveness of the CSM in performing probabilistic seismic assessment considering record-to-record variability with application to a case-study database of 2160 SDoF systems and 100 natural recorded ground motions. The SDoF systems are represented by multi-linear parametric backbone curves with variable elastic period, yield base shear coefficient, ductility at peak strength, hardening ratio, residual strength. Five types of hysteresis rules are adopted: Modified Takeda Fat, Modified Takeda Thin, Elastic-Perfectly Plastic, Bilinear and Flag-Shaped. An efficient algorithm to perform the CSM with real, as-recorded spectra is proposed, combined with a cloud-based approach (Cloud-CSM) to derive fragility relationships. The effectiveness of the Cloud-CSM in fragility analysis is discussed by means of comparisons with NLTHA, the N2 method and a proposed simple method involving an intensity measure, the geometric average of spectral displacement within a given period range, as a direct proxy for the performance displacement. The first relevant outcome is related to the issue of multiple CSM solutions which can be obtained if the CSM is applied with real spectra. In multiple-solution cases, the performance point (PP) is the solution whose displacement best mimics the geometric average of the spectral displacements calculated in an appropriate range of periods (i.e. elastic to elon-

gated period of the considered ground-motion excitation). An incorrect choice of the PP may imply errors on the median fragility and dispersion higher than 20% if the percentage of multiple-solution ground motions is higher than 20% of the total number of adopted records. The Cloud-CSM provides errors lower than $\pm 20\%$ in predicting the median fragility. Its accuracy reduces for cases with particularly low strength and long period or if an elastic-perfectly plastic hysteresis rule is adopted (errors higher than 20%). Moreover, the CSM outperform the N2 and the proposed intensity measure-based method in predicting the dispersion of fragility curves. Indeed, N2 and the intensity measure-based method can strongly underestimate the dispersion in fragility curves depending on the adopted intensity measure. Contrarily, the Cloud-CSM can be applied regardless of the selected intensity measure, implying generally an increasing dispersion with respect to NLTHA.

- Chapter 6 proposes a framework for performing seismic risk assessment of bridges directly accounting for epistemic uncertainties. The methodology is feasible for the seismic risk assessment of bridges in case of lacking knowledge input data. The uncertainties are modelled by means of the statistical generation of a population of index-bridges. The seismic performance analysis of the index-bridges is based on simplified modelling approaches, suitable for different bridge structural schemes, and the Cloud-CSM. The fragility of the main bridge is represented by a population of fragility curves. The influence of the knowledge-based uncertainty on the fragility of the main bridge can be quantified by analysing the variability of the fragility curves around the central value. Fragility curves corresponding to 10th and 90th percentiles are used to calculate the variability of seismic risk given the knowledge-based uncertainty. The methodology is applied on a dataset of eight reinforced-concrete case-study bridges described in Chapter 2. After the simplified data collection is carried out, the knowledge-based uncertainties are identified and are modelled with statistical distributions retrieved by the literature. The outcomes of the study are related to the definition of an appropriate sample size to generate a representative population of index-bridges for charac-

terising the effect of epistemic uncertainty. It is observed that the response in the longitudinal direction can be critical for the damage state of the bridges whose deck-abutment gap size is not seismically designed. In this case, the abutment-backfill system determines the reaching of the damage states. Consequently, the employment of typological approaches that neglect this component could involve severe inaccuracies in fragility estimations of bridge portfolios. In the transverse direction, the bearing typology can considerably affect the hierarchy of the strength between the substructure and the deck-substructure connection system and, therefore, the fragility of the investigated bridge. Particularly, a beneficial effect on the fragility in the transverse direction is registered for the bridges whose neoprene bearings enhance the ductility capacity of the subassemblies. The variability in fragility analysis due to the knowledge-based uncertainties is quantified. In the cases where the bearing typology is known, the variation between the 50th percentile of the median fragility and the corresponding 10th-90th percentiles is, generally, lower than $\pm 20\%$ in the transverse direction regardless of the considered damage state. For the bridge whose bearing typology is unknown, the influence of the uncertainties reaches the $\pm 45\%$. In the longitudinal direction, the variation between the 50th percentiles and the 10th/90th ones of the median fragility arises at $\pm 30 - 40\%$, but it is mainly related to the uncertainty of the properties of the abutment-backfill system. A second set of fragility curves is calculated using the peak ground acceleration as IM and it is used for computing the mean annual frequency of exceeding a damage state which is commonly used as a seismic risk index. Finally, one of the selected case studies is subjected to a more accurate data collection and the effect of the reduction of epistemic uncertainties is evaluated on the fragility analysis. Moreover, the approximations introduced by the simplified methodology are briefly evaluated by means of comparisons with NLTHA performed on a refined numerical model. The errors involved by the simplifications in the modelling approach and the analysis reach a maximum of 13% in terms of median fragility. Moreover, a maximum difference of 3% is detected comparing the variability with respect to the 50th percentile of the median fragility calculated by means of the simplified and re-

fined approaches. These findings prove that the adopted simplified procedure is promising at least for bridges similar to the investigated case studies.

7.2. Future research

Based on the presented outcomes, recommendations for future research on the considered topics are proposed.

- The proposed methodology (and all the other state-of-the-art approaches) for seismic risk assessment strongly rely on the availability of knowledge data about the structure/s to be analysed. As evidenced in this study, the initial knowledge is a decisive variable for the accuracy of the assessment process. In future, the availability of data is expected to increase. Consistently to the technological advances in geomatics, satellite platforms will provide open-access or low-cost images characterised by high resolution with high potentials in data extraction for structural assessment purposes. In this process, expertises in geomatics and informatics for data mining will contaminate the conventional structural engineering.

The data-sharing should be encouraged. In Italy, the innovative platform AINOP <https://ainop.mit.gov.it/portale#/> aims at storing and increasing the availability of knowledge data about public infrastructures. The platform is designed to allocate contributions by privates which can signal disruptions or damages in public infrastructure assets. The sharing of the data with researchers, together with private structural engineers, will be essential to increase the safety of infrastructure systems in the name of the public interest.

- The advances about the application of iterative analytical DBA approaches for the seismic performance prediction of bridges enrich an extended literature on the theme proposed in the state-of-the-art presentation. Further developments to increase the applicability of these approaches can be oriented to the inclusion of soil-structure interaction contributions in the algorithms. Preliminary recommendations are reported in Ni et al. (2014). Also, the inclusion of the contribution of environmental deterioration on RC components, such as the corrosion of steel

reinforcements (e.g. Zanini et al. (2013)), should be considered in the modelling the force-displacement curves in the RC members.

- The proposed methodology for calculating fragility curves via the CSM (Cloud-CSM) is promising in fragility analysis of portfolio of structures. In this study, its accuracy is assessed for single-degree-of-freedom systems. Further studies on the applicability of Cloud-CSM for multi-degree-of-freedom systems are needed for quantifying the error sources associated to the transformation of the refined MDoF pushover curve to the SDoF multi-linear one for different structural typologies and the influence of higher-mode contribution varying the degree of structural regularity. It is worth noting that the simple ductility-based coefficients applied within the algorithm are originally proposed with displacement-based design purposes. Improvements on the accuracy of the method can be obtained by developing more refined equivalent viscous damping formulation suitable for structural assessment purposes considering secondary backbone parameters.
- The proposed seismic risk assessment approach is tested for the typology of multi-span isostatic RC bridges. Its effectiveness should be evaluated for hyperstatic (e.g. continuous-deck) bridges. Furthermore, at this stage of the development the algorithm calculates the risk in terms of mean annual frequency of exceeding a damage state. According to Federal Emergency Management Agency (2012) expected annual losses are more efficient risk metrics being directly connected to economic consequences or service downtime and facilitating communication with stakeholders. Therefore, further developments of the proposed methodology should consider the integration of consequence models in the process to calculate vulnerability curves (loss ratio vs intensity measure) and expected annual losses considering the associated uncertainty.
- The future of the management of existing infrastructure assets will be governed by digital databases connected to automatic algorithms for the calculation of structural risk/safety indexes. The data will be stored in terms of Geographical Information Systems and Building Information Models. Current research fo-

cuses on developing algorithms for the automatic generation of Finite Element Models which can be directly used by the analysts to analyse the structural performance. The research products of the study are completely consistent with this framework. Currently, the proposed algorithms for analytical displacement-based seismic performance assessment and fragility analysis are developed in MATLAB environment. However, simple conversions can be performed to run the procedure in GIS environment, fostering the representation of user-friendly risk maps for addressing inspections and retrofit interventions. Based on the proposed routines (and future developments aimed at the applicability for a larger catalogue of bridge typologies) simple applications or plug-in for state-of-the-art GIS tools can be developed. Also appropriate software packages can be developed and implemented within bridge management systems. Graphical interfaces should be associated to the proposed routines to foster the adoption of these algorithms by the transportation authorities' operators who are not familiar with simple programming. An example of a user-friendly application for continuous-deck bridge assessment is already provided by the author (and colleagues) at <https://www.robertogentile.org/en/DBAb>.

References

- Abraham, L. & Sasikumar, M. (2014), 'Analysis of satellite images for the extraction of structural features', *IETE Technical Review (Institution of Electronics and Telecommunication Engineers, India)* **31**(2), 118–127.
- Şadan, O. B., Petrini, L. & Calvi, G. M. (2013), 'Direct displacement-based seismic assessment procedure for multi-span reinforced concrete bridges with single-column piers', *Earthquake Engineering and Structural Dynamics* .
- Adhikari, G., Petrini, L. & Calvi, G. M. (2010), 'Application of direct displacement based design to long span bridges', *Bulletin of Earthquake Engineering* **8**(4), 897–919.
- AISC (2010), 'American Institute of Steel Construction - Seismic Provisions for Structural Steel Buildings'.
- Ambraseys, N. N., Smit, P., Douglas, J., Margaris, B., Sigbjörnsson, R., Ólafsson, S., Suhadolc, P. & Costa, G. (2004), 'Internet site for European strong-motion data', *Bollettino di Geofisica Teorica ed Applicata* .
- Antoniou, S. & Pinho, R. (2004), 'Advantages and limitations of adaptive and non-adaptive force-based pushover procedures', *Journal of Earthquake Engineering* **8**(4), 497–522.
- Antoniou, S., Pinho, R. & Volta, C. A. (2004), 'Development and verification of a displacement-based adaptive pushover procedure', *Journal of Earthquake Engineering* **8**(5), 643–661.
- ATC (1983), 'Applied Technology Council (ATC-6) Seismic Retrofitting Guidelines for Highway Bridges'.
- ATC (1996), 'Applied Technology Council (ATC-40) - Seismic evaluation and retrofit of concrete buildings'.

- Avşar, Ö., Yakut, A. & Caner, A. (2011), 'Analytical fragility curves for ordinary highway bridges in Turkey', *Earthquake Spectra* .
- Ayele, Y. Z. & Droguett, E. L. (2020), Application of UAVs for bridge inspection and resilience assessment, *in* 'Proceedings of the 29th European Safety and Reliability Conference, ESREL 2019'.
- Barba, S., Barbarella, M., Di Benedetto, A., Fiani, M. & Limongiello, M. (2019), QUALITY ASSESSMENT of UAV PHOTOGRAMMETRIC ARCHAEOLOGICAL SURVEY, *in* 'ISPRS Annals of the Photogrammetry, Remote Sensing and Spatial Information Sciences'.
- Barrile, V., Candela, G. & Fotia, A. (2019), Point cloud segmentation using image processing techniques for structural analysis, *in* 'ISPRS Annals of the Photogrammetry, Remote Sensing and Spatial Information Sciences'.
- Barrile, V., Candela, G., Fotia, A. & Bernardo, E. (2019), UAV Survey of Bridges and Viaduct: Workflow and Application, *in* 'Lecture Notes in Computer Science (including subseries Lecture Notes in Artificial Intelligence and Lecture Notes in Bioinformatics)'.
- Bazzucchi, F., Restuccia, L. & Ferro, G. A. (2018), 'Considerations over the Italian road bridge infrastructure safety after the polcevera viaduct collapse: Past errors and future perspectives', *Frattura ed Integrità Strutturale* .
- Berry, M. P. & Eberhard, M. O. (2005), 'Practical performance model for bar buckling', *Journal of Structural Engineering* .
- Bertolesi, E., Buitrago, M., Adam, J. M. & Calderón, P. A. (2021), 'Fatigue assessment of steel riveted railway bridges: Full-scale tests and analytical approach', *Journal of Constructional Steel Research* .
- Borzi, B., Ceresa, P., Franchin, P., Noto, F., Calvi, G. M. & Pinto, P. E. (2014), 'Seismic Vulnerability of the Italian Roadway Bridge Stock', *Earthquake Spectra* .
- Borzi, B., Dell'Acqua, F., Faravelli, M., Gamba, P., Lisini, G., Onida, M. & Polli, D. (2011), 'Vulnerability study on a large industrial area using satellite remotely sensed images', *Bulletin of Earthquake Engineering* **9**(2), 675–690.

- Borzi, B., Pinho, R. & Crowley, H. (2008), 'Simplified pushover-based vulnerability analysis for large-scale assessment of RC buildings', *Engineering Structures* **30**(3), 804–820.
- Bovenga, F., Nutricato, R., Refice, A., Guerriero, L. & Chiaradia, M. T. (2005), 'SPINUA: A flexible processing chain for ERS / ENVISAT long term interferometry', *European Space Agency, (Special Publication) ESA SP (572)*, 473–478.
- Bradley, B. A. (2010), 'Epistemic uncertainties in component fragility functions', *Earthquake Spectra* **26**(1), 41–62.
- Buitrago, M., Bertolesi, E., Calderón, P. A. & Adam, J. M. (2021), 'Robustness of steel truss bridges: Laboratory testing of a full-scale 21-metre bridge span', *Structures* .
- Cademartori, M., Sullivan, T. J. & Osmani, S. (2020), 'Displacement \square based assessment of typical Italian RC bridges', *Bulletin of Earthquake Engineering* (0123456789).
URL: <https://doi.org/10.1007/s10518-020-00861-9>
- Caltrans (2013), 'Seismic Design Criteria Version 1.7', *California Department of Transportation: Sacramento, CA, U.S.* (April).
- Calvi, G. M., Pavese, A. & Pinto, P. E. (1993), *Progettazione Antisismica di Ponti Non Regolari [Seismic design of irregular bridges]*, Giornate AICAP, Pisa.
- Calvi, G. M., Pinto, P. E. & Franchin, P. (2013), *Seismic design practice in Italy*, in W.-F. Chen & L. Duan, eds, 'Bridge Engineering Handbook 2nd edition: Seismic design', CRC-Press.
- Calvi, G. M., Rodrigues, D. & Silva, V. (2018), 'Introducing new design spectra derived from Italian recorded ground motions 1972 to 2017', *Earthquake Engineering and Structural Dynamics* **47**(13), 2644–2660.
- Campbell, K. W. & Bozorgnia, Y. (2008), 'NGA ground motion model for the geometric mean horizontal component of PGA, PGV, PGD and 5% damped linear elastic response spectra for periods ranging from 0.01 to 10 s', *Earthquake Spectra* .

- Cardone, D. (2014), 'Displacement limits and performance displacement profiles in support of direct displacement-based seismic assessment of bridges', *Earthquake Engineering and Structural Dynamics* .
- Cardone, D., Perrone, G. & Sofia, S. (2011), 'A performance-based adaptive methodology for the seismic evaluation of multi-span simply supported deck bridges', *Bulletin of Earthquake Engineering* .
- Carr, A. J. (2016), 'RUAUMOKO3D - The Maori God of Volcanoes and Earthquakes. Inelastic Analysis Finite Element program- Tech. Rep.'.
- Casarotti, C., Monteiro, R. & Pinho, R. (2009), 'Verification of spectral reduction factors for seismic assessment of bridges', *Bulletin of the New Zealand Society for Earthquake Engineering* .
- Casarotti, C. & Pinho, R. (2007), 'An adaptive capacity spectrum method for assessment of bridges subjected to earthquake action', *Bulletin of Earthquake Engineering* .
- Castellazzi, G., D'Altri, A. M., Bitelli, G., Selvaggi, I. & Lambertini, A. (2015), 'From laser scanning to finite element analysis of complex buildings by using a semi-automatic procedure', *Sensors (Switzerland)* .
- Ceballos C, J. L. & Sullivan, T. J. (2012), 'Development of improved inelastic displacement prediction equations for the seismic design of hybrid systems', *Bulletin of the New Zealand Society for Earthquake Engineering* **45**(1), 1–14.
- Celik, O. C. & Ellingwood, B. R. (2010), 'Seismic fragilities for non-ductile reinforced concrete frames - Role of aleatoric and epistemic uncertainties', *Structural Safety* **32**(1), 1–12.
URL: <http://dx.doi.org/10.1016/j.strusafe.2009.04.003>
- CEN (2004), 'Eurocode 8 (EN 1998-1: 2004) Design of structures for earthquake resistance – Part 1: General rules, seismic actions and rules for buildings'.

- CEN (2005), 'Eurocode 8 (EN 1998-3: 2004) Design of structures for earthquake resistance—Part 3: Assessment and retrofitting of buildings'.
- CEN (2009), 'Eurocode 3 (EN 1991-1-4) Design of steel structures - Part 1-1: General rules and rules for buildings'.
- Chan, B., Guan, H., Jo, J. & Blumenstein, M. (2015), 'Towards UAV-based bridge inspection systems: a review and an application perspective', *Structural Monitoring and Maintenance* .
- Chioccarelli, E., Cito, P., Iervolino, I. & Giorgio, M. (2019), 'REASSESS V2.0: software for single- and multi-site probabilistic seismic hazard analysis', *Bulletin of Earthquake Engineering* .
- Choi, E., DesRoches, R. & Nielson, B. (2004), 'Seismic fragility of typical bridges in moderate seismic zones', *Engineering Structures* .
- Chopra, A. & Goel, R. (1999), *Capacity-Demand-Diagram Methods for Estimating Seismic Deformation of Inelastic Structures: SDF Systems*.
- Computer and Structures INC (CSI) (2017), 'CSiBridge v 20.1.1: Integrated 3-D Bridge Analysis, Design and Rating'.
- Computer and Structures INC (CSI) (2018), 'SAP2000 - Structural Analysis Program'.
- Conde-Carnero, B., Riveiro, B., Arias, P. & Caamaño, J. C. (2016), 'Exploitation of Geometric Data provided by Laser Scanning to Create FEM Structural Models of Bridges', *Journal of Performance of Constructed Facilities* .
- Cordova, P. P., Deierlein, G. G., Mehanny, S. S. & Cornell, C. (2001), 'Development of a two-parameter seismic intensity measure and probabilistic assessment procedure', *The Second U.S.- 13 Japan Workshop on Performance-Based Earthquake Engineering Methodology for Reinforced Concrete Building Structures* .

Cornell, C. A., Jalayer, F., Hamburger, R. O. & Foutch, D. A. (2002), 'Probabilistic basis for 2000 SAC federal emergency management agency steel moment frame guidelines', *Journal of Structural Engineering* .

Cosenza, E., Galasso, C. & Maddaloni, G. (2011), 'A simplified method for flexural capacity assessment of circular RC cross-sections', *Engineering Structures* .

Costa, C., Figueiredo, R., Silva, V. & Bazzurro, P. (2020), 'Application of open tools and datasets to probabilistic modeling of road traffic disruptions due to earthquake damage', *Earthquake Engineering and Structural Dynamics* .

Crosetto, M., Monserrat, O., Cuevas-González, M., Devanthery, N. & Crippa, B. (2016), 'Persistent Scatterer Interferometry: A review', *ISPRS Journal of Photogrammetry and Remote Sensing* **115**, 78–89.

URL: <http://dx.doi.org/10.1016/j.isprsjprs.2015.10.011>

Darby, P., Hollerman, W. & Miller, J. (2019), 'Exploring the Potential Utility of Unmanned Aerial Vehicles for Practical Bridge Inspection in Louisiana', *MATEC Web of Conferences* .

D'Ayala, D., Meslem, A., Vamvatsikos, D., Porter, K., Rossetto, T., Crowley, H. & Silva, V. (2013), 'Guidelines for Analytical Vulnerability Assessment - Low/Mid-Rise', *GEM Technical Report* **08**, 162.

De Luca, F., Vamvatsikos, D. & Iervolino, I. (2013), 'Near-optimal piecewise linear fits of static pushover capacity curves for equivalent SDOF analysis', *Earthquake Engineering and Structural Dynamics* .

Decreto Ministro dei Lavori Pubblici (DM) 24 gennaio 1986 - Norme tecniche relative alle costruzioni antisismiche. (1986).

Decreto Ministro dei Lavori Pubblici (DM) 3 marzo 1975 -Approvazione delle norme tecniche per le costruzioni in zone sismiche. (1975), Technical report.

- Della Corte, G. & Landolfo, R. (2017), 'Lateral loading tests of built-up battened columns with semi-continuous base-plate connections', *Journal of Constructional Steel Research* **138**, 783–798.
URL: <https://doi.org/10.1016/j.jcsr.2017.08.018>
- Della Corte, G. & Mazzolani, F. M. (2008), Theoretical developments and numerical verification of a displacementbased design procedure for steel braced structures, in 'Proceedings of the 14th world conference on earthquake engineering', Beijing.
- Dell'Acqua, F., Polli, D., Tenerelli, P. & Ehrlich, D. (2011), *D2.14 - Methods to extract building and road infrastructures from remote sensing and integration with ancillary information*, SYNER-G Deliverable Report.
- Dolšek, M. (2012), 'Simplified method for seismic risk assessment of buildings with consideration of aleatory and epistemic uncertainty', *Structure and Infrastructure Engineering* **8**(10), 939–953.
- Duque, L., Seo, J. & Wacker, J. (2018), 'Synthesis of Unmanned Aerial Vehicle Applications for Infrastructures', *Journal of Performance of Constructed Facilities* **32**(4), 04018046.
URL: <http://ascelibrary.org/doi/10.1061/%28ASCE%29CF.1943-5509.0001185>
- Dwairi, H. & Kowalsky, M. J. (2006), 'Implementation of inelastic displacement patterns in direct displacement-based design of continuous bridge structures', *Earthquake Spectra* **22**(3), 631–662.
- Eads, L., Miranda, E., Krawinkler, H. & Lignos, D. G. (2013), 'An efficient method for estimating the collapse risk of structures in seismic regions', *Earthquake Engineering and Structural Dynamics* .
- Ehrlich, D. & Tenerelli, P. (2013), 'Optical satellite imagery for quantifying spatio-temporal dimension of physical exposure in disaster risk assessments'.
- Elnashai, A. S. (2001), 'Advanced inelastic static (pushover) analysis for earthquake applications'.

ENAC (2020), 'Regolamento Mezzi Aerei a Pilotaggio Remoto'.

Esmaily, A. & Peterman, R. J. (2007), 'Performance analysis tool for reinforced concrete members'.

Fajfar, P. (1999), 'Capacity spectrum method based on inelastic demand spectra', *Earthquake Engineering and Structural Dynamics* **28**(9), 979–993.

Fajfar, P. & Gašpersič, P. (1996), 'The N2 method for the seismic damage analysis of RC buildings', *Earthquake Engineering and Structural Dynamics* .

Federal Emergency Management Agency (2012), 'Seismic Performance Assessment of Buildings, Volume 1 – Methodology'.

URL: www.ATCCouncil.org

Federal Emergency Management Agency (FEMA) (2012), 'Multi-hazard loss estimation methodology technical manuals and user's manuals for the earthquake advanced engineering building module (AEBM), the earthquake model, the flood model, and the hurricane model'.

FEMA (2003), Multi-Hazard Loss Estimation Methodology, Earthquake Model, Hazus®-MH, Technical Manual, Technical report.

FHWA (1995), 'Federal Highway Administration - Seismic Retrofitting Manual for Highway Bridges - FHWA-RD-94 052'.

FHWA (2006), 'Federal Highway Administration - Seismic Retrofitting Manual for Highway Structures : Part 1 – Bridges'.

Forte, G., Chioccarelli, E., De Falco, M., Cito, P., Santo, A. & Iervolino, I. (2019), 'Seismic soil classification of Italy based on surface geology and shear-wave velocity measurements', *Soil Dynamics and Earthquake Engineering* **122**.

Freeman, S. A. (1998a), Development and use of capacity spectrum method, *in* 'Proc. 6th U.S. National Conf. Earthquake Engng.', CD-ROM, EERI, Oakland, Seattle.

- Freeman, S. A. (1998b), 'Development and use of capacity spectrum method'.
- Gamba, P., Dell'Acqua, F. & Lisini, G. (2009), BREC: The built-up area RECOgnition tool, *in* '2009 Joint Urban Remote Sensing Event'.
- Gentile, R. (2019), DBA bridges - practical manual. Free internal report and software (www.robertogentile.org, last access: 15/12/2019). Alpha version of the app can be requested at www.robertogentile.org., Technical report.
- Gentile, R., del Vecchio, C., Pampanin, S., Raffaele, D. & Uva, G. (2019), 'Refinement and Validation of the Simple Lateral Mechanism Analysis (SLaMA) Procedure for RC Frames', *Journal of Earthquake Engineering* (January), 1–29.
URL: <https://www.tandfonline.com/doi/full/10.1080/13632469.2018.1560377>
- Gentile, R. & Galasso, C. (2020), 'Gaussian process regression for seismic fragility assessment of building portfolios', *Structural Safety* .
- Gentile, R., Galasso, C. & Pampanin, S. (2020), 'Materials vs structural detailing : relative effect of their epistemic uncertainties on the seismic fragility of reinforced concrete frames', *Journal of Structural Engineering in press*.
- Gentile, R., Nettis, A. & Raffaele, D. (2020), 'Effectiveness of the Displacement-Based seismic performance Assessment for continuous RC bridges and proposed extensions', *Engineering Structures* .
URL: <https://doi.org/10.1016/j.engstruct.2020.110910>
- Gentile, R., Pampanin, S., Raffaele, D. & Uva, G. (2019a), 'Analytical seismic assessment of RC dual wall/frame systems using SLaMA: Proposal and validation', *Engineering Structures* .
- Gentile, R., Pampanin, S., Raffaele, D. & Uva, G. (2019b), 'Non-linear analysis of RC masonry-infilled frames using the SLaMA method: part 1—mechanical interpretation of the infill/frame interaction and formulation of the procedure', *Bulletin of Earthquake Engineering* .

- Gentile, R., Pampanin, S., Raffaele, D. & Uva, G. (2019c), 'Non-linear analysis of RC masonry-infilled frames using the SLaMA method: part 2—parametric analysis and validation of the procedure', *Bulletin of Earthquake Engineering* .
- Gentile, R., Porco, F., Raffaele, D. & Uva, G. (2018a), 'Simplified moment-curvature relationship in analytical form for circular RC sections', *Bulletin of the New Zealand Society for Earthquake Engineering* **51**(3), 145–158.
- Gentile, R., Porco, F., Raffaele, D. & Uva, G. (2018b), 'Simplified moment-curvature relationship in analytical form for circular RC sections', *Bulletin of the New Zealand Society for Earthquake Engineering* .
- Gentile, R. & Raffaele, D. (2018), 'Simplified analytical Moment-Curvature relationship for hollow circular RC cross-sections', *Earthquake and Structures* **15**(4), 419–429.
- Georgiev, T. S., Zhelev, D. S. & Raycheva, L. D. (2017), Performance assessment of concentrically braced frames with modified braces depending on the applied beam-column joints, in 'COMPDYN 2017 - Proceedings of the 6th International Conference on Computational Methods in Structural Dynamics and Earthquake Engineering'.
- Giovenale, P., Cornell, C. A. & Esteva, L. (2004), 'Comparing the adequacy of alternative ground motion intensity measures for the estimation of structural responses', *Earthquake Engineering and Structural Dynamics* .
- Goggins, J. G. & Sullivan, T. J. (2009), Displacement-based seismic design of SDOF concentrically braced frames, in 'Mazzolani, Ricles, Sause (eds) STESSA 2009.', Taylor & Francis Group.
- Grande, E. & Rasulo, A. (2013), 'Seismic assessment of concentric X-braced steel frames', *Engineering Structures* **49**(April 2013), 983–995.
- Gupta, B. & Kunnath, S. K. (2000), 'Adaptive spectra-based pushover procedure for seismic evaluation of structures', *Earthquake Spectra* .

- Hammad, A. & Moustafa, M. A. (2020), 'Modeling sensitivity analysis of special concentrically braced frames under short and long duration ground motions', *Soil Dynamics and Earthquake Engineering* **128**(August 2019), 105867.
URL: <https://doi.org/10.1016/j.soildyn.2019.105867>
- Han, Q., Zhou, Y., Ou, Y. & Du, X. (2017), 'Seismic behavior of reinforced concrete sacrificial exterior shear keys of highway bridges', *Engineering Structures* .
- Hancilar, U. & Taucer, F. (2013), *Guidelines for typology definition of European physical assets for earthquake risk assessment - SYNER-G Reference Report 2*.
- Harris, D. K., Brooks, C. N. & Ahlborn, T. T. M. (2016), 'Synthesis of Field Performance of Remote Sensing Strategies for Condition Assessment of In-Service Bridges in Michigan', *Journal of Performance of Constructed Facilities* .
- Haselton, C. B., Baker, J. W., Liel, A. B. & Deierlein, G. G. (2011), 'Accounting for Ground-Motion Spectral Shape Characteristics in Structural Collapse Assessment through an Adjustment for Epsilon', *Journal of Structural Engineering* .
- Housner, G. W. & Jennings, P. C. (1972), 'The San Fernando California earthquake', *Earthquake Engineering & Structural Dynamics* .
- Housner, G. W. & Thiel, C. C. (1990), 'Competing against Time: Report of the Governor's Board of Inquiry on the 1989 Loma Prieta Earthquake', *Earthquake Spectra* .
- Hsiao, P. C., Lehman, D. E. & Roeder, C. W. (2012), 'Improved analytical model for special concentrically braced frames', *Journal of Constructional Steel Research* **73**, 80–94.
- Iervolino, I., Galasso, C. & Cosenza, E. (2010), 'REXEL: Computer aided record selection for code-based seismic structural analysis', *Bulletin of Earthquake Engineering* .
- Isakovic, T. (2006), 'Higher modes in simplified inelastic seismic analysis of single column bent viaducts', (April 2005), 95–114.

- Isaković, T., Nino Lazaro, M. & Fischinger, M. (2008), 'Applicability of pushover methods for the seismic analysis of single-column bent viaducts', *Earthquake Engineering and Structural Dynamics* **37**(8), 1185–1202.
- Jacobsen, L. (1960), 'Damping in composite structures'.
- Jalayer, F., Ebrahimian, H., Miano, A., Manfredi, G. & Sezen, H. (2017), 'Analytical fragility assessment using unscaled ground motion records', *Earthquake Engineering and Structural Dynamics* **46**(15), 2639–2663.
- Kappos, A. J., Gkatzogias, K. I. & Gidaris, I. G. (2013), 'Extension of direct displacement-based design methodology for bridges to account for higher mode effects', *Earthquake Engineering & Structural Dynamics* (July 2012), 581–602.
- Katsanos, E. I. & Sextos, A. G. (2015), 'Inelastic spectra to predict period elongation of structures under earthquake loading', *Earthquake Engineering and Structural Dynamics* .
- Kazantzi, A. K. & Vamvatsikos, D. (2015), 'Intensity measure selection for vulnerability studies of building classes', *Earthquake Engineering and Structural Dynamics* .
- Khaloo, A., Lattanzi, D., Cunningham, K., Dell'Andrea, R. & Riley, M. (2018), 'Unmanned aerial vehicle inspection of the Placer River Trail Bridge through image-based 3D modelling', *Structure and Infrastructure Engineering* **14**(1), 124–136.
URL: <http://doi.org/10.1080/15732479.2017.1330891>
- Khan, E., Kowalsky, M. J. & Nau, J. M. (2016), 'Equivalent Viscous Damping Model for Short-Period Reinforced Concrete Bridges', *Journal of Bridge Engineering* **21**(2).
- King, D. J., Priestley, M. J. N. & Park, R. (1986), 'Computer programs for concrete column design, Research Report 86/12'.
- Kohrangi, M., Bazzurro, P. & Vamvatsikos, D. (2016), 'Vector and scalar IMs in structural response estimation, Part II: Building demand assessment', *Earthquake Spectra* **32**(3), 1525–1543.

- Kohrangi, M., Bento, R. & Lopes, M. (2015a), 'Seismic performance of irregular bridges - comparison of different non linear static procedures', *Structure and Infrastructure Engineering* **11**(12), 1632–1650.
- Kohrangi, M., Bento, R. & Lopes, M. (2015b), 'Seismic performance of irregular bridges – comparison of different nonlinear static procedures', *Structure and Infrastructure Engineering* **11**(12), 1632–1650.
- Kohrangi, M., Kotha, S. R. & Bazzurro, P. (2018), 'Ground-motion models for average spectral acceleration in a period range: Direct and indirect methods', *Bulletin of Earthquake Engineering* .
- Kowalsky, M. J. (2002), 'A displacement-based approach for the seismic design of continuous concrete bridges', *Earthquake Engineering and Structural Dynamics* **31**(3), 719–747.
- Kowalsky, M. J. & Priestley, M. J. (2000), 'Improved analytical model for shear strength of circular reinforced concrete columns in seismic regions', *ACI Structural Journal* .
- Kwan, W.-P. & Billington, S. L. (2003), 'Influence of Hysteretic Behavior on Equivalent Period and Damping of Structural Systems', *Journal of Structural Engineering* .
- Lee, K. & Bruneau, M. (2008a), 'Seismic vulnerability evaluation of axially loaded steel built-up laced members I: Experimental results', *Earthquake Engineering and Engineering Vibration* .
- Lee, K. & Bruneau, M. (2008b), 'Seismic vulnerability evaluation of axially loaded steel built-up laced members II: Evaluations', *Earthquake Engineering and Engineering Vibration* .
- Lee, K. W. & Park, J. K. (2019), 'Modeling and management of bridge structures using unmanned aerial vehicle in Korea', *Sensors and Materials* .
- Lin, Y. Y. & Chang, K. C. (2003), 'An improved capacity spectrum method for ATC-40', *Earthquake Engineering and Structural Dynamics* .

- Lin, Y.-Y. & Miranda, E. (2008), 'Noniterative Equivalent Linear Method for Evaluation of Existing Structures', *Journal of Structural Engineering* .
- Liu, W., Chen, S.-e. & Hauser, E. (2009), 'Remote sensing for bridge health monitoring', **7456**, 1–10.
- Lowe, G. (2004), 'SIFT - The Scale Invariant Feature Transform', *International Journal* .
- Lubowiecka, I., Armesto, J., Arias, P. & Lorenzo, H. (2009), 'Historic bridge modelling using laser scanning, ground penetrating radar and finite element methods in the context of structural dynamics', *Engineering Structures* .
- Mander, J. B., Priestley, M. J. N. & Park, R. (1988), 'Theoretical Stress–Strain Model for Confined Concrete', *Journal of Structural Engineering* .
- Mangalathu, S., Jeon, J.-S., Padgett, J. E. & DesRoches, R. (2017), 'Performance-based grouping methods of bridge classes for regional seismic risk assessment: Application of ANOVA, ANCOVA, and non-parametric approaches', *Earthquake Engineering and Structural Dynamics* .
- MATLAB (2018), *version 9.5.0.944444 (R2018b)*, The MathWorks Inc., Natick, Massachusetts.
- MCEER (2006), *Seismic retrofitting guidelines for complex steel truss highway bridges*, Technical report.
- McKenna, F. (2011), 'OpenSees: A framework for earthquake engineering simulation', *Computing in Science and Engineering* .
- Megally, S. H., Silva, P. F. & Seible, F. (2002), *Seismic response of sacrificial shear keys in bridge abutments*, Technical report.
- Mehanny, S. S. F. (2009), 'A broad-range power-law form scalar-based seismic intensity measure', *Engineering Structures* **31**(7), 1354–1368.
URL: <http://dx.doi.org/10.1016/j.engstruct.2009.02.003>

- Meletti, C., Galadini, F., Valensise, G., Stucchi, M., Basili, R., Barba, S., Vannucci, G. & Boschi, E. (2008), 'A seismic source zone model for the seismic hazard assessment of the Italian territory', *Tectonophysics* .
- Menderes, A., Erener, A. & Sarp, G. (2015), 'Automatic Detection of Damaged Buildings after Earthquake Hazard by Using Remote Sensing and Information Technologies', *Procedia Earth and Planetary Science* .
- Minas, S. & Galasso, C. (2019), 'Accounting for spectral shape in simplified fragility analysis of case-study reinforced concrete frames', *Soil Dynamics and Earthquake Engineering* **119**(November 2018), 91–103.
URL: <https://doi.org/10.1016/j.soildyn.2018.12.025>
- Ministero delle Infrastrutture e dei Trasporti (2008), 'Decreto Ministeriale (DM) 14 gennaio 2008. Norme Tecniche per le costruzioni. Gazzetta Ufficiale n.29 del 4 febbraio 2008'.
- Ministero delle Infrastrutture e dei Trasporti (2018), Decreto Ministeriale (DM) 17 gennaio 2018. Aggiornamento delle norme tecniche per le costruzioni. Gazzetta ufficiale n.42 del 20 febbraio 2018, Technical report.
- Ministero delle Infrastrutture e dei Trasporti (2019), 'Decreto Ministeriale (DM) n. 430, 08 ottobre 2019. Realizzazione dell'archivio informatico nazionale delle opere pubbliche (AINOP)'.
- Ministero delle Infrastrutture e dei Trasporti (2020), 'Linee Guida per la Classificazione e Gestione del Rischio, la Valutazione della Sicurezza ed il Monitoraggio dei Ponti Esistenti'.
- Misra, S. & Padgett, J. E. (2019), 'Seismic Fragility of Railway Bridge Classes: Methods, Models, and Comparison with the State of the Art', *Journal of Bridge Engineering* .
- Monteiro, R. (2016), 'Sampling based numerical seismic assessment of continuous span RC bridges', *Engineering Structures* **118**, 407–420.
URL: <http://dx.doi.org/10.1016/j.engstruct.2016.03.068>

Monteiro, R., Zelaschi, C., Silva, A. & Pinho, R. (2019), 'Derivation of Fragility Functions for Seismic Assessment of RC Bridge Portfolios Using Different Intensity Measures', *Journal of Earthquake Engineering* **23**(10), 1678–1694.

URL: <http://dx.doi.org/10.1080/13632469.2017.1387188>

Montejo, L. A. & Kowalsky, M. J. (2007), 'Set of codes for the analysis of reinforced concrete members'.

Morgenthal, G., Hallermann, N., Kersten, J., Taraben, J., Debus, P., Helmrich, M. & Rodehorst, V. (2019), 'Framework for automated UAS-based structural condition assessment of bridges', *Automation in Construction* **97**(May 2018), 77–95.

Moschonas, I. F., Kappos, A. J., Panetsos, P., Papadopoulos, V., Makarios, T. & Thanopoulos, P. (2009), 'Seismic fragility curves for greek bridges: Methodology and case studies', *Bulletin of Earthquake Engineering* .

Mouroux, P. & Le Brun, B. (2006), 'Presentation of RISK-UE project', *Bulletin of Earthquake Engineering* .

Mueller, M., Segl, K., Heiden, U. & Kaufmann, H. (2006), 'Potential of high-resolution satellite data in the context of vulnerability of buildings', *Natural Hazards* .

Nations, U. (2015), 'Sendai Framework for Disaster Risk Reduction 2015–2030'.

URL: https://www.preventionweb.net/files/43291_sendaiframeworkfordrren.pdf

Nettis, A., Gentile, R., Raffaele, D., Uva, G. & Galasso, C. (2021), 'Cloud Capacity Spectrum Method: accounting for record-to-record variability in fragility analysis using nonlinear static procedures', *Soil Dynamics and Earthquake Engineering* .

Nettis, A., Gentile, R., Uva, G. & Raffaele, D. (2019a), SOME APPLICATIONS OF A DISPLACEMENT-BASED PROCEDURE FOR THE SEISMIC RESPONSE OF CONTINUOUS GIRDER RC-BRIDGES, in '3rd International Conference on International Conference on Recent Advances in Nonlinear Design, Resilience and Rehabilitation of Structures (CoRASS 2019)'.

- Nettis, A., Gentile, R., Uva, G. & Raffaele, D. (2019b), Validation of an analytical displacement-based pushover for multi-span continuous deck bridges, *in* 'COMPdyn Proceedings'.
- Nettis, A., Raffaele, D. & Uva, G. (2021), SIMPLIFIED FRAGILITY ANALYSIS OF MULTI-SPAN ISOSTATIC RC-BRIDGES CONSIDERING AN INCOMPLETE KNOWLEDGE LEVEL, *in* 'COMPdyn Proceedings', number June, pp. 27–30.
- Nettis, A., Saponaro, M. & Nanna, M. (2020), 'RPAS-based framework for simplified seismic risk assessment of Italian RC-bridges', *Buildings* .
- Ni, P., Petrini, L. & Paolucci, R. (2014), 'Direct displacement-based assessment with nonlinear soil-structure interaction for multi-span reinforced concrete bridges', *Structure and Infrastructure Engineering* **10**(9), 1211–1227.
- Nielson, B. G. (2005), Analytical fragility curves for highway bridges in moderate seismic zones, PhD thesis.
- Nielson, B. G. & DesRoches, R. (2007), 'Seismic fragility methodology for highway bridges using a component level approach', *Earthquake Engineering and Structural Dynamics* .
- Nolte, E., Khazi, A. & Wenzel, F. (2011), *D2.16 - Vulnerability assessment by optical satellite imagery*, SYNER-G Deliverable Report.
- NZSEE (2017), 'New Zealand Society for Earthquake Engineering - The seismic assessment of existing buildings - technical guidelines for engineering assessments'.
- (OJ), O. J. o. t. E. U. (2019), 'Commission Implementing Regulations (EU) 2019/947. Rules and Procedures for the Operation of Unmanned Aircraft'.
- Olsson, A., Sandberg, G. & Dahlblom, O. (2003), 'On Latin hypercube sampling for structural reliability analysis', *Structural Safety* .

- OPCM (2003), 'Ordinanza del Presidente del Consiglio dei ministri (OPCM) 20 marzo 2003, n. 3274. Primi elementi in materia di criteri generali per la classificazione sismica del territorio nazionale e di normative tecniche per le costruzioni in zona sismica.'
- O'Reilly, G. J., Jiménez, A. A., Monteiro, R., Borzi, B. & Calvi, G. M. (2019), 'Towards regional safety assessment of bridge infrastructure', *13th International Conference on Applications of Statistics and Probability in Civil Engineering, ICASP 2019* pp. 1–8.
- O'Reilly, G. J. & Monteiro, R. (2019), On the efficient risk assessment of bridge structures, *in* 'COMPADYN Proceedings'.
- Otani, S. (1974), 'SAKE: A COMPUTER PROGRAM FOR INELASTIC RESPONSE OF R/C FRAMES TO EARTHQUAKES.', *III Univ Dep Civ Eng Struct Res Ser* .
- Otero, L. D. (2015), 'Proof of Concept for using Unmanned Aerial Vehicles for High Mast Pole and Bridge Inspections', *Florida Department of Transportation, Research Center* .
- Padgett, J. E., Nielson, B. G. & DesRoches, R. (2008), 'Selection of optimal intensity measures in probabilistic seismic demand models of highway bridge portfolios', *Earthquake Engineering and Structural Dynamics* .
- Palermo, A., Liu, R., Rais, A., McHaffie, B., Andisheh, K., Pampanin, S., Gentile, R., Nuzzo, I., Granerio, M., Loporcaro, G., McGann, C. & Wotherspoon, L. (2017), 'Performance of road bridges during the 14 November 2016 Kaikoura earthquake', *Bulletin of the New Zealand Society for Earthquake Engineering* .
- Pan, Y., Dong, Y., Wang, D., Chen, A. & Ye, Z. (2019), 'Three-dimensional reconstruction of structural surface model of heritage bridges using UAV-based photogrammetric point clouds', *Remote Sensing* .
- Paraskeva, T. & Kappos, A. (2010), 'Further development of a multimodal pushover analysis procedure for seismic assessment of bridges', *Earthquake Engineering and Structural Dynamics* **39**(2), 211–222.

- Paraskeva, T. S., Kappos, A. J. & Sextos, A. G. (2006), 'Extension of modal pushover analysis to seismic assessment of bridges', *Earthquake Engineering and Structural Dynamics* **35**(10), 1269–1293.
- Pennucci, D., Sullivan, T. J. & Calvi, G. M. (2011), 'Displacement reduction factors for the design of medium and long period structures', *Journal of Earthquake Engineering* **15**(SUPPL. 1), 1–29.
- Perdomo, C. & Monteiro, R. (2020), 'Extension of displacement-based simplified procedures to the seismic loss assessment of multi-span RC bridges', *Earthquake Engineering and Structural Dynamics* .
- Perdomo, C., Monteiro, R. & Sucuoğlu, H. (2017), 'Generalized force vectors for multi-mode pushover analysis of bridges', *Bulletin of Earthquake Engineering* **15**(12), 5247–5280.
- Perdomo, C., Monteiro, R. & Sucuoğlu, H. (2020), 'Development of Fragility Curves for Single-Column RC Italian Bridges Using Nonlinear Static Analysis', *Journal of Earthquake Engineering* .
- Pinho, R., Casarotti, C. & Antoniou, S. (2007), 'A comparison of single-run pushover analysis techniques for seismic assessment of bridges', *Earthquake Engineering and Structural Dynamics* .
- Pinho, R., Monteiro, R., Casarotti, C. & Delgado, R. (2009), 'Assessment of continuous span bridges through nonlinear static procedures', *Earthquake Spectra* **25**(1), 143–159.
- Pinto, P. E. & Franchin, P. (2010), 'Issues in the upgrade of Italian highway structures', *Journal of Earthquake Engineering* **14**(8), 1221–1252.
- Pipinato, A. (2018), 'Extending the lifetime of steel truss bridges by cost-efficient strengthening interventions', *Structure and Infrastructure Engineering* **14**(12), 1611–1627.
- URL:** <http://doi.org/10.1080/15732479.2018.1465103>

- Pipinato, A. (2019), 'Extending the fatigue life of steel truss bridges with tuned mass damper systems', *Advances in Civil Engineering* .
- Pipinato, A., Pellegrino, C., Bursi, O. S. & Modena, C. (2009), 'High-cycle fatigue behavior of riveted connections for railway metal bridges', *Journal of Constructional Steel Research* **65**(12), 2167–2175.
- Pipinato, A., Pellegrino, C. & Modena, C. (2011), 'Fatigue assessment of highway steel bridges in presence of seismic loading', *Engineering Structures* **33**(1), 202–209.
- Pollino, M. & Bruneau, M. (2007), 'Seismic Retrofit of Bridge Steel Truss Piers Using a Controlled Rocking Approach', *Journal of Bridge Engineering* .
- Pollino, M. & Bruneau, M. (2008), 'Dynamic seismic response of controlled rocking bridge steel-truss piers', *Engineering Structures* **30**(6), 1667–1676.
- Priestley, M. J. N., Calvi, G. M. & Kowalsky, M. J. (2007), *Displacement-based seismic design of structures*, IUSS Press, Pavia, Italy.
- Priestley, M. J. N., Seible, F. & Calvi, G. M. (1996), *Seismic design and retrofit of bridges*, John Wiley and Sons, New York, USA.
- ReLUIs (2009), 'Linee Guida e Manuale Applicativo per la Valutazione della Sicurezza Sismica e il consolidamento dei ponti esistenti in C.A.'.
- Riveiro, B., DeJong, M. & Conde, B. (2016), An automatic method for geometric segmentation of masonry arch bridges for structural engineering purposes, in 'International Archives of the Photogrammetry, Remote Sensing and Spatial Information Sciences - ISPRS Archives'.
- Rossetto, T., Gehl, P., Minas, S., Galasso, C., Duffour, P., Douglas, J. & Cook, O. (2016), 'FRACAS: A capacity spectrum approach for seismic fragility assessment including record-to-record variability', *Engineering Structures* **125**, 337–348.
URL: <http://dx.doi.org/10.1016/j.engstruct.2016.06.043>

- Ruiz-García, J. & Miranda, E. (2003), 'Inelastic displacement ratios for evaluation of existing structures', *Earthquake Engineering and Structural Dynamics* **32**(8), 1237–1258.
- Ruiz-García, J. & Miranda, E. (2007), 'Probabilistic estimation of maximum inelastic displacement demands for performance-based design', *Earthquake Engineering and Structural Dynamics* .
- Saiidi, M. & Sozen, M. (1979), Simple and complex models for nonlinear seismic response of reinforced concrete structures, Technical Report Report No 465, University of Illinois, Urbana, Illinois, USA.
- Saponaro, M., Turso, A. & Tarantino, E. (2020), Parallel Development of Comparable Photogrammetric Workflows Based on UAV Data Inside SW Platforms, *in* 'Lecture Notes in Computer Science (including subseries Lecture Notes in Artificial Intelligence and Lecture Notes in Bioinformatics)'.
- Sarkar, S. & Sahoo, D. R. (2016), 'Effect of chord configuration and spacing on cyclic flexural response of built-up columns', *International Journal of Steel Structures* **16**(2), 441–453.
- Seo, J., Duque, L. & Wacker, J. (2018), 'Drone-enabled bridge inspection methodology and application', *Automation in Construction* **94**(May), 112–126.
URL: <https://doi.org/10.1016/j.autcon.2018.06.006>
- Sextos, A., Mackie, K., Stojadinovic, B. & Taskari, O. (2008), Simplified P-y relationships for modeling embankment-abutment systems of typical California bridges, *in* '14th World Conference on Earthquake Engineering, Beijing, China'.
- Shamsabadi, A. & Kapuskar, M. (2010), 'Nonlinear soil-abutment-foundation- Structure interaction analysis of skewed bridges subjected to near-field ground motions', *Transportation Research Record* .
- Sharpe, R. D. (1976), The Seismic Response of Inelastic Structures, PhD thesis, Department of Civil Engineering, University of Canterbury, Christchurch, New Zealand.

- Silva, A. L., Correia, J. A., Xin, H., Lesiuk, G., De Jesus, A. M., Augusto Fernandes, A. & Berto, F. (2021), 'Fatigue strength assessment of riveted details in railway metallic bridges', *Engineering Failure Analysis* .
- Silva, V., Akkar, S., Baker, J., Bazzurro, P., Castro, J. M., Crowley, H., Dolsek, M., Galasso, C., Lagomarsino, S., Monteiro, R., Perrone, D., Pitilakis, K. & Vamvatsikos, D. (2019), 'Current challenges and future trends in analytical fragility and vulnerability modeling', *Earthquake Spectra* .
- Silva, V., Crowley, H., Varum, H., Pinho, R. & Sousa, R. (2014), 'Evaluation of analytical methodologies used to derive vulnerability functions', *Earthquake Engineering and Structural Dynamics* .
- Smerzini, C., Galasso, C., Iervolino, I. & Paolucci, R. (2014), 'Ground motion record selection based on broadband spectral compatibility', *Earthquake Spectra* **30**(4), 1427–1448.
- Soergel, U., Thiele, A., Gross, H. & Thoennessen, U. (2007), Extraction of bridge features from high-resolution InSAR data and optical images, in '2007 Urban Remote Sensing Joint Event, URS'.
- Soleimani, F. (2020), 'Propagation and quantification of uncertainty in the vulnerability estimation of tall concrete bridges', *Engineering Structures* .
- Stefanidou, S. P. & Kappos, A. J. (2017), 'Methodology for the development of bridge-specific fragility curves', *Earthquake Engineering and Structural Dynamics* **46**(1), 73–93.
- Stefanidou, S. P. & Kappos, A. J. (2019), *Bridge-specific fragility analysis: when is it really necessary?*, Vol. 17, Springer Netherlands.
URL: <https://doi.org/10.1007/s10518-018-00525-9>
- Syifa, M., Kadavi, P. R. & Lee, C. W. (2019), 'An artificial intelligence application for post-earthquake damage mapping in Palu, central Sulawesi, Indonesia', *Sensors (Switzerland)* .

Tavares, D. H., Padgett, J. E. & Paultre, P. (2012), 'Fragility curves of typical as-built highway bridges in eastern Canada', *Engineering Structures* **40**, 107–118.

URL: <http://dx.doi.org/10.1016/j.engstruct.2012.02.019>

Tenerelli, P. & Crowley, H. (2013a), *Development of inventory datasets through remote sensing and direct observation data for earthquake loss estimation*.

Tenerelli, P. & Crowley, H. (2013b), 'Development of inventory datasets through remote sensing and direct observation data for earthquake loss estimation'.

Tortolini, P., Petrangeli, M. & Lupoi, A. (2011), Criteri per la verifica e la sostituzione degli appoggi in neoprene di viadotti esistenti in zona sismica, in '14th italian conference on seismic engineering (ANIDIS)', number October 2014, Bari.

URL: <https://www.researchgate.net/publication/266941512>

Transforming our World: The 2030 Agenda for Sustainable Development (A/RES/70/1) (2015).

URL: <https://www.refworld.org/docid/57b6e3e44.html>

Vaghefi, K., Oats, R. C., Harris, D. K., Ahlborn, T. T. M., Brooks, C. N., Endsley, K. A., Roussi, C., Shuchman, R., Burns, J. W. & Dobson, R. (2012), 'Evaluation of Commercially Available Remote Sensors for Highway Bridge Condition Assessment', *Journal of Bridge Engineering* .

Vamvatsikos, D. & Cornell, C. A. (2006), 'Direct estimation of the seismic demand and capacity of oscillators with multi-linear static pushovers through IDA', *Earthquake Engineering and Structural Dynamics* .

Vidic, T., Fajfar, P. & Fischinger, M. (1994), 'Consistent inelastic design spectra: Strength and displacement', *Earthquake Engineering & Structural Dynamics* .

Wang, C., Cho, Y. K. & Kim, C. (2015), 'Automatic BIM component extraction from point clouds of existing buildings for sustainability applications', *Automation in Construction* .

- Wijesundara, K. K., Nascimbene, R. & Sullivan, T. J. (2011), 'Equivalent viscous damping for steel concentrically braced frame structures', *Bulletin of Earthquake Engineering* **9**(5), 1535–1558.
- Yang, L., Cheng, J. C. & Wang, Q. (2020), 'Semi-automated generation of parametric BIM for steel structures based on terrestrial laser scanning data', *Automation in Construction* .
- Yilmaz, M. F. & Çalayan, B. (2018), 'Seismic assessment of a multi-span steel railway bridge in Turkey based on nonlinear time history', *Natural Hazards and Earth System Sciences* **18**(1), 231–240.
- Zanini, M. A., Pellegrino, C., Morbin, R. & Modena, C. (2013), 'Seismic vulnerability of bridges in transport networks subjected to environmental deterioration', *Bulletin of Earthquake Engineering* **11**(2), 561–579.
- Zelaschi, C. & Monteiro, R. (2017), 'Towards a Taxonomy for Portuguese Rc Bridges', (June), 652–662.
- Zelaschi, C., Monteiro, R. & Pinho, R. (2016), 'Parametric Characterization of RC Bridges for Seismic Assessment Purposes', *Structures* **7**.

Appendix A

Filled forms for data collection on real case-study bridges

In this Appendix, the data forms adopted to collect data for the case-study bridges analysed in Chapter 6 are reported. The following spreadsheets are developed in Microsoft Excel and populated using the multi-source approach described in Chapter 2.

Identification		Commentary		Piers		Commentary	
101	Name	Galderne Bridge		P01	Pier typology	SC	Commentary SC: single column - W: Wall - H: Portal
102	Manager	Providence		P02	Degree of fixity (longitudinal)	U	X: fixed displacement, R: free displacement. Insert a vector of {PXR} if HPP, a vector of {PRX/RX/RB} if ISO. The length of the vector is equal to the number of beams.
103	Position	40.464		P03	Degree of fixity (transverse)	XXX.XXX.XX	X: fixed displacement, R: free displacement. Insert a vector of {PXR} if HPP, a vector of {PRX/RX/RB} if ISO. The length of the vector is equal to the number of beams.
104		16.4707		P04	Bearing type (longitudinal)	U	Type of the fixed bearings - Insert a vector of N: Neoprene or X: Fixed generic
105	Region	Basilicata		P05	Bearing type (transverse)	U	Type of the fixed bearings - Insert a vector of N: Neoprene or X: Fixed generic
106	Province	Matera		P06	Cap beam	9.3.1.1.3	Dimension of the cap beam. Insert a vector of {B1: B2: H1: H2: W}
107	Municipality	Grattale		P07	Pier section	CIRC	Fill in if SC: RECT: Rectangular - CIRC: Circular - Polygonal: Elliptical
108	Infrastructure type	Bridge		P08	Pier dimensions		Fill in if W: RECT: Rectangular
109	Road category	C		P09	Support height	2.6-2.6-2.6-2.6	Fill in if P07 & RECT with the dimension parallel to the axis of the bridge
General structural				P10	Pier height	8.4.14.15.6 9.2	Fill in if P07 & CIRC with the diameter
G01	Structure type	GIR	Commentary GIR: Girder bridge - ARC: Arch bridge - CB: Cable-stayed - Truss	P11	Distance between supports	0.65-0.65	Fill in with a vector of bent heights from the base to top of cap beam
G02	Deck type	BwS	BwS: Beams with slab - BG: Box girder - NS: Monolithic slab - Truss	P12	Design compressive strength of concrete	U	Fill in with a vector of bent heights from the base to top of cap beam
G03	Stark scheme	ISO	ISO: Isostatic - HYP: Hyperstatic	P13	Steel bars Young's modulus	200000	Insert the characteristic design strength of concrete (Rsk or Rck)
G04	Deck-pier connections	SUPP	Fill in only if HPP - SUPP: Pinned connection - MON: Monolythic connections	P14	Design yielding strength of steel bars	U	Insert the Young's modulus of the steel (E)
G05	Deck-abutments connections	SUPP	SUPP: Pinned connection - MON: Monolythic connections	P15	Concrete Young's modulus	30000	Insert the characteristic design strength of steel (Rsk or Rck)
G06	Year/period of design	1980	Fill in design year/period	Abutments			
G07	Bridge category	1	1: first category; 2: second category	A01	Degree of fixity (longitudinal)	U	Commentary X: fixed displacement, R: free displacement. Insert a vector of {PXR} if HPP, a vector of {PRX/RX/RB} if ISO. The length of the vector is equal to 2.
G08	Séismic category	0	Fill in the following values [0,1,2] if period of design is 1939-1964.	A02	Degree of fixity (transverse)	FXFX	X: fixed displacement, R: free displacement. Insert a vector of {PXR} if HPP, a vector of {PRX/RX/RB} if ISO. The length of the vector is equal to 2.
G09	Séismic coefficient	0	Fill in the following values [0.6, 9, 12] if period of design is 1964-2008.	A03	Bearing type (longitudinal)	U	Type of the fixed bearings - Insert a vector of 2 component: Neoprene or X: Fixed generic.
G10	Soil type	B	Fill in one of the following values [A - B - C - D - E] for soil category	A04	Bearing type (transverse)	U	Type of the fixed bearings - Insert a vector of 2 component: Neoprene or X: Fixed generic.
G11	Topography	T1	Fill in the following values [T1 - T2 - T3 - T4] for topographic category	A05	Gap dimension	U	Dimension of the gap in longitudinal dimension
G12	Total length	150	Insert the total length of the bridge	A06	Width of abutment backwall	10.5	Insert the width of the abutment backwall
G13	Number of spans	5	Insert the number of spans	A07	Height of abutment backwall	1.75	Insert the height of the abutment backwall
G14	Span length	30.30.30.30	Insert a vector of span lengths	Deck			
Deck				A08	Stiffness of abutment backwall	U	Insert the stiffness coefficient of the abutment backwall (stiffness per unit of width)
D01	Girder material	PC	RC: Reinforced Concrete - PC: Precast - ST: Steel	Bearings			
D02	Slab material	RC	RC: Reinforced Concrete - PC: Precast	B01	Bearing height	U	Height of the bearing devices
D03	Deck width	10.5	Insert the total width of the deck	B02	Bearing stiffness	350000	Fill in if there are NEOPRENE bearings with the stiffness at the single bearing device Fill in if there are FIXED bearings with the stiffness of the single bearing device
D04	Road width	9.2	Insert the width of the road only	Materials			
D05	Sidewalk width	0.65	Insert the width of the sidewalk only	M01	Compressive strength of concrete	U	Insert the mean strength of concrete (fc)
D06	Girder height	1.75	Insert the height of the girder (from lower edge of slab to top of the bearing device)	M02	Tensile strength of steel	U	Insert the mean strength of concrete (fy)
D07	Girder area	0.45	Insert the cross section area of the girder	Constructive details			
D08	Number of girder	U	Fill in with the number of girders	C01	Number of long bars	U	Commentary Insert the number of long bars. If P07 & RECT, insert a vect of 2 components. If P07 is CIRC insert one number
D09	Slab thickness	0.3	Insert the height of the slab (from top edge of girder to top slab)	C02	Diameter of long bars	U	Diameter of longitudinal bars. RECT: insert a vect of 2 components. If CIRC insert a vector of one component
D10	Deck cross area	[m²]	Fill in only if D07. D08-D09 are not available	C03	Step of transv reinf	U	Step of transverse bars
D11	Fluore moment of inertia	[m⁴]	Fill in only if G03 is HYP with the moment of inertia in transverse direction	C04	Diameter of transv reinf	U	Diameter of transverse reinforcements
D12	G2 deck	36	Fill in with the non-structural permanent weight				
D13	Concrete Young's modulus	U	Fill in with the concrete Young's modulus of the deck				

Figure A.1: Data collected for case-study B1

Identification		Commentary	Piers	Commentary
101	Name	Corradò	P01	Pier typology
102	Manager	Province	SC	SC: single column - W: Wall - R: Portal
103	Position	40.4.208	P02	Degree of fixity (longitudinal)
104	Region	15.4.845	P03	Degree of fixity (transverse)
105	Province	Basilicata	P04	Bearing type (longitudinal)
106	Municipality	Pedersa	P05	Bearing type (transverse)
107	Infrastructure type	Fermeata Tiera Bridge	P06	Cap beam
108	Road category	C	P07	Pier section
General structural				
G01	Structure type	GIR	P08	Pier dimensions
G02	Deck type	BWS	P09	Support height
G03	Static scheme	ISO	P10	Pier height
G04	Deck-pier connections	SUPP	P11	Distance between supports
G05	Deck-abutments connections	SUPP	P12	Design compressive strength of concrete
G06	Year/period of design	1990	P13	Steel bars Young's modulus
G07	Bridge category	1	P14	Design yielding strength of steel bars
G08	Seismic category	0	P15	Concrete Young's modulus
G09	Seismic coefficient	2	Abutments	
G10	Soil type	B	A01	Degree of fixity (longitudinal)
G11	Topography	T1	A02	Degree of fixity (transverse)
G12	Total length	102	A03	Bearing type (longitudinal)
G13	Number of spans	3	A04	Bearing type (transverse)
G14	Span length	34.34.34	A05	Gap dimension
Deck				
D01	Girder material	PC	A06	Width of abutment backwall
D02	Slab material	RC	A07	Height of abutment backwall
D03	Deck width	14.5	A08	Stiffness of abutment backwall
D04	Road width	13.5	Bearings	
D05	Sidewalk width	0.5	B01	Bearing height
D06	Girder height	2	B02	Bearing stiffness
D07	Girder area	0.9	Materials	
D08	Number of girder	5	M01	Compressive strength of concrete
D09	Slab thickness	0.3	M02	Tensile strength of steel
D10	Deck cross area	(m ²)	Constructive details	
D11	Flexure moment of inertia	(m ⁴)	C01	Number of long bars
D12	C2 deck	(kN/m)	C02	Diameter of long bars
D13	Concrete Young's modulus	(MPa)	C03	Step of transverse
			C04	Diameter of transverse

Figure A.2: Data collected for case-study B2

Identification		Commentary		Piers		Commentary	
101	Name	S. Francesco		P01	Pier typology	SC	Commentary SC: single column - W: Wall - H: Portal
102	Manager	Provincia		P02	Degree of fixity (longitudinal)	XXX	X: fixed displacement, R: free displacement. Insert a vector of {PXR} if PXR, a vector of {PRX}/XX/RR. If ISO. The length of the vector is equal to the number of beams.
103	Position	40.7007		P03	Degree of fixity (transverse)	XXX	X: fixed displacement, R: free displacement. Insert a vector of {PXR} if PXR, a vector of {PRX}/XX/RR. If ISO. The length of the vector is equal to the number of beams.
104	Region	15.8121		P04	Bearing type (longitudinal)	NN	Type of the fixed bearings - Insert a vector of N: Neoprene or X: Fixed generic
105	Province	Basilicata		P05	Bearing type (transverse)	XX	Type of the fixed bearings - Insert a vector of N: Neoprene or X: Fixed generic
106	Municipality	Potenza		P06	Cap beam	10.81.05.2.7	Dimension of the cap beam. Insert a vector of {B1: B2 - H1 - H2 - W}
107	Infrastructure type	S. Francesco		P07	Pier section	CIRC	Fill in if SC: RECT: Rectangular - CIRC: Circular - Polygonal: Elliptical
108	Road category	Bridge		P08	Pier dimensions		Fill in if W: RECT: Rectangular
109	General structural	C		P09	Pier dimensions		Fill in if P07 & RECT with the dimension parallel to the axis of the bridge
G01	Structure type	GIR	Commentary GIR: Girder bridge - ARC: Arch bridge - CB: Cable-stayed - Truss	P10	Support height	2.8.2.8	Fill in if P07 & RECT with the dimension normal to the axis of the bridge
G02	Deck type	BwS	BwS: Beams with slab - BG: Box girder - NS: Monolithic slab - Truss	P11	Support height	0.2.0.2	Fill in if P07 & CIRC with the diameter
G03	Stake scheme	ISO	ISO: Isostatic - HYP: Hyperstatic	P12	Pier height	8.5.7.4	Fill in with a vector of bearing heights (top of cap beam - bottom of the deck)
G04	Deck-pier connections	SUPP	Fill in only if HYP - SUPP: Pinned connection - MON: Monolithic connections	P13	Distance between supports	0.75.0.75	Fill in with a vector of bearing distances from the axis of the pier on the capbeam
G05	Deck-abutments connections	SUPP	Fill in only if ISO - SUPP: Pinned connection	P14	Design compressive strength of concrete	U	Insert the characteristic design strength of concrete (R _{ik} o R _{ck})
G06	Year/period of design	1990	SUPP: Pinned connection - MON: Monolithic connections	P15	Steel bars Young's modulus	200000	Insert the Young's modulus of the steel (E)
G07	Bridge category	1	Fill in design year/period		Design yielding strength of steel bars	U	Insert the characteristic design strength of steel (R _{sk} o R _{ck})
G08	Seismic category	0	1: first category; 2: second category		Concrete Young's modulus	30000	Insert the characteristic design strength of steel (R _{sk} o R _{ck})
G09	Seismic coefficient	2	Fill in the following values [0.6 9 12] if period of design is 1964-1984.	Abutments			
G10	Soil type	B	Fill in the following values [A - B - C - D - E] for soil category	A01	Degree of fixity (longitudinal)	FXFX	Commentary X: fixed displacement, R: free displacement. Insert a vector of {PXR} if PXR, a vector of {PRX}/XX/RR. If ISO. The length of the vector is equal to 2.
G11	Topography	T1	Fill in one of the following values [T1 - T2 - T3 - T4] for topographic category	A02	Degree of fixity (transverse)	FXFX	X: fixed displacement, R: free displacement. Insert a vector of {PXR} if PXR, a vector of {PRX}/XX/RR. If ISO. The length of the vector is equal to 2.
G12	Total length	99	Insert the total length of the bridge	A03	Bearing type (longitudinal)	NN	Type of the fixed bearings - Insert a vector of 2 component: Neoprene or X: Fixed generic.
G13	Number of spans	3	Insert the number of spans	A04	Bearing type (transverse)	XX	Type of the fixed bearings - Insert a vector of 2 component: Neoprene or X: Fixed generic.
G14	Span length	33.33.33	Insert a vector of span lengths	A05	Gap dimension	U	Dimension of the gap in longitudinal dimension
Deck				A06	Width of abutment backwall	10.5	Insert the width of the abutment backwall
D01	Girder material	PC	Commentary RC: Reinforced Concrete - PC: Precast - ST: Steel	A07	Height of abutment backwall	1.7	Insert the height of the abutment backwall
D02	Slab material	RC	RC: Reinforced Concrete - PC: Precast	A08	Stiffness of abutment backwall	U	Insert the stiffness coefficient of the abutment backwall (stiffness per unit of width)
D03	Deck width	10.5	Insert the total width of the deck	Bearings			
D04	Road width	10.5	Insert the width of the road only	B01	Bearing height	U	Height of the bearing devices
D05	Sidewalk width	0	Insert the width of the sidewalk only	B02	Bearing stiffness	350000	Fill in if there are NEOPRENE bearings with the stiffness at the single bearing device Fill in if there are FIXED bearings with the stiffness of the single bearing device
D06	Girder height	1.7	Insert the height of the girder (from lower edge of slab to top of the bearing device)	Materials			
D07	Girder area	0.65	Insert the cross section area of the girder	M01	Compressive strength of concrete	U	Commentary Insert the mean strength of concrete (f _c)
D08	Number of girder	4	Fill in with the number of girders	M02	Tensile strength of steel	U	Insert the mean strength of concrete (f _y)
D09	Slab thickness	0.3	Insert the height of the slab (from top edge of girder to top slab)	Constructive details			
D10	Deck cross area	[m ²]	Fill in only if D07: D08: D09 are not available	C01	Number of long bars	U	Commentary Insert the number of long bars, if P07 & RECT, insert a vect of 2 components, if P07 is CIRC insert one number
D11	Flexure moment of inertia	[m ⁴]	Fill in only if G03 is HYP with the moment of inertia in transverse direction	C02	Diameter of long bars	U	Diameter of longitudinal bars, RECT: insert a vect of 2 components, if CIRC insert a vector of one component
D12	G2 deck	36	Fill in with the non-structural permanent weight	C03	Step of transv reinf	U	Step of transverse bars
D13	Concrete Young's modulus	U	Fill in with the concrete Young's modulus of the deck	C04	Diameter of transv reinf	U	Diameter of transverse reinforcements

Figure A.3: Data collected for case-study B3

Identification		Commentary		Piers		Commentary	
101	Name	Vadeto Cava		P01	Pier typology	SC	SC: single column - W: Wall - R: Portal
102	Manager	ANAS		P02	Degree of fixity (longitudinal)	XX XXXXXX	X: fixed displacement, R: free displacement. Insert a vector of {P,X,R} if HPP, a vector of {f00/R00/Xf00} if ISO. The length of the vector is equal to the number of beams.
103	Position	46,7208		P03	Degree of fixity (transverse)	XX XXXXXX	X: fixed displacement, R: free displacement. Insert a vector of {P,X,R} if HPP, a vector of {f00/R00/Xf00} if ISO. The length of the vector is equal to the number of beams.
104	Region	15.8003		P04	Bearing type (longitudinal)	NN NN	Type of the fixed bearings - Insert a vector of N: Neoprene or X: Fixed generic
105	Province	Basilicata		P05	Bearing type (transverse)	XX XX	Type of the fixed bearings - Insert a vector of N: Neoprene or X: Fixed generic
106	Municipality	Potenza		P06	Cap beam	10.1.03.2.7 [m]	Dimension of the cap beam. Insert a vector of {B1 - B2 - H1 - H2 - W}
107	Infrastructure type	S. Nicola Bridge		P07	Pier section	CIRC	Fill in if SC: RECT: Rectangular - CIRC: Circular - Polygonal: Elliptical
108	Infrastructure type						Fill in if W: RECT: Rectangular
109	Road category	C					Fill in if P07 is RECT with the dimension parallel to the axis of the bridge
General structural							Fill in if P07 is RECT with the dimension normal to the axis of the bridge
G01	Structure type	GIR		P08	Pier dimensions		Fill in if P07 is CIRC with the diameter
G02	Deck type	BWS		P09	Support height	2.7 2.7 2.7 2.7 [m]	Fill in with a vector of bearing heights (top of cap beam - bottom of the deck)
G03	Slab scheme	ISO		P10	Pier height	6.5 5.7 10.9 5 [m]	Fill in with a vector of bent heights from the base to top of capbeam
G04	Deck-pier connections	SUPP		P11	Distance between supports	0.75 0.75 [m]	Fill in with a vector of bearing distances from the axis of the pier on the capbeam
G05	Deck-abutments connections	SUPP		P12	Design compressive strength of concrete	U	Insert the characteristic design strength of concrete (f _{bk} or f _{ck})
G06	Year/period of design	1990		P13	Steel bars Young's modulus	200000	Insert the Young's modulus of the steel (E)
G07	Bridge category	1		P14	Design yielding strength of steel bars	U	Insert the characteristic design strength of steel (f _{yk} or f _{yk})
G08	Seismic category	0		P15	Concrete Young's modulus	30000	Insert the Young's modulus of the concrete (E)
G09	Seismic coefficient	2		Abutments			
G10	Soil type	B		A01	Degree of fixity (longitudinal)	FX FX	X: fixed displacement, R: free displacement. Insert a vector of {P,X,R} if HPP, a vector of {f00/R00/Xf00} if ISO. The length of the vector is equal to 2.
G11	Topography	T1		A02	Degree of fixity (transverse)	FX FX	X: fixed displacement, R: free displacement. Insert a vector of {P,X,R} if HPP, a vector of {f00/R00/Xf00} if ISO. The length of the vector is equal to 2.
G12	Total length	162		A03	Bearing type (longitudinal)	NN	Type of the fixed bearings - Insert a vector of 2 component Neoprene or X: Fixed generic
G13	Number of spans	5		A04	Bearing type (transverse)	XX	Type of the fixed bearings - Insert a vector of 2 component Neoprene or X: Fixed generic
G14	Span length	32.32.32.32		A05	Gap dimension	10.5	Dimension of the gap in longitudinal dimension
Deck				A06	Width of abutment backwall	10.5	Insert the width of the abutment backwall
D01	Girder material	PC		A07	Height of abutment backwall	1.7	Insert the height of the abutment backwall
D02	Slab material	RC		A08	Stiffness of abutment backwall	U	Insert the stiffness coefficient of the abutment backwall (at fives per unit of width)
D03	Deck width	10.5		Bearings			
D04	Road width	10.5		B01	Bearing height	U	Height of the bearing devices
D05	Sidewalk width	0		B02	Bearing stiffness	350000	Fill in if there are NEOPRENE bearings with the stiffness of the single bearing device
D06	Girder height	1.7		Materials			
D07	Girder area	0.65		M01	Compressive strength of concrete	U	Insert the mean strength of concrete (f _c)
D08	Number of girder	4		M02	Tensile strength of steel	U	Insert the mean strength of concrete (f _y)
D09	Slab thickness	0.3		Constructive details			
D10	Deck cross area			C01	Number of long bars	U	Insert the number of long bars, if P07 is RECT, insert a vect of 2 components, if P07 is CIRC, insert one number
D11	Flexure moment of inertia			C02	Diameter of long bars	U	Diameter of longitudinal bars, RECT: insert a vect of 2 components, if CIRC, insert a vector of one component
D12	G2 deck	36		C03	Step of transverse reinf	U	Step of transverse bars
D13	Concrete Young's modulus	U		C04	Diameter of transverse reinf	U	Diameter of transverse reinforcements

Figure A.4: Data collected for case-study B4

Identification		Commentary		Piers		Commentary	
101	Name	Changali		P01	Pier typology	SC	Commentary SC: single column - W: Wall - H: Portal
102	Manager	ANAS		P02	Degree of fixity (longitudinal)	XXX	X: fixed displacement, R: free displacement. Insert a vector of {PXR} if PXR, a vector of {PRX/RX/RB} if ISO. The length of the vector is equal to the number of beams.
103	Position	40.7236		P03	Degree of fixity (transverse)	XXX	X: fixed displacement, R: free displacement. Insert a vector of {PXR} if PXR, a vector of {PRX/RX/RB} if ISO. The length of the vector is equal to the number of beams.
104	Region	15.804		P04	Bearing type (longitudinal)	NN	Type of the fixed bearings - Insert a vector of N: Neoprene or X: Fixed generic
105	Province	Basilicata		P05	Bearing type (transverse)	XX	Type of the fixed bearings - Insert a vector of N: Neoprene or X: Fixed generic
106	Municipality	Potenza		P06	Cap beam	10.81.05.27	Dimension of the cap beam. Insert a vector of {B1: B2 - H1 - H2 - W1}
107	Infrastructure type	S. Nicola		P07	Pier section	CIRC	Fill in if SC: RECT: Rectangular - CIRC: Circular - Polygonal: Elliptical
108	Road category	Bridge		P08	Pier dimensions		Fill in if W: RECT: Rectangular
109	General structural	C		P09	Pier dimensions	2.7-2.7	Fill in if P07 & RECT with the dimension parallel to the axis of the bridge
G01	Structure type	GIR	Commentary GIR: Girder bridge - ARC: Arch bridge - CB: Cable-stayed - Truss	P10	Support height	0.3 0.3	Fill in if P07 & CIRC with the diameter
G02	Deck type	Bw5	Bw5: Beams with slab - BG: Box girder - NS: Monolithic slab - Truss	P11	Pier height	7.5 6.7	Fill in with a vector of bent heights (top of cap beam - bottom of the deck)
G03	Static scheme	ISO	ISO: Isostatic - HYP: Hyperstatic	P12	Distance between supports	0.75 0.75	Fill in with a vector of bent heights from the base to top of cap beam
G04	Deck-pier connections	SUPP	Fill in only if HYP - SUPP: Pinned connection - MON: Monolythic connections	P13	Design compressive strength of concrete	U	Insert the characteristic design strength of concrete (R _{ik} or R _{ck})
G05	Deck-abutments connections	SUPP	SUPP: Pinned connection - MON: Monolythic connections	P14	Steel bars Young's modulus	200000	Insert the Young's modulus of the steel (E)
G06	Year/period of design	1990	Fill in design year/period	P15	Design yielding strength of steel bars	30000	Insert the characteristic design strength of steel (R _{sk} or R _{ck})
G07	Bridge category	1	1: first category; 2: second category	Abutments			
G08	Seismic category	0	Fill in the following values [0,1,2] if period of design is 1939-1964.	A01	Degree of fixity (longitudinal)	FXFX	Commentary X: fixed displacement, R: free displacement. Insert a vector of {PXR} if PXR, a vector of {PRX/RX/RB} if ISO. The length of the vector is equal to 2.
G09	Seismic coefficient	2	Fill in the following values [0.6 9 12] if period of design is 1964-2008.	A02	Degree of fixity (transverse)	FXFX	X: fixed displacement, R: free displacement. Insert a vector of {PXR} if PXR, a vector of {PRX/RX/RB} if ISO. The length of the vector is equal to 2.
G10	Soil type	B	Fill in one of the following values [A - B - C - D - E] for soil category	A03	Bearing type (longitudinal)	NN	Type of the fixed bearings - Insert a vector of 2 component: Neoprene or X: Fixed generic.
G11	Topography	T1	Fill in the following values [T1 - T2 - T3 - T4] for topographic category	A04	Bearing type (transverse)	XX	Type of the fixed bearings - Insert a vector of 2 component: Neoprene or X: Fixed generic.
G12	Total length	102	Insert the total length of the bridge	A05	Gap dimension	U	Dimension of the gap in longitudinal dimension
G13	Number of spans	4	Insert the number of spans	A06	Width of abutment backwall	10.5	Insert the width of the abutment backwall
G14	Span length	34-34-34	Insert a vector of span lengths	A07	Height of abutment backwall	1.7	Insert the height of the abutment backwall
Deck				A08	Stiffness of abutment backwall	U	Insert the stiffness coefficient of the abutment backwall (stiffness per unit of width)
D01	Girder material	PC	RC: Reinforced Concrete - PC: Precast - ST: Steel	Bearings			
D02	Slab material	RC	RC: Reinforced Concrete - PC: Precast	B01	Bearing height	U	Commentary Height of the bearing devices
D03	Deck width	10.5	Insert the total width of the deck	B02	Bearing stiffness	1000000000	Fill in if there are NEOPRENE bearings with the stiffness at the single bearing device Fill in if there are FIXED bearings with the stiffness of the single bearing device
D04	Road width	10.5	Insert the width of the road only	Materials			
D05	Sidewalk width	0	Insert the width of the sidewalk only	M01	Compressive strength of concrete	U	Commentary Insert the mean strength of concrete (f _c)
D06	Girder height	1.7	Insert the height of the girder (from lower edge of slab to top of the bearing device)	M02	Tensile strength of steel	U	Insert the mean strength of concrete (f _y)
D07	Girder area	0.65	Insert the cross section area of the girder	Constructive details			
D08	Number of girder	4	Fill in with the number of girders	C01	Number of long bars	U	Commentary Insert the number of long bars, if P07 & RECT; insert a vect of 2 components, if P07 is CIRC insert one number
D09	Slab thickness	0.3	Insert the height of the slab (from top edge of girder to top slab)	C02	Diameter of long bars	U	Diameter of longitudinal bars, RECT: insert a vect of 2 components, if CIRC insert a vector of one component
D10	Deck cross area	[m ²]	Fill in only if D07: D08-D09 are not available	C03	Step of transv reinf	U	Step of transverse bars
D11	Flexure moment of inertia	[m ⁴]	Fill in only if G03 is HYP with the moment of inertia in transverse direction	C04	Diameter of transv reinf	U	Diameter of transverse reinforcements
D12	G2 deck	36	Fill in with the non-structural permanent weight				
D13	Concrete Young's modulus	U	Fill in with the concrete Young's modulus of the deck				

Figure A.5: Data collected for case-study B5

Identification		Commentary		Piers		Commentary	
101	Name	Miracoli		P01	Pier typology	SC	SC: single column - W: Wall - R: Portal
102	Manager	ANAS		P02	Degree of fixity (longitudinal)	XX XX	X: fixed displacement, R: free displacement. Insert a vector of {P,X,R} if HPP, a vector of {f00/R00/X/R00} if ISO. The length of the vector is equal to the number of beams.
103	Position	40,8.01		P03	Degree of fixity (transverse)	XX XX	X: fixed displacement, R: free displacement. Insert a vector of {P,X,R} if HPP, a vector of {f00/R00/X/R00} if ISO. The length of the vector is equal to the number of beams.
104	Region	15,7494		P04	Bearing type (longitudinal)	NN	Type of the fixed bearings - Insert a vector of N: Neoprene or X: Fixed generic
105	Province	Basilicata		P05	Bearing type (transverse)	XX	Type of the fixed bearings - Insert a vector of N: Neoprene or X: Fixed generic
106	Municipality	Potenza		P06	Cap beam	10.1.1.03.3	Dimension of the cap beam. Insert a vector of {B1 - B2 - H1 - H2 - W}
107	Infrastructure type	Arigliano Bridge		P07	Pier section	CIRC	Fill in if SC: RECT: Rectangular - CIRC: Circular - Polygonal: Elliptical
108	Infrastructure type	Bridge					Fill in if P07 is RECT with the dimension normal to the axis of the bridge
109	Road category	C					Fill in if P07 is RECT with the dimension parallel to the axis of the bridge
General structural							
G01	Structure type	GIR	Commentary	P08	Pier dimensions		Fill in if P07 is RECT with the dimension normal to the axis of the bridge
G02	Deck type	BWS	GIR: Girder bridge - ARC: Arch bridge - CB: Cable stayed... BWS: Beams with slab - BG: Box girder - MS: Monolithic slab - TB: Truss	P09	Support height	03 03	Fill in with a vector of bearing heights (top of cap beam - bottom of the deck)
G03	Slab scheme	ISO	ISO: Isostatic - HYP: Hyperstatic	P10	Pier height	5.9 5.2	Fill in with a vector of bent heights from the base to top of capbeam
G04	Deck-pier connections		Fill in only if HPP - SUPP: Pinned connection - MON: Monolithic connections	P11	Distance between supports	11	Fill in with a vector of bearing distances from the axis of the pier on the capbeam
G05	Deck-abutments connections	SUPP	SUPP: Pinned connection	P12	Design compressive strength of concrete	U	Insert the characteristic design strength of concrete (f _{bk} or f _{ck})
G06	Year/period of design	SUPP	SUPP: Pinned connection - MON: Monolithic connections	P13	Steel bars Young's modulus	200000	Insert the Young's modulus of the steel (E)
G07	Bridge category	1990	Fill in design year/period	P14	Design yielding strength of steel bars	U	Insert the characteristic design strength of steel (f _{sk} or f _{yk})
G08	Sismic category	1	1: first category; 2: second category	P15	Concrete Young's modulus	30000	Insert the Young's modulus of the concrete (E)
G09	Sismic coefficient	0	Fill in the following values [0.12] if period of design is 1939-1964.	Abutments			
G10	Soil type	2	Fill in the following values [0.69 12] if period of design is 1964-2008.	A01	Degree of fixity (longitudinal)	FX FX	X: fixed displacement, R: free displacement. Insert a vector of {P,X,R} if HPP, a vector of {f00/R00/X/R00} if ISO. The length of the vector is equal to 2.
G11	Topography	B	Fill in one of the following values [A - B - C - D - E] for soil category	A02	Degree of fixity (transverse)	FX FX	X: fixed displacement, R: free displacement. Insert a vector of {P,X,R} if HPP, a vector of {f00/R00/X/R00} if ISO. The length of the vector is equal to 2.
G12	Total length	T1	Fill in one of the following values [T1 - T2 - T3 - T4] for topographic category	A03	Bearing type (longitudinal)	NN	Type of the fixed bearings - Insert a vector of 2 component Neoprene or X: Fixed generic
G13	Number of spans	102	Insert the total length of the bridge	A04	Bearing type (transverse)	XX	Type of the fixed bearings - Insert a vector of 2 component Neoprene or X: Fixed generic
G14	Span length	33.33.33	Insert a vector of span lengths	A05	Gap dimension	U	Dimension of the gap in longitudinal dimension
Deck							
D01	Girder material	PC	RC: Reinforced Concrete - PC: Precast - ST: Steel	A06	Width of abutment backwall	9.5	Insert the width of the abutment backwall
D02	Slab material	RC	RC: Reinforced Concrete - FC: Precast	A07	Height of abutment backwall	1.4	Insert the height of the abutment backwall
D03	Deck width	9.5	Insert the total width of the deck	A08	Stiffness of abutment backwall	U	Insert the stiffness coefficient of the abutment backwall (at fives per unit of width)
D04	Road width	9.5	Insert the width of the road only	Bearings			
D05	Sidewalk width	0	Insert the width of the sidewalk only	B01	Bearing height	U	Height of the bearing devices
D06	Girder height	1.4	Insert the height of the girder (from lower edge of slab to top of the bearing device)	B02	Bearing stiffness	U	Fill in if there are NEOPRENE bearings with the stiffness of the single bearing device
D07	Girder area	0.65	Insert the cross section area of the girder	Materials			
D08	Number of girder	4	Fill in with the number of girders	M01	Compressive strength of concrete	U	Insert the mean strength of concrete (f _c)
D09	Slab thickness	0.35	Insert the height of the slab (from top edge of girder to top slab)	M02	Tensile strength of steel	U	Insert the mean strength of concrete (f _y)
D10	Deck cross area		Fill in only if D07-D08-D09 are not available	Constructive details			
D11	Flexure moment of inertia		Fill in only if G03 is HPP with the moment of inertia in transverse direction	C01	Number of long bars	U	Insert the number of long bars, if P07 is RECT, insert a vect of 2 components, if P07 is CIRC, insert one number
D12	G2 deck		Fill in with the non-structural permanent weight	C02	Diameter of long bars	U	Diameter of longitudinal bars, RECT: insert a vect of 2 components, if CIRC, insert a vector of one component
D13	Concrete Young's modulus	36	Fill in with the concrete Young's modulus of the deck	C03	Step of transv. reinf	U	Step of transverse bars
				C04	Diameter of transv. reinf	U	Diameter of transverse reinforcements

Figure A.6: Data collected for case-study B6

Identification		Commentary		Piers		Commentary	
101	Name	San Domentica		P01	Pier typology	SC	Commentary SC: single column - W: Wall - H: Portal
102	Manager	ANAS		P02	Degree of fixity (longitudinal)	XX	X: fixed displacement, R: free displacement. Insert a vector of (R/R) if RHP, a vector of (R/R)/(X/R) if ISO. The length of the vector is equal to the number of bents.
103	Position	40.467		P03	Degree of fixity (transverse)	XX	X: fixed displacement, R: free displacement. Insert a vector of (R/R) if RHP, a vector of (R/R)/(X/R) if ISO. The length of the vector is equal to the number of bents.
104	Region	15.634		P04	Bearing type (longitudinal)	N	Type of the fixed bearings - insert a vector of N: Neoprene or X: Fixed generic
105	Province	Basilicata		P05	Bearing type (transverse)	N	Type of the fixed bearings - insert a vector of N: Neoprene or X: Fixed generic
106	Municipality	Potenza		P06	Cap beam	9.9 1.0 9.22	Dimension of the cap beam. Insert a vector of B1: B2 - H1 - H2 -W1
107	Infrastructure type	Bridge		P07	Pier section	RECT	Fill in if SC: RECT: Rectangular - CIRC: Circular - POLIGON: Elliptical
108	Road category	C		P08	Pier dimensions		Fill in if R: RECT with the dimension parallel to the axis of the bridge
General structural							
G01	Structure type	GIR	Commentary GIR: Girder bridge - ARC: Arch bridge - CB: Cable stayed - TR: Truss	P09	Support height	0	Fill in if R: RECT with the dimension normal to the axis of the bridge
G02	Deck type	Bw5	Bw5: Beams with slab - BC: Box girder - MS: Monolithic slab - TR: Truss	P10	Pier height	0.3	Fill in if R: RECT with the dimension normal to the axis of the bridge
G03	Static scheme	ISO	ISO: Isostatic - HYP: Hyperstatic	P11	Distance between supports	8	Fill in with a vector of bearing heights (top of cap beam - bottom of the deck)
G04	Deck-pier connections	SUPP	Fill in only if HYP - SUPP: Pinned connection - MON: Monolithic connections	P12	Design compressive strength of concrete	0.75-0.75	Fill in with a vector of bearing heights from the base to top of cap beam
G05	Deck-abutments connections	SUPP	SUPP: Pinned connection - MON: Monolithic connections	P13	Steel bars Young's modulus	200000	Fill in with a vector of bearing distances from the axis of the pier on the cap beam
G06	Year/period of design	1985	Fill in design year/period	P14	Design yielding strength of steel bars	U	Insert the characteristic design strength of concrete (Rk or Rck)
G07	Bridge category	1	1: first category, 2: second category	P15	Concrete Young's modulus	30000	Insert the characteristic design strength of steel (Rsk or Rsk)
G08	Seismic category	0	Fill in the following values [0 1 2] if period of design is 1939-1964.	Abutments			
G09	Seismic coefficient	2	Fill in the following values [0 6 9 12] if period of design is 1964-2008.	A01	Degree of fixity (longitudinal)	FXFX	Commentary X: fixed displacement, R: free displacement. Insert a vector of (R/R) if RHP, a vector of (R/R)/(X/R) if ISO. The length of the vector is equal to 2.
G10	Soil type	B	Fill in one of the following values [A - B - C - D - E] for soil category	A02	Degree of fixity (transverse)	FXFX	X: fixed displacement, R: free displacement. Insert a vector of (R/R) if RHP, a vector of (R/R)/(X/R) if ISO. The length of the vector is equal to 2.
G11	Topography	T1	Fill in one of the following values [T1 - T2 - T3 - T4] for topographic category	A03	Bearing type (longitudinal)	N N	Type of the fixed bearings - insert a vector of 2 component: Neoprene or X: Fixed generic.
G12	Total length	66	Insert the total length of the bridge	A04	Bearing type (transverse)	N N	Type of the fixed bearings - insert a vector of 2 component: Neoprene or X: Fixed generic.
G13	Number of spans	2	Insert the number of spans	A05	Gap dimension	U	Dimension of the gap in longitudinal dimension
G14	Span length	33.33	Insert a vector of span lengths	A06	Width of abutment backwall	9.5	Insert the width of the abutment backwall
Deck							
D01	Girder material	PC	RC: Reinforced Concrete - PC: Precast - ST: Steel	A07	Height of abutment backwall	1.7	Insert the height of the abutment backwall
D02	Slab material	RC	RC: Reinforced Concrete - PC: Precast	A08	Stiffness of abutment backwall	U	Insert the stiffness coefficient of the abutment backwall (stiffness per unit of width)
D03	Deck width	9.5	Insert the total width of the deck	Bearings			
D04	Road width	9.5	Insert the width of the road only	B01	Bearing height	0.03	Height of the bearing devices
D05	Sidewalk width	0	Insert the width of the sidewalk only	B02	Bearing stiffness	U	Fill in if there are NEOPRENE bearings with the stiffness of the single bearing device
D06	Girder height	1.7	Insert the height of the girder (from lower ridge of slab to top of the bearing device)	Materials			
D07	Girder area	0.65	Insert the cross section area of the girder	M01	Compressive strength of concrete	U	Commentary Insert the mean strength of concrete (fc)
D08	Number of girder	3	Fill in with the number of girders	M02	Tensile strength of steel	U	Insert the mean strength of concrete (fy)
D09	Slab thickness	0.3	Insert the height of the slab (from top edge of girder to top slab)	Constructive details			
D10	Deck cross area	[m²]	Fill in only if D07-D08-D09 are not available	C01	Number of long bars	U	Commentary Insert the number of long bars. If R: RECT, insert a vect of 2 components, if R: HYP is CIRC insert one number
D11	Flexure moment of inertia	[m⁴]	Fill in only if G03 is HYP with the moment of inertia in transverse direction	C02	Diameter of long bars	U	Diameter of longitudinal bars. RECT: insert a vect of 2 components, if CIRC insert a vector of one component
D12	G2 deck	36	Fill in with the non-structural permanent weight	C03	Step of transveinif	U	Step of transverse bars
D13	Concrete Young's modulus	U	Fill in with the concrete Young's modulus of the deck	C04	Diameter of transveinif	U	Diameter of transverse reinforcements

Figure A.7: Data collected for case-study B7

Identification		Commentary		Piers		Commentary	
101	Name	San Domètica		P01	Pier typology	SC	SC: single column - W: Wall - R: Portal
102	Manager	ANAS		P02	Degree of fixity (longitudinal)	XX	X: fixed displacement, R: free displacement. Insert a vector of (F, X, R) if HPP, a vector of (f, R, X, X, R, R) if ISO. The length of the vector is equal to the number of beams.
103	Position	40.467	Latitude	P03	Degree of fixity (transverse)	XX	X: fixed displacement, R: free displacement. Insert a vector of (F, X, R) if HPP, a vector of (f, R, X, X, R, R) if ISO. The length of the vector is equal to the number of beams.
104	Region	15.634	Longitude	P04	Bearing type (longitudinal)	N	Type of the fixed bearings - Insert a vector of N: Neoprene or X: Fixed generic
105	Province	Basilicata		P05	Bearing type (transverse)	N	Type of the fixed bearings - Insert a vector of N: Neoprene or X: Fixed generic
106	Municipality	Potenza		P06	Cap beam	9.91.03.22	Dimension of the cap beam. Insert a vector of (B): B2 - H2 - H2 - V6
107	Infrastructure type	Bridge		P07	Pier section	RECT	Fill in if SC: RECT: Rectangular - CIRC: Circular - Polygonal: Polygonal
108	Infrastructure type	Bridge					Fill in if W: RECT: Rectangular
109	Road category	C					Fill in if P07 is RECT with the dimension normal to the axis of the bridge
General structural							Fill in if P07 & CIRC with the diameter
G01	Structure type	GIR	Commentary	P08	Pier dimensions	2	Fill in if P07 is RECT with the dimension parallel to the axis of the bridge
G02	Deck type	BWS	BWS: Beams with slab - BG: Box girder - MS: Monolithic slab - TB: Truss	P09	Support height	0.3	Fill in with a vector of bearing heights (top of cap beam - bottom of the deck)
G03	Slab scheme	ISO	ISO: Isostatic - HYP: Hyperstatic	P10	Pier height	8	Fill in with a vector of bent heights from the base to top of capbeam
G04	Deck-pier connections	SUPP	Fill in only if HPP - SUPP: Pinned connection - MON: Monolithic connections	P11	Distance between supports	0.75 0.75	Fill in with a vector of bearing distances from the axis of the pier on the capbeam
G05	Deck-abutments connections	SUPP	SUPP: Pinned connection - MON: Monolithic connections	P12	Design compressive strength of concrete	U	Insert the characteristic design strength of concrete (f _{bk} or f _{ck})
G06	Year/period of design	1985	Fill in design year/period	P13	Steel bars Young's modulus	200000	Insert the Young's modulus of the steel (E)
G07	Bridge category	1	1: first category; 2: second category	P14	Design yielding strength of steel bars	U	Insert the characteristic design strength of steel (f _{sk} or f _{yk})
G08	Seismic category	0	Fill in the following values [0,1,2] if period of design is 1939-1964.	P15	Concrete Young's modulus	30000	Insert the Young's modulus of the concrete (E)
G09	Seismic coefficient	2	Fill in the following values [0.69 12] if period of design is 1964-2008.	Abutments			
G10	Soil type	B	Fill in one of the following values [A - B - C - D - E] for soil category	A01	Degree of fixity (longitudinal)	FXFX	X: fixed displacement, R: free displacement. Insert a vector of (F, X, R) if HPP, a vector of (f, R, X, X, R, R) if ISO. The length of the vector is equal to 2.
G11	Topography	T1	Fill in one of the following values [T1 - T2 - T3 - T4] for topographic category	A02	Degree of fixity (transverse)	FXFX	X: fixed displacement, R: free displacement. Insert a vector of (F, X, R) if HPP, a vector of (f, R, X, X, R, R) if ISO. The length of the vector is equal to 2.
G12	Total length	66	Insert the total length of the bridge	A03	Bearing type (longitudinal)	NN	Type of the fixed bearings - Insert a vector of 2 component Neoprene or X: Fixed generic
G13	Number of spans	2	Insert the number of spans	A04	Bearing type (transverse)	NN	Type of the fixed bearings - Insert a vector of 2 component Neoprene or X: Fixed generic
G14	Span length	33.33	Insert a vector of span lengths	A05	Gap dimension	U	Dimension of the gap in longitudinal dimension
Deck				A06	Width of abutment backwall	9.5	Insert the width of the abutment backwall
D01	Girder material	PC	RC: Reinforced Concrete - PC: Precast - ST: Steel	A07	Height of abutment backwall	1.7	Insert the height of the abutment backwall
D02	Slab material	RC	RC: Reinforced Concrete - FC: Precast	A08	Stiffness of abutment backwall	U	Insert the stiffness coefficient of the abutment backwall (at fives per unit of width)
D03	Deck width	9.5	Insert the total width of the deck	Bearings			
D04	Road width	9.5	Insert the width of the road only	B01	Bearing height	0.03	Height of the bearing devices
D05	Sidewalk width	0	Insert the width of the sidewalk only	B02	Bearing stiffness	U	Fill in if there are NEOPRENE bearings with the stiffness of the single bearing device
D06	Girder height	1.7	Insert the height of the girder (from lower edge of slab to top of the bearing device)	Materials			
D07	Girder area	0.65	Insert the cross section area of the girder	M01	Compressive strength of concrete	U	Insert the mean strength of concrete (f _c)
D08	Number of girder	3	Fill in with the number of girders	M02	Tensile strength of steel	U	Insert the mean strength of concrete (f _y)
D09	Slab thickness	0.3	Insert the height of the slab (from top edge of girder to top slab)	Constructive details			
D10	Deck cross area		Fill in only if D07-D08-D09 are not available	C01	Number of long bars	U	Insert the number of long bars, if P07 is RECT, insert a vect of 2 components, if P07 is CIRC, insert one number
D11	Flexure moment of inertia		Fill in only if G03 is HPP with the moment of inertia in transverse direction	C02	Diameter of long bars	U	Diameter of longitudinal bars, RECT: insert a vect of 2 components, if CIRC, insert a vector of one component
D12	G2 deck	36	Fill in with the non-structural permanent weight	C03	Step of transverse reinf	U	Step of transverse bars
D13	Concrete Young's modulus	U	Fill in with the concrete Young's modulus of the deck	C04	Diameter of transverse reinf	U	Diameter of transverse reinforcements

Figure A.8: Data collected for case-study B8

Appendix B

Extended result collection of DBA and NSPs on parametric multi-span continuous-deck RC bridges

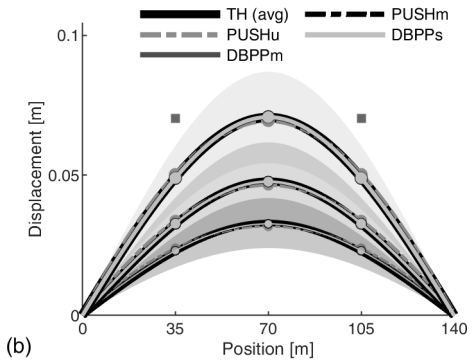
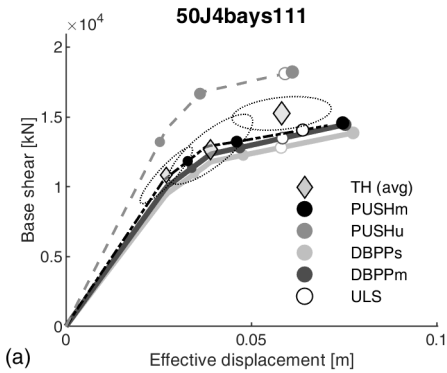
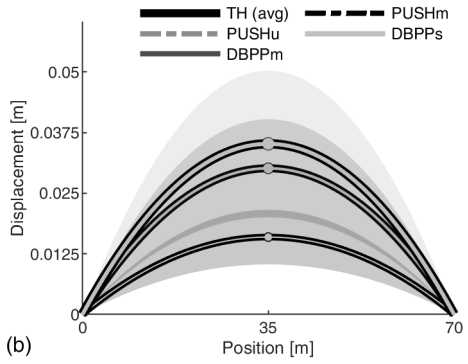
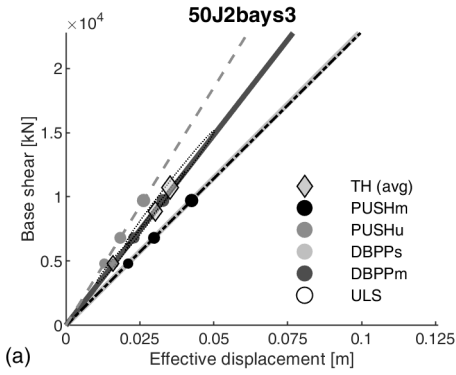
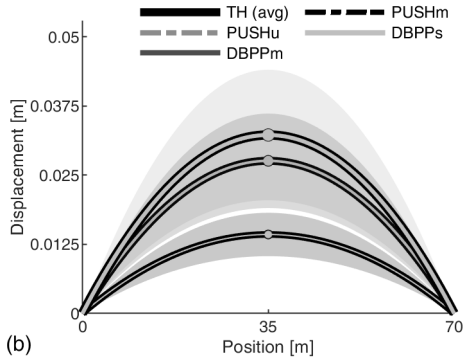
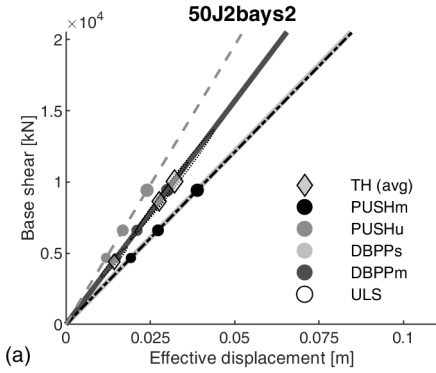
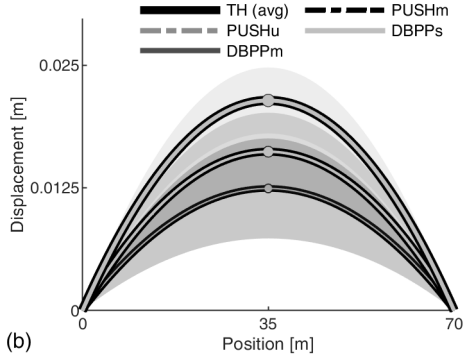
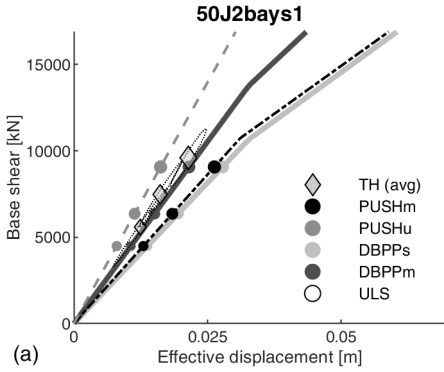
In this Appendix, an extended collection of the results related to the parametric analysis carried out in Chapter 3, Section 3.3.1 is provided.

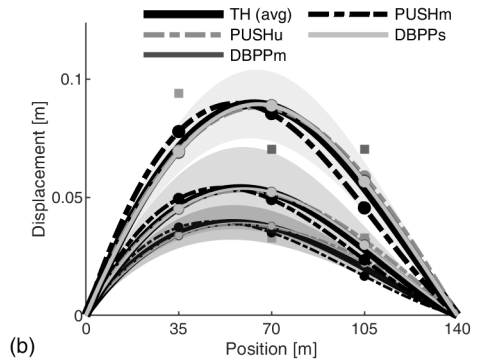
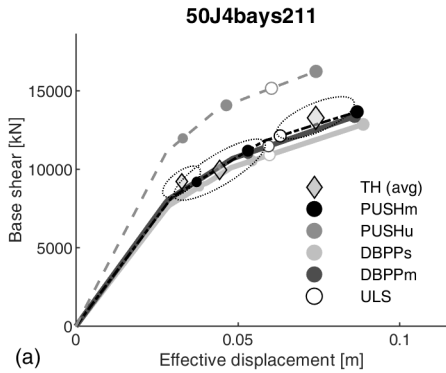
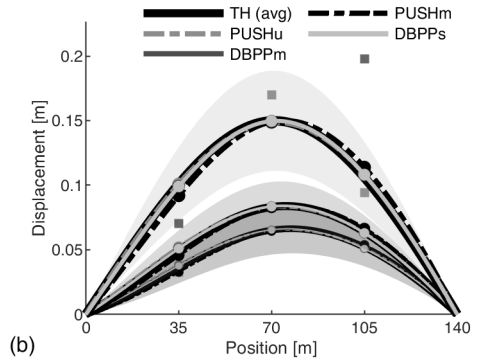
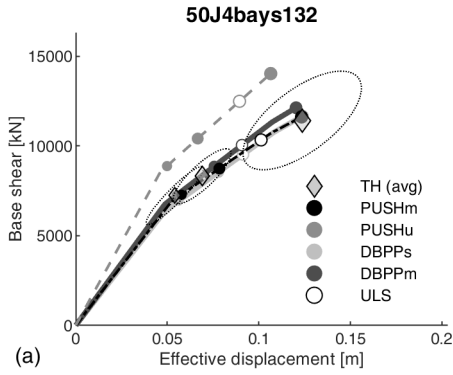
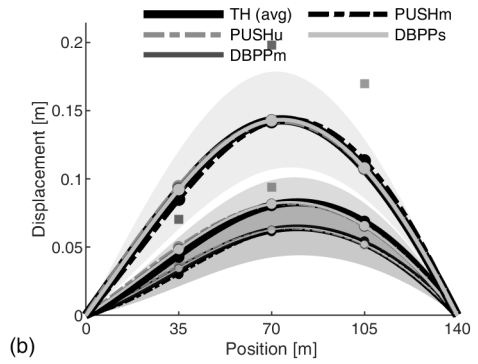
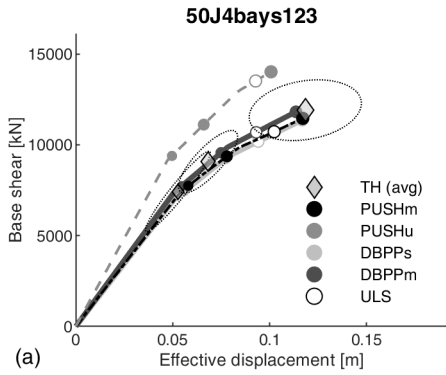
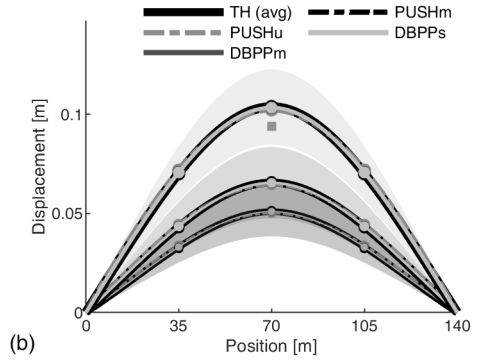
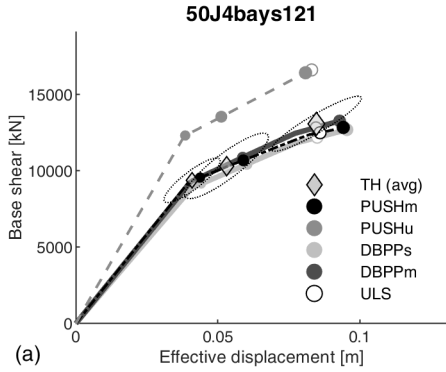
The results are identified with the following code: $XJ-N/bays-P$ where:

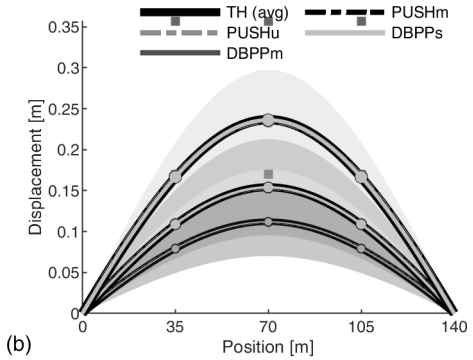
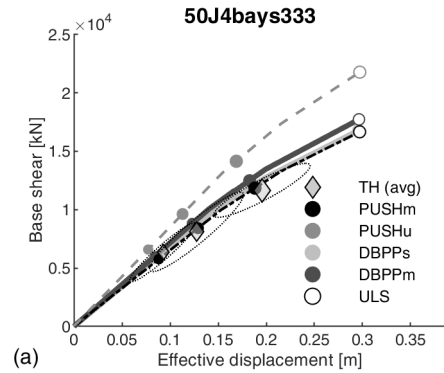
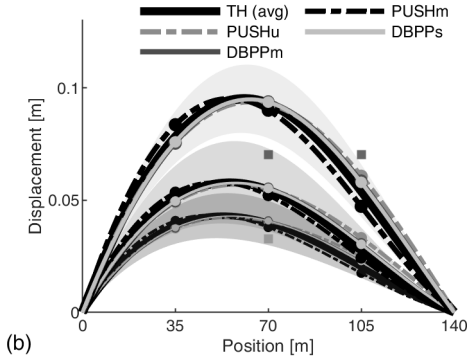
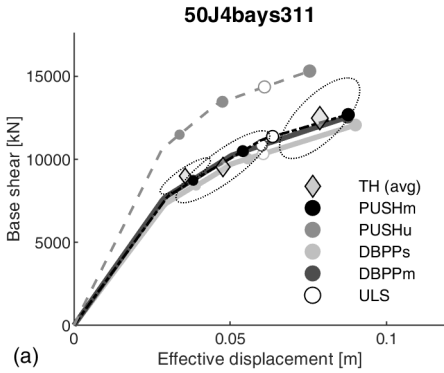
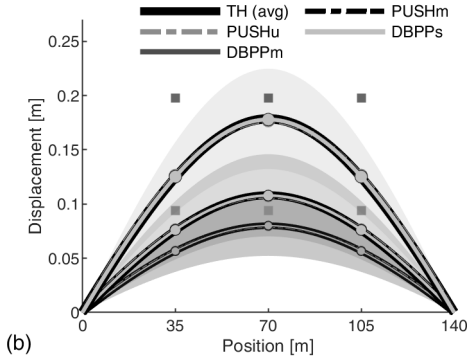
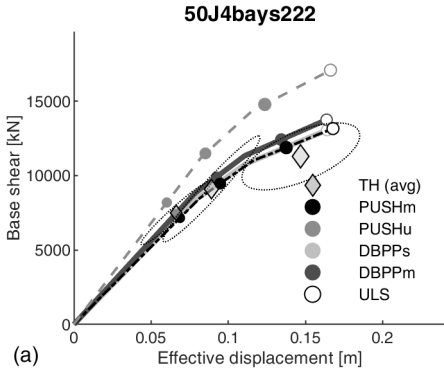
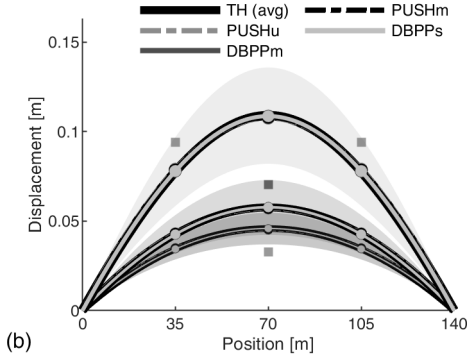
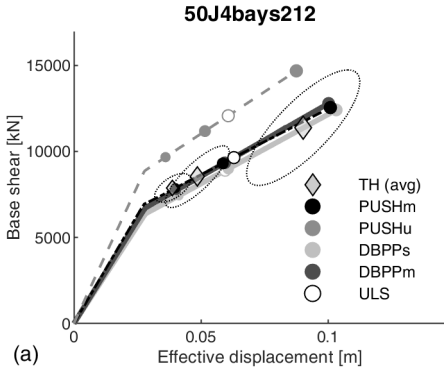
- X is 50 or 100 identifying the J50 and J100 subsets
- N is the number of spans
- P is the sub-code identifying the longitudinal pier distribution as indicated in Section 3.3.1. As an example, the case study labelled as 132 is a four-span bridge with a $8m$ -, $20m$ - and $15m$ -high piers.

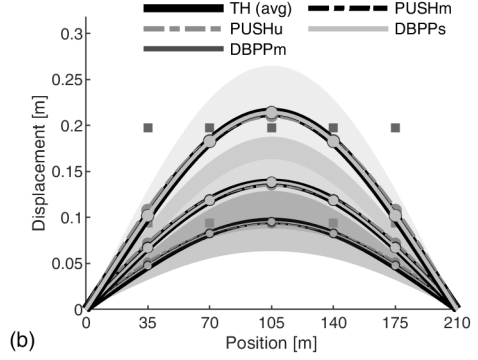
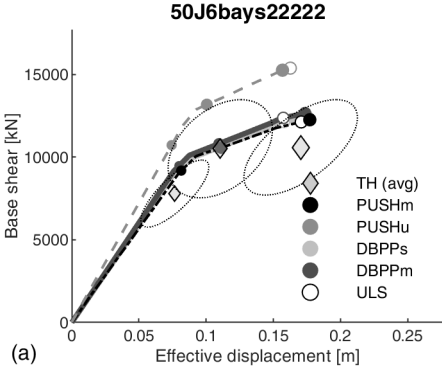
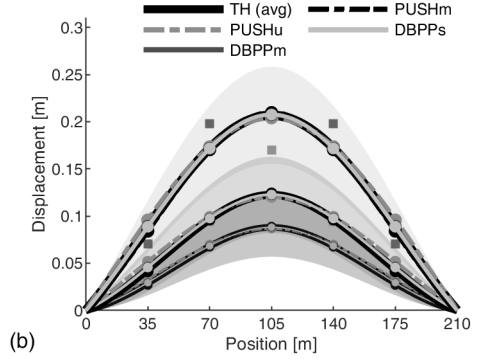
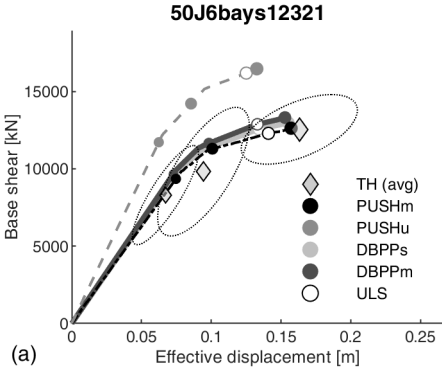
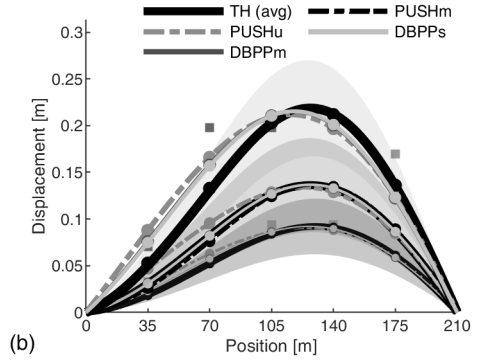
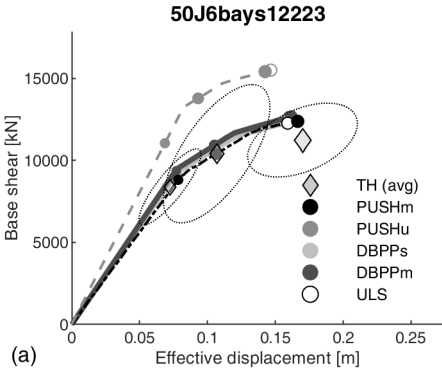
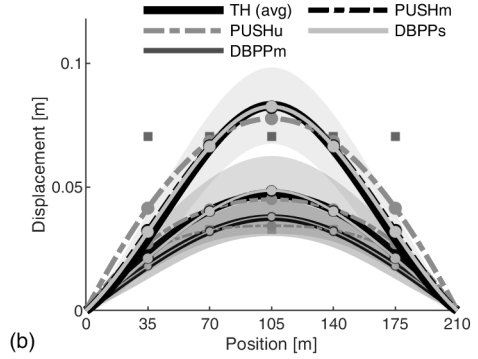
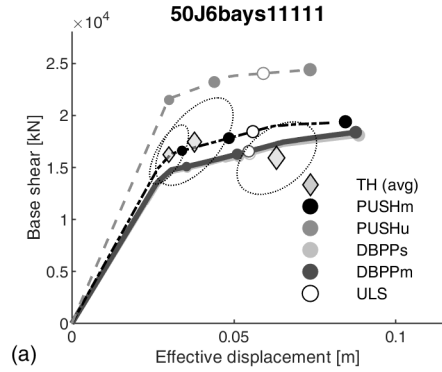
The following figures show:

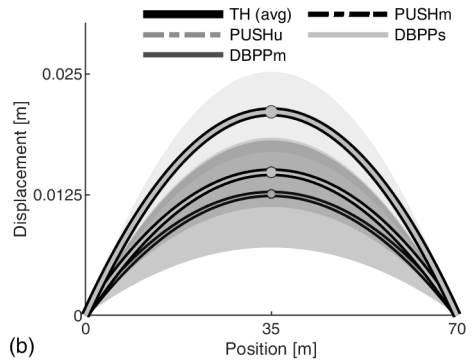
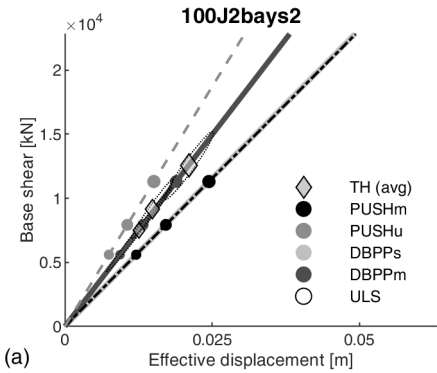
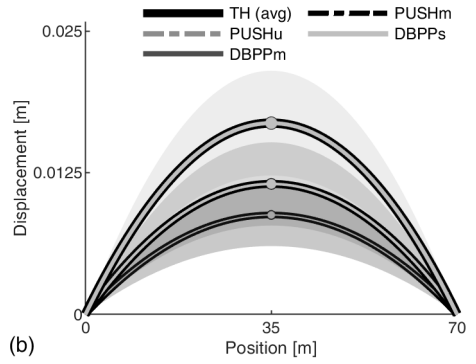
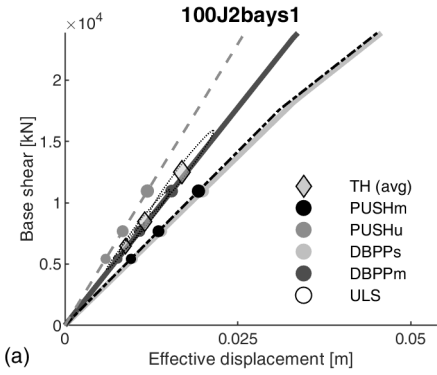
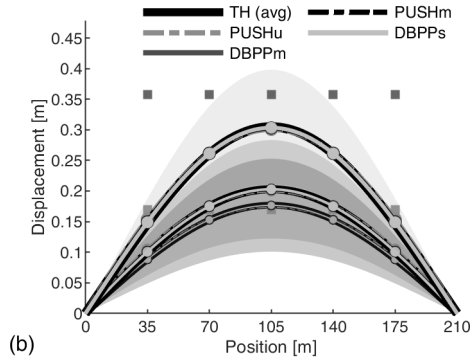
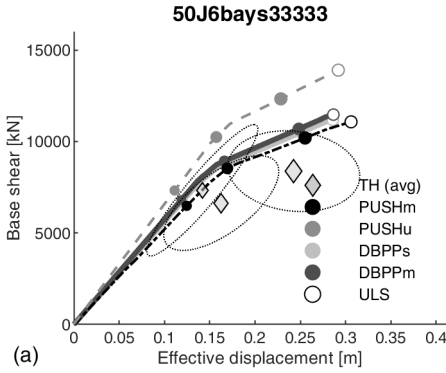
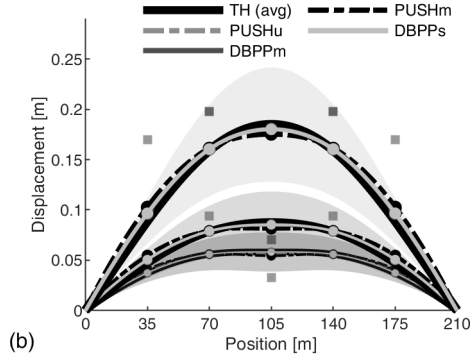
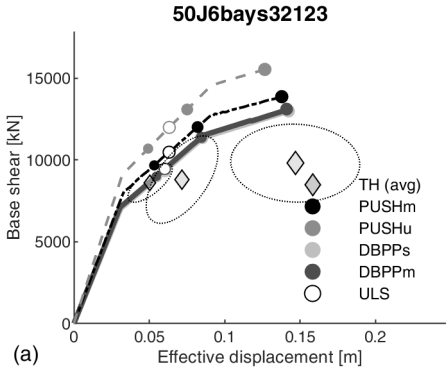
- a) the equivalent SDoF base shear vs effective displacement relationships curves calculated with the considered NSPs together with the corresponding performance points and average NLTHA result and its ellipse of confidence for each adopted IM;
- b) the displacement profiles from the NSPs and NLTHA (average \pm standard deviation) for each considered IM. The displacement profiles predicted by each NSP are shown for an SDoF displacement equal to the NLTHA average (Δ_{SDoF}^{TH} defined in Section 3.4.1). A cubic interpolation is adopted to somehow reflect the topology of the elastic deformation of the continuous deck. The yielding and ultimate displacements of each pier are also shown with squared grey markers (light: yielding, dark: ultimate).

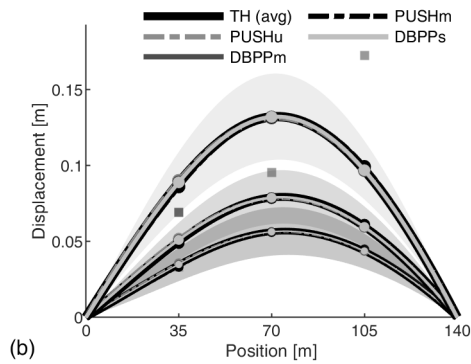
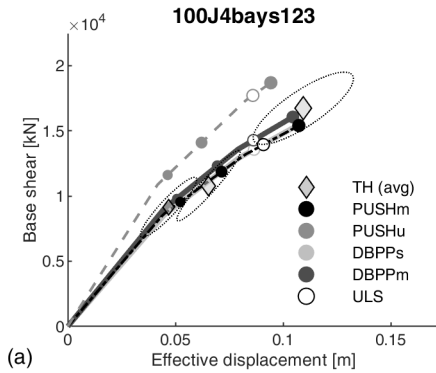
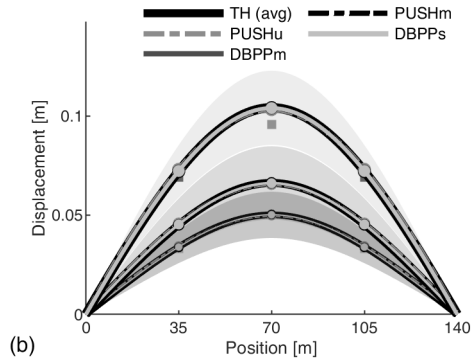
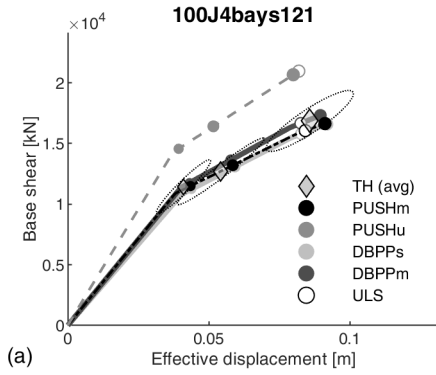
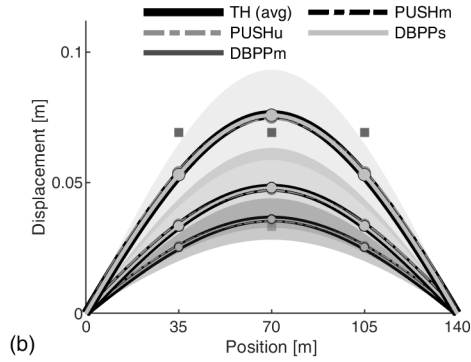
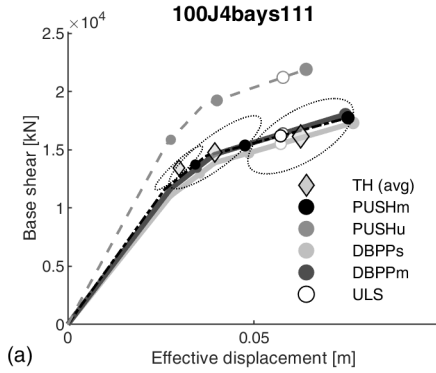
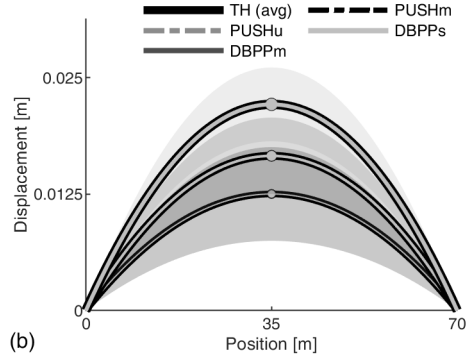
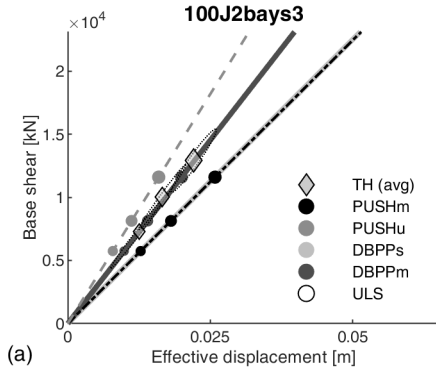


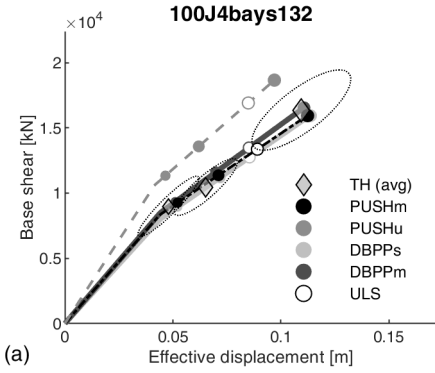




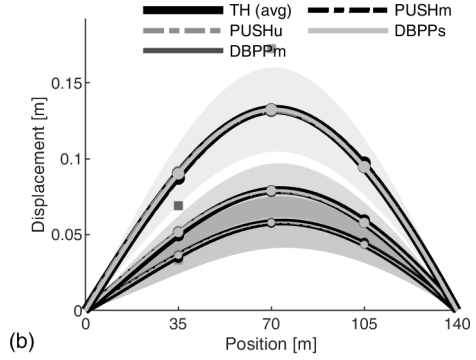




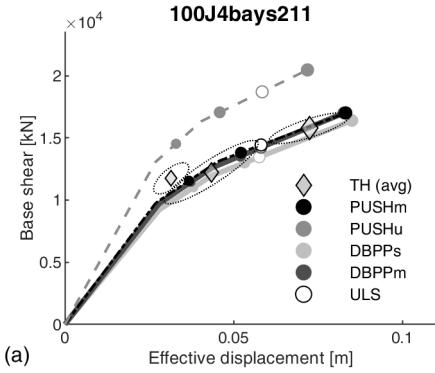




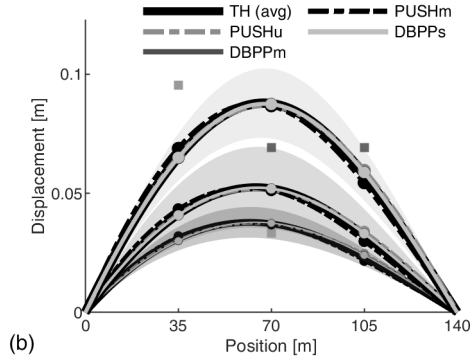
(a)



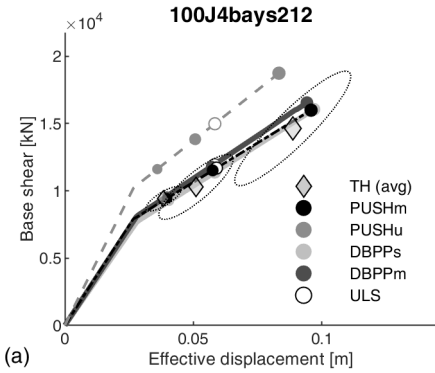
(b)



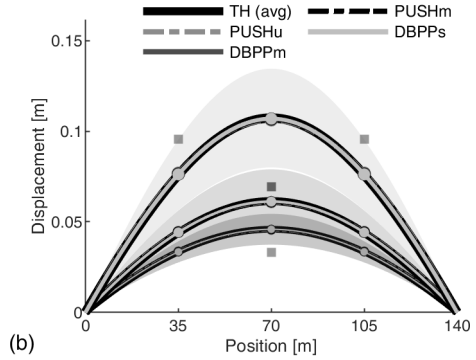
(a)



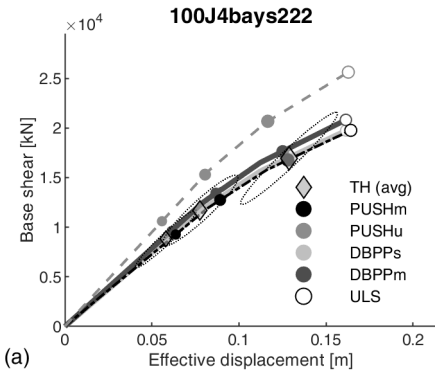
(b)



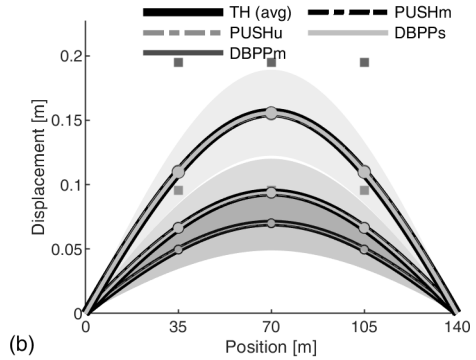
(a)



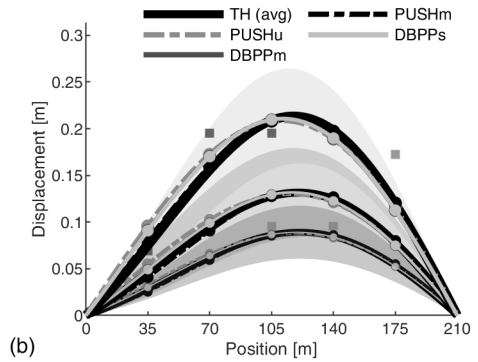
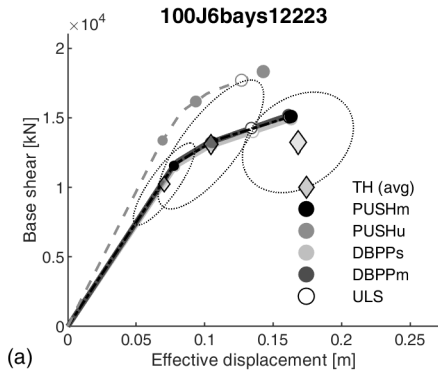
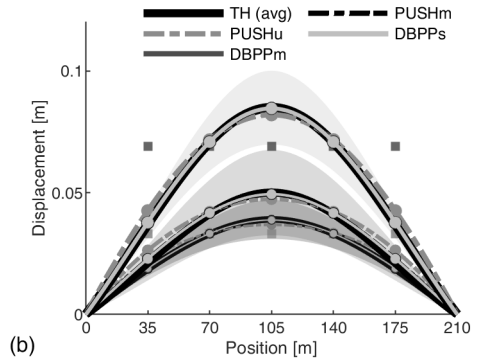
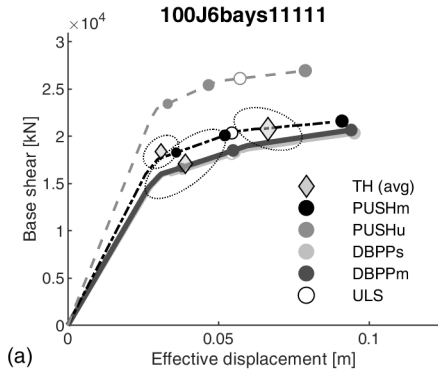
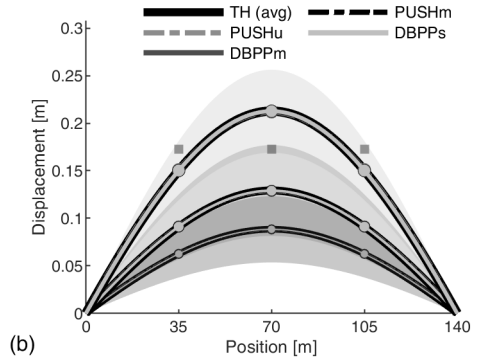
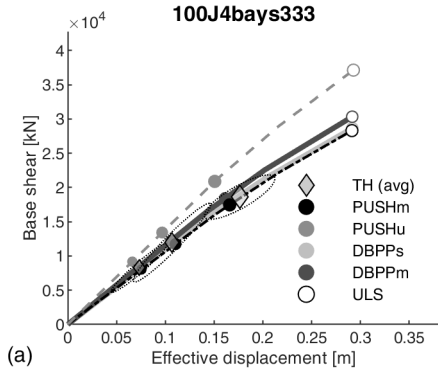
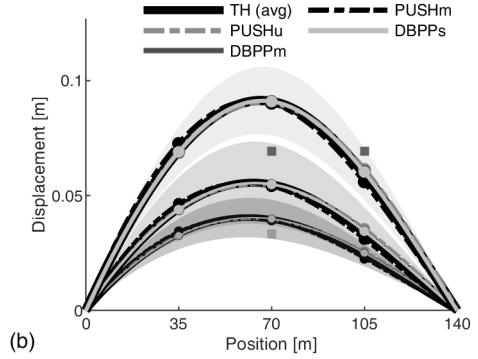
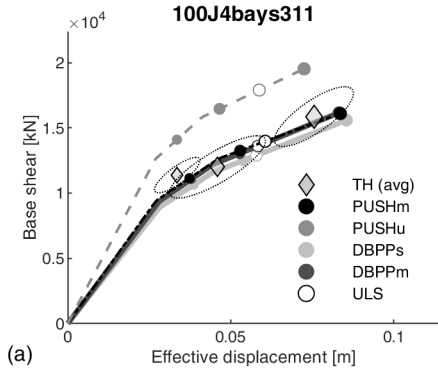
(b)

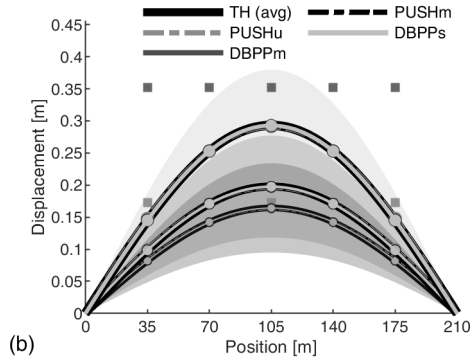
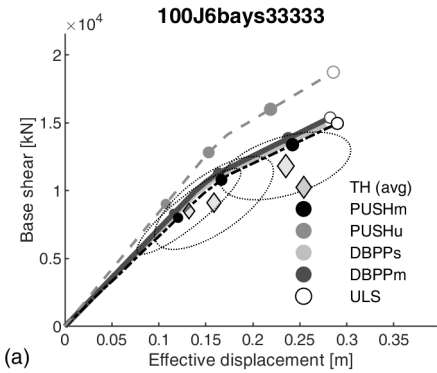
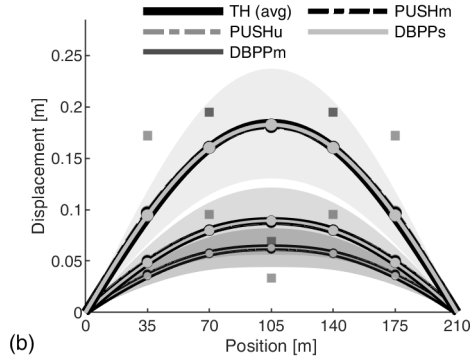
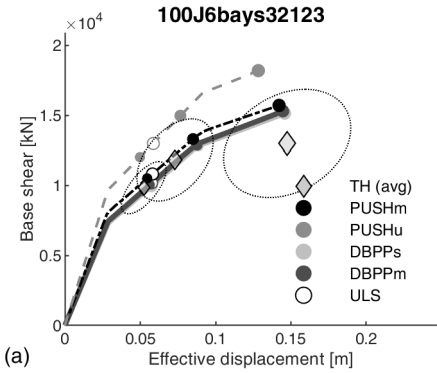
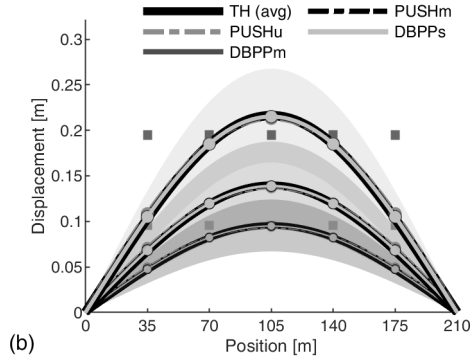
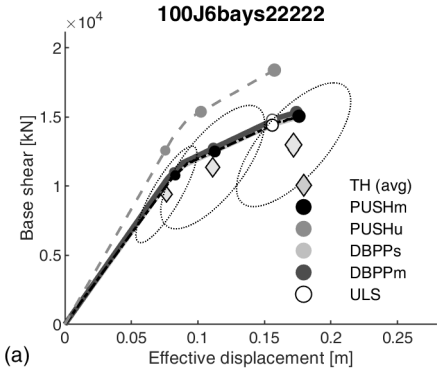
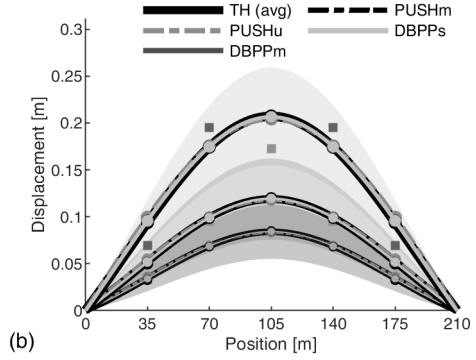
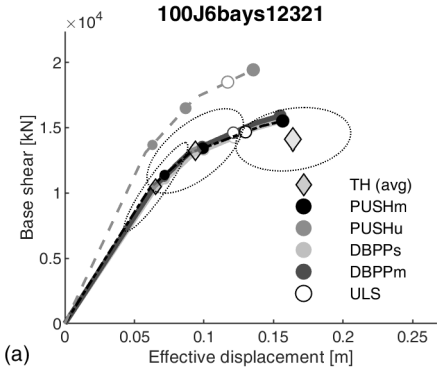


(a)



(b)





Appendix C

Example dataset of fragility curves calculated with Cloud-CSM and benchmark approaches

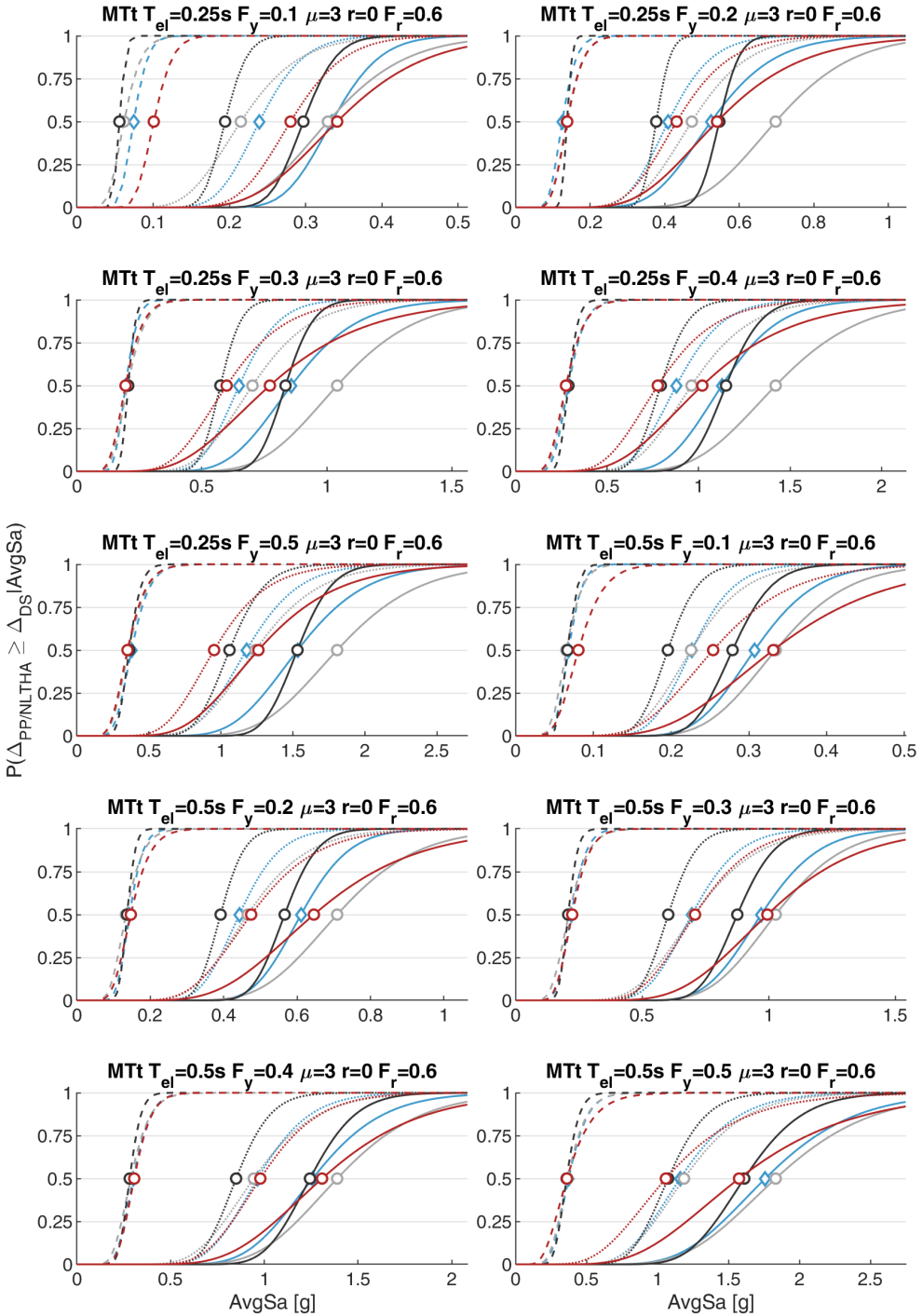
In this Appendix, the fragility curves associated to the results of Chapter 5, Section 5.4.1 and 5.4.2 are explicitly reported to allow the reader for a better comprehension of the findings. The fragility curves calculated via Cloud-CSM, the N2 method, the proposed IM-based method (distinguished by colours) and the NLTHA are calculated and shown for DS1, DS2 and DS3 (reported with different line patterns).

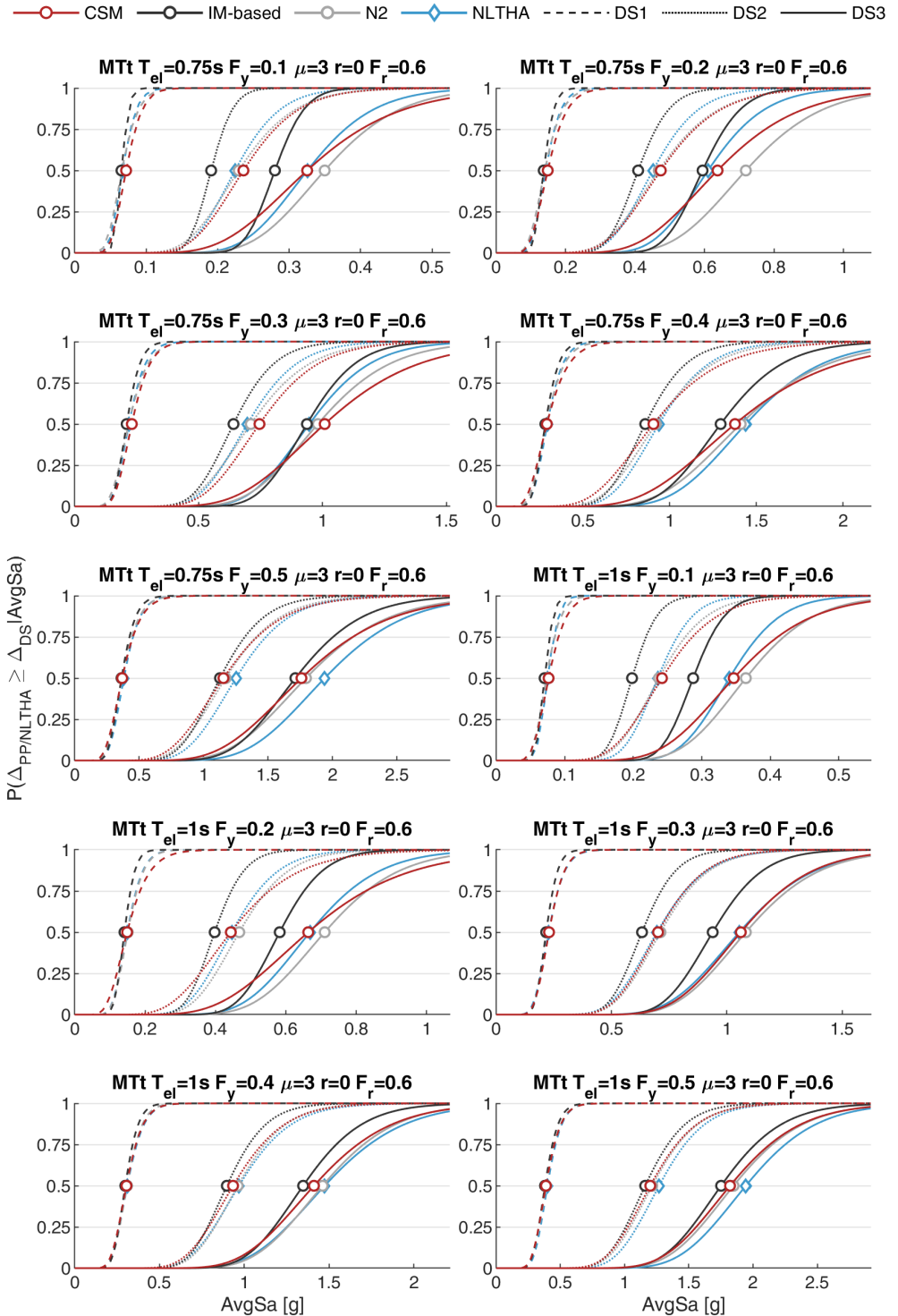
The results are identified with the following code: $Hyst - T_{el} - F_y - \mu - r - F_r$ where:

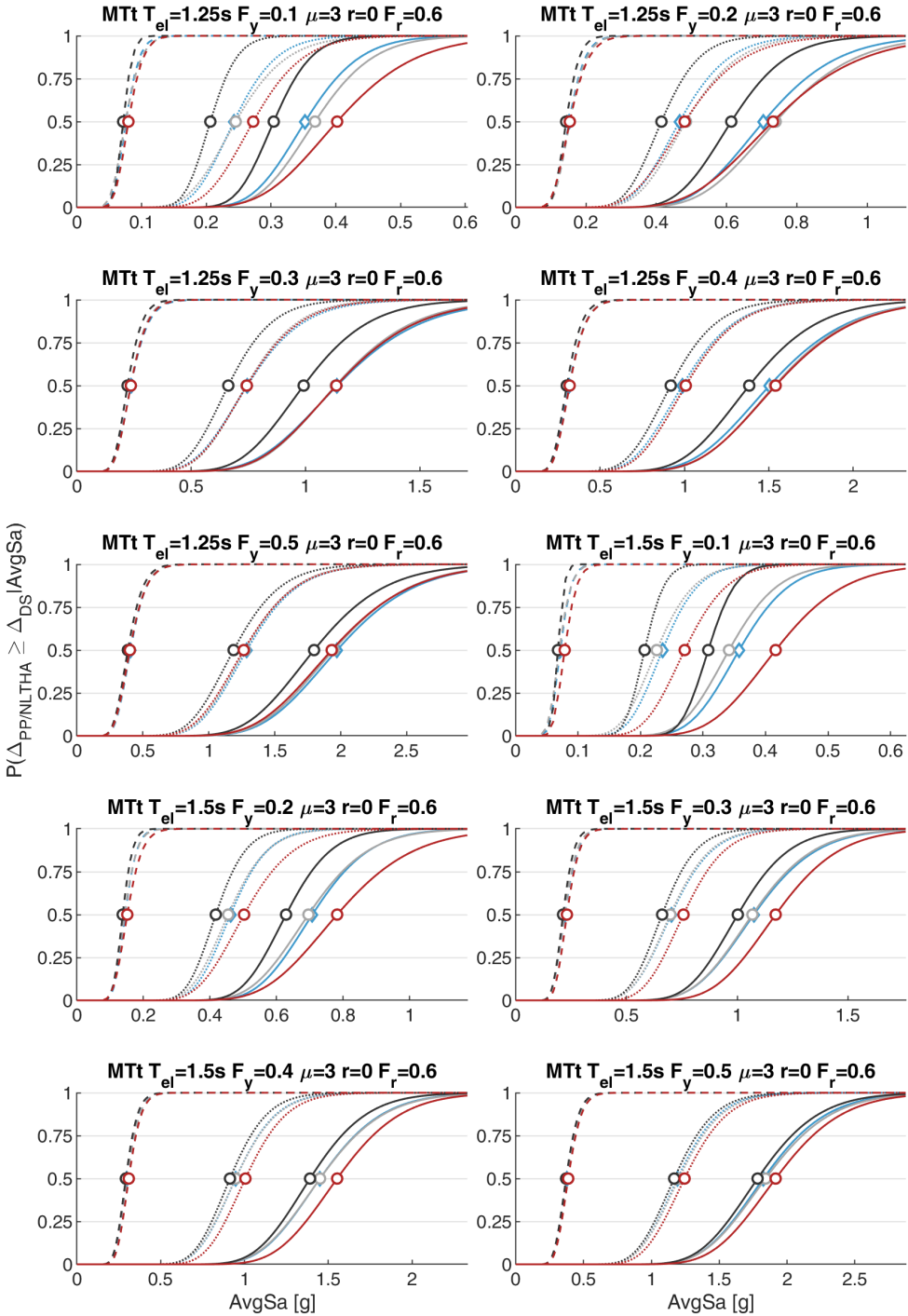
- $Hyst = [MTt, MTf, FS, BIL, EPP]$ is the hysteresis rule;
- $T_{el} = [0.25 - 0.5 - 0.75 - 1 - 1.25 - 1.5 - 1.75 - 2]s$ is the elastic period;
- $F_y = [0.1 - 0.2 - 0.3 - 0.4 - 0.5]$ is the yielding base shear coefficient;

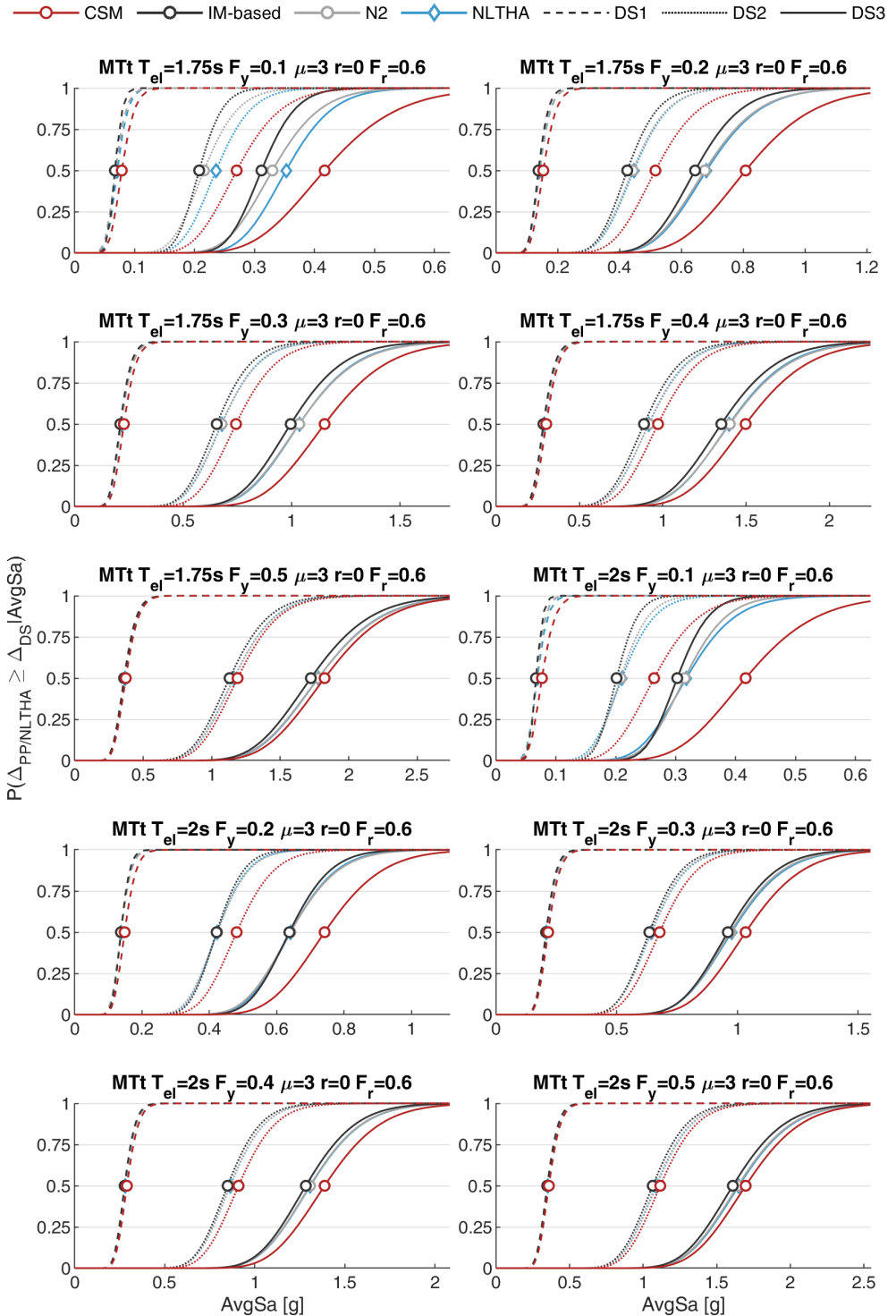
All the reported results refer to cases having ductility capacity $\mu = 3$, hardening ratio $r = 0\%$ and residual strength $F_r = 0.6$.

○ CSM
 ○ IM-based
 ○ N2
 ◇ NLTHA
 - - - - - DS1
 ······ DS2
 ———— DS3

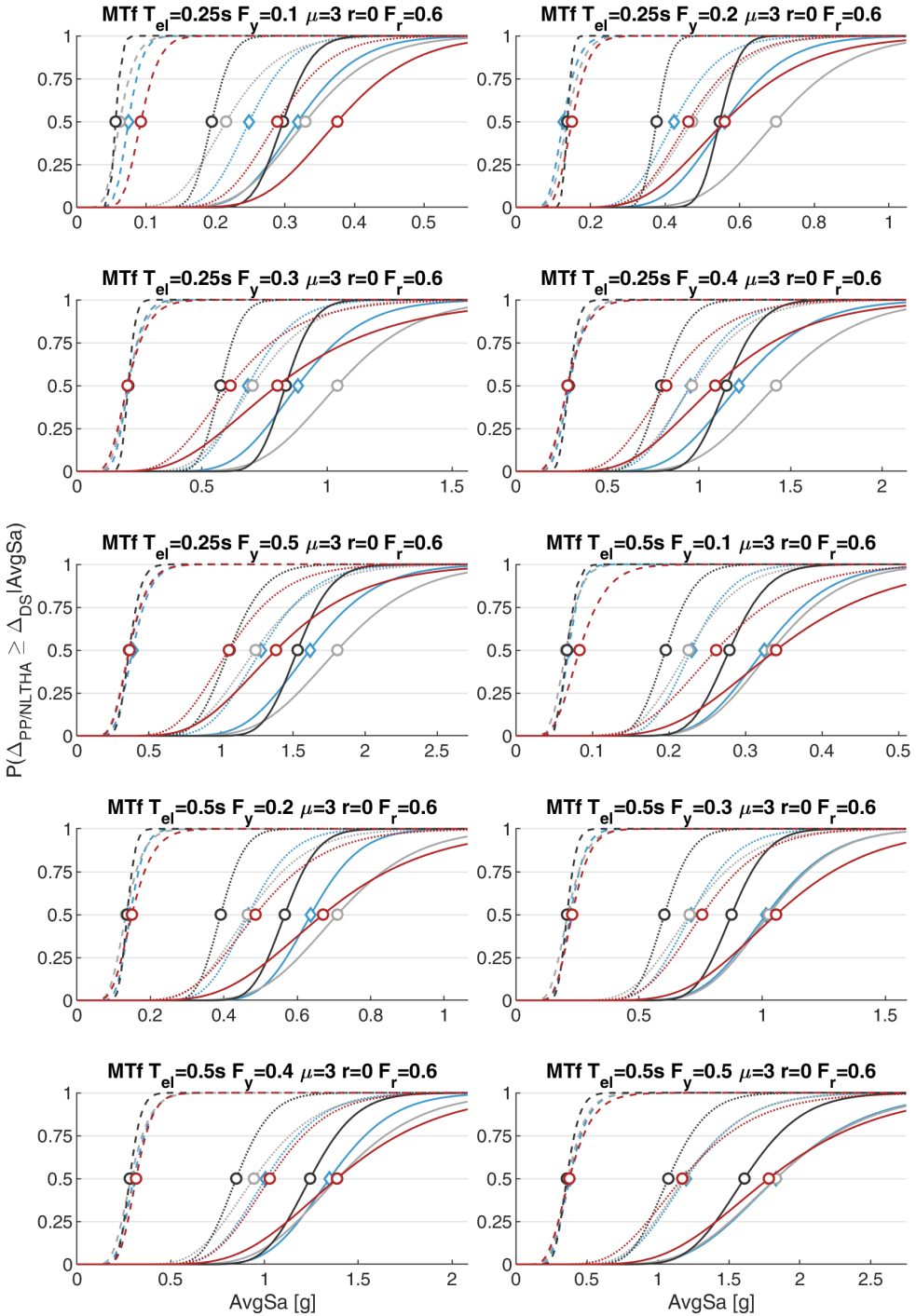


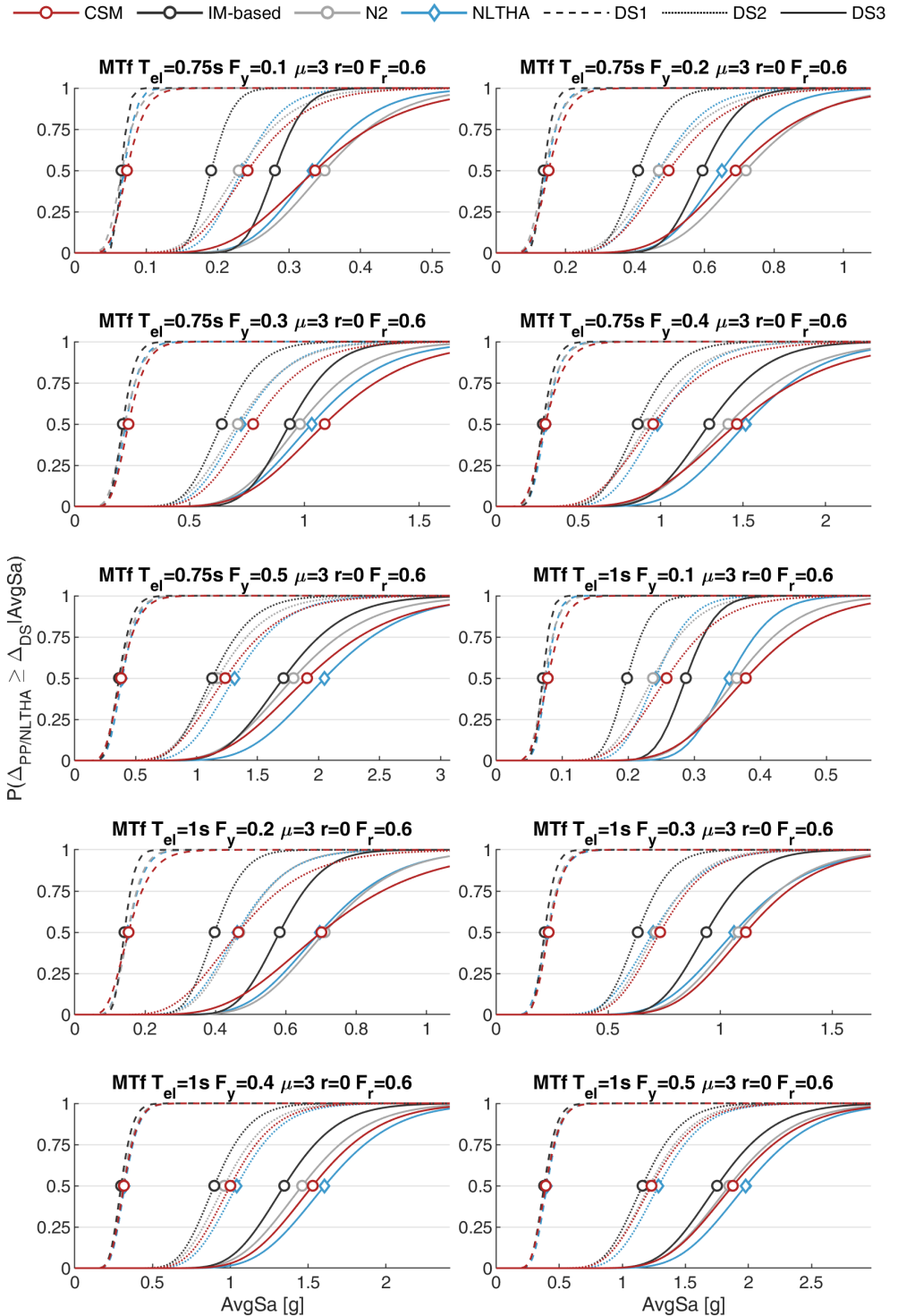




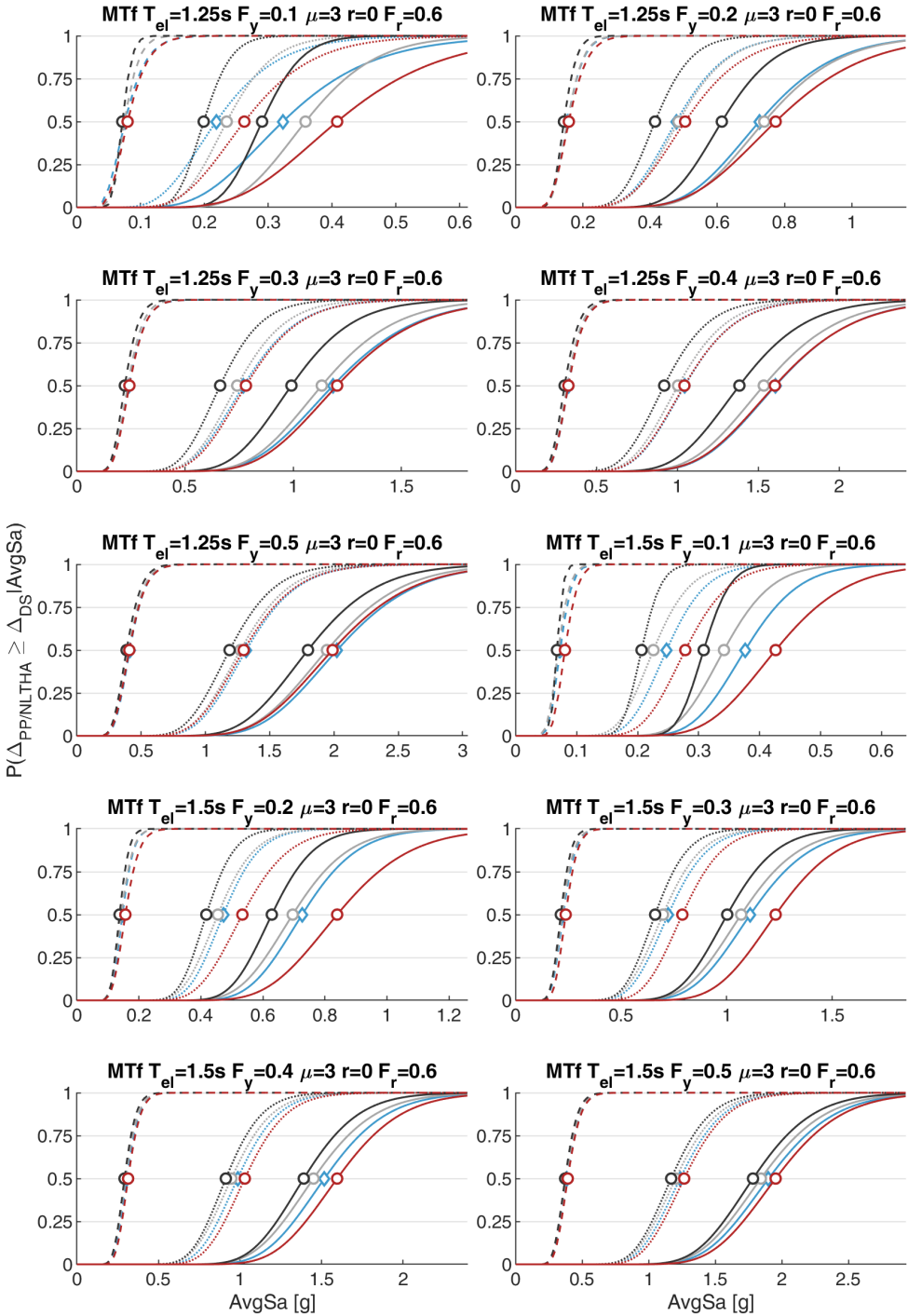


—○— CSM
 —○— IM-based
 —○— N2
 —◇— NLTHA
 - - - - - DS1
 ······ DS2
 ——— DS3

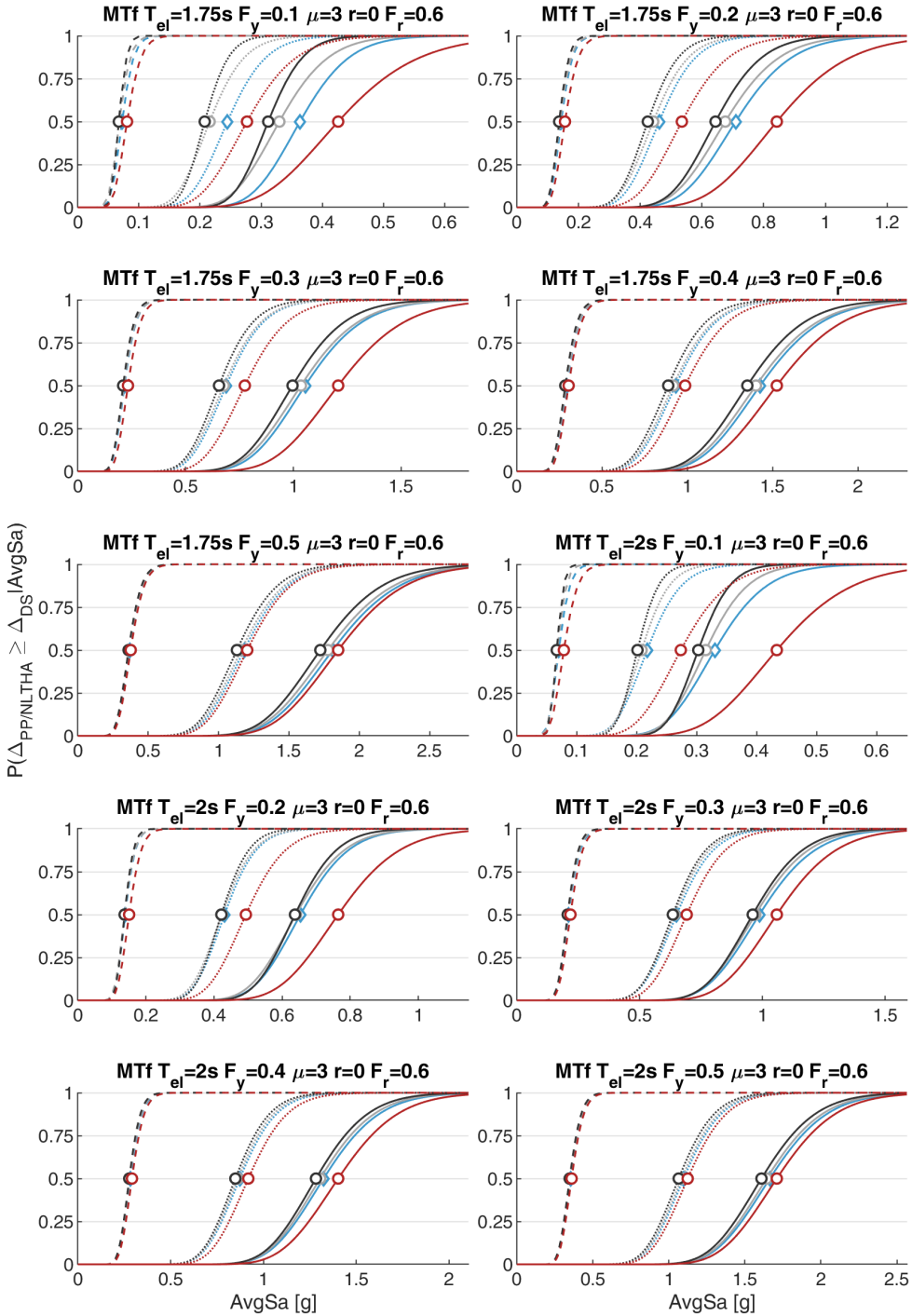




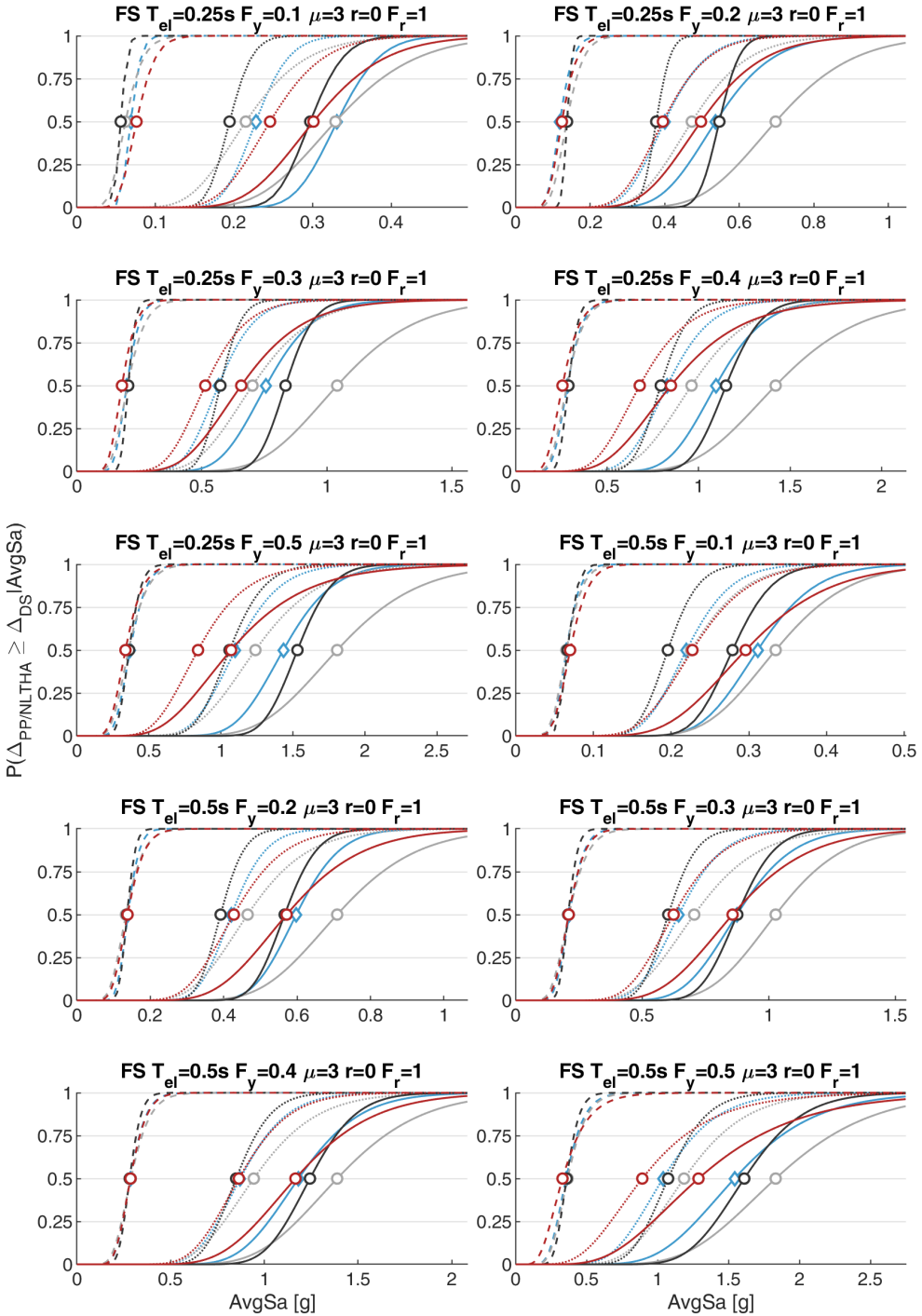
—○— CSM
 —○— IM-based
 —○— N2
 —◇— NLTHA
 - - - - - DS1
 DS2
 — DS3

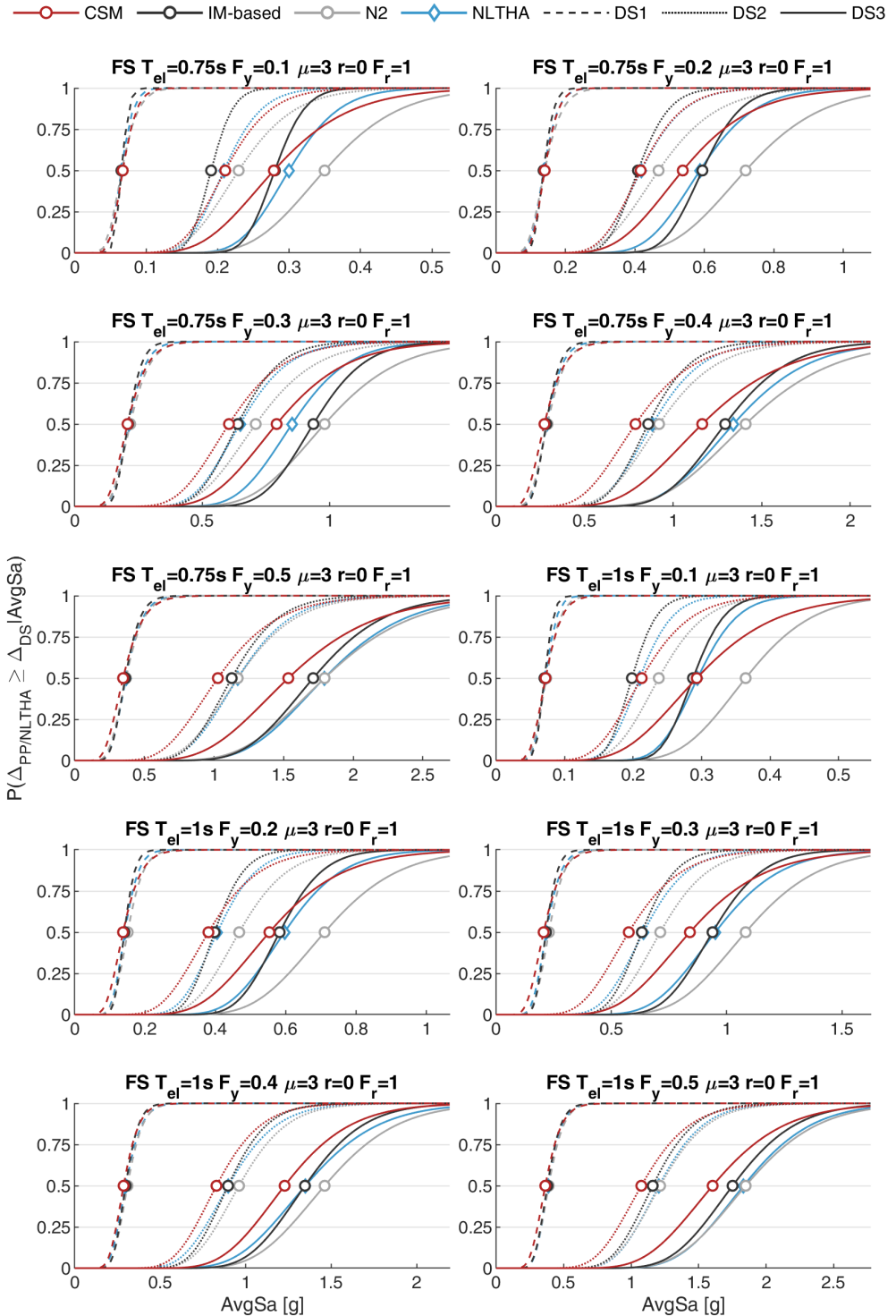


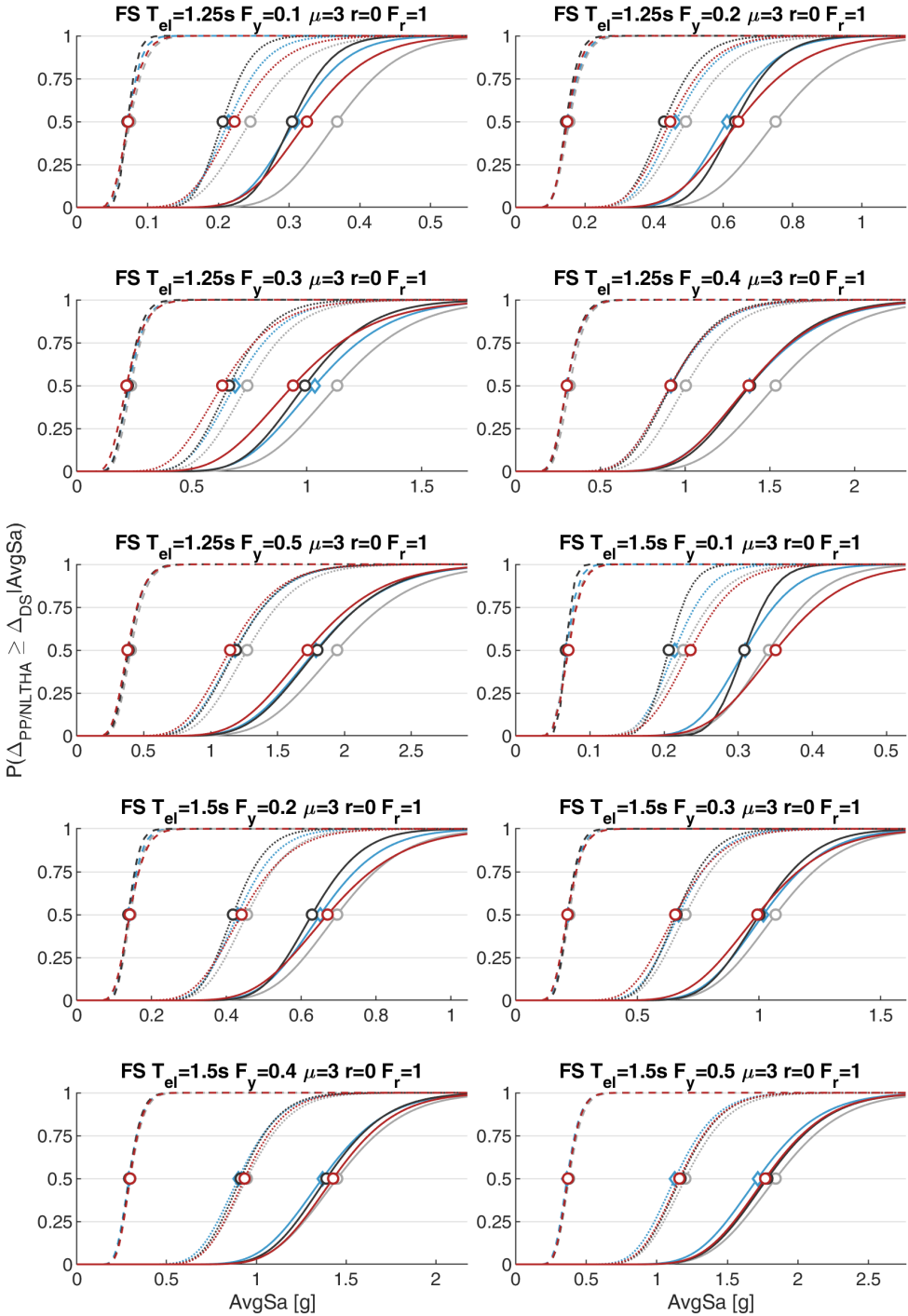
—○— CSM
 —○— IM-based
 —○— N2
 —◇— NLTHA
 - - - - - DS1
 ······ DS2
 — DS3



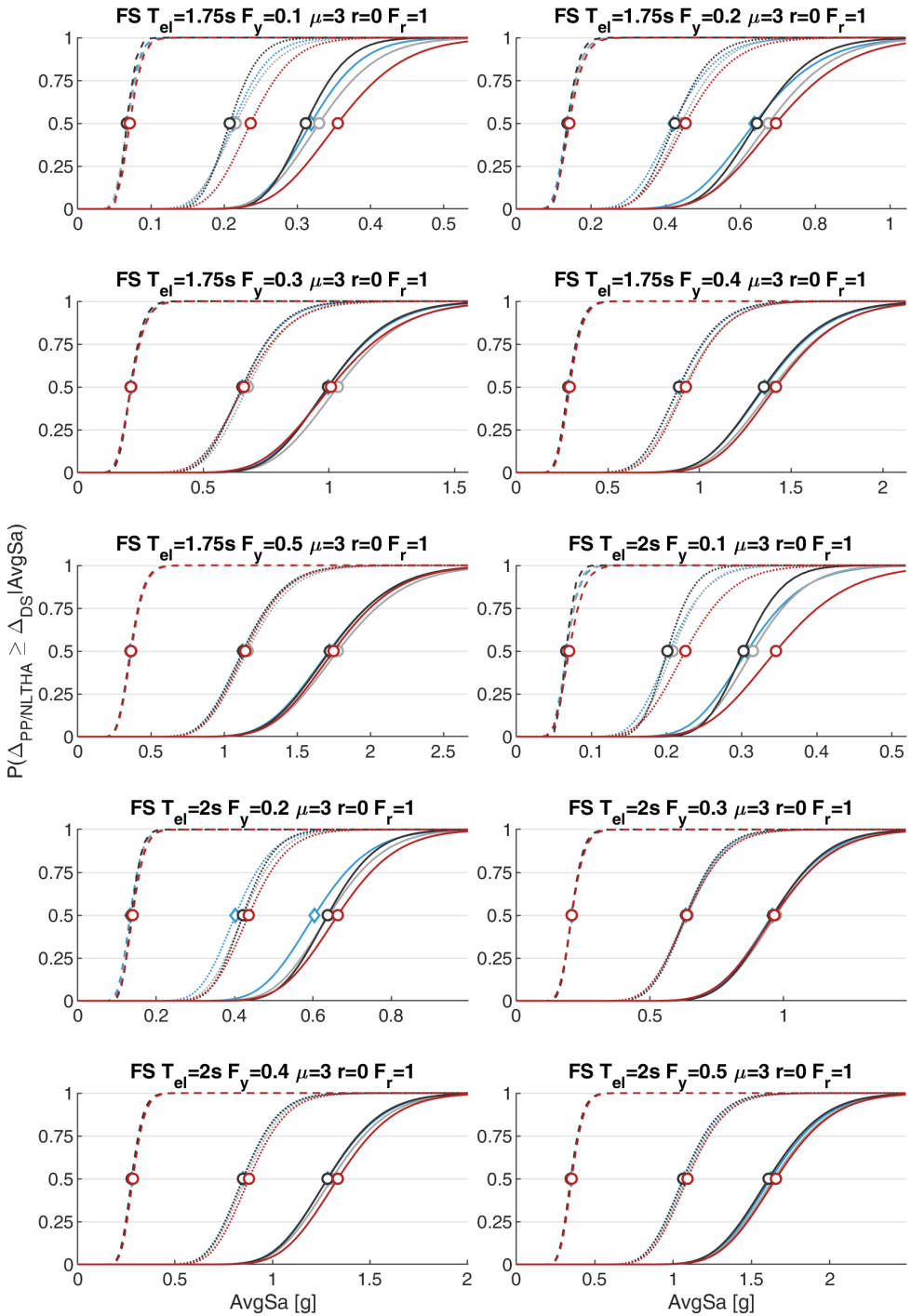
—○— CSM
 —○— IM-based
 —○— N2
 —◇— NLTHA
 - - - - - DS1
 ······ DS2
 ——— DS3

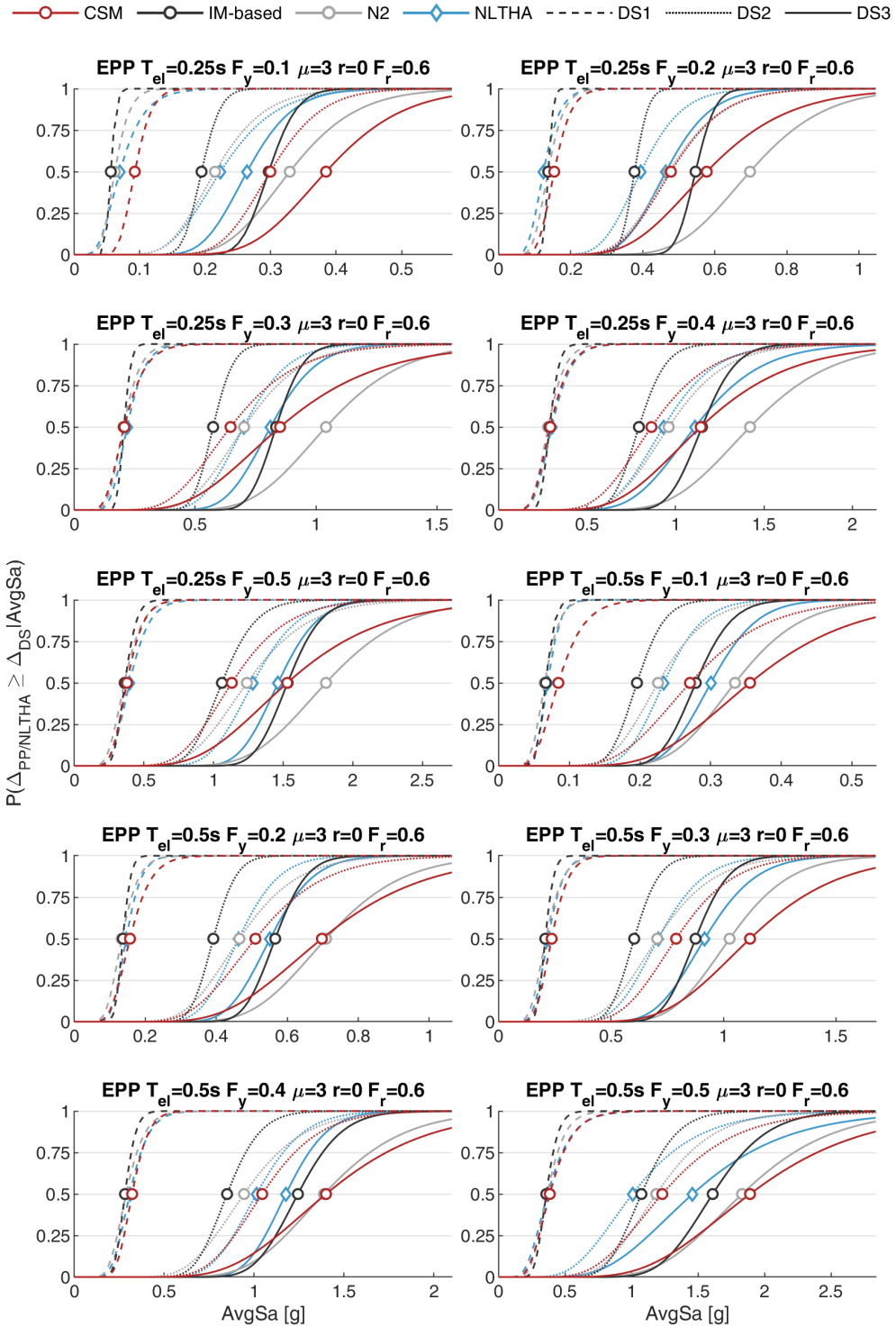


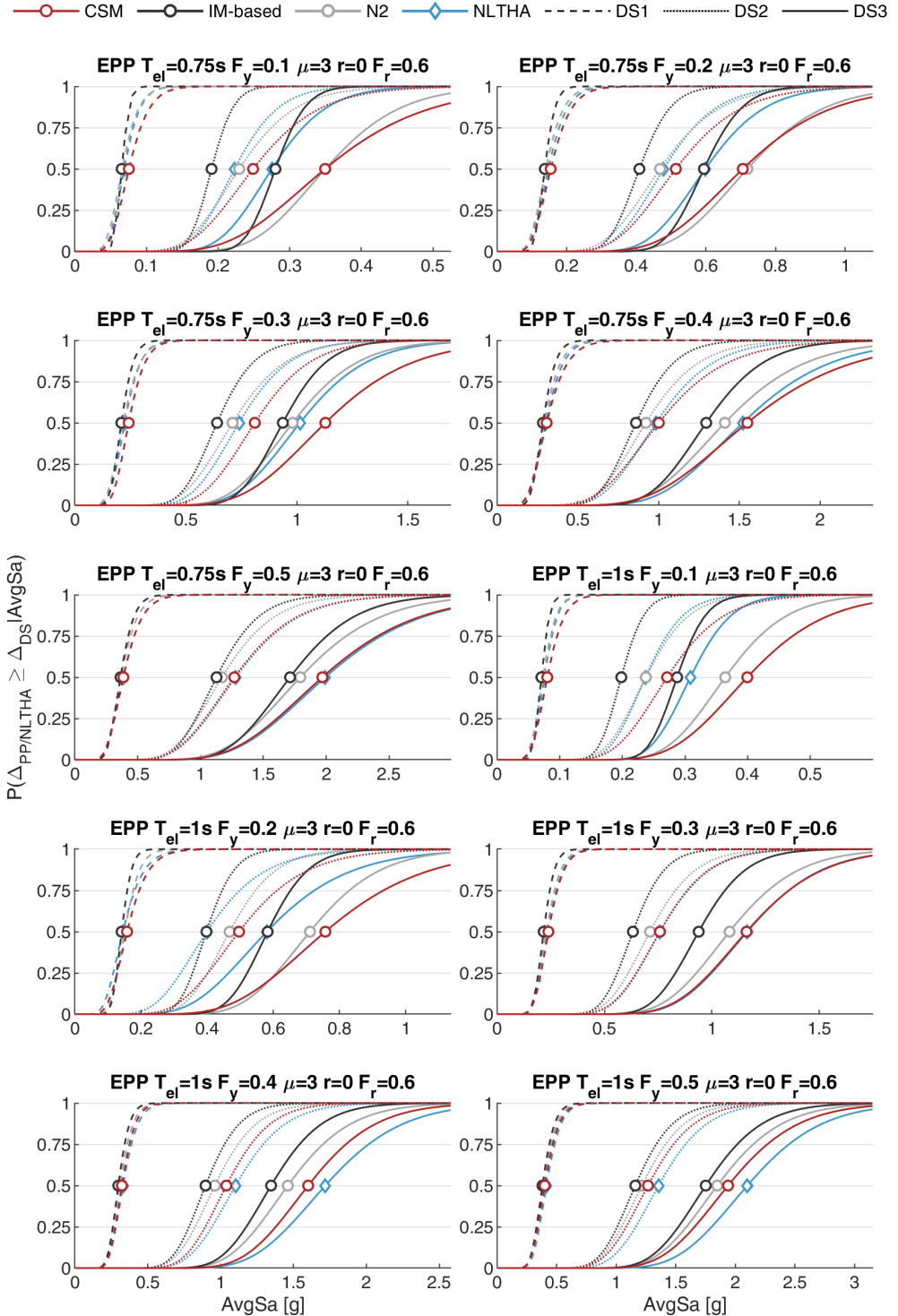




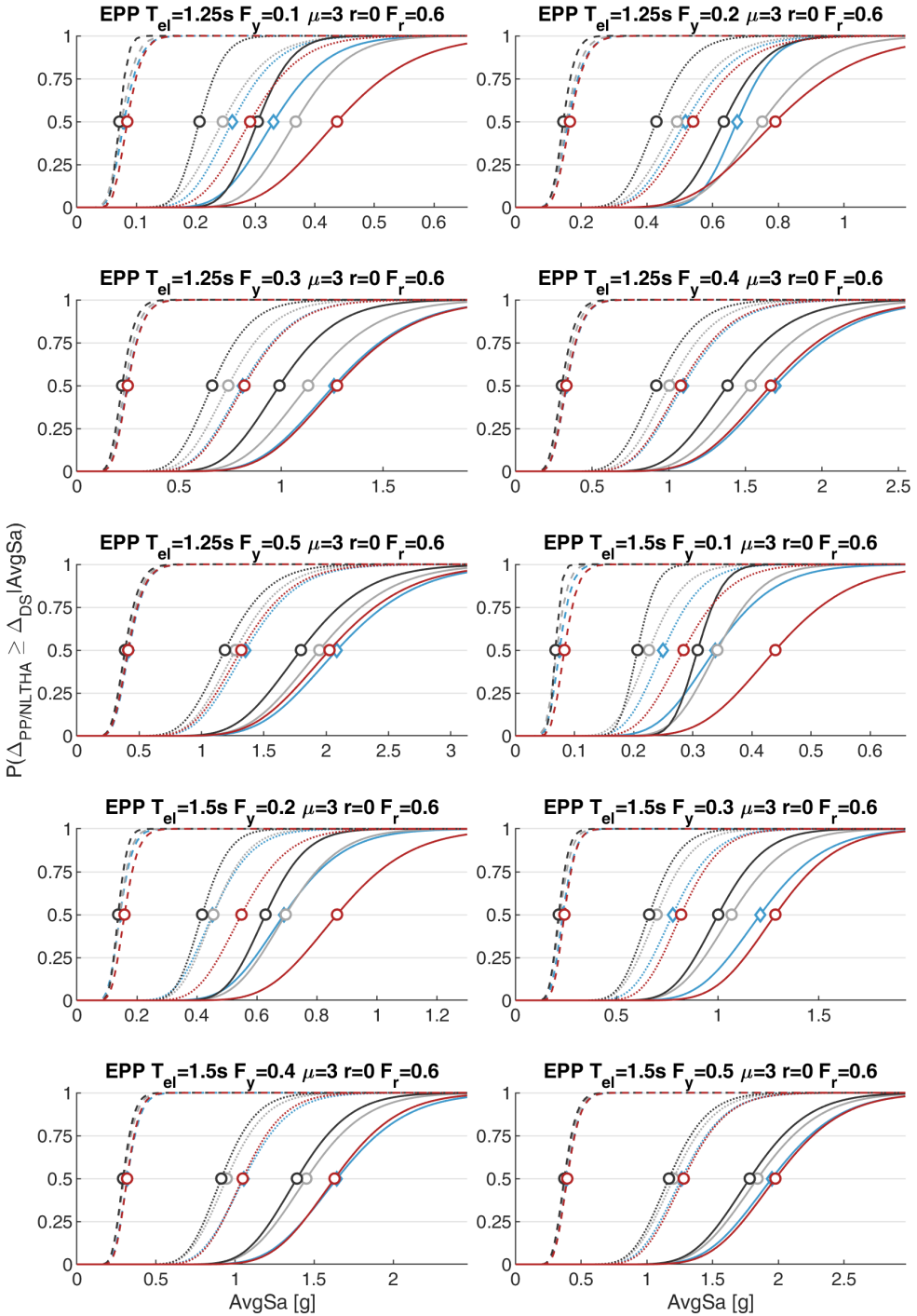
—○— CSM
 —○— IM-based
 —○— N2
 —◇— NLTHA
 - - - - - DS1
 ······ DS2
 ——— DS3

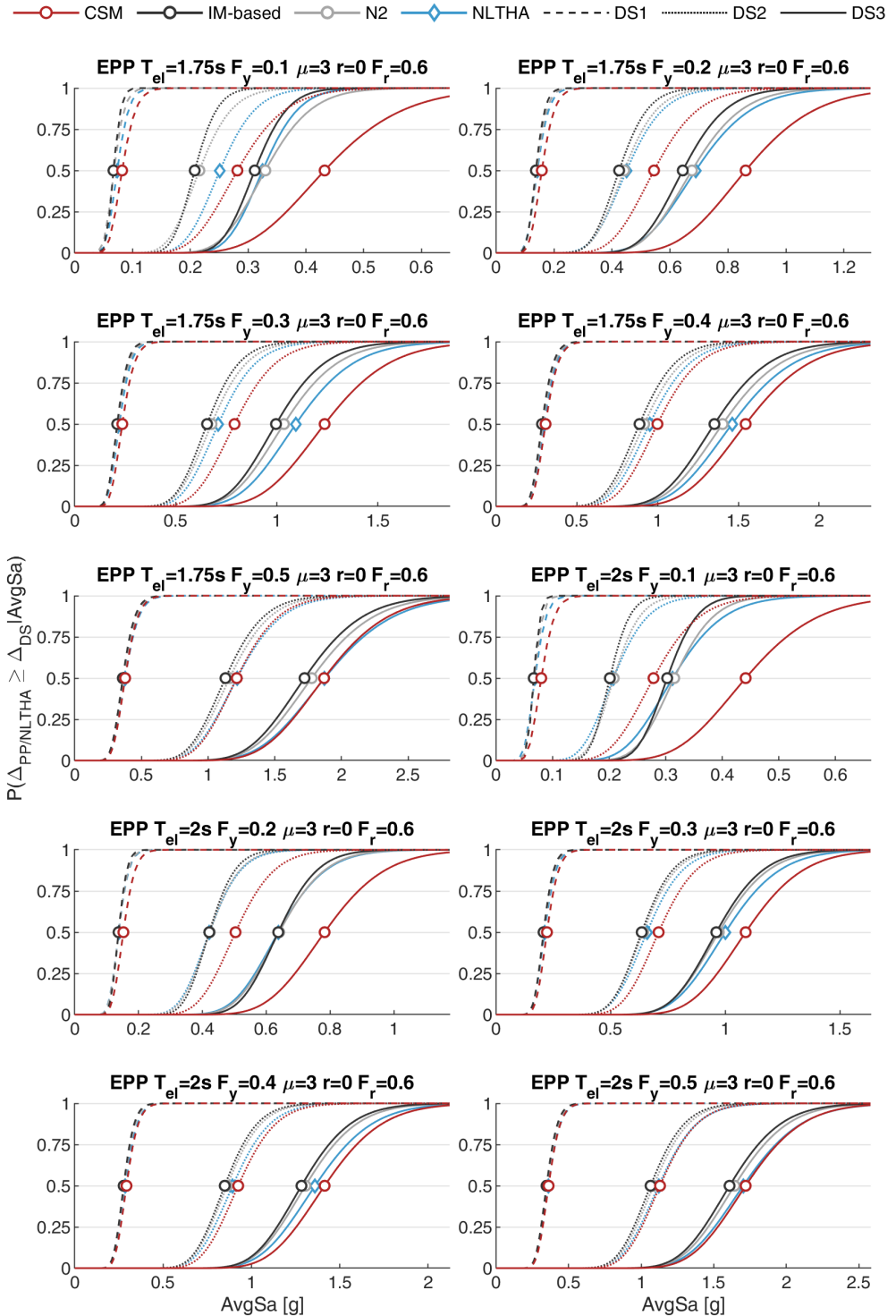




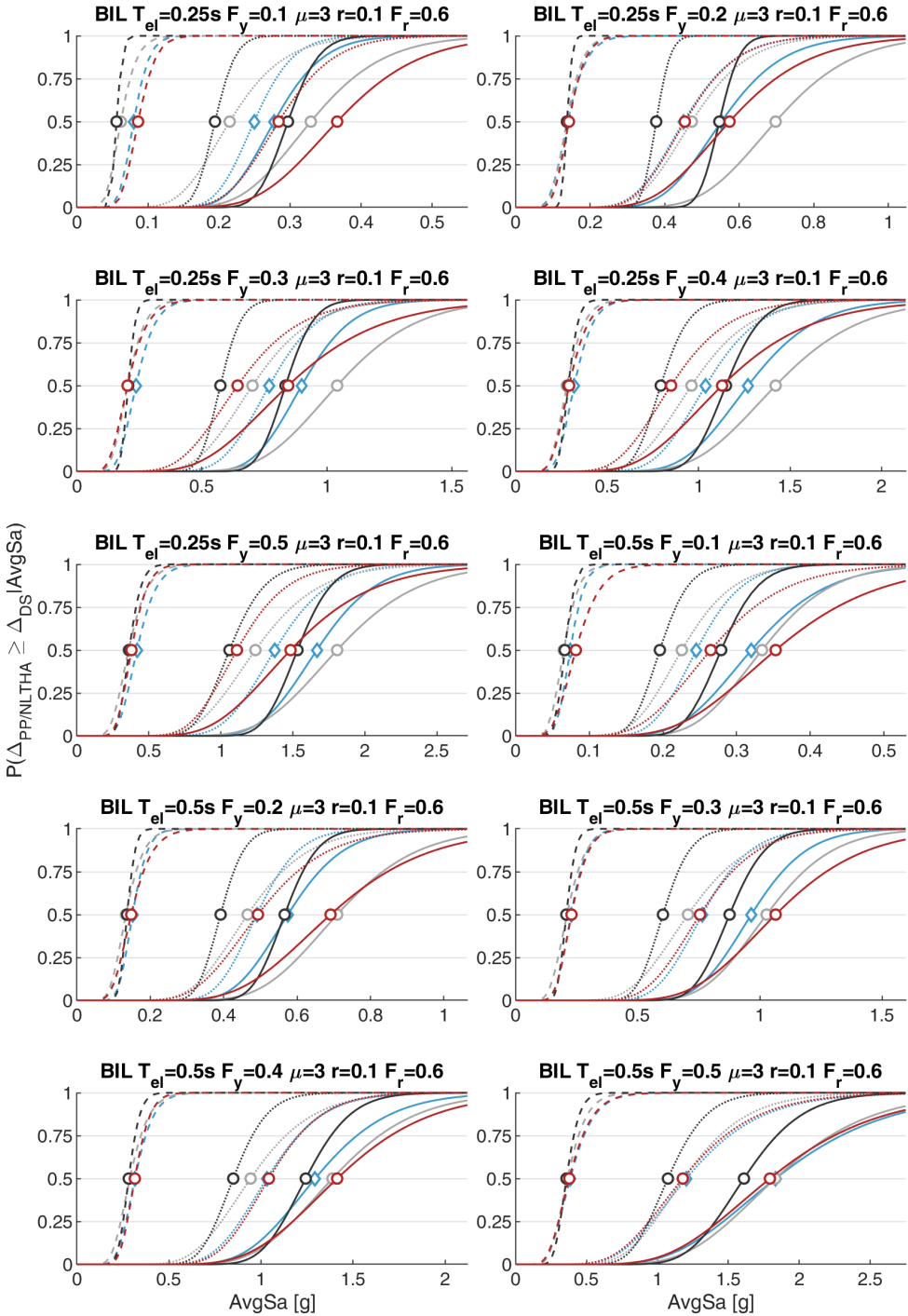


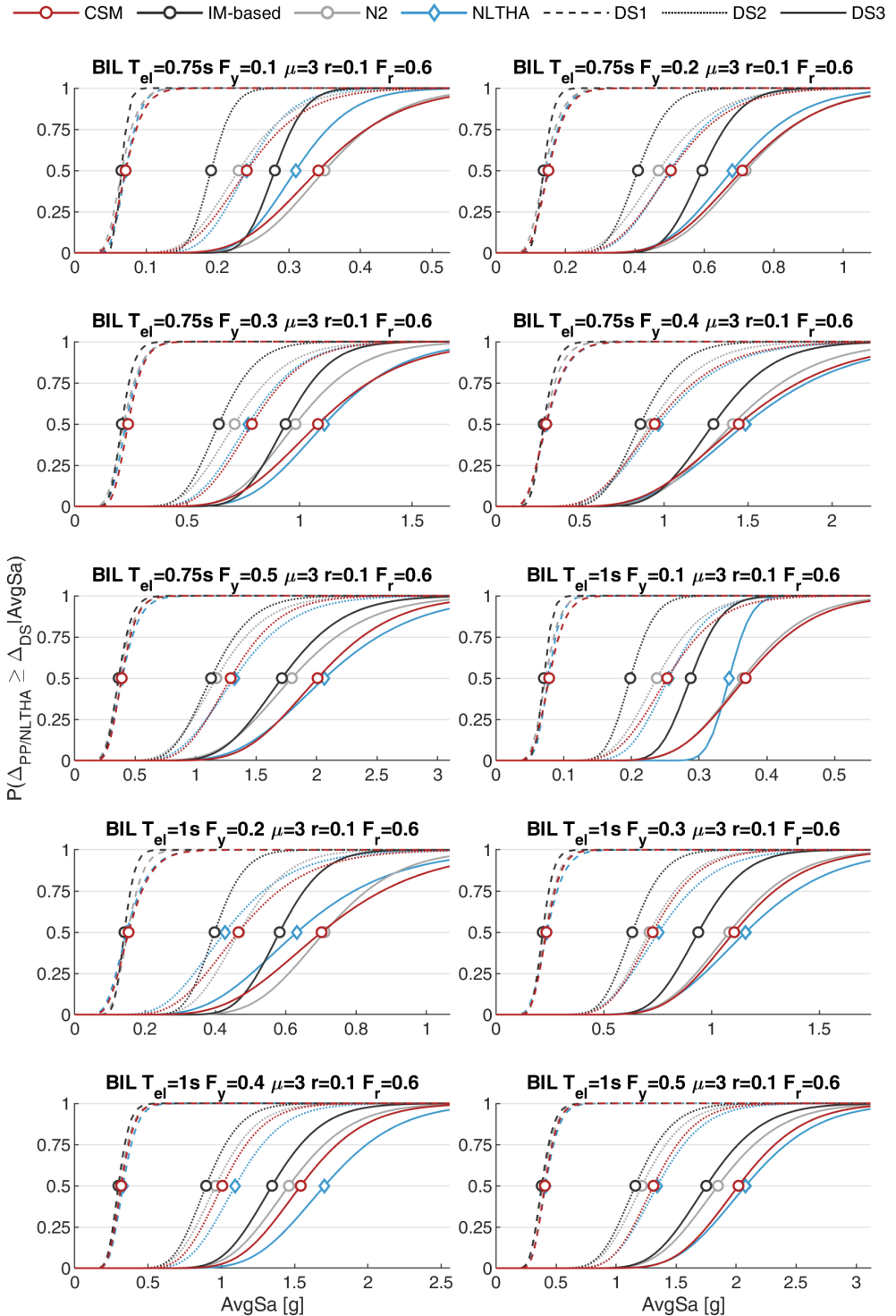
—○— CSM
 —○— IM-based
 —○— N2
 —◇— NLTHA
 - - - - - DS1
 ······ DS2
 ——— DS3



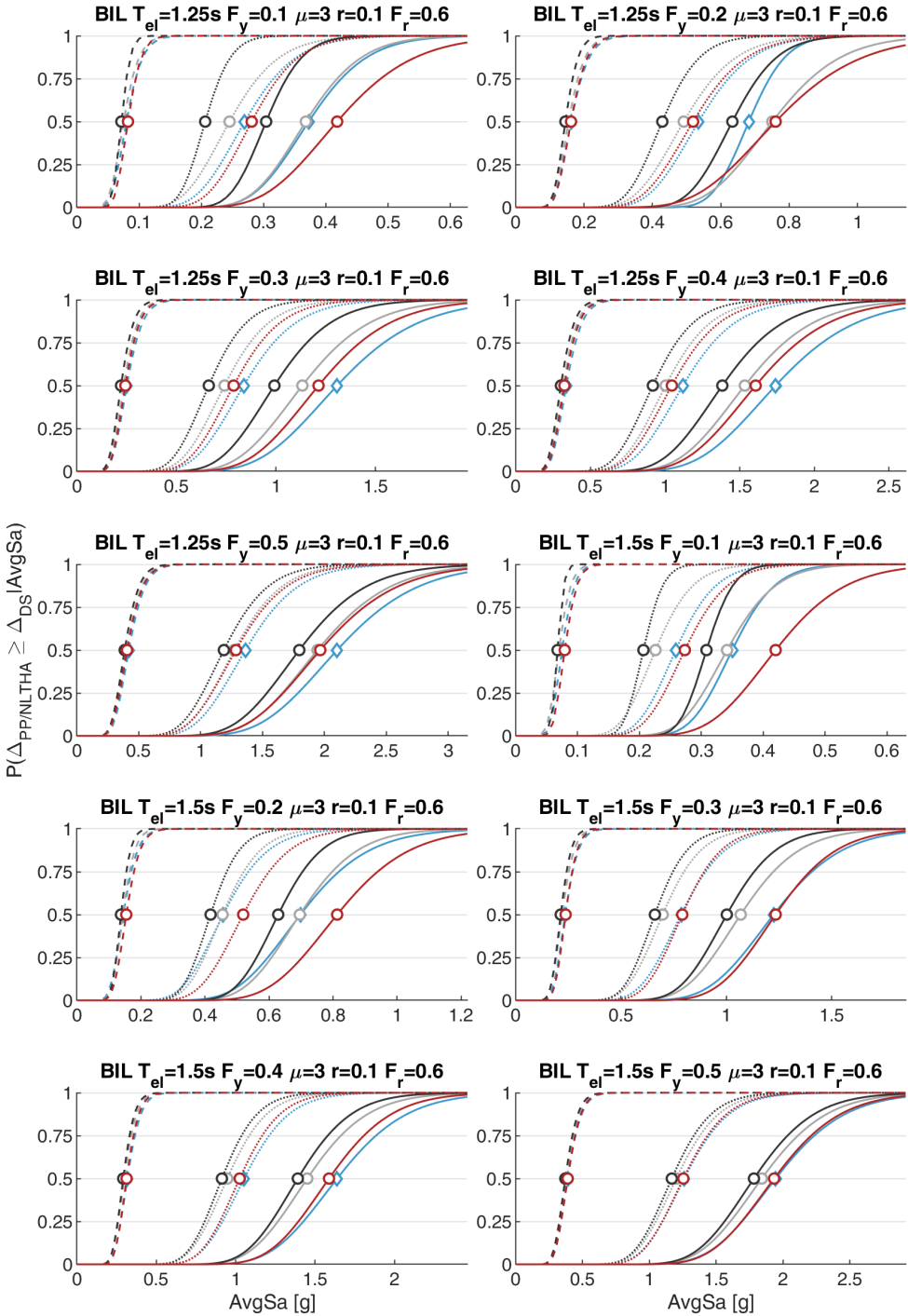


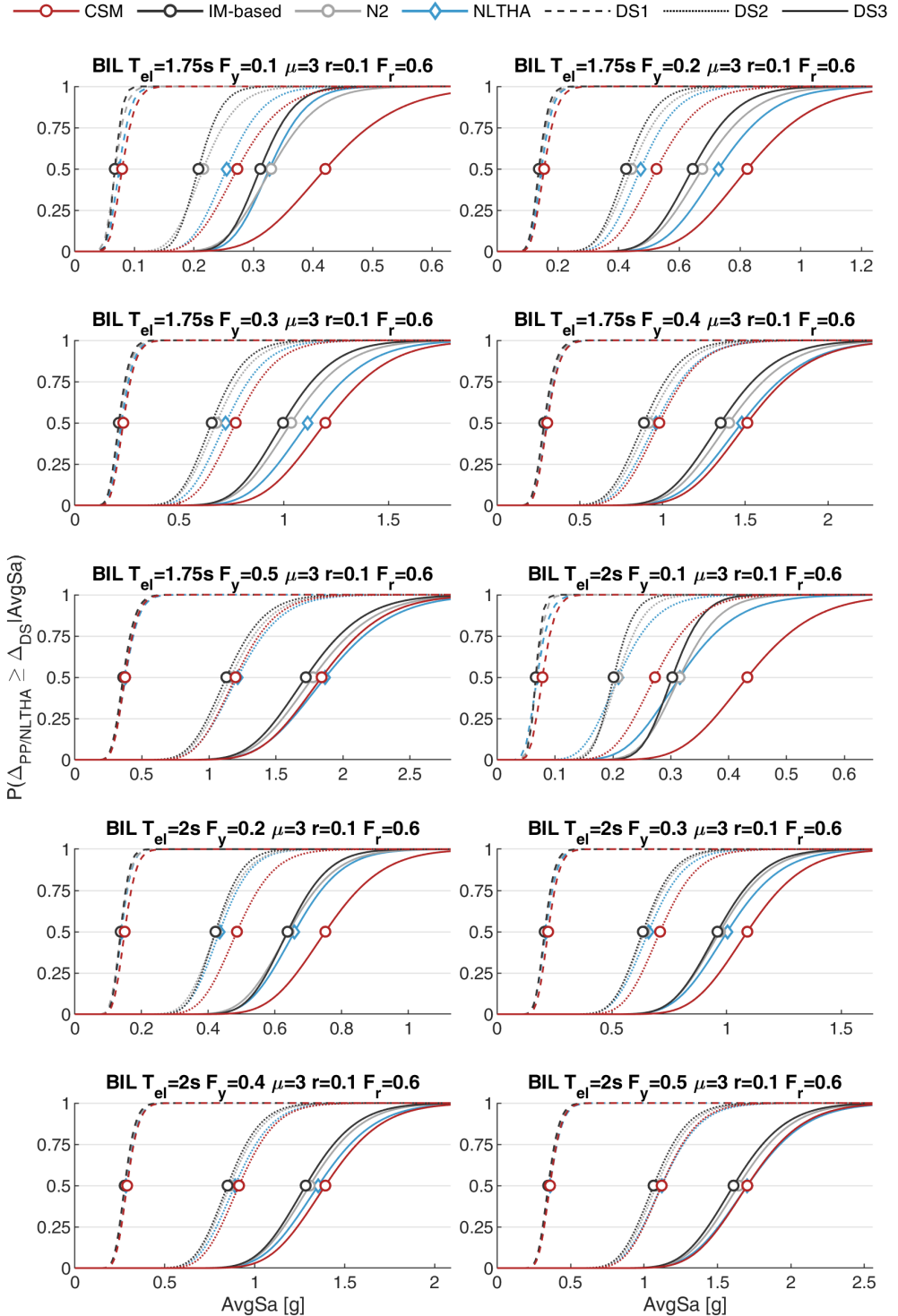
—○— CSM
 —○— IM-based
 —○— N2
 —◇— NLTHA
 - - - - - DS1
 ······ DS2
 ——— DS3





—○— CSM
 —○— IM-based
 —○— N2
 —◇— NLTHA
 - - - - - DS1
 ······ DS2
 — DS3





Acknowledgements

This study was conducted as part of the Industrial PhD research program (PON-RI 2014-2020) sponsored by the Italian Ministry of Education, University and Research (DOT130UZWT). I would like to thank all those who have accompanied me day after day, step by step, consciously or unconsciously on this journey, teaching me to run towards what I want to be the goal of my life.

Curriculum Vitae

Andrea Nettis

👤 Personal Info



Date of Birth: 31/05/1992
Nationality: Italian
Phone: +39 3335371728
Email: nettisandrea92@gmail.com
Skype: nettisandrea_1
LinkedIn: <https://www.linkedin.com/in/andrea-nettis-0283b475/>
ResearchGate: <https://www.researchgate.net/profile/Andrea-Nettis-2>

👤 About

Specialist in structural engineering with special focus on seismic vulnerability of existing structures. Expertise in structural modelling, vulnerability analysis and risk assessment. Research in innovative approaches for management of existing construction heritage (remote-sensing, GIS and BIM). Professional goals: multi-hazard risk engineering and catastrophe modelling.

📅 Academic and professional experience

01/2019 – 07/2019
Bari, Italy

Visiting researcher Planetek Italia

Data-driven structural assessment approach for existing highway bridges via satellite-based persistent scatter interferometry.

08/2020 – 02/2021
Valencia, Spain

Visiting PhD student Universitat Politècnica De València - ICITECH

Structural monitoring and displacement-based seismic assessment for steel truss railway bridges supported by steel towers.

01/2019 – 02/2021
Bari, Italy

Teaching assistant Polytechnic University of Bari - DICATECH

- Teaching support for the course "Seismic Design" and "Design laboratory"
- Seminars for the course "Theory and Design of Bridges"
- Co-supervision of final dissertations for the MSc in Civil Engineering (specialisation in Structures)

07/2017 – 07/2019
Acquaviva delle Fonti,
Bari
, Italy

Self-employed building engineer (part-time)

Support to architectural and structural design, graphics, architectural rendering

03/2014 – 09/2016
Bari, Italy

Peer-Tutor Polytechnic University of Bari - DICAR

Educational support in basic scientific subjects (mathematics, calculus, physics)

🎓 Education

01/2018 – 03/2021
Bari, Italy

PhD in Risk and Environmental, Territorial and Building Development Polytechnic University of Bari

- Simplified approaches for the displacement-based seismic assessment of

- common Italian bridge typologies.
- Fragility analysis via nonlinear static procedures
- Effectiveness of Remotely Piloted Aircraft Systems and photogrammetry for data collection on bridges.
- Proposal of a simplified framework for probabilistic seismic assessment and risk quantification of existing bridges considering an incomplete knowledge level.

09/2011 – 07/2017
Bari, Italy


MSc in Building Engineering - Architecture
Polytechnic University of Bari

110/110 cum laude

Final dissertation: Evaluation of the seismic behaviour and structural recovery of mixed buildings: the case of Piave building complex.

09/2006 – 06/2011
Cassano delle Murge, Bari
, Italy

High School Diploma
Liceo scientifico "Leonardo da Vinci"
92/100

 Journal papers

05/2020

Gentile R., Nettis A., Raffaele D., Effectiveness of the displacement-based seismic performance assessment for continuous RC bridges and proposed extensions
Engineering Structures - Elsevier Ltd.
DOI: 10.1016/j.engstruct.2020.110910

09/2020

Nettis A., Saponaro M., Nanna M., RPAS-Based Framework for Simplified Seismic Risk Assessment of Italian RC-Bridges Buildings - MDPI
DOI: 10.3390/buildings10090150

Nettis A., Gentile R., Raffaele D., Uva G., Galasso C., Cloud Capacity Spectrum Method: including record-to-record variability in fragility analysis using nonlinear static
DOI: 10.1016/j.soildyn.2021.106829

Nettis A., Raffaele D., Adam J. M., Uva G., Displacement-based seismic performance assessment of railway multi-span steel truss bridges
(final draft - internal review)

Nettis A., Raffaele D., Uva G., Efficient seismic risk assessment of multi-span reinforced concrete isostatic bridges accounting for epistemic uncertainty
(final draft - internal review)

Conference papers

- 06/2019 **Nettis A., Gentile R., Uva G., Raffaele D., Validation of an analytical displacement-based pushover for multi-span continuous deck bridges**
COMPDYN 2019 - 7th ECCOMAS Thematic Conference on Computational Methods in Structural Dynamics and Earthquake Engineering
DOI:10.7712/120119.6968.19202
- 06/2019 **Uva G., Ciampoli P., Leggieri V., Nettis A., Ruggieri R., A mechanical approach for estimating regional fragility curves of existing RC building stock in Puglia**
COMPDYN 2019 - 7th ECCOMAS Thematic Conference on Computational Methods in Structural Dynamics and Earthquake Engineering
DOI: 10.7712/120119.7027.19153
- 09/2019 **Nettis A., Gentile R., Uva G., Raffaele D., Some applications of a displacement-based procedure for the seismic response of continuous girder RC-bridges**
CoRASS 2019 - 3rd International Conference on International Conference on Recent Advances in Nonlinear Design, Resilience and Rehabilitation of Structures

Skills

- STRUCTURAL ENGINEERING

SAP2000 ADVANCED	OPENSEES ADVANCED	RUAUMOKO LIMITED	OpenQuake LIMITED
3MURI ADVANCED	CSI Bridge ADVANCED		

- PROGRAMMING SKILLS

MATLAB ADVANCED	PHYTON LIMITED		
--------------------	-------------------	--	--

- GIS AND GEOSPATIAL ANALYSIS

QGIS ADVANCED	ArcGIS ADVANCED	ERDAS LIMITED	
------------------	--------------------	------------------	--

- GRAPHICS

Autocad ADVANCED	Adobe Photoshop ADVANCED	Adobe InDesign BASIC	CINEMA 4D LIMITED
---------------------	-----------------------------	-------------------------	----------------------

- OTHER

macOS ADVANCED	Windows ADVANCED	Latex BASIC	Microsoft Office ADVANCED
-------------------	---------------------	----------------	------------------------------

Certificates

- 03/2018 **Professional training for Civil and Environmental Engineer**
Ordine degli Ingegneri di Bari

06/2017

IELTS Academic - Score 7.0
British Council
CEFR Level C1

La borsa di dottorato è stata cofinanziata con risorse del
Programma Operativo Nazionale Ricerca e Innovazione 2014-2020 (CCI 2014IT16M2OP005),
Fondo Sociale Europeo, Azione I.1 "Dottorati Innovativi con caratterizzazione Industriale"



UNIONE EUROPEA
Fondo Sociale Europeo



*Ministero dell'Università
e della Ricerca*



PON
RICERCA
E INNOVAZIONE
2014 - 2020